MOLECULAR BEAM EPITAXY GROWTH AND CHARACTERIZATION OF CdTe HETEROSTRUCTURES ON GaAs- EFFECT OF INTERFACE, GROWTH, AND ANNEALING CONDITIONS TO CRYSTAL QUALITY

A Thesis Submitted to
the Graduate School of Engineering and Sciences of
İzmir Institute of Technology
in Partial Fulfillment of the Requirements for the Degree of

DOCTOR OF PHILOSOPHY

in Physics

by
Ozan ARI

July 2017
İZMİR

We approve the thesis of **Ozan ARI**

Examining Committee Members:

Prof. Dr. Orhan ÖZTÜRK
Department of Physics, İzmir Institute of Technology

Assoc. Prof. Dr. Özgür ÇAKIR
Department of Physics, İzmir Institute of Technology

Assoc. Prof. Dr. Uğur SERİNCAN
Department of Physics, Anadolu University

Prof. Dr. Sezai ELAGÖZ
Department of Nanotechnology Engineering, Cumhuriyet University

Assoc. Prof. Dr. Serkan ATEŞ
Department of Physics, İzmir Institute of Technology

27 July 2017

Prof. Dr. Orhan ÖZTÜRK
Supervisor, Department of Physcis
İzmir Institute of Technology

Prof. Dr. Ramazan Tuğrul SENGER
Head of the Department of
Physics

Prof. Dr. Aysun SOFUOĞLU
Dean of the Graduate School of
Engineering and Sciences

ACKNOWLEDGMENTS

First of all, I would like to express my deepest gratitude to my previous advisor Professor Yusuf Selamet whom recently deceased for his continued support and guidance through my Ph.D. study. His enthusiasm for science has greatly impressed me. His expertise on molecular beam epitaxy has helped me to overcome critical problems and prepared for future challenges. I am also deeply grateful to my advisor Professor Orhan Öztürk for his editorial advice which was essential to the completion of this dissertation. I also thank my co-advisor Professor Sivalingam Sivananthan for his support.

I am grateful for the use of x-ray electron spectroscopy in AQUAREC and I thank Professors Lütfi Özyüzer and Gülnur Aygün Özyüzer for their technical support.

Particular thanks to our former research group members for their help during the study this study. I want to thank Mustafa Polat for help on the XRD measurements, Elif Bilgilisoy for EPD, AFM and help on the XRD measurements, Elif Özçeri for PL and XPS measurements, Selin Özden for AFM measurements, Hasan Aydın for AFM measurements, Begum Yavaş for Nomarski images, Emine Bakali and Atike İnce for SEM measurements.

Last, but not least, I would like to thank my love, my best friend, and my wife Özge for her understanding, trust, support and confidence in me; and my parents and sisters for unconditional love and support through my life.

ABSTRACT

MOLECULAR BEAM EPITAXY GROWTH AND CHARACTERIZATION OF CdTe HETEROSTRUCTURES ON GaAs- EFFECT OF INTERFACE, GROWTH, AND ANNEALING CONDITIONS TO CRYSTAL QUALITY

Highly crystalline CdTe structures are desired for solar cells, x-ray detectors, electro-optical modulators, and especially in $Hg_{1-x}Cd_xTe$ infra-red detectors. Epitaxial growth of $Hg_{1-x}Cd_xTe$ infra-red layers are usually performed on lattice matched bulk CdZnTe substrates. But, limited size and fragile nature of the CdZnTe have led to a push for alternative substrates such as GaAs. The large lattice mismatch between $Hg_{1-x}Cd_xTe$ and GaAs requires an implantation of a buffer layer such as CdTe. In addition (211)B orientation is preferred due to high sticking coefficient of Hg on this orientation and suppression of twin formation. In the first part of this study, the effect of the thermal deoxidation of GaAs(211)B surface on which CdTe layers grown was investigated by various *in situ* and *ex situ* experimental techniques. The changes in the surface chemical structure and morphology of GaAs(211)B substrates with As_4 and In assisted deoxidation under various conditions were presented. Secondly, the effect of the growth conditions on CdTe epilayers by using molecular beam epitaxy were investigated in two parts; (1) the initiation of the CdTe growth and (2) the equilibrium growth conditions. The correlations between the structural defects, twins, point defects, and dislocations with the growth conditions are determined. Thirdly, the effect of the cyclic annealing to the crystal and surface quality of the CdTe epilayers were investigated by using different temperatures during the annealing. Finally, the effect of the temperature uniformity during the production of the CdTe layers was investigated by the two substrate heater geometries consisting of rotational symmetric and tilted at the edge. A new approach to study the dislocations with different types of cores proposed by Ayers is applied to the zinc blende (211) crystal orientation. It has been shown that the dislocations having two different cores responded differently to both growth and annealing conditions. The results of the experimental techniques probing the dislocation density in CdTe layers are not well correlated with each other due to dual origin of these dislocations. The compressive and biaxial stresses building in the CdTe layers due to growth and annealing conditions were resolved with the investigation of the optical properties of the layers.

ÖZET

CdTe HETERO-YAPILARININ GaAs ÜZERİNE MOLEKÜLER DEMET EPİTAKSİ ile BÜYÜTÜLMESİ ve KARAKTERİZASYONU - ARAYÜZ, BÜYÜTME ve TAVLAMA KOŞULLARININ KRİSTAL KALİTESİNE ETKİSİ

Güneş pilleri, x-ışını detektörleri, elektro-optik modülatörler ve özellikle de HgCdTe kızılötesi dedektörler için yüksek kristal kalite CdTe yapıları arzu edilmektedir. HgCdTe kızıl ötesi tabakaların epitaksiyel büyütülmesi genellikle örgü uyumlu CdZnTe alt-tabanları üzerinde gerçekleştirilir. Ancak, CdZnTe'nin sınırlı boyutu ve kırılganlığı GaAs gibi alternatif alt-tabanlara yönenilmesine yol açmıştır. HgCdTe ve GaAs arasındaki büyük örgü uyuşmazlığı, CdTe gibi bir tampon katmanın GaAs taban üstüne büyütülmesini gerektirir. Ek olarak, (211) B yüzey yönelimi seçilerek, Hg'nın yapışma katsayısının yüksek olması ve ikiz oluşumunun bastırılması sağlanabilir. Bu çalışmanın ilk bölümünde, CdTe tabakalarının büyütülmesinde alt-taban olan GaAs (211)B yüzeyinin termal deoksidasyonunun etkisi, çeşitli *in situ* ve *ex situ* karakterizasyon teknikleriyle araştırılmıştır. Çeşitli koşullar altında gerçekleştirilen As_4 ve In akısı altında deoksidasyonun, GaAs (211) B tabanlarının yüzey kimyasal yapısı ve morfolojisine etkisi sunulmuştur. İkinci olarak, büyüme koşullarının moleküler demet epitaksi yöntemi ile büyütülen CdTe epi-katmanlara etkisi iki bölümde incelenmiştir; (1) CdTe büyütmesinin başlatılması ve (2) kararlı durumda gerçekleştirilen büyütme koşulları. Yapısal kusurlar, ikizler, nokta kusurları ve dislokasyonlar ile büyütme koşulları arasındaki korelasyonlar belirlenmiştir. Üçüncü olarak, tekrarlı tavlamanın CdTe epikatmanların kristal ve yüzey kalitesine etkisi farklı tavlama sıcaklıkları ile araştırılmıştır. Son olarak, CdTe katmanlarının büyütülmesi ve tavlanması sırasındaki sıcaklık homojenitesinin etkisi, dairesel simetri ve bu simetrinin kırılmasıyla oluşan ısıtıcı geometrisi ile araştırılmıştır. Ayers tarafından önerilen ve Çinko-blend yapıdaki kristallerde bulunan farklı kökenli dislokasyonların incelemek için sunulan yöntem, (211) kristal yönelimine uygulanmıştır. İki farklı çekirdeğe sahip dislokasyonların büyütme ve tavlama şartlarından farklı olarak etkilendiği gösterilmiştir. CdTe katmanlarındaki dislokasyon yoğunluğunu ölçen deneysel tekniklerin sonuçları arasındaki uyumsuzluğa Çinko-blende yapılardaki dislokasyonların iki farklı çekirdeğe sahip olmasının neden olduğu tespit edilmiştir. CdTe katmanlarında büyütme ve tavlama koşulları nedeniyle oluşan baskı ve çift eksenli gerilmeler, katmanların optik özelliklerinin incelenmesi ile tespit edilmiştir.

TABLE OF CONTENTS

LIST OF FIGURES

LIST OF TABLES

LIST OF ABBREVIATIONS

0D	Zero dimension
1D	One dimension
2D	Two dimension
3D	Three dimension
AFM	Atomic force microscopy
β	Full width at maximum
BEP	Beam equivalent pressure
BFM	Beam flux monitor
CLS	Core level shift
CP	Critical point
CVD	Chemical vapour deposition
DF	Dual filament
E_g	Near-gap emission
EMA	Effective medium approach
EPD	Etch pit density
E_Y	Emission line located at 1.47 eV in PL spectrum
FCC	Face-centered cubic
FTIR	Fourier transform infra-red
FWHM	Full width at half maximum
GM	Growth module
HRXRD	High resolution x-ray diffraction
IR	Infra-red
LL	Load Lock
LN2	Liquid nitrogen
LPE	Liquid phase epitaxy
LWIR	Long-wave infra-red
MBE	Molecular beam epitaxy
MOCVD	Metal-organic chemical vapour deposition
MSE	Mean squared error
MWIR	Middle-wave infra-red
PID	Proportional, integral, and derivative
PL	Photoluminescence
RC	Rocking curve

RHEED	Reflection high energy electron diffraction
RMS	Root mean square
RPM	Rotations per minute
RSM	Reciprocal space map
SE	Spectroscopic ellipsometry
SEM	Scanning electron microscopy
SK	Skewness
SWIR	Short-wave infra-red
T/C	Thermo-couple
UHV	Ultra high vacuum
UV	Ultra-violet
VIS	Visible
XRD	X-ray diffraction
XRR	X-ray reflectivity
XPS	X-ray photo-electron spectroscopy

CHAPTER 1

INTRODUCTION

CdTe has wide range of application areas such as solar cells [1], x-ray detectors [2, 3], and electro-optical modulators [4, 5]. Alternatively, CdTe has been used as substrate [6, 7] or buffer layer [8–11] for epitaxial growth of $Hg_{1-x}Cd_xTe$ which is a ternary alloy of Hg, Cd, and Te. $Hg_{1-x}Cd_xTe$ is an important material for IR detection applications. $Hg_{1-x}Cd_xTe$ is leading the infra-red (IR) detection research area with the properties as high absorption coefficient and carrier mobility with long carrier lifetime [12–14]. Band gap of $Hg_{1-x}Cd_xTe$ can be tuned with the mole fraction of Cd (x) in $Hg_{1-x}Cd_xTe$ between -0.15 eV and ~1.5 eV at 293 K [15]. Due to controllable band gap property, $Hg_{1-x}Cd_xTe$ can be used as absorber layer in detector structures for short-wave IR (SWIR) (1-2.5 μm), mid-wave IR (MWIR) (3-5 μm), long-wave (LWIR) (8-14 μm), and very long-wave (VLWIR) (16-22 μm) bands of the IR electromagnetic spectrum (Figure 1.1).

The range of $Hg_{1-x}Cd_xTe$ IR detectors varies from medical imaging[16] (i.e. monitoring blood flow) to space applications [17] (i.e. monitoring black holes). In particular, $Hg_{1-x}Cd_xTe$ IR detectors are widely used for thermal imaging cameras since black body radiation of objects at room temperature peaks at ~ 9.7 μm. Additionally, LWIR region of the electromagnetic spectrum is transparent, allowing penetration of emission from objects at far distances (Figure 1.1). Thus, LWIR $Hg_{0.8}Cd_{0.2}Te$ are commonly used by defense industry for military applications such as missile guidance, threat identification, and perimeter monitoring [12, 14].

Discovery of $Hg_{1-x}Cd_xTe$ dates back to 1959 [19]. Growth of highly crystalline $Hg_{1-x}Cd_xTe$ has initially started with bulk growth methods later following with epitaxial growth. Epitaxial growth of $Hg_{1-x}Cd_xTe$ has been accomplished on IR-transparent substrates. Today, three main epitaxial growth techniques dominates $Hg_{1-x}Cd_xTe$ research and manufacturing areas: liquid phase epitaxy (LPE), metal-organic chemical vapour deposition (MOCVD), and molecular beam epitaxy (MBE) [20]. Between all the three, LPE is the most mature and commonly used growth method to achieve higher crystal quality with low defect density [20]. Highly crystalline growth of $Hg_{1-x}Cd_xTe$ requires lattice matched substrate. LPE growth of $Hg_{1-x}Cd_xTe$ has been mostly performed on lattice matched CdZnTe (4% Zn) which initially started at 1981 [21]. Change in lattice constant of $Hg_{1-x}Cd_xTe$ for all range of Cd mole fraction is only 0.6 % [15]. Therefore,

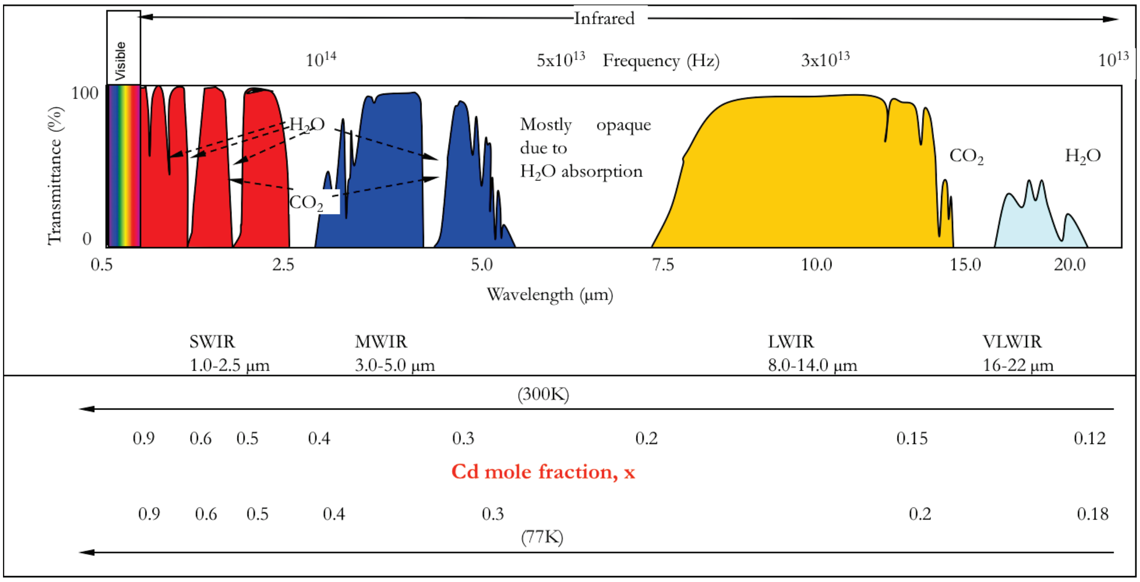

Figure 1.1.: Transmission chart of the IR electromagnetic radiation through atmosphere. SWIR, MWIR, LWIR, and VLWIR bands with the required Cd mole fractions in $Hg_{1-x}Cd_xTe$. [18]

CdZnTe with approximately 4 % Zn mole fraction is suitable as lattice matched substrate to $Hg_{1-x}Cd_xTe$ (Figure 1.2).

Highly crystalline $Hg_{1-x}Cd_xTe$ layers grown by LPE on CdZnTe layers are routinely obtained. The crystal quality of these layers are characterized with the X-ray diffraction (XRD) rocking curve (RC) measurements and defect decorative etching. The measured full width at half maximum (FWHM) of XRD RC and etch pit density (EPD) of these layers are 25-40 arc-s and 1×10^4 - 1×10^5 cm^{-2}, respectively. [20].

As technological development of IR detectors proceeds, 3rd and 4th generation IR detector technologies (i.e. multi-color detection, high operating temperature) require complex structures such as multi-layers. LPE method can not deliver the requirements of these detector technologies. Therefore, focus of the $Hg_{1-x}Cd_xTe$ based IR detector research area was shifted to vapour phase epitaxy methods: MBE and MOCVD [20]. Growth of large area layers with homogeneous doping and composition profiles for complex structures is readily obtainable with vapour phase epitaxy methods. In particular, MBE has the advantages of *in situ* characterization tools and precise control of molecular or atomic fluxes hence controlling growth rate and vertical composition changes. These advantages makes the MBE most popular vapour epitaxy method for $Hg_{1-x}Cd_xTe$ based IR detector applications.

Epitaxial growth of $Hg_{1-x}Cd_xTe$ are mostly conducted on lattice constant and nearly thermal expansion coefficient matched substrate such as CdZnTe with ~ 4 % Zn content. An important advantage of using CdZnTe as substrate for heteroepitaxial growth of the $Hg_{1-x}Cd_xTe$ is the prevention of dislocation generation due to lattice mismatch and thermal expansion coefficient difference. On the other hand, CdZnTe has many disadvantages. CdZnTe is very fragile and can easily be damaged during handling. Growth of CdZnTe is mainly carried out by few companies only with limited sized up to 7 × 7 cm^2 and square shape. Currently, most of the semiconductor manufacturing facilities are compatible with round shaped wafers. In addition, $Hg_{1-x}Cd_xTe$ IR detectors grown on CdZnTe wafers suffer from the defects propagating from CdZnTe surface. Finally, unit cost of CdZnTe wafers is quite high compared to other possible lattice mismatched substrates. Therefore, $Hg_{1-x}Cd_xTe$ growth on alternative substrates has been highly attractive research area for 3rd and 4th generation IR detectors [20].

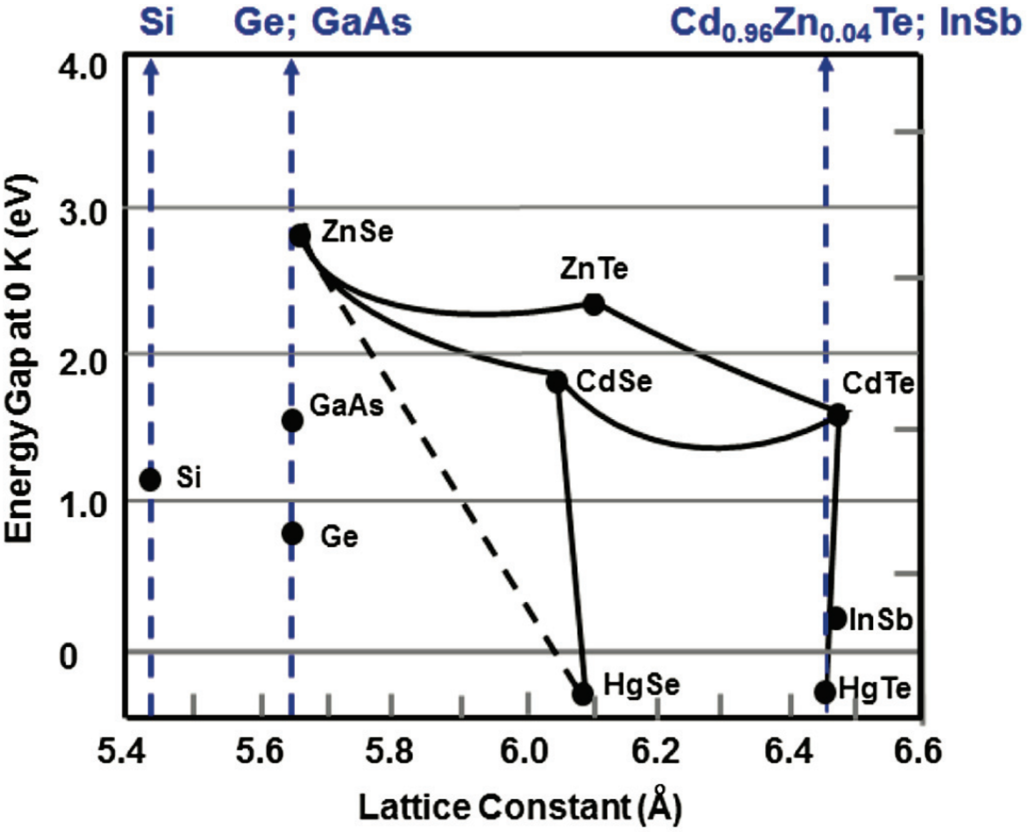

Figure 1.2.: Energy gap of semiconductors (zinc blende and diamond) as a function of lattice constant. Room temperature values are shown [22].

Alternative substrates for epitaxial growth of $Hg_{1-x}Cd_xTe$ such as Si, Ge, InSb, GaSb, and GaAs which have attracted attention during last decades, do not suffer from the consequences explained above. Especially, large size availability and mature bulk growth technology of Si, Ge, and GaAs differentiate these alternative substrates from others. Figure 1.2 shows band gap and lattice constant values of different substrates.

Lattice mismatch between $Hg_{1-x}Cd_xTe$ and Si, Ge, and GaAs is 19 %, 14.1 %, and 14.3 %, respectively. $Hg_{1-x}Cd_xTe$ layers grown directly on alternative substrates have very high dislocation density dramatically reducing IR detector performance. In order to reduce the lattice constant mismatch between $Hg_{1-x}Cd_xTe$ and substrates, commonly a buffer layer is grown in between the substrates and HgCdTe epilayers [20]. Growth of polar crystal structures on non-polar substrates is another issue due to low sticking coefficient of the molecules or individual atoms of these polar structures on non-polar crystals [15]. Therefore, surfaces of Si and Ge crystals are terminated with As or Te atoms prior to buffer layer growth. Buffer layer choice for $Hg_{1-x}Cd_xTe$ growth on alternative substrates is usually CdTe. Lattice mismatch between $Hg_{0.8}Cd_{0.2}Te$ and CdTe is 0.25 % [15]. Thermal expansion coefficients of $Hg_{1-x}Cd_xTe$ and CdTe are also compatible [15]. Additionally, contamination by foreign atoms through diffusion from CdTe buffer layer to $Hg_{1-x}Cd_xTe$ is not possible.

Crystal and surface defects of substrates and buffer layers are detrimental to epitaxy of $Hg_{1-x}Cd_xTe$. These defects propagate from substrates/buffer layers to $Hg_{1-x}Cd_xTe$ layers with deleterious effects on the overall performance of IR detector structures. Crystal defects originate from either substrate or buffer layers. Bulk CdZnTe crystals with a low defect density of $\sim 10^4$ cm^{-2} are commercially available. Therefore, $Hg_{1-x}Cd_xTe$ layers grown on lattice matched CdZnTe substrates with defect density on the order of 10^5 cm^{-2} are readily obtainable. On the other hand, the lowest reported defect density values of $Hg_{1-x}Cd_xTe$ layers grown on alternative substrates are $\sim 2 \times 10^6$ cm^{-2} [23, 24]. Dislocations at the interface between alternative substrate and buffer layer thread to buffer layers surface and $Hg_{1-x}Cd_xTe$. Threading dislocations originate from the misfit dislocations at the interface between alternative substrate and buffer layer due to lattice constant and thermal expansion coefficient differences of substrate and buffer layer. Crystal defects create shallow and deep impurity states in the band-gap of $Hg_{1-x}Cd_xTe$ layers reducing the minority carrier lifetime in IR FPA detectors [15]. As a figure of merit, R_0A is generally used to determine IR FPA performance. R_0A, dynamic resistance at zero applied voltage (R_0) multiplied by area of the diode (A), is indirectly correlated with threading dislocation density [25]. In figure 1.3, R_0A product versus dislocation density (measured with defect decorating etching) is plotted in terms of EPD. At 77 K, R_0A begins to decrease at EPD of $\sim 5 \times 10^5$ cm^{-2}. Therefore, maximum dislocation density of 5×10^5 cm^{-2} is essentially required for $Hg_{1-x}Cd_xTe$ based IR FPA devices operates at LWIR bandwidth.

Significant progress has been achieved in $Hg_{1-x}Cd_xTe$ growth on Si, Ge, and GaAs alternative substrates. Typically, EPD values of $Hg_{1-x}Cd_xTe$ layers grown on CdTe/GaAs

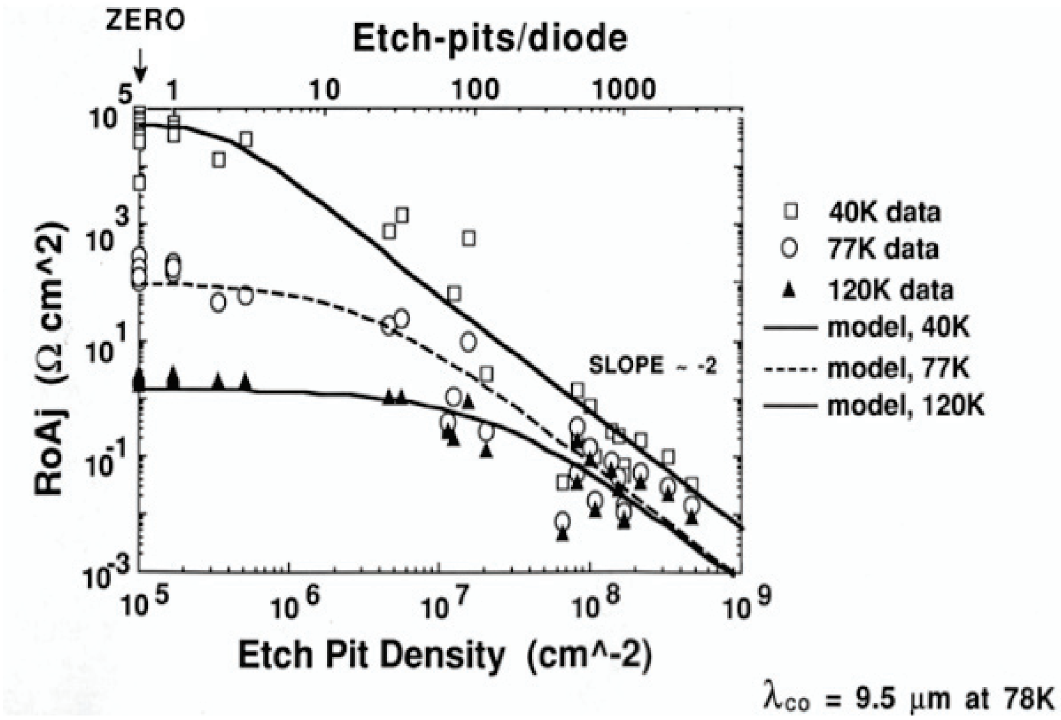

Figure 1.3.: R_0A versus EPD, displaying data from an array with a junction with cut off of 9.5 μm [25].

or CdTe/Si layers with 2×10^6 cm^{-2} to 4×10^6 cm^{-2} are repeatedly obtained which are 4 to 8 times higher than the required EPD value for LWIR operation [24, 26, 27]. In order to further reduce dislocation density of (LWIR) $Hg_{1\text{-}x}Cd_xTe$ layers grown on alternative substrates, many approaches has been investigated. These approaches can be summarized as growing thick (~10 μm) CdTe buffer layers [26, 28], applying in situ [29] or ex situ [30] annealing of CdTe buffer layers, initiating of buffer layer growth with a layer with reduced lattice mismatch (i.e. ZnTe) [28], forming reticulated structures [31] on CdTe buffer layer, and selective area growth of CdTe on nanopatterned substrates [32].

The aim of this thesis is to study effects of the interface, growth, and annealing conditions to crystal quality of the epitaxial CdTe layers grown on GaAs substrates. In Chapter 2, crystallographic properties and defect structures of the zinc-blende crystals are summarized. Defect types for the zinc-blende crystals are given in detail. In particular, a detailed description of the dislocations in zinc-blende crystals are given. Chapter 3 includes basics of growth and characterization techniques. Characterization techniques including spectroscopic ellipsometry (SE), reflection high energy electron diffraction (RHEED), XRD, x-ray reflectivity (XRR), Fourier transform IR (FTIR) transmission spectroscopy, x-ray photo-electron spectroscopy (XPS), atomic force microscopy (AFM), and photoluminescence (PL). To investigate the effect of the interface to the CdTe crystal quality and surface morphology, thermal surface preparation of the GaAs layers were studied and the experimental results are given in Chapter 4. A new thermal surface preparation method is proposed for GaAs(211) substrates. Chapter 5 explores nucleation and growth dynamics of heteroepitaxy of CdTe on GaAs(211). Effect of the equilibrium growth parameters on CdTe layers are presented. The annealing of CdTe layers were studied and the experimental results are given in Chapter 6. Additionally, the effects of the temperature uniformity during deoxidation, growth and the annealing was investigated. Finally, Chapter 7 summarizes the results and the conclusions.

CHAPTER 2

PHYSICAL PROPERTIES AND DISLOCATION STRUCTURE

The purpose of this chapter is to briefly give crystallographic properties and defect structures of zinc blende lattice, especially GaAs and CdTe, which have crucial effect on heteroepitaxy of these materials. In particular, dislocations, interaction of dislocations and related slip systems in zinc-blende crystals are reviewed which will be continuously regarded in the following chapters for evaluation of characterization results from different techniques.

2.1. Structural Properties of Zinc Blende Crystals

Periodic array of atoms form solids in three-dimension. Semiconductor materials are mostly studied under their crystalline structures. III-V and II-VI compound semiconductors such as GaAs and CdTe have zincblende crystal structure (see Figure 2.1). Every atom has four nearest neighbors in zincblende crystal structure. Bonds between the atoms have covalent and ionic bond characteristics, while bonds between II-VI atoms tend to be more ionic than the bonds in III-V structures. Primitive unit cell of zincblende structure has a tetrahedron shape with two basis. However, this arrangement of atoms may be understood easily as two interpenetrating face-centered cubic (FCC) unit cells which is called as conventional unit cell of zincblende crystal structure. In this arrangement, the second FCC lattice is shifted from the first FCC unit cell as one-fourth of the body diagonal of the first FCC unit cell. There are two atoms in the primitive unit cell of the zincblende structure, similar to the diamond structure. However, in the zincblende structure one atom is from group III-A (II-B) while the other atom is from group V-A (VI-A). Therefore, there are two FCC sublattices which are formed from different group of elements. The space group of zinc blende structure is F$\bar{4}$3m.

Crystallographic directions and planes of the crystals are usually identified by Miller indices (hkl). Lattice planes of cubic systems are denoted by reciprocal space vectors which intersection of planes are given with $\frac{1}{h}\hat{a}_1$, $\frac{1}{k}\hat{a}_2$, $\frac{1}{l}\hat{a}_3$ vectors and where $\hat{a}_1$,

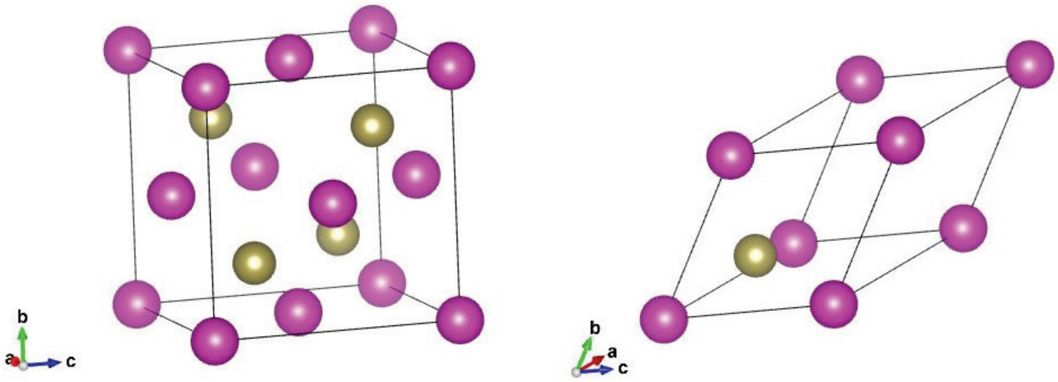

Figure 2.1.: Zincblende structure. Left:Conventional Unit cell; Right: primitive unit cell.

$\hat{a}_2$, and $\hat{a}_3$ are the lattice unit vectors of conventional unit cell. Direction of the lattice planes is given by [hkl] which is normal to lattice plane. Additionally, family of lattice planes which are equivalent under symmetry operations are identified by {hkl}. Cations and anions in the zinc blende crystal take on net positive and negative electrical charges, respectively. Therefore, {111} planes in zinc blende structure are not equivalent. Alternating layers of cations and anions are stacked in the [111] direction. Layers forming separately from cations and anions does not have equal distance in between them. Each cation atom will be bonded to three cation atoms in the layer below and one cation atom in the upper layer where bond geometry is tetrahedral. If crystal is terminated with (111) surface, surface will have either cation or anion atoms with dangling bonds (Figure 2.2). Cation (anion) atoms will have one (three) dangling bond(s) on the surface. In this context, (111) surface formed with only cations (anions) are identified with (111)A ((111)B). Due to higher electronic instability of B surfaces, growth and etching procedures are faster on the (111)B face of zinc blende crystals. Also, epitaxial growth layers on (111)B face results in smoother surfaces with higher crystal quality compared to growth on the (111)A surface.

The electrostatic properties of the epilayer and substrate interface can be influenced by the difference between the number of bonding orbitals and the number of available valance electrons. For orientations with Miller indexes satisfying h±k±l=0, such as (110) or (211), the electrostatic potential fluctuates along the interface. However, the mean potential in the interface is unchanged and therefore, the electrostatic dipole formation is not observed at the interface. On the other hand, for orientations with the Miller indices satisfying h±k±l≠0, such as (100) or (111), an atomic configuration composed

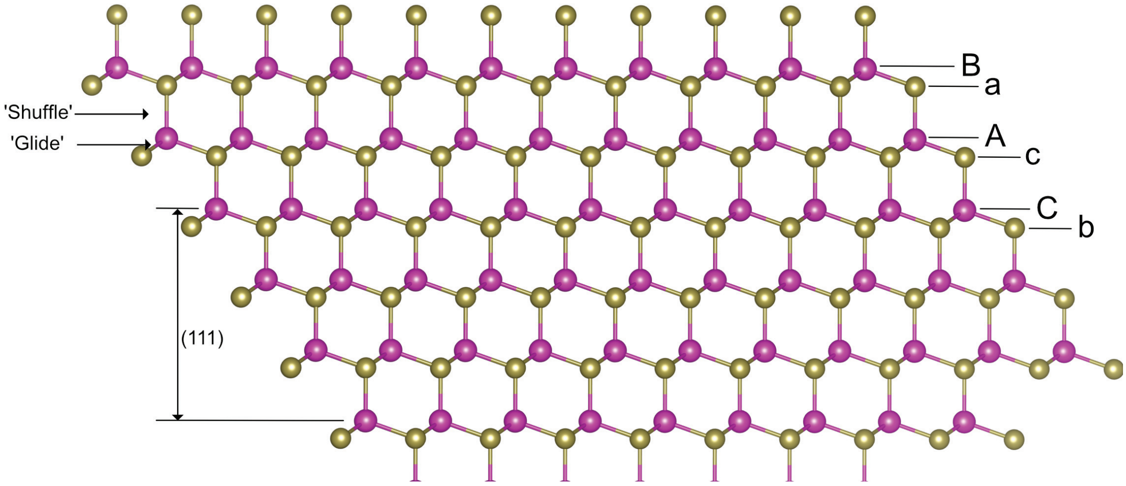

Figure 2.2.: Diagram of zinc blende structure which is terminated with (111)B surface.

of unbroken bulk planes is energetically highly unfavorable [33]. Therefore, a very large charge density at the interface can occur leading to a very high electric field inside the growing layer. In order to neutralize the interface charge, massive atomic rearrangements can occur during the growth of epilayer.

Periodicity of crystal structures are usually defined by lattice constants. For cubic crystal (i.e. zinc blende) structures, lattice constant is usually given in terms of conventional unit cell which is the length of the sides of the cube. In heteroepitaxy, the lattice constants and of substrate and epitaxial layer determine the lattice mismatch which has a big impact on epitaxial growth. Thermal expansion of lattice also affects the lattice constant. The latter is important for heteroepitaxy of materials. Heteroepitaxy or epitaxial growth of the epilayers on substrates are usually carried out on elevated temperatures. Therefore, the difference in thermal expansion coefficient of epilayer and substrate at growth temperature have direct impact on crystal quality of epilayers. In figure 2.3, the temperature dependence of lattice mismatch between CdTe and GaAs materials are given. The temperature dependence of lattice constant of CdTe and GaAs is calculated from [34] and the lattice mismatch is calculated for temperature range of 33-428 °C. It is seen from the figure that, difference in the lattice mismatch due to thermal expansion coefficients have a maximum value of ~ 0.07 %. Thermal expansion coefficient of CdTe and GaAs can be considered as compatible.

Lattice and thermal expansion mismatch may create elastic strain on epitaxially grown layers. Built-in strains in epitaxially grown layers can change the band structure of material hence shift the critical points in the dielectric function of the materials [35,

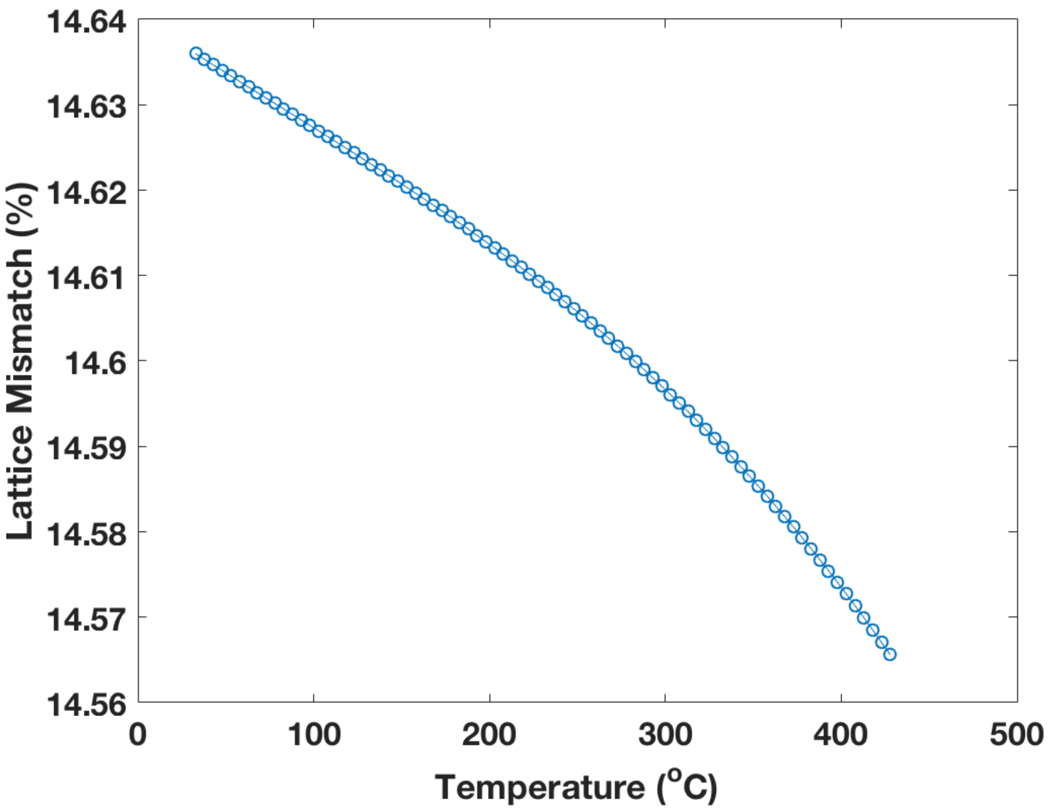

Figure 2.3.: Temperature dependence of lattice mismatch between CdTe and GaAs where temperature effects on lattice constant is introduced with thermal expansion coefficient. Graph is produced with the data from [34].

36]. Elastic strains create stress in crystals. For epitaxial growth of layers on lattice mismatched substrates, in most cases only biaxial stress is considered. Assuming that growth is in z-direction, in-plane stress due to substrate is equal in all directions in the plane of growth ($\sigma_{xx} = \sigma_{yy} = \sigma_{\|}$). On the other hand, out of plane stress which is in the growth direction is zero ($\sigma_{zz} = \sigma_{\perp} = 0$) since substrate does not apply a strain to the epitaxial layer in the growth direction. The elastic strain is reduced in the epitaxial layer by introducing dislocations to the layer.

2.2. Defects

Imperfections naturally exist in all real crystal structures. They include point (0D), line (1D), surface (2D), and volume (3D) defects. Imperfections disturb the crystal lattice locally significantly alter the physical properties of crystal semiconductors. The defects with different dimensions may have originate from different sources, but they are intimately related.

3D defects can be classified in general of four group; precipitates, dispersants, inclusions, and voids. During heteroepitaxial growth of epitaxial layers, dislocation related surface defects can be observed. 3D defects originate from un-optimized growth and annealing temperatures as well as un-balanced molecular fluxes [37].

2.2.1. Point Defects

In a perfect crystal, all atoms oscillate around their equilibrium position. Point defects occur in pure crystals as vacancy and self-interstitial atoms. Generally, plastic deformation or high energy particle irradiation can produce these type of intrinsic point defects. Concentration of the vacancy and self-interstitial atom defects in the crystals depend on the formation energy of the defects. Typical formation energy of vacancies are around 1 to 3 eV while this energy may go up to 12 eV for self-interstitial atoms [38]. Intrinsic point defects may migrate in the crystals. Typical migration energy is given to be in range from 0.1 to 1 eV [38]. Another type of the point defect is the impurities. Impurity atoms are considered as extrinsic defects which occur in crystals as substitutional and interstitial. In substitutional geometry, lattice atom is replaced by impurity atom.

All types of the points defects distort the crystal around them. The impact of the local distortion depends on the defect geometry and the type of the atom in the extrinsic defect case. Interstitial defects can produce larger distortions around the defect in the crystal. Point defects may also affect the local charge distributions in the crystal. Change in the local charge distribution is especially important in ionic crystals and II-VI alloy semiconductors. In zinc-blende structure, every group II-B atom is surrounded by an group VI-A atom. The removal of either type of the atom produces a local charge in the vacant site. Conservation of charge neutrality enforces the vacancies to exist as either Schottky or Frenkel type defects. In Schottky type defects, ions are removed from the lattice in pairs of opposite sign while ions are removed from lattice site to interstitial position, in Frenkel type defects.

2.2.2. Dislocations

In case of lattice mismatched heteroepitaxy, the strain induced by lattice mismatch is given

$$f = \frac{a_s - a_e}{a_e} \tag{2.1}$$

where a_s and a_e are the relaxed lattice constants of substrate and epilayer, respectively. The lattice mismatch may take the either sign, where $f < 0$ and $f > 0$ accounts for compressive and tensile strain, respectively. Epilayer is strained during epitaxial growth of a layer on a lattice mismatched substrate until the critical thickness is reached. The critical thickness is less than monolayer for the systems with lattice mismatch higher than 10 %.[39] At the critical thickness, introduction of misfit dislocations to the epilayer becomes energetically favorable. Some of the strain due to lattice mismatch is relieved by introducing misfit dislocations to the crystal. Therefore beyond the critical thickness, part of the strain induced by lattice mismatch is accommodated by misfit dislocations which is given as;

$$\varepsilon_{\|} = f - \delta\,(partially\ relaxed) \tag{2.2}$$

where $\varepsilon_{\|}$ is the in plane strain, δ is the relaxiation of the strain due to the misfit dislocations. The residual strain in a epitaxial layer grown on a lattice mismatched substrate is generally a function of the strain induced by the mismatch and thickness of the epilayer. Generation and movement of the dislocations limits the further relaxation of the residual strain in epilayer. Growth conditions and annealing process are the other parameters that affecting the residual strain in the layer. On the other hand, depending on the thermal expansion coefficient difference of the materials, a thermal strain may be induced in the epilayer during the cooldown of the epilayer [34]. Similarly, cyclic annealing during growth or post-growth annealing processes may introduce thermal strain to the epilayer.

Threading dislocations associated with misfit dislocations can extend from the core of the misfit dislocations through to the surface of epilayer. Threading dislocations are detrimental to the performance of the II-VI based devices. Misfit dislocations are expected to be present in the layers grown under thermal equilibrium while threading dislocations can be completely removed from the epilayer due to the their none-equilibrium character [34].

Dislocations are linear defects where bonds between the atoms are disturbed. In the core of the dislocation, large local strains occur due to dangling bonds. Interatomic bonds near the core of the dislocation are slightly distorted. Observed structure of the dislocations is generally quite complex. On the other hand, even most complex dislocations can be understood in terms of simple types of dislocations; screw and edge.

Screw dislocation can be formed in crystals with the presence of the shear stress. If the shear stress is larger then the elastic limit of the crystal, atoms will be displaced on either side of the shear plane (Figure 2.4). In the figure, shear stress is applied to the ABCD plane on which forces are represented by arrows. AD represents the screw dislocation line. Atoms around this line are displaced by one atom distance which overall shape is named as surface helicoid.

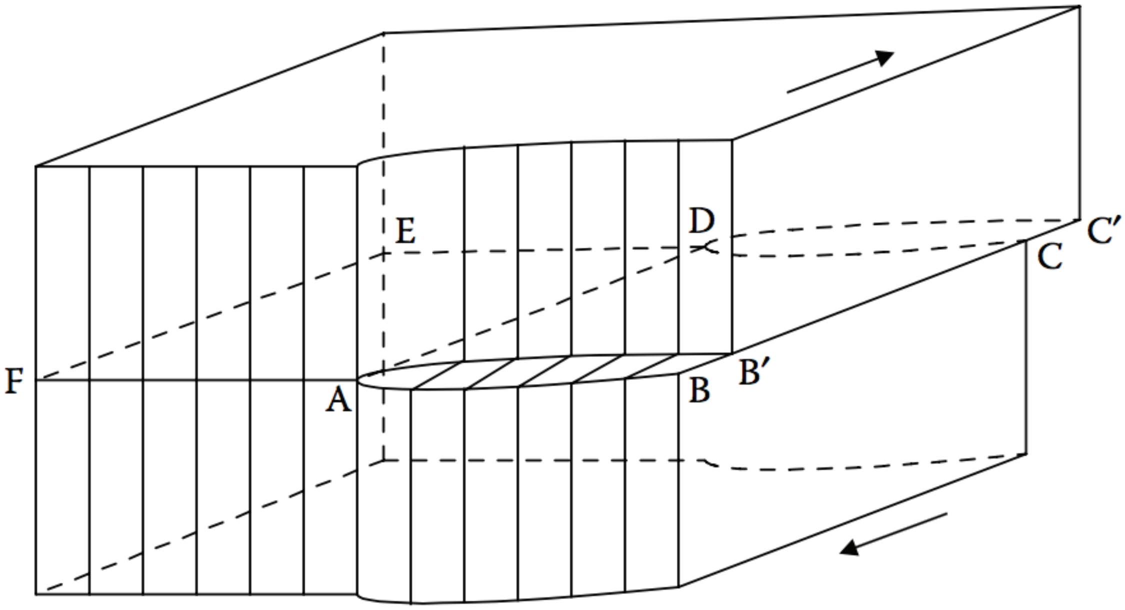

Figure 2.4.: Screw Dislocation [34].

Edge dislocations are crated by inclusion of an extra half-plane of atoms to the perfect crystal. In figure 2.5, ABCD half-plane is added on which AD is the dislocation line. This type of dislocation can be created by applying of a shear stress to the EFGH plane which is perpendicular to the dislocation line.

Structure of dislocations are defined with geometric parameters which are line vector, Burgers vector, and glide plane. The line vector is parallel to the line of the dislocation and it is expressed with the combination of the lattice translations. Burgers vector is given within the definition of the Burgers circuit which is any atom to atom path

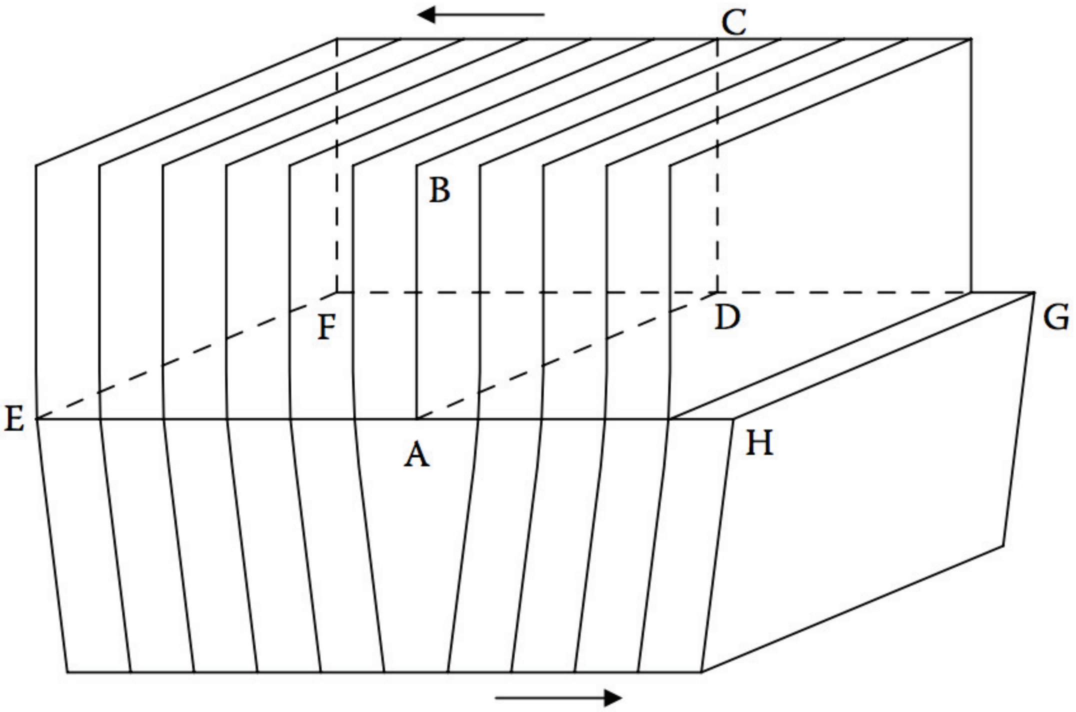

Figure 2.5.: Edge Dislocation [34].

that forms a closed loop around the core of the dislocation (MNOP loop in Figure 2.6.a). The difference between the Burgers circuit and the loop formed in case of ideal crystal without dislocation core (MNOP loop in figure 2.6.b) is the Burgers vector. Dislocations are characterized with the angle between the Burgers and line vector. In figure 2.6, an edge dislocation with 90° is shown. In case of the screw dislocation, the characteristic angle is 0°. Pure edge and screw dislocations are rarely observed in crystals. Instead, mixture of edge and screw dislocations are encountered in crystal structures. 60° dislocations are commonly observed in zinc-blende and diamond crystals which can be considered part edge and part screw in nature. Direction of the crystal distortion that created the dislocation is also shown with Burgers vector. If further stress is applied to the crystal, in response dislocations may move with a mechanism called slip. Burgers vector is parallel to the slip direction. The plane which contains Burgers vector with the line vector is defined as the slip plane.

The Burgers vector can be defined with lattice translation vectors. For a perfect dislocation, the Burgers vector connects two lattices points. As long as the Burgers vector is conserved, dislocations may dissociate into two partial dislocations. Additionally, reactions between two or more dislocations are possible but the Burgers vector has to be conserved. Reaction between the dislocations with the opposite Burgers vector causes the annihilation of both dislocations.

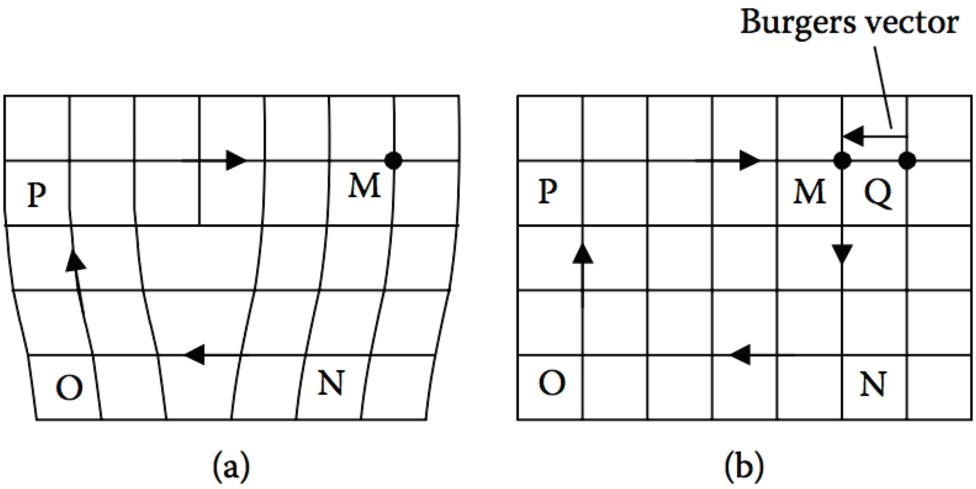

Figure 2.6.: Burgers circuit for (a) edge dislocation and (b) perfect crystal [34].

2.2.2.1. Dislocations in Zinc-Blende Crystals

Dislocations are formed generally in the planes with the highest density of atoms (the close-packed planes) which has the greatest inter-planar distance. Burgers vectors in the cubic crystal structure are of the type $\frac{a}{2}$<011>. {111} is the usual slip plane for zinc-blende crystal structure. Cubic crystals have four {111} planes each of which has three <110> directions. In total, the available number of slip systems is 12 [34]. They are given in Table 2.1. Crystal surface orientation determines the active slip systems during the lattice mismatched heteroepitaxy. In the cubic crystal structure, the line vectors for dislocations have also <110> direction. Therefore, dislocations on the cubic crystals with 12 active slip system will be pure edge, pure screw, or 60° dislocations while 60° dislocations are the most prevalent. For moderate lattice mismatch ($|f| < 1$ %) between the substrate and epilayer, most of the dislocations will be of 60° type. In highly mismatched epilayers, however, the misfit dislocation population by defect types may be less regular.

60° dislocations in a zinc-blende crystal can be further classified according to the chemical species of their core atoms [40, 41]. Dislocations with different atoms at the their core can be expected to behave differently. In an AB zinc-blende crystal, the α dislocations will have all A atoms at the core while the β dislocations will be formed from the cores of B atoms. It has been shown that α and β defects have different mobility [42] and dissociation [43] properties. These differences in properties of different type of defects can alter the dynamics of lattice relaxation.

Dislocations can be further classified as a glide or shuffle set depending on whether the dislocation was formed from the breaking of narrowly or widely spaced $\{111\}$ planes, respectively (Figure 1.2). Dislocations in zinc-blende structure are of the glide set which can dissociate into partial dislocations [44].

The dislocations in a crystal can move, if they are under the influence of a stress. The force on a dislocation created by stress on the crystal can be given as[45];

$$F = \tau b \tag{2.3}$$

where τ and b is the shear stress resolved on the slip plane and in the slip direction and amplitude of the Burgers vector, respectively. If a tensile force F is producing the stress to cross section of area A, the stress is $\sigma = F/A$ and the resolved shear stress can be given as;

$$\tau = \sigma \ \cos(\phi)\cos(\lambda) \tag{2.4}$$

where ϕ is the angle between the applied force and the normal to the slip plane, and λ is the angle between the applied force and the slip direction. The $\cos(\phi)\cos(\lambda)$ is the Schmid factor (Figure 2.7). Active slip systems will have the highest Schmid factor.

Dislocations can move with glide and climb motions. As a conservative motion, glide process is in the direction of the Burgers vector while climb is motion out of the glide plane and non-conservative motion. While both dislocation motions are considered as thermally active, climb motion involves long-range diffusion and is important only at high temperatures. Glide motion occurs by deforming a crystal and reforming bonds around the dislocation to the next site. Planes of the glide motion are the slip planes which is $\{111\}$ for zinc-blende structure. On the other hand, climb motion happens when dislocations move perpendicular to the applied stress which point defects allows the shifting of the dislocation planes. Due to the temperature dependence of the point defects, climb motion of dislocations is highly temperature dependent.

At high temperatures, both climb and glide motion is allowed. If the density of the point defects (e.g. vacancies and interstitials) is sufficiently high, climb motion dislocations can become energetically favorable. Dislocations will climb perpendicular to the slip plane. The displacement of the dislocation creates strain that results as stress on the crystal. The force due to climb motion per unit length, F, that resulting from normal

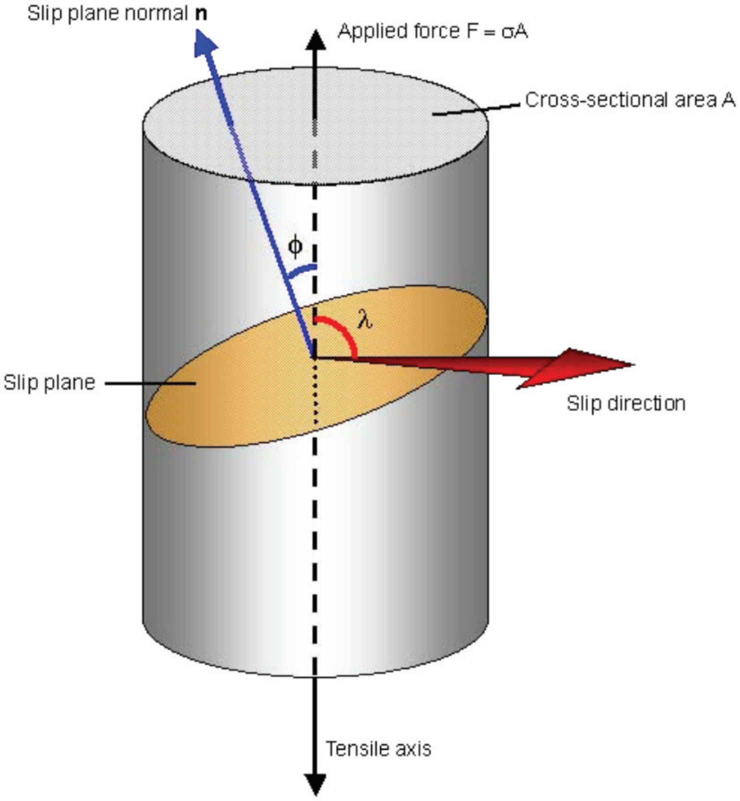

Figure 2.7.: Slip plane and slip direction of a dislocation which is under the influence of a shear stress (Source: University of Cambridge, DoITPoMS web page)

stress of an edge dislocation, is given as;

$$F = \sigma_{xx} b \tag{2.5}$$

The applied stress does work on the crystal. To move dislocation of a line segment (l), over distance of s, the required work can be given as;

$$W = F\ l\ s \tag{2.6}$$

However, since the creation and annihilation of point defects are involved in the motion of the climb, defect concentration changes must be involved in addition to the mechanical forces. The number of vacancies absorbed in the local volume change ($\vec{b} \times \vec{l} \cdot \vec{s}$) per unit volume of the atom Ω is given as bls/Ω. The vacancy formation energy (E_f^v) is then changed by $F\Omega/b$. The equilibrium vacancy concentration at temperature T with the

Table 2.1.: Slip Systems in Zinc-Blende Crystals

Glide Plane	Burgers Vector
(111)	$\frac{a}{2}$[10-1]
(111)	$\frac{a}{2}$[01-1]
(111)	$\frac{a}{2}$[1-10]
(-1-11)	$\frac{a}{2}$[101]
(-1-11)	$\frac{a}{2}$[011]
(-1-11)	$\frac{a}{2}$[1-10]
(-111)	$\frac{a}{2}$[101]
(-111)	$\frac{a}{2}$[01-1]
(-111)	$\frac{a}{2}$[110]
(1-11)	$\frac{a}{2}$[10-1]
(1-11)	$\frac{a}{2}$[011]
(1-11)	$\frac{a}{2}$[110]

presence of the dislocations become;

$$c = \exp\Big[-(E_f + F\Omega/b)/kT\Big] \tag{2.7}$$

$$c = c_0\ \exp[-F\Omega/b/kT] \tag{2.8}$$

where c_0 is the equilibrium concentration in a stress-free crystal, k is the Boltzmann constant and T is the temperature in K. Chemical force per unit length on the line due to the vacancy concentration deviations from c_0;

$$f = \frac{bkT}{\Omega}\ln(c/c_0) \tag{2.9}$$

$$\text{and shear stress} \tag{2.10}$$

$$\tau = \frac{kT}{\Omega}\ln(c/c_0) \tag{2.11}$$

Motion of the dislocation occurs if the applied shear stress is greater than the critically resolved shear stress (τ_c) of CdTe which is 1.64, 1.74, 2.48 MPa at 420 °C, 400 °C, 300 °C, respectively [46]. Typically CdTe growth is carried out under Te_2 rich conditions. The temperatures above ~ 367 °C is determined to be enough to induce stress greater than the critical shear stress by using vacancy concentration changes under different Cd and Te_2 overpressures are given in [47].

Glide motion can be induced by thermal stress if the difference of the thermal expansion mismatch of the substrate and epilayer is sufficiently enough. During the heating and cooling of annealing procedures, significant thermal stresses can be induced. Thermal stress induced is given by using Hooke's Law as;

$$\sigma = -E\varepsilon \tag{2.12}$$

where σ is the stress, E is the Young's modulus, and ϵ is the strain. Considering a heteroepitaxial layer grown at temperature T_g and heated to the annealing temperature of T_a, the thermal strain is given as;

$$\varepsilon_{Th} = \int_{T_g}^{T_a} [\alpha_s(T) - \alpha_e(T)]\, dT \tag{2.13}$$

where α_s and α_e is the thermal expansion coefficients for the substrate and epilayer, respectively. If the temperature dependence of thermal expansion coefficients are chosen to be constant for a temperature window from growth to annealing temperature;

$$\varepsilon_{Th} \approx (\alpha_s - \alpha_e)(T_a - T_g) \tag{2.14}$$

The thermal strain will be tensile if the substrate has a larger thermal expansion coefficient compared to the epilayer. Similarly, during the cool-down to growth temperature after annealing, the thermal strain can be written as;

$$\varepsilon_{Th} \approx -(\alpha_s - \alpha_e)(T_a - T_g) \tag{2.15}$$

The thermal strain will be compressive if the substrate has a larger thermal expansion coefficient than that of the epilayer. During the cool-down to room temperature after growth is completed thermal strain will be the same as the during cool-down after annealing.

However, thermal stress the during cool-down to the room temperature cannot usually be relaxed by the dislocation motion since the dislocation glide velocities are thermally activated and may be reduced by a factor of 10 for every 25 °C reduction in temperature [34].

To calculate the thermal stress during annealing of the heteroepitaxy of CdTe on GaAs, Young's modulus is chosen as 36 GPa of which the measured values are found to be in the range of 24 to 52 GPa. Employing the thermal expansion coefficients from [34], it is estimated that the thermal stresses at the annealing temperatures greater than 345 °C exceeds critically resolved shear stress. Therefore, the annealing temperatures above 345 °C are enough to induce dislocation motion in CdTe/GaAs system. In this study, annealing experiments are carried out to reduce dislocation density and improve crystal quality of CdTe layers.

Interaction of the dislocations can also repel or attract the dislocations to each other inducing motion of the dislocations. Dislocations tend to repel or attract each other to reduce total elastic energy. Elastic energy of the edge, screw, and mixed dislocations are given as[34];

$$E_{edge} = \frac{Gb^2}{4\pi(1-\nu)}[\ln(R/b)+1] \tag{2.16}$$

$$E_{screw} = \frac{Gb^2}{4\pi}[\ln(R/b)+1] \tag{2.17}$$

$$E_{mixed} = \frac{Gb^2(1-\nu\cos^2(\alpha))}{4\pi(1-\nu)}[\ln(R/b)+1] \tag{2.18}$$

where G is the shear modulus, ν is the Poisson's ratio, α is the angle between the Burgers vector and the line vector, R is the limit of the strain field, and b is the Burgers vector. By using the Poisson's ratio of 0.41 [34], the energy difference between screw and edge dislocation is found to be only ~ 1.7 for CdTe. For edge, screw, and mixed type dislocations, the elastic energy is proportional to b^2. Reaction of dislocations is favorable[34] (Frank's rule) only if $\sum b^2$ for the products is less than or equal $\sum b^2$ for the reactants. If the two dislocations with opposite Burgers vectors may react and annihilate each other then, $\sum b^2 = 0$. Therefore, in this case annihilation processes is energetically favored. In zinc-blende lattices, two 60° dislocations may combine to form an edge type misfit dislocation at the interface of epitaxial layer. As an example, the interaction of two 60° misfit dislocations with the same line vector [110], and Burgers vector $\frac{a}{2}$[101] and $\frac{a}{2}$[0-1-1] can be given as;

$$\frac{a}{2}[101] + \frac{a}{2}[0-11] = \frac{a}{2}[1-10] \tag{2.19}$$

This reaction is also energetically favorable by Frank's rule [34]. Therefore, an edge dislocation relaxes the total strain composed the of two 60° misfit dislocations.

2.2.3. Planar Defects

The planar defects encountered during heteroepitaxy include stacking faults, twins, and inversion domain boundaries. In a perfect crystals atomic layers are considered to be stacked in a particular sequence. Inversion domain boundaries or also known as antiphase domain boundaries are only important for the heteroepitaxy of a polar semiconductor on a nonpolar substrate which is not the focus of this thesis.

2.2.3.1. Stacking Faults

Stacking of the zinc-blende structure occurs in [111] direction with ...ABC... order where A, B, and C represents planes with different atomic orientations (Figure 1.2). If an extra plane of atoms inserted into the stacking sequence (extrinsic), stacking fault may occur which can be represented by ...ABCBABC.... Another mechanism to generate stacking fault is the removal of one plane (intrinsic) which can be shown as ...ABCBC....

Stacking faults are partial dislocations since their Burgers vector is not a lattice translation vector. Stacking faults are created by the dissociation of perfect dislocations into partial dislocations which occur naturally during the glide of dislocations. In zinc-blende crystals, the perfect 60 ° dislocation may dissociate into two Shockley partial dislocations by;

$$\frac{a}{2}[011] \rightarrow \frac{a}{6}[112] + \frac{a}{6}[-121] \tag{2.20}$$

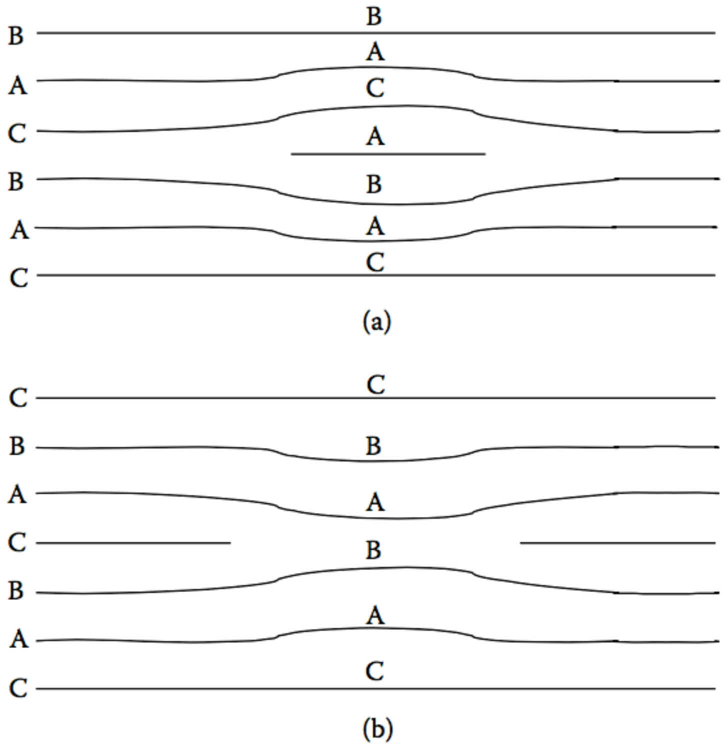

Figure 2.8.: Schematic illustration of stacking faults in zinc-blende crystal. (a) Intrinsic and (b) extrinsic stacking faults [34].

The total Burgers vector is conserved and the energy of the dissociation is;

$$\frac{a^2}{4}[0 + 1^2 + 1^2] \rightarrow \frac{a^2}{36}[1^2 + 1^2 + 2^2] + \frac{a^2}{36}[1^2 + 2^2 + 1^2] \tag{2.21}$$

$$\frac{a^2}{2} > \frac{a^2}{3} \tag{2.22}$$

energetically favorable according to the Frank's rule. These partial dislocations lie on the (11-1) plane and between the two partial dislocations a stacking fault exists. The equilibrium width of the stacking fault can be calculated from the repelling force between the partial dislocations[34];

$$F = \frac{Gb^2(2-\nu)}{8\pi(1-\nu)d} \tag{2.23}$$

where d is the separation between the stacking faults. The stacking fault energy provides a force (ζ) per unit length of line tending to pull the dislocations closer. An equilibrium will be formed when the repulsive and attractive forces balances. The equilibrium separation can be calculated by equating the forces;

$$d = \frac{Gb^2}{4\pi\zeta} \tag{2.24}$$

By using the stacking fault energy as 10 mJ/m^2 [48], the corresponding equilibrium stacking fault width is estimated to be 70 nm for CdTe.

2.2.3.2. Twins

Twin is another type of the planar defect which results from a change in the stacking sequence. Twinning occurs exclusively on (111) plane of zinc-blende crystals during heteroepitaxy. Twin boundary in zinc-blende crystal can be shown with ...ABCABACBA... stacking notation. The original crystal and twin are mirror images of each other by reflection in a composition plane as shown in Figure 2.9. Black circles represent atomic positions after twinning. The atoms above $x - y$ plane are mirror images of the atoms below. A homogeneous shear applied to the lattice due to twinning is shown with arrows.

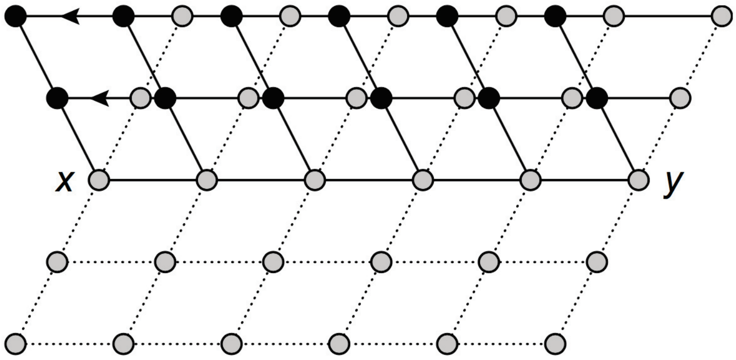

Figure 2.9.: Arrangement of atoms in a twin related lattice [38].

Formation of twinning involves a change in the long-range order of the crystal. Therefore, simple insertion or removal of an atomic plane which were created by the glide of dislocations cannot create twins. Instead, the twinning occurs during growth of heteroepitaxial layers. For zinc-blende crystals, twinning occurs about a {111} plane.

Twin boundaries are commonly found in heteroepitaxial II-VI crystals grown on (111) [34] and (100) [49] substrates. On the other hand, the substrates with high miller indices such as (211) has been shown to suppress twinning [50]. The (211) surface consists of (111) terraces and (100) edges that allow a step flow (Frank-van der Merwe) growth mechanism that leads to minimum twinning formation.

2.2.4. Tilting

In general, it is expected that an epitaxial layer grown on lattice mismatched substrate will take on the same crystal orientation as substrate. However, both strained and relaxed layers are grown with small tilting with respect to their substrates. In highly mismatched heteroepitaxy, gross tilting (with the angle larger than 0.1°) are sometimes observed. The reason for this tilt can be attributed to the lattice mismatch between epilayer and substrate. In the epitaxial growth on (211) surface, the epilayer can relieve the mismatch strain by tilting the epilayer terrace growth away from the nominal (111) plane. Each terrace of epilayer can grow wider along [2-1-1] direction than the associated substrate terrace, but in order to keep the step-edge locations of the atoms aligned, the epilayer terraces becomes tilted with respect to the substrate. This tilting allows the epilayer to be nucleated with a larger lattice spacing having a lattice constant similar to its bulk value.

Epitaxial growth of the epilayers on highly mismatched substrates with (211) orientation may result in epilayers growing in a twinned orientation with a tilt. That twinned orientation has been identified as (133) and this is referred as "dual epitaxy" [51]. In fact, with the (111) as the mirror plane, [255] is the first order twin of (211) [52]. However, the diffraction from (255) planes is forbidden from measurement by X-ray diffraction for zinc-blende systems. (133) is the closest lower index plane and its reflection is allowed.

Epitaxial growth of layers on highly mismatched substrates with the (211) orientation results in tilted epitaxy about the [01-1] direction towards [-111] [53]. In general, the epilayer tilting is found to be linearly scaling with mismatch strain. The calculation of the tilt angle (δ) for (211) systems is given by an empirical formula [53];

$$\frac{a_{epilayer}}{\sqrt{3}\sin(19.471^\circ + \delta)} = \frac{a_{substrate}}{\sqrt{3}\sin(19.471^\circ)} \tag{2.25}$$

$$\frac{a_{epilayer}}{2\sin(74.207^\circ + \delta)} = \frac{a_{substrate}}{\sqrt{3}} \tag{2.26}$$

where both equations should be satisfied simultaneously. Tilt in diffraction angle for heteroepitaxy systems is observed from XRD RC measurements where Bragg angle is shifted with a tilt angle. Additionally, the effect of the tilting on XRD RC FWHM values are studied theoretically [54]. It is found that for ZnSe epitaxial layers grown on slightly mismatched GaAs substrate with small tilt (10 arc-s), only a small (6 %) deviation in FWHM^2 is detected. Broadening of FWHM is explained with Pendellösung diffraction interference fringes [54]. On the other hand, in highly mismatched systems such as CdTe/GaAs, RC diffraction peaks are well separated and Pendellösung diffraction interference fringes from substrate and epilayer should not have significant effect on FWHM broadening.

CHAPTER 3

EXPERIMENTAL METHODS

3.1. Molecular Beam Epitaxy

There are large number of methods used to deposit CdTe thin films. These include physical Vapour deposition techniques such as sputtering and thermal evaporation, chemical vapour deposition (CVD) and metal-organic CVD, close space sublimation, liquid-phase deposition techniques such as spray pyrolysis, screen printing, inkjet printing, chemical bath deposition, electrodeposition, and MBE. Details of these techniques are given in Ref. [55]. In this study, MBE as an ultra high vacuum epitaxial growth technique is used for deposition of CdTe layers.

MBE is a versatile and ultra high vacuum (UHV) technique for epitaxial growth of highly crystalline films. In MBE, thin film is deposited with precise control of the growth rate at relatively low temperatures. UHV evaporations techniques had been used long before, while their application to compound semiconductors with fundamental understanding of the process was not ready until 1970s [56]. Subsequently, other researchers evolved the basic process to reach today's MBE systems. MBE systems made possible to obtain monolayer (ML) control of the epitaxial growth of the layers as well as atomically abrupt crystalline interfaces and rapid changes in atomic composition. Additionally, precise control of the beam fluxes and growth conditions with in situ control of growth by RHEED or SE significantly improve reproducibility of the growth. These technological advantages allowed growth of quantum devices and nano-structures such as quantum dots, and high quality epilayers such as high electron mobility transistors. In MBE, atoms and molecules are evaporated from solid/liquid/gas sources, then atomic and/or molecular flux migrate into an UHV environment which they are directed to a heated substrate. During the growth, substrate temperature is usually higher than room temperature to provide enough energy for adatoms to migrate on the surface. Molecular flux impinging on the heated surface allows the diffusion and finally incorporation into producing a layer. In MBE, the growth rate is slow (~ 1 μm/h) allowing migration of atoms and molecules to find appropriate positions for bonding. Consequently, the incident molecules or atoms

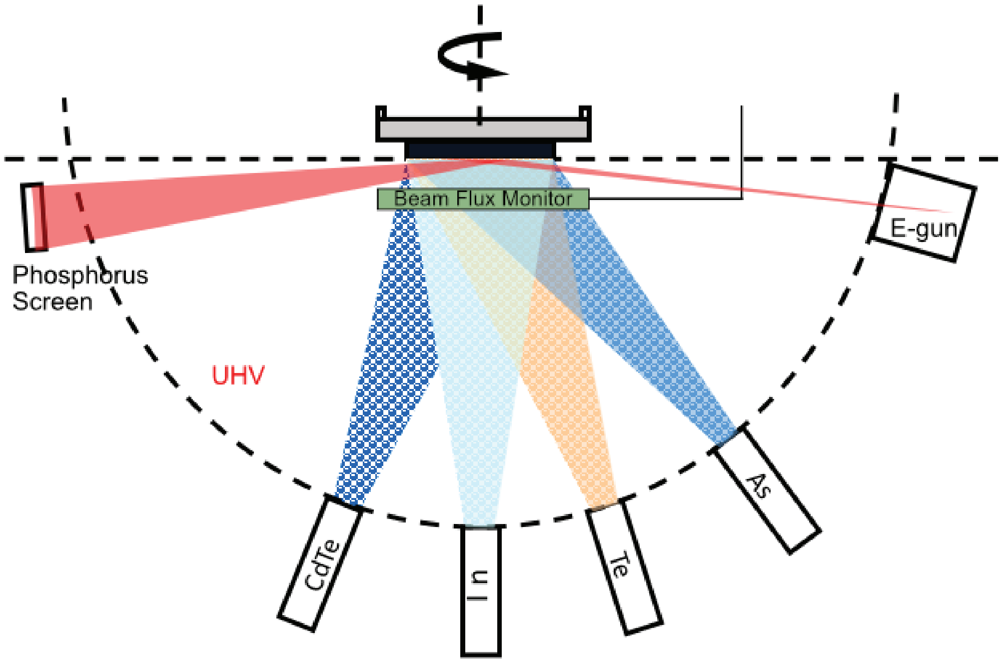

Figure 3.1.: Schematic of a general MBE design.

form the surface structure of the substrate, producing an epitaxial structure of the deposited layer. Therefore, single crystal thin films is synthesized on a single-crystalline substrate and the surface of the epilayer grown by MBE becomes very smooth. The essential elements of a growth chamber of a MBE system are shown in Figure 3.1.

MBE systems, generally consists of a growth module (GM) where growth process is carried out, and a load lock (LL) where the samples are introduced into the system (Figure 3.2.a). Additionally, MBE systems may have storage and preparation chambers. Growth module is a relatively larger chamber where all the cells with the source materials, in situ characterization devices, substrate holder and heater, UHV pumps and usually with the liquid nitrogen (LN2) panel (Cryopanel) are located (Figure 3.2.b). Growth chambers and all the other modules are separated from each other with isolation valves to prevent cross-contamination of chambers. Loading of the substrate to MBE system is carried out by introducing them to LL which then is transferred to the GM by magnetic arms. The atomic/molecular fluxes are directed to a heated substrate by effusion cells in GM during growth of the desired epitaxial layer. Effusion cell design is based on crucibles with resistive heaters. Evaporation of the different kind of chemical species require the usage of different type of the effusion cells. The most basic effusion cell design is the Knudsen cell with two heating (DF, dual filament) zone. The DF cells are commonly

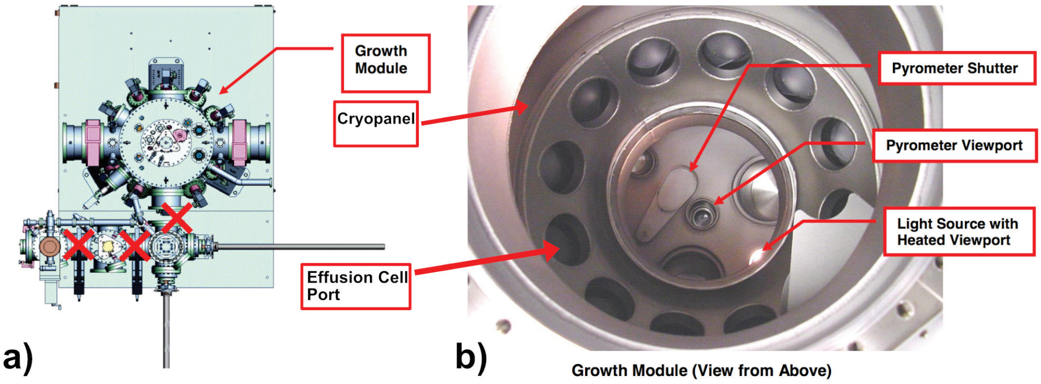

Figure 3.2.: a) Schematic drawing of Veeco Gen20MZ MBE GM, ST, and LL sections. b) A photo from the inside of GM showing sources and other components

used in MBE systems for source materials such as Ga, In, Zn, ZnTe. To obtain atomic fluxes from molecular source materials such as As_4, another type of the effusion cells are employed. These cells are designed with two largely separated zones where a heating source to evaporate material and a cracking zone is used to crack molecules to smaller molecules and atoms. Also for the materials such as Hg, continuous source cells are used where the source usage is high compared to other methods.

Precise control of the molecular flux is crucial to obtain sharp interfaces and reproducibility of the epilayers. In general, there are two types of flux controlling mechanisms which are mechanical shutter/valve systems and vapor pressure of effusion cells with the direct temperature control. Effusion cell shutters in MBE systems are controlled by pneumatically via electronic switches. These high speed controlling mechanisms allow the interruption of molecular fluxes within few mili-seconds, thus, growth of the quantum structures with the dimensions of Angstroms become possible. On the other hand, effusion cell valves allow the control of the molecular/atomic fluxes without changing the effusion cell temperatures.

Measurement of the molecular/atomic fluxes with high precision is important for the growth of the semiconductor alloys. MBE systems are equipped with an ion-gauge to measure beam equivalent pressure (BEP) of molecular/atomic fluxes which is called as beam flux monitor (BFM). BFM, ionizes the atoms around itself then collects them to produce a current equivalent to vapor pressure produced by atoms. The BFM can be made to rotated into the front of the substrate holder which allows the measurement of BEP at the substrate's position. In Figure 3.3, Te_2 corrosive cracking cell valve position

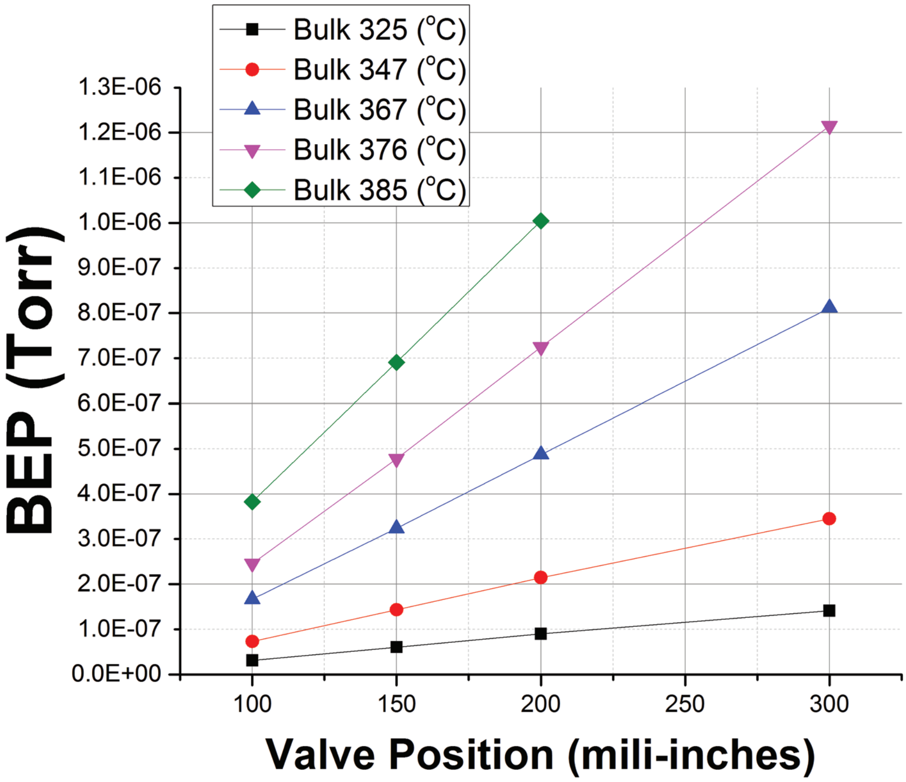

Figure 3.3.: BEP values of Te effusion cell for different bulk temperatures and valve openings.

versus BEP chart for different bulk temperatures are shown. It is seen from this figure that the desired BEP values can be obtainable by controlling the cell temperature and the valve position.

The substrate and effusion cell heaters are controlled by PID (proportional, integral, derivative) controllers in MBE devices. PID controllers allow highly sensitive and fast control of the temperature of the heating zones which is critical for layer growth. Temperature measurements are carried out by contact thermo-couples (T/C) for heating zones of the effusion cells. The measurement and the control of the substrate temperature can be accomplished by contact or non-contact T/C or optic measurements such as pyrometry, band-edge detection (semiconductor only), and ellipsometry (with theoretical real time experimental data fitting procedures).

The amount of the Cd and Te atoms on the substrate during growth of epilayer, has a critical impact on the crystal quality and the surface morphology of the epitaxially grown layer. The required overpressures of the Cd and Te atoms from the effusion sources to form an epitaxial layer may vary depending on the sticking coefficients of the individual

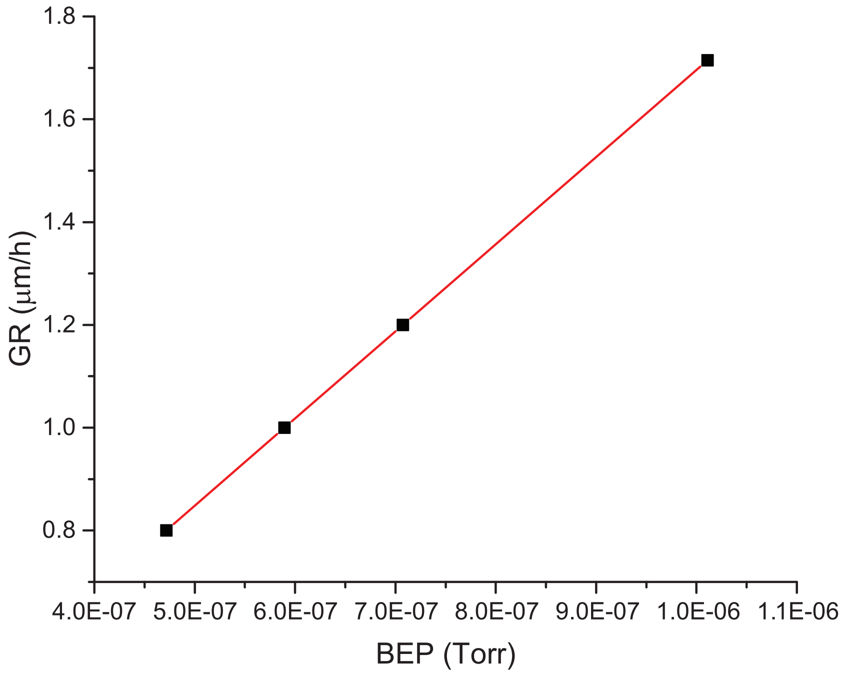

Figure 3.4.: Growth rate of CdTe epilayer as a function of CdTe flux (BEP)

atoms [57]. The sticking coefficients and thus the amount of the Cd or Te atoms on the surface of the substrate can not be determined directly. Instead, growth rate of the epitaxial layer is used. The change in the growth rate as a function of the CdTe flux was shown in Figure 3.4 when a stoichiometric CdTe source is used. Since only CdTe source was used to grow epitaxial layers, CdTe flux source directly controls the growth rate.

Pyrometer is an optical device which detects the radiant flux from a hot object at a certain wavelength or in a range of wavelengths (Figure 3.5). The detected radiant flux is compared with the calibration data and the temperature of the object is calculated according to the Planck's law. Emissivity of the object is important for the calculation of the temperature. Typically, epitaxial growth if II-VI alloys are performed around 600° C surface temperatures [58]. On the other hand, highly crystalline growth of II-VI alloys require surface temperatures of 150-400° C. At these low temperatures, the optical pyrometers might detect false readings from the substrate or effusion cell heaters. To focus radiation from only the substrate to the optical pyrometer, special focusing lens are used in MBE systems.

Another aproach to the detection of substrate temperature in MBE system is the band-edge detection systems [59]. In these systems, the electromagnetic spectrum radiating from the substrate is collected and analyzed with a spectrometer. If the substrate is a semiconductor then band-edge (electronic band-gap) of the semiconductor can be detected. The band-edge of the semiconductors is known to change with the temperature. Therefore, by comparing the detected band-edge of the substrate with a temperature band-edge library, the temperature of the substrate can be precisely detected (Figure 3.5). The resolution and the accuracy of the band-edge detection system ($BandiT^{TM}$) which was used in this study is 0.1 °C and ±2°C, respectively. For all temperature detection systems, the measured temperature is not the real surface temperature rather it is a reliable surface energy parameter. The pyrometry and the band-edge techniques suffer from the optical measurement related disadvantages. Additionally, the pyrometer sensor reads all the intensity from the substrate, heater and reflection from the chamber walls which radiation from these sources can vary for different growth runs. Temperature calculation from the incoming radiant flux rely on the emissivity factor which is a material and temperature dependent parameter and can not be known precisely. Nevertheless, the band-edge detection system calculates the temperature of the substrate by real time fitting of reflec-

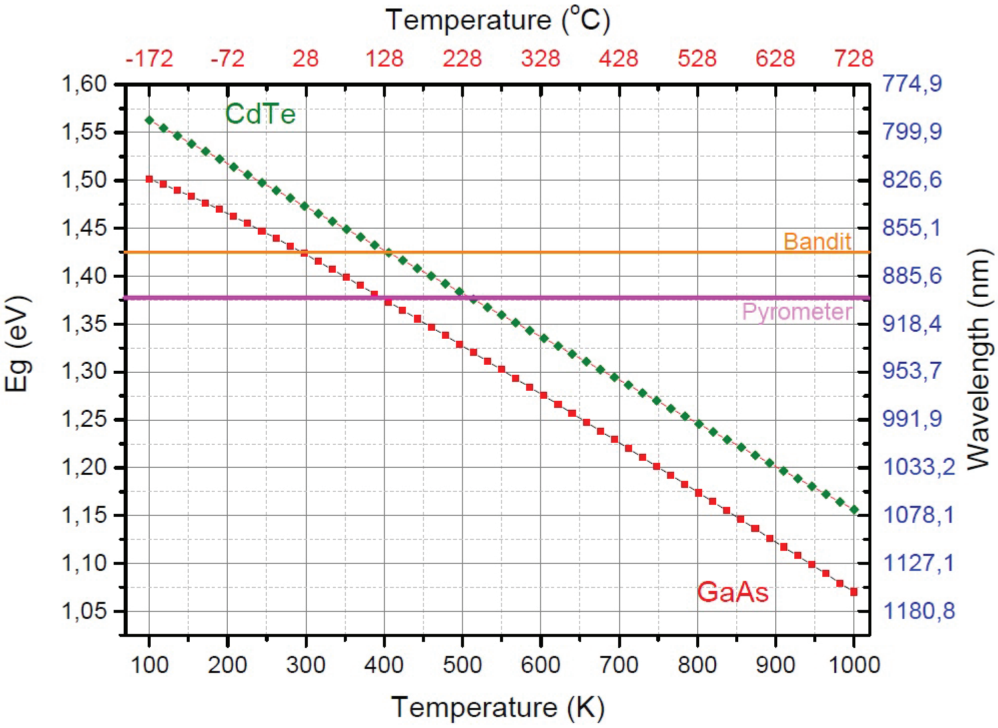

Figure 3.5.: Band gap energy of bulk udoped GaAs and CdTe semiconductors versus surface temperature [60, 61]. The short wave-length working limit of the band-edge detection system which is used in this study is shown with orange line. The detected radiation wavelength of the gray body emission for detection of the temperature with pyrometer system is shown with magenta.

tion or transmission data which requires a very fast and clever algorithm to work. At low temperatures, the substrate heater does not emit enough radiation through the sample to be detected by the band-edge system therefore additional radiation (light) sources are required in the growth chamber for the band-edge system to work.

Data Pt.: 100

Elapsed Time: 3584.19

Band Edge: 1088.799

Fit Y: 0

Figure 3.6.: The normalized transmission versus wavelength spectrum which was taken from a heated GaAs substrate with the band-edge detection system in the MBE system. Blue line represents the detected spectrum while red line shows the result fitting with a linear model.

Temperature measurement of the substrate can be calculated indirectly with the spectroscopic ellipsometer which is a system that detects the changes in the electric field component of the radiation due to the sample's dielectric function. To obtain dielectric function of the layer, the ellipsometric data can be evaluated with simple models as harmonic oscillators and Kramers-Kronig relationships or other macroscopic models (Effective Medium Approach, EMA). The surface temperature of a semiconductor can be determined with temperature dependency of the dielectric function at critical points.

The substrate preparation and introduction of substrates to the MBE system play a crucial role to obtain highly crystalline and pure epitaxial layers. Most of the commercial substrates for epitaxial growth are sold with epi-ready condition. Following the bulk crystal growth of the substrates, substrates are cut and polished with the required specifications. Finally, the surface of the substrate is covered with an protective oxide layer. This oxide layer can be thermally removed in MBE systems, while some of the substrate materials requires additional chemical etching prior to the introduction of substrates to the MBE system.

The substrates are not introduced to the MBE-GM directly. Initially, the substrates are loaded to LL. Then LL is baked at 200° C under ultra high vacuum ($\sim 10^{-8}$ Torr) to get rid of water vapour and other contaminants. In some MBE systems, there is an additional chamber called preparation chamber which is located right after the LL. This chamber is used for thermal surface deoxidation of the substrates prior to the growth of epilayers. The substrates are transferred to the GM following bake process at LL.

3.1.1. Dynamics of Epitaxial Growth

Growth process is iniated by evoparation of the atoms/molecules from the effusion cells. The evoparated molecules diffuse to the heated substrate surface. These atoms/molecules may be chemically or physically absorbed at the surface or they can diffuse back to the UHV environment by elastic scatterings. Results from the atomistic models suggest that atoms may undergo interactions with the surface and other atoms. When the impinging atoms from the effusion cells arrive to surface, they may diffuse at the surface, bind with the other atoms to form nucleation centers, or inter-diffuse with an surface atom, or get trapped at special sites, or get re-evaporated to the environment (see Figure 3.7). Essentially, absorption of the atoms/molecules to surface of the substrate is required to form layers or islands at the surface. Chemically absorbed atoms/molecules are considered to make bonds with the surface states with bonding energies of 1-10 eV [62]. In the physically absorption case, atoms/molecules are weakly connected to the surface via Van der Waals forces where the binding energies are in 50-500 meV range [62]. Following the initial absorption of the atoms/molecules, the nucleation process starts. The growth of the epitaxial layers for the different epilayer-substrate systems are given with three models. In 1958, Bauer [63] classified the three growth modes of thin film growth as; (1) Volmer-Weber growth, (2) Stranski-Krastanov growth, (3) Frank-van der Merwe growth (see Figure 3.8). The classification of the growth modes are based on the interaction potential between the atoms/ molecules and between the atoms/molecules to surface states. If the interaction potential between the atoms at the surface is greater then the atoms-surface state interaction potential, atoms and molecules form strong bonds with each other which leads to formation of islands (3D growth) at the surface (Figure 3.8 (a), Volmer-Weber mode). On the contrary, if the interaction potential between the atoms and surface state is greater, atoms are deposited to the surface (2D growth) which they create layers (Figure 3.8 (c), Frank-van der Merwe mode). As an intermediate case, if the both

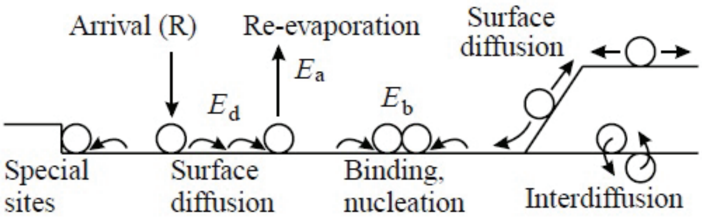

Figure 3.7.: Surface processes under the molecular/atomic flux through a surface [62].

interaction potentials are comparable with each other, the epilayer growth includes layers plus islands (Figure 3.8 (b), Stranski-Krastanov mode). A transition between the growth modes are possible during growth due to change in growth dynamics such as flux and temperature.

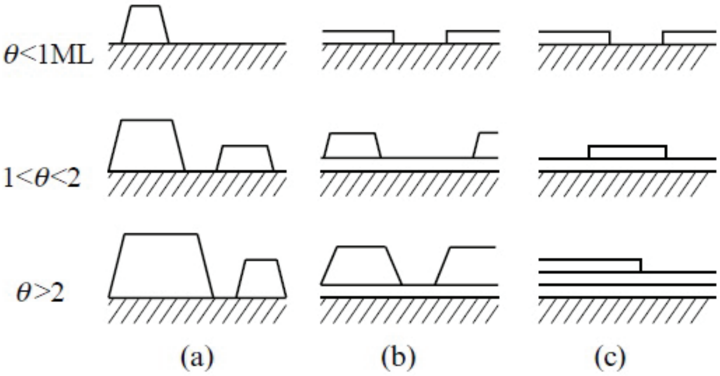

Figure 3.8.: Schematic representations of the three growth modes as a function of θ in ML; (a) Volmer-Weber, (b) Stranski-Krastanov, (c) Frank-van der Merve [62].

3.2. Characterization

3.2.1. Reflection High Energy Electron Diffraction

RHEED is an excellent tool to probe surface structure of epilayers during MBE growth. A RHEED system is composed of an e-gun and a fluorescent screen. Highly energized electrons from an e-gun are focused into a surface point with very low incident angles which then are scattered through a fluorescent window (see Figure 3.9). To create a diffraction pattern from the sample surface, the glancing angle and the rocking angle of the electron beam from the e-gun is controlled. Electrons leaving the electron gun hits the substrate surface which are either absorbed, transmitted or reflected. The wavelength

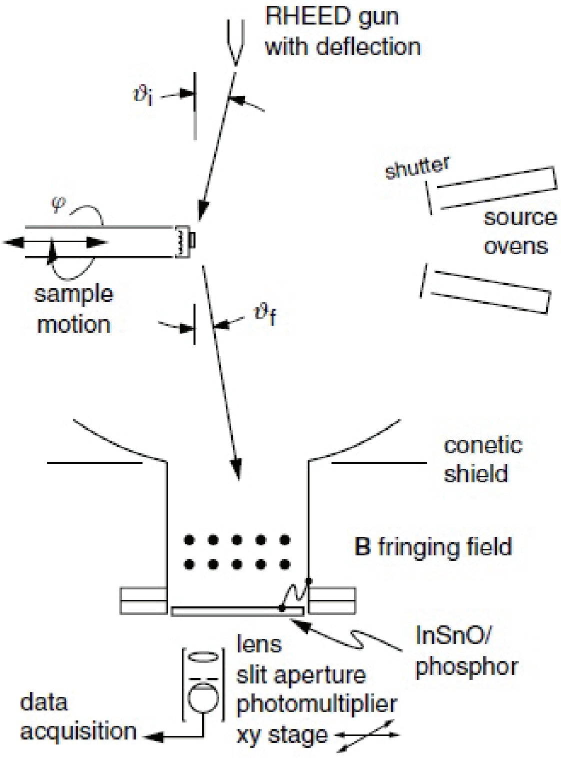

Figure 3.9.: Schematic illustration of a RHEED system in the growth chamber of a MBE system. [64].

of the free electrons are given as;

$$\lambda = \sqrt{\frac{h^2}{2mE}} \tag{3.1}$$

$$\lambda = \sqrt{\frac{150.4}{E}}\ \text{Å} \tag{3.2}$$

$$\text{where} \tag{3.3}$$

$$E = \frac{p^2}{2m_e} \tag{3.4}$$

and E is given in terms of eV. If the relativistic effects are important, the wavelength of the electrons is obtained by Dirac equation;

$$\lambda = \sqrt{\frac{h^2}{2m_o E(1 + E/E_0)}} \tag{3.5}$$

For a free electron $E_0 = 511$ keV, therefore the electrons with kinetic energies are greater then 50 keV can be considered as relativistic. In this study, electrons were accelerated with 20-24 kV potential which are considered as non-relativistic.

The electrons entering crystal undergo elastic and inelastic scatterings with the crystal. The main elastic process is the Bragg scattering. However inelastic scattering processes include plasmon excitations, thermal diffusive scattering and single-electron excitations. The Schrödinger equation for the elastic scattering event of the free particles is given as;

$$(H_0 + V)|\psi > = E|\psi > \tag{3.6}$$

and the solution is

$$|\psi > = \frac{1}{E - H_0} V|\psi > + |\phi > \tag{3.7}$$

$$|\psi^{(\pm)} > = |\phi > + \frac{1}{E - H_0 \pm i\epsilon} V|\psi^{(\pm)} > \tag{3.8}$$

where $|\phi >$ is energy eigenket of H_0. This is the Lippmann-Schwinger equation [65].

Here + sign represents the outgoing wave and − sign stands for the incoming wave. Since we are concerned about the scattered outgoing waves, solutions only with the + sign will be given further. The equation in the position representation is given by;

$$< x|\psi^+ > = < x|\phi > + \int d^3x' \left\langle x \left| \frac{1}{E - H_0 + i\epsilon} \right| x' \right\rangle < x'|V|\psi^+ > \tag{3.9}$$

Assuming that the perturbing potential V is local and by employing Green functions with a plane-wave state $< x|\phi > = \frac{e^{i\vec{p}\vec{x}/\hbar}}{(2\pi\hbar)^{3/2}}$, the solution becomes [65];

$$< x|\psi^+ > = < x|\phi > - \frac{2m}{\hbar^2} \int d^3x' \frac{e^{ik|\vec{x}-\vec{x}'|}}{4\pi|\vec{x} - \vec{x}'|} V(\vec{x}') < x'|\psi^+ > \tag{3.10}$$

At large distances $|\vec{x}| >> |\vec{x}'|$, and using $r = |\vec{x}|$ and $r' = |\vec{x}'|$,

$$|\vec{x} - \vec{x}'| = \sqrt{r^2 - 2rr'cos\alpha + r^2} \tag{3.11}$$

$$= r\left(1 - \frac{2r'}{r}cos\alpha + \frac{r'^2}{r^2}\right)^{1/2} \tag{3.12}$$

$$\simeq r - \hat{r} \cdot \vec{x}' \tag{3.13}$$

where $\hat{r} = \frac{\vec{x}}{|\vec{x}|}$, and defining $\vec{k}' \equiv k\hat{r}$, we can write

$$e^{ik|\vec{x}-\vec{x}'|} \simeq e^{ikr} e^{-i\vec{k}'\cdot\vec{x}'} \tag{3.14}$$

Finally, at large r, we have;

$$< x|\psi^+ > \simeq < x|k > - \frac{1}{4\pi} \frac{2m}{\hbar^2} \frac{e^{ikr}}{r} \int d^3x' e^{-i\vec{k}'\cdot\vec{x}'} V(\vec{x}') < x'|\psi^+ > \tag{3.15}$$

Defining outgoing spherical wave amplitude by;

$$f(\vec{k},\vec{k}') \equiv -\frac{1}{4\pi}\frac{2m}{\hbar^2}(2\pi)^3 \int d^3x' e^{-i\vec{k}'\cdot\vec{x}'} V(\vec{x}') < x'|\psi^+ > \tag{3.16}$$

$$f(\vec{k},\vec{k}') \equiv -\frac{1}{4\pi}\frac{2m}{\hbar^2}(2\pi)^3 < k'|V|\psi^+ > \tag{3.17}$$

And the solution;

$$< x|\psi^+ > \simeq \frac{1}{(2\pi)^{3/2}}\left[e^{i\vec{k}\cdot\vec{x}} + \frac{e^{ikr}}{r} f(\vec{k}',\vec{k})\right] \tag{3.18}$$

Under the weak scattering potentials, the $< x'|\psi^+ >$ term can be approximated as;

$$< x'|\psi^+ > \rightarrow < x'|\phi > = \frac{e^{i\vec{k}\cdot\vec{x}'}}{(2\pi)^{3/2}} \tag{3.19}$$

This is the Born approximation [65]. The amplitude becomes;

$$f(\vec{k}',\vec{k}) = -\frac{1}{4\pi}\frac{2m}{\hbar^2}\int d^3x' e^{i(\vec{k}-\vec{k}')\cdot\vec{x}'} V(\vec{x}') \tag{3.20}$$

where the integral is just the Fourier transform of the potential V with respect to the scattering vector, $\vec{k} - \vec{k}'$. For a crystal, this amplitude is non-zero only for certain values of V. For a single scatter located at $\vec{R}$ with respect to the origin, the phase difference for the electrons at this point is $e^{i\vec{R}\cdot\vec{k}}$ with respect to the origin. And the distance ($|\vec{r}|$) becomes $|\vec{x} - \vec{R}|$. The wave-function is given as;

$$< x|\psi^+ > \simeq \frac{e^{i\vec{k}\cdot\vec{R}}}{(2\pi)^{3/2}}\left[e^{i\vec{k}\cdot\vec{x}} + \frac{e^{ik|\vec{x}-\vec{R}|}}{|\vec{x}-\vec{R}|} f(\vec{k}',\vec{k})\right] \tag{3.21}$$

Since $r >> R$,

$$k|\vec{x} - \vec{R}| \approx kr - k\frac{\vec{x}}{r}\cdot\vec{R} \tag{3.22}$$

and the energy is conserved so the momentum;

$$\vec{k}' = k\frac{\vec{x}}{r} \tag{3.23}$$

$$\vec{q} \equiv \vec{k} - \vec{k}' \tag{3.24}$$

The wavefunction becomes;

$$< x|\psi^+ > \simeq \frac{1}{(2\pi)^{3/2}}\left[e^{i\vec{k}\cdot\vec{x}} + \frac{e^{ikr+i\vec{q}\cdot\vec{R}}}{r} f(\vec{k}', \vec{k})\right] \tag{3.25}$$

Considering the lattice points in the crystal as scatters which are located at $\vec{R}_l$ (Figure 3.10),

$$< x|\psi^+ > \simeq \frac{1}{(2\pi)^{3/2}}\left[e^{i\vec{k}\cdot\vec{x}} + \sum_l \frac{e^{ikr+i\vec{q}\cdot\vec{R}_l}}{r} f_l(\vec{k}', \vec{k})\right] \tag{3.26}$$

The contribution from the first term is zero when $\theta \neq 0$. The intensity per unit solid angle

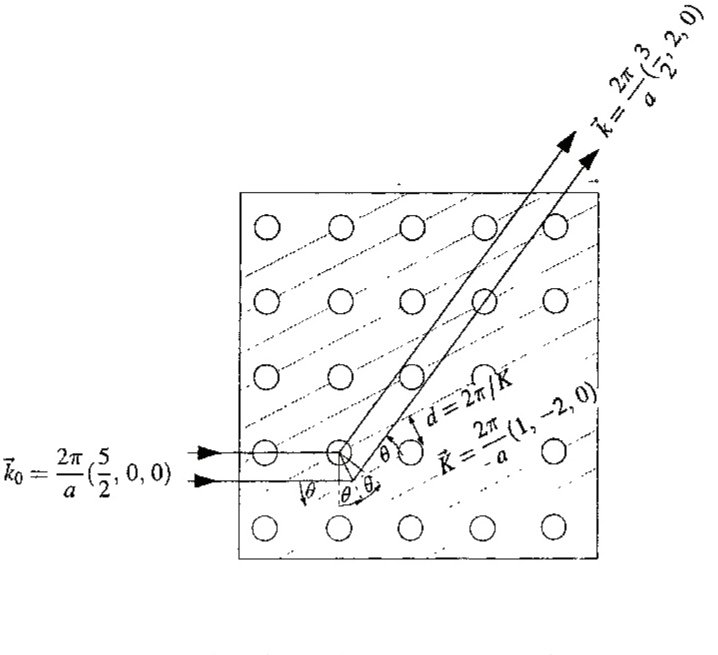

Figure 3.10.: Bragg scattering from the (21) planes of a square lattice [66].

for the incoming beam from the identical atoms and arranged in a Bravais lattice becomes [66];

$$I = I_{atom} \left| \sum_{l} e^{i\vec{q}\vec{R}_l} \right|^2 \tag{3.27}$$

where $I_{atom} = |f(\vec{k}, \vec{k}')|^2$ is the intensity per unit solid angle from a single atom.

In a RHEED experiment, only the few top layers contribute to the reflection electron diffraction, so only the two-dimensional surface lattice is considered [64]. In this case Bravais lattice vector becomes $\vec{R}_l = l_1\vec{a}_1 + l_2\vec{a}_2$. These Bravais lattice vectors may differ from the crystal's usual lattice vectors.

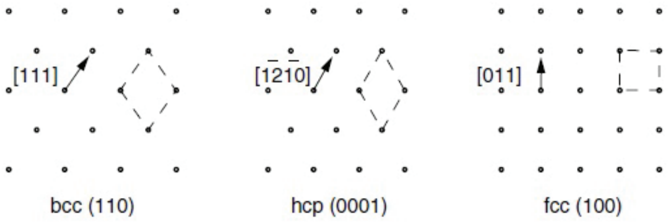

Figure 3.11.: Surface unit cells of different crystal types [64].

In Figure 3.11 the unit cell vectors for different type of the perfect crystal surfaces are shown. The surface atoms can move from the bulk crystal positions in order to minimize surface energy [67]. The top surface planes can also relax towards to the surface [67]. Re-positioning of the surface atoms under different physical conditions is defined as surface reconstruction. An example to the surface reconstruction is given in Figure 3.12 (c), where the surface periodicity in perpendicular direction is twice as the bulk lattice and same in the horizontal direction. This surface has a different periodicity with respect to the its bulk.

In a RHEED experiment only the low glancing angles are used. Momentum of the electrons are used in RHEED experiments is approximately 50 Å^{-1} while reciprocal spacing of the surface of crystal is about 3 Å^{-1}. Diffraction from the rows of atoms is equivalent to diffraction from the lines of a grating in classical optics and the interference

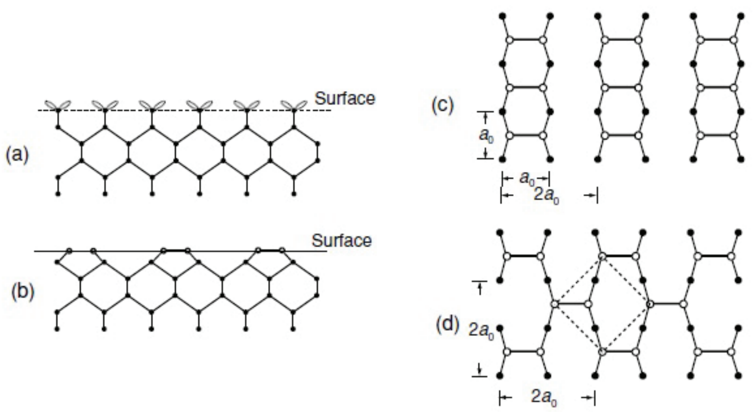

Figure 3.12.: Surface reconstruction of a Si(001) surface. Surface is just cut before and after reconstruction (side view) (a) and (b). Plan view of 2 x 1 (c) and c(2 x 2) reconstruction. [64].

from the surface states are produced by only the reciprocal lattice points as;

$$I \propto \sum_{l,m} e^{i\vec{q}(\vec{R}_l+\vec{\tau}_m)} \tag{3.28}$$

and the term $e^{i\vec{q}\vec{R}_l}$ is non zero only when $|\vec{q}| = |\vec{G}|$ where $\vec{G}$ is the reciprocal lattice vector of the lattice. Assuming the e-beam is striking from the y direction, the intensity becomes;

$$I \propto \sum_{m} e^{i\vec{q}\vec{\tau}_m} \sum_{l} e^{i\vec{q}\vec{R}_l}. \tag{3.29}$$

Diffraction pattern from a 2D lattice is shown in Figure 3.13.

Experimentally observed RHEED patterns contains streak formations at low glancing angles. The intensity of the diffraction spots in the RHEED patterns involve sums of the all lattice points. Spot intensities contain geometric series leading to the $\sin^2(x)$. Therefore, diffraction spots become streaks.

The measurement and the analysis of the RHEED pattern of a non-ideal surface which contain structures such as steps and terraces may become a difficult task. To calculate the spot intensity from a surface containing step-wise structure with equal lengths and heights (L, d), the amplitude of the scattering of electrons from the top layer only can

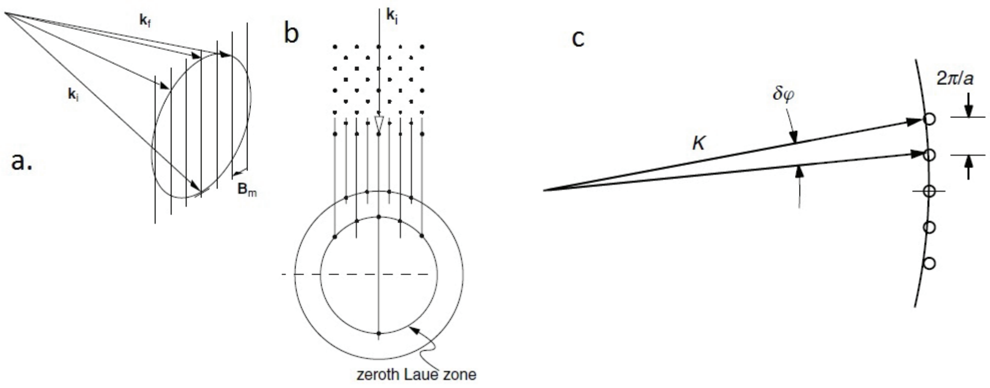

Figure 3.13.: (a) Ewald sphere construction of a surface mesh.(b) Diffraction pattern formation from a c(4 x 4) reconstructed surface. (c) Lattice parameter measurement from a diffraction pattern. [64].

be calculated as;

$$A(\vec{q}) \propto \sum_{n,m} e^{iq_x(na+mL)} e^{-iq_z md} \tag{3.30}$$

$$A(\vec{q}) \propto \sum_{n} e^{iq_x na} \sum_{m} e^{im(q_x L - q_z d)} \tag{3.31}$$

where only a one-dimensional lattice is used as a Bravais lattice. A geometrical diagram of the lattice s given in the top-left part of Figure 3.14. The pattern due to the geometric

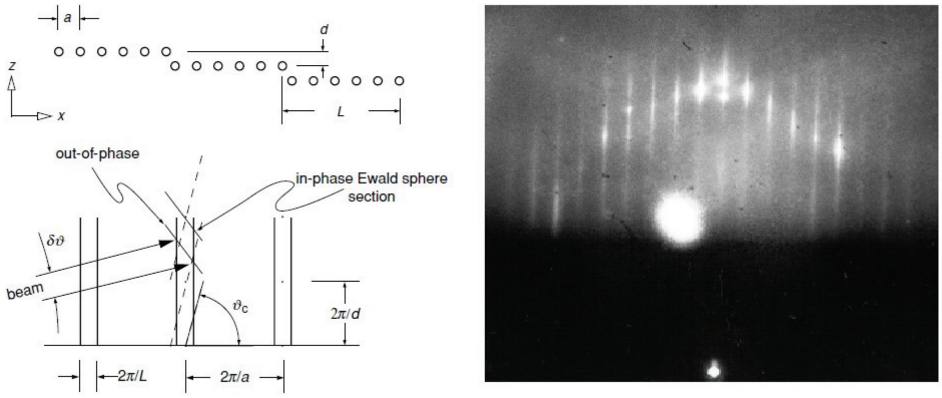

Figure 3.14.: Left; Geometrical diagram for real space (upper part), and reciprocal space (bottom part). Right; Diffraction pattern from GaAs staircase of steps [64].

series in the Eq. 3.31 are superimposed RHEED patterns consisting of two sub-patterns. (see Figure 3.14, right part).

3.2.2. X-ray Diffraction and Reflection

The orientation and the crystal quality of the epitaxial layers can be determined with the XRD measurements. The XRD technique differs from the RHEED with the usage of X-ray photons instead of the high energy electrons and ability to work with large range of incident and scattered angle geometries. The typical wavelength of the photons used in XRD experiment is approximately 1.5 Å which is smaller than the lattice constant of the crystals. The short wavelength of the photons allow them to be scattered from the deep lattice points in the crystal. The penetration depth of the Cu $K\alpha_1$ x-rays from a highly crystalline CdTe film is ~ 8 µm.

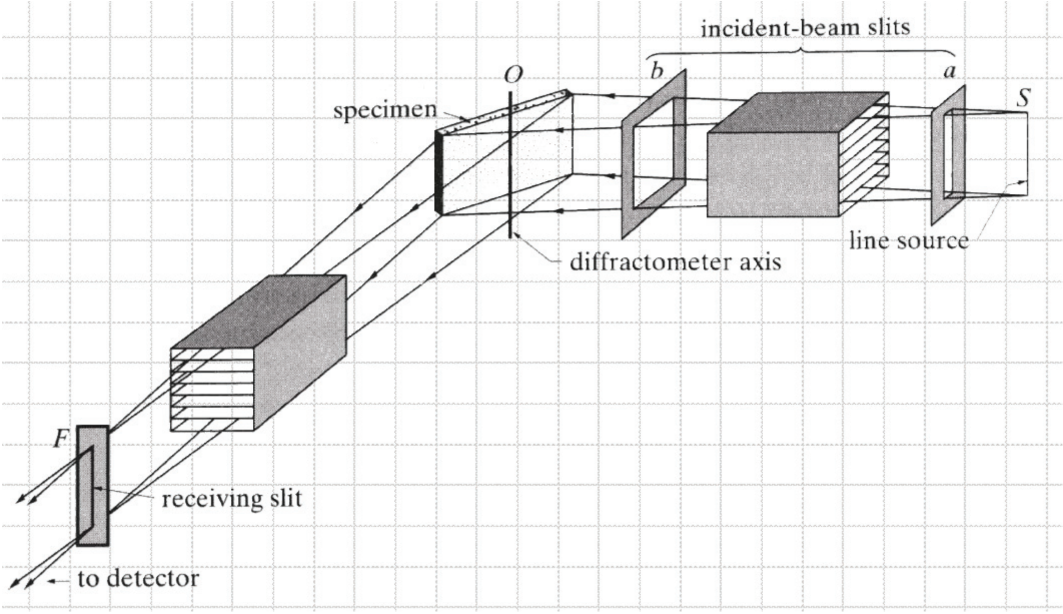

Figure 3.15.: A general optic setup for an XRD experiment. [68]

The experimental setup of an XRD measurement is shown in Figure 3.15. The generated X-rays from a X-ray source tube are directed to a sample with the incident optics and diffracted photons from the crystal are collected at detector with the receiving optics. X-ray photon spectra of a X-ray tube is shown in Figure 3.16. There are 3 dominant peaks in the spectra; $K\alpha_1$, $K\alpha_2$, and $K\beta$. In an XRD experiment with normal resolution and without any specific wavelength filters, diffraction from the crystal planes create more than one peak in XRD spectra. However, in a high resolution XRD (HRXRD) experiment, monochromators such as Ge(220) crystals are employed for the beam conditioning. The resulting HRXRD spectra from the individual crystal planes contains single peaks only. The scattering of the parallel beams of photons with the wavelengths comparable to lattice constant of the crystals creates diffraction patterns at a distance from the sample. The diffraction patterns can be analyzed with the Bragg's law as;

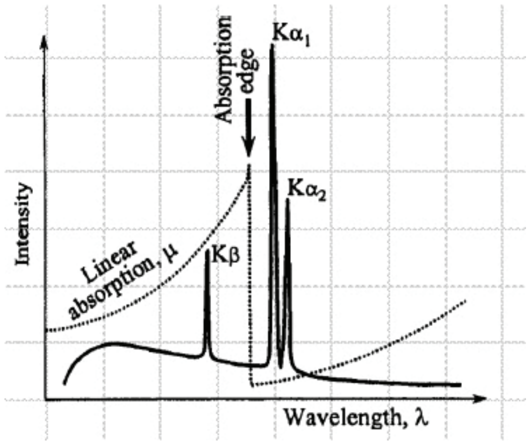

Figure 3.16.: Generated X-ray photon spectrum (solid line) from a X-ray source and filter effect (dotted line) are shown [68].

$$n\lambda = 2d_{hkl}sin\theta \tag{3.32}$$

where n is diffraction order parameter, d_{hkl} is inter-planar distance of the planes parallel to the surface direction, λ is incident photon wavelength, and θ is the angle between the surface and incoming beam. Diffraction from a perfect crystal must have multiple reflections from the parallel crystal planes resulting in single peaks. On the other hand, XRD from poly-crystal or amorphous materials create multiple diffraction patterns from different crystal orientations. The intensities related to these diffraction patterns can be calculated from the scattering of free particles from a crystal surface (see previous section).

The epitaxially grown thin films may have multiple diffraction spots due to the diffraction from the substrate and film planes. To locate the diffraction from crystal planes, a Gonio scan is performed. The Gonio scan is a low resolution surface symmetric scan with Bragg-Brentano geometry. After determination of the diffraction peak positions in the XRD spectra, the diffraction peaks are further investigated with the HRXRD experiments. The HRXRD experiments involves geometric scans around the surface diffraction peaks in reciprocal space (right part of Figure 3.17). The scanned angles and their spanning ranges which were used in this study are shown in the left side of Figure 3.17. The

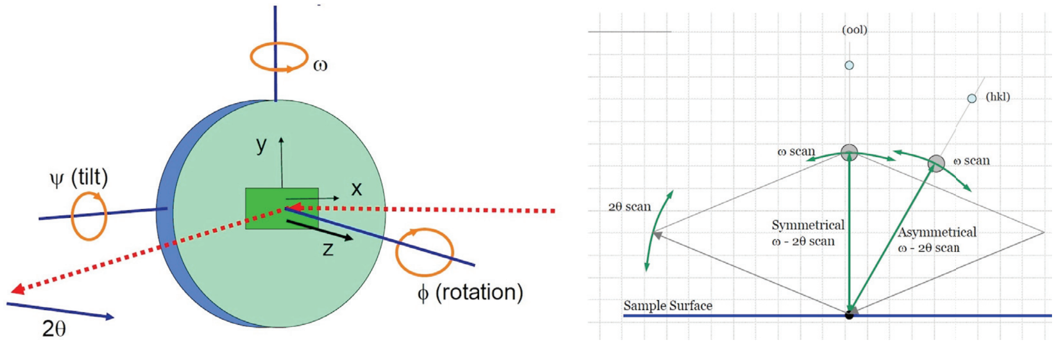

Figure 3.17.: Left: 3 scanning angles and 3 movement axes in a XRD experiment. Right: relative scanning postions in reciprocal space during different XRD experiments [68].

diffraction spot is formed from the constructive interference of multiple reflections from the every single plane in a crystal. The single layer dependence of the diffraction spots transform the diffraction spots to the distributions in the reciprocal space of the crystal lattice system. High resolution scans around the diffraction points allows the evaluation of the crystal quality of the sample which are named as RC. The RC scans are separated from the regular symmetric Gonio scans in terms of the asymmetry around the ω angle. A RC scan is capable of scanning 2D projection of the diffraction peak in reciprocal space. The RC scans are performed with a Bartels type double-axis diffractometer. The Bartels diffractometer uses an arrangement of two channel-cut crystals with four diffracting surfaces as a monochromator. The Bartels monochromator produces a conditioned beam with a divergence and wavelength spread that are both determined by the intrinsic rocking curve width of the monochromator reflections with a divergence of 5 arc-s and a wavelength spread of $\delta\lambda/\lambda = 2.3 \times 10^{-5}$ for a four Ge (110) crystal monochromator. The broadening of the RC in terms of FWHM may give the information about the structural properties of the epilayers such as defect density, in-plane strains, distribution of compositions. The triple-axis diffractometer geometry has also been used for mapping of the diffraction spots in the reciprocal space. The reciprocal space mapping allows the separation of strain broadening and angular broadening of defects. A reciprocal space map (RSM) from a HRXRD experiment of a Si(001) crystal is shown in Figure 3.18.

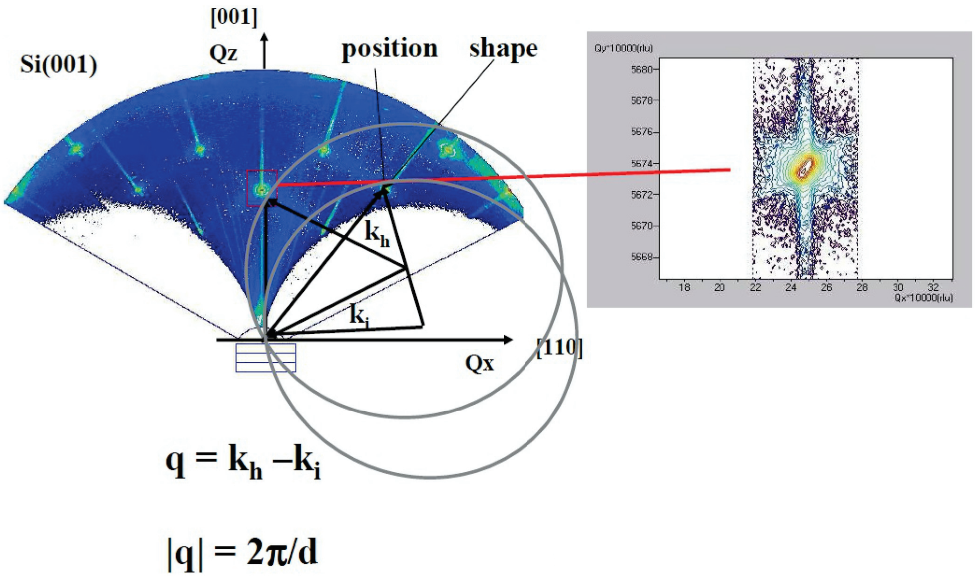

Figure 3.18.: Reciprocal scape maps of a Si(001) crystal on Ewald's sphere. [68].

Alternatively, X-rays may be used at low incident angles to obtain additional information from the surface and the interfaces [69]. Using the Fresnel equations and modelling the complex refractive index of the layer and the substrate with the classical theory of dispersion allows the calculation of the reflections from the multiple layers and substrate. The interface roughness, the layer thickness, the substrate and the layer densities can be modelled to fit experimental x-ray reflectivity data [69]. The effects of the thickness, roughness, and densities to the reflectivity of a sample are shown in Figure 3.19.

3.2.3. X-ray Photoelectron Spectroscopy

The crystals which are irradiated with soft x-rays will emit electrons. If the energy of the x-ray photon is greater than the binding energy of the electron in its shell, the electron will be released with a kinetic energy which has not been spent during the electron removal from the shell. The binding energies of the atomic species in the materials are quantized and unique. The use of the monochromatic x-ray photons allows determination of the binding energies of the electrons from the different atomic orbitals. The measured kinetic energy is unique for the ejected electron. In a such process, photon energy is spent

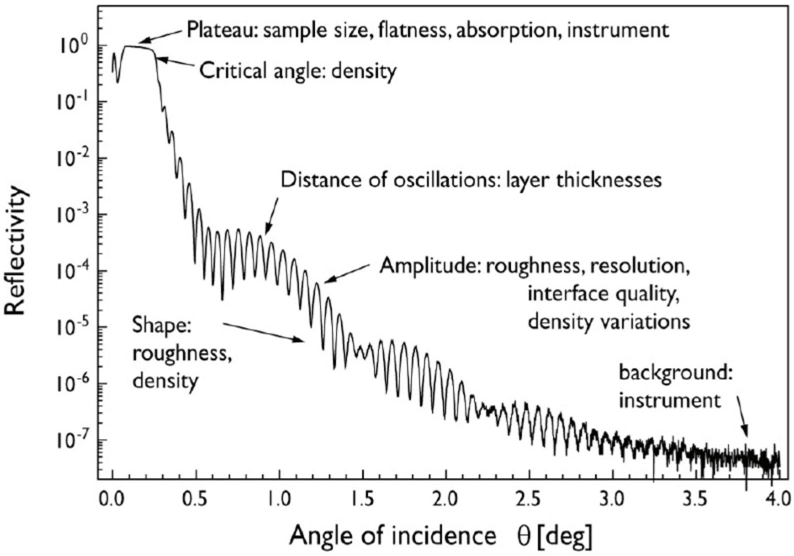

Figure 3.19.: X-ray reflectivity experiment data around the critical point of the material and features of the reflectivity plot [68].

to create a free electron as;

$$h\nu = \frac{p^2}{2m_e} + (E_{vacuum} - E_{core}). \tag{3.33}$$

where the E_{vacuum} is the vacuum level energy and the E_{core} is the core level energy of the electron. Only a few top layers of the materials contribute to the XPS signal which makes XPS a surface sensitive characterization technique.

After an electron is removed from its core state it may undergo different scattering processes resulting in kinetic energy loses and these electrons may not be detected. The ion relaxes through different processes following the ejection of the electron from its shell. An important ion relaxation process is the generation of Auger electrons. The empty electron state is filled from a high energy state to core state electron transition and a secondary electron is emitted to conserve total energy in Auger process. In Figure 3.20, photoelectron generation and secondary electron generation are shown. A sample XPS spectrum of Sn is given in Figure 3.21. At high energies a strong background is dominating the spectrum while at low energies the background is relatively weak. The Auger electrons are responsible from for strong background in the XPS spectrum.

Another important feature of the XPS spectrum is the observation of separation

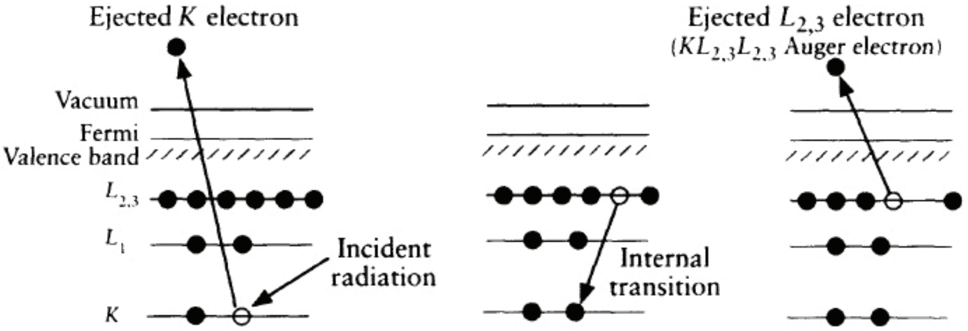

Figure 3.20.: Left: Photoelectron generation by X-ray photons. Middle and Right; Auger electron generation process [70].

of energy levels due to the spin-orbit splitting. The Coulomb interaction between the electrons and atom results in an effective electric field to electrons. Therefore, electrons are affected by a magnetic field since they are moving in orbitals. Magnetic moment and this magnetic field interacts to create a spin-orbit contribution to electrons total energy which is given as [65];

$$\begin{aligned} V_{LS} &= -\vec{\mu}\cdot\vec{B}_{eff} && (3.34)\\ &= \vec{\mu}\cdot\left(\frac{\vec{v}}{c}\times\vec{E}\right) && (3.35)\\ &= \left(\frac{e\vec{S}}{m_e c}\right)\cdot\left[\frac{\vec{p}}{m_e C}\times\left(\frac{\vec{x}}{r}\right)\frac{1}{(-e)}\frac{dV_c}{dr}\right] && (3.36)\\ &= \frac{1}{m_e^2c^2}\frac{1}{r}\frac{V_c}{dr}\left(\vec{L}\cdot\vec{S}\right) && (3.37) \end{aligned}$$

The splitting of the energy levels may be given as;

$$\begin{aligned} L\cdot S &= \frac{1}{2}\left[J^2 - L^2 - S^2\right] && (3.38)\\ &= \frac{1}{2}\left[j(j+1) - l(l+1) - \frac{3}{4}\right] && (3.39)\\ & && (3.40) \end{aligned}$$

where total angular momentum quantum number is $j = l\pm\frac{1}{2}$. Therefore spin-orbit splitting

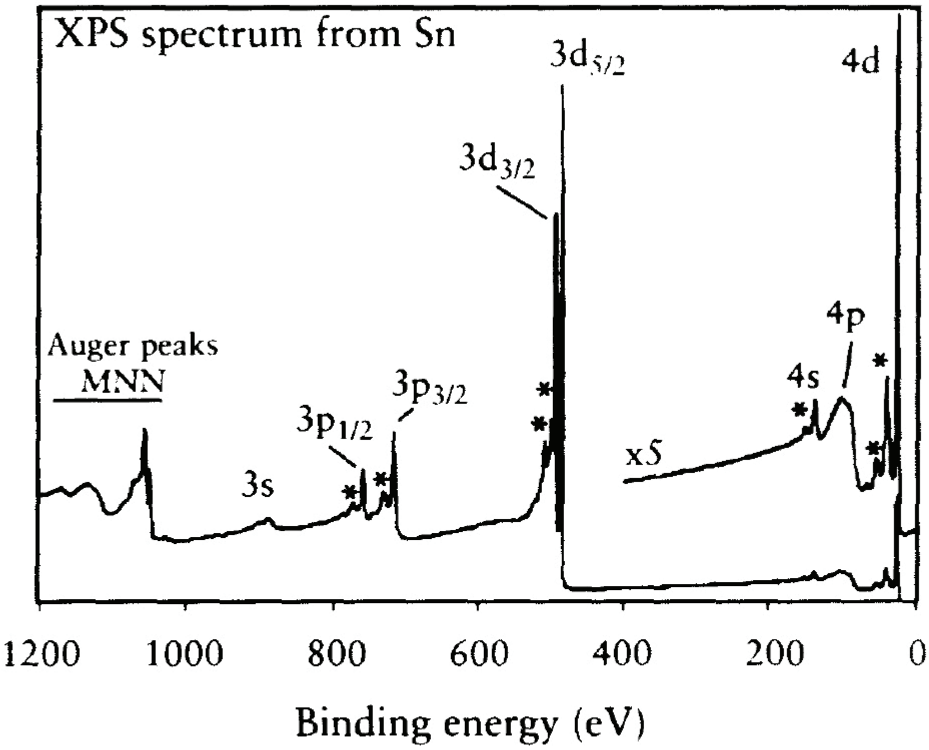

Figure 3.21.: XPS spectrum of Sn taken with Al K_α radiation [70].

may be observed in XPS spectra with the states $l \neq 0$ only. A p state level is split to 2 levels with $p_{1/2}$ and $p_{3/2}$. The occupancy of the p states are given with degeneracy of the level as $2j + 1$. Therefore a $p_{1/2}$ state will have 2 degenerate states while a $p_{3/2}$ state will have 4 degenerate states. The spin-orbit splitting effect is a quantum mechanical phenomena. The energy of the spin-orbit splitting for the same elements are constant and the relative contributions from these states can be calculated from the area of the peaks in the XPS spectrum. The fitting of the peaks must be performed with Gauss or Lorentz like distributions. The spin-orbit level splitting energy and the contribution of the spin states to area of the peaks must be constrained.

Another important feature of the XPS spectrum is the observation of the different oxide states of the transition-metals. Metals or transition metals can bond with oxygen molecules or atoms with different oxide states. Different oxidizing states such as Ga_2O and Ga_2O_3 can be observed from the XPS spectrum. The bonding energy of the high oxidizing states are greater compared to the bonding energy of the low oxidizing states. GaAs and GaO_x oxidizing states are shown in Figure 3.22.

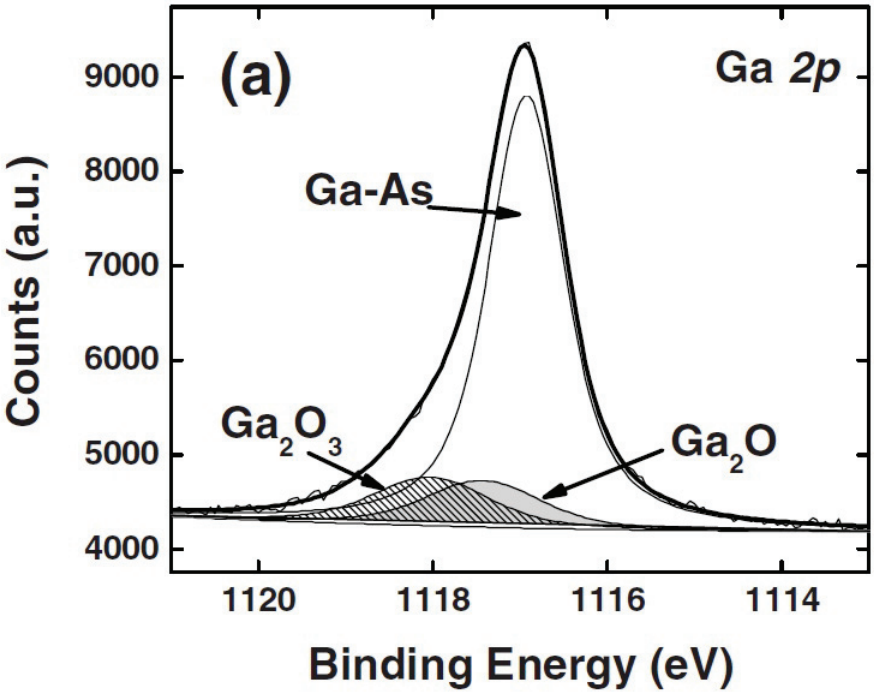

Figure 3.22.: Ga 2p XPS spectrum of a GaAs sample with GaAs and different oxidizing states [71].

3.2.4. Spectroscopic Ellipsometry

The SE technique is based on the measurement of the change of the polarization of the light due to material-electromagnetic wave interaction. The SE is the best known technique to measure the dielectric function of the solid state material systems. The electronic structure and the optical properties of the semiconductor crystals are characterized by the dielectric function. The capability to measure phase changes in materials makes SE a highly sensitive characterization tool for thin film epitaxy. SE is extremely sensitive to surface changes during epitaxial growth since it measures the change in polarization of reflected light rather than the intensity.

In a basic SE experimental setup (Figure 3.23), a linearly polarized light with a known orientation is directed to the material surface and the elliptically reflected light from the material is collected. The change of the polarization for different wavelength is analyzed in SE. The change in the polarization of the p and s polarization components

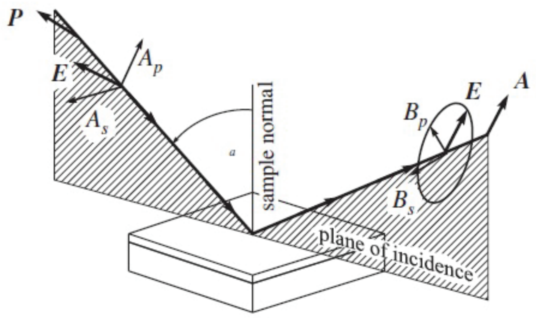

Figure 3.23.: A simple SE experiment with the electric and magnetic field components [72].

due to the material is given as;

$$\rho = \left(\frac{B_p}{B_s}\right) / \left(\frac{A_p}{A_s}\right) \tag{3.41}$$

where A and B amplitudes correspond to the incident and exiting waves, respectively. The ρ is mapped to real-valued Ψ and Δ parameters as;

$$\rho = tan\Psi e^{i\Delta} \tag{3.42}$$

where Ψ and Δ are the coordinate systems of the Poincaré sphere [73]. Δ is the differential phase retardation or phase change on reflection of the two orthogonal polarization states. The Poincaré sphere is a three dimensional sphere with the Stokes parameters as axes. The Stoke parameters define the polarization states of un-polarized waves. In the right side of Figure 3.24, the electric field components of an elliptically polarized light are shown in (Ψ, Δ) coordinate system. Transformation between the Stoke parameters and the (Ψ, Δ) coordinate parameters can be given as [73];

$$S_1 = -cos2\Psi \tag{3.43}$$

$$S_2 = sin2\Psi cos\Delta \tag{3.44}$$

$$S_3 = -sin2\Psi sin\Delta\ . \tag{3.45}$$

The complex reflection ratio can be used for the modeling of the dielectric function of the material which material may have layered or bulk type structure. The simplest case of the macroscopic model is a bulk material with its native oxide or contamination layer. The analysis of the ellipsometric signals yields a pseudo dielectric function which depends on the dielectric function and thickness of each optically accessible layer and the angle of incidence. As the layer number and thickness changes the theoretical model has to be changed accordingly. In Figure 3.24 (left side), the interference of light during the reflection from a layered structure is shown. Additionally, dielectric function of every single layer has to be modeled separately. Finally, a compact model including the layer and the bulk dielectric function components with interference effects is used for data fitting of SE spectra.

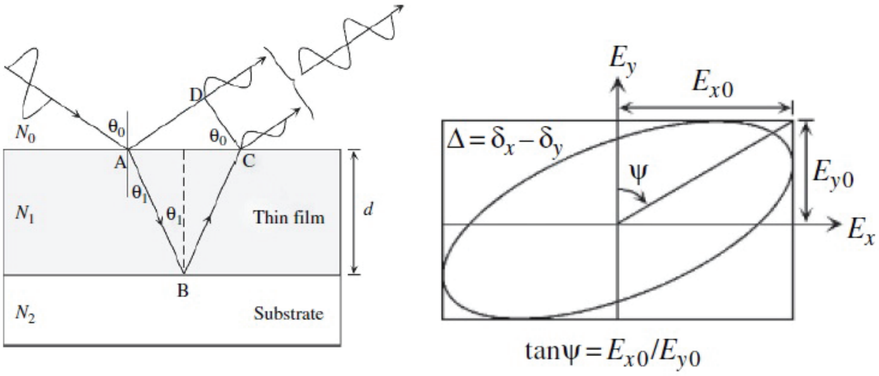

Figure 3.24.: Left: Interference of light due to the layered structure during the reflection. Right: Representation of (Ψ, Δ) coordinate system [73].

Dielectric constant of a material is given in classical electromagnetic theory [73];

$$\epsilon = 1 + \frac{P}{\epsilon_0 E} = 1 + \chi \tag{3.46}$$

where P is polarization, E is applied electric field, and χ susceptibility. And relation between the complex refractive index and dielectric functions can be given as [73];

$$N^2 = \epsilon \tag{3.47}$$

$$n + ik = \epsilon_1 - i\epsilon_2 \tag{3.48}$$

$$\epsilon_1 = n^2 - k^2 \tag{3.49}$$

$$\epsilon_2 = 2nk \tag{3.50}$$

which the dielectric function has frequency ω dependency. To understand frequency dependency of dielectric function, a quantum mechanical approach is needed;

$$\epsilon_{total} = \epsilon_\infty + \frac{\epsilon_0 - \epsilon_\infty}{1 - \omega^2/\omega_{TO}^2} - v_q P(q, \omega) \tag{3.51}$$

where first term is high frequency response of the dielectric function, the second term is due to the atomic vibrations (phonons) and last term from the renormalized electron-electron interaction part of the dielectric function [74]. Fitting the SE data using a quantum mechanical model is not practical. Instead, classical models are used. When a transparent layer is present in the material structure Cauchy or Sellmeier models are used or when strong free carriers concentrations are present, the Drude model is used. The electric polarization is expressed in visible/ultra-violet (VIS/UV) region with the oscillator models (Tauc-Lorentz, Lorentz, Harmonic oscillator) which are used for modeling of crystalline semiconductors. Additionally, the interface and surface effects are incorporated into optical models with approaches such as Effective Medium Approach (EMA).

3.2.5. Photoluminescence

A semiconductor perturbed with the energies greater than the band gap or the defect formation energies of the semiconductor may result in relaxation through photon emitting at various energies. The relaxation of the semiconductor after the photo-excitation with laser may give information about the transitions between defect levels, excitonic energies, and band gap energies. The temperature related effects broaden the spectrum collected during a PL experiment. The excitonic or defect related levels can be less occupied with respect to the electronic levels of semiconductor. The emission from the transitions involving excitonic or defect levels may become suppressed during a room temperature measurement since density of states at the conduction and valance bands are broadened by the thermally excited electrons. In this context, PL measurements are taken at very low temperatures close to 4 K. In the left side of Figure 3.25, PL spectra of bulk and thin film CdTe samples at 5 K are shown. The shallow defect states due to the point defects can be observed from the figure. In the right side of Figure 3.25, PL spectra of a CdTe thin film at 77 K is presented. The extended defect related Y-emission peaks can be observed around 1.47 eV. It can be seen from the figure that the defect density in thin film clearly affects the PL emission from the extended defect states.

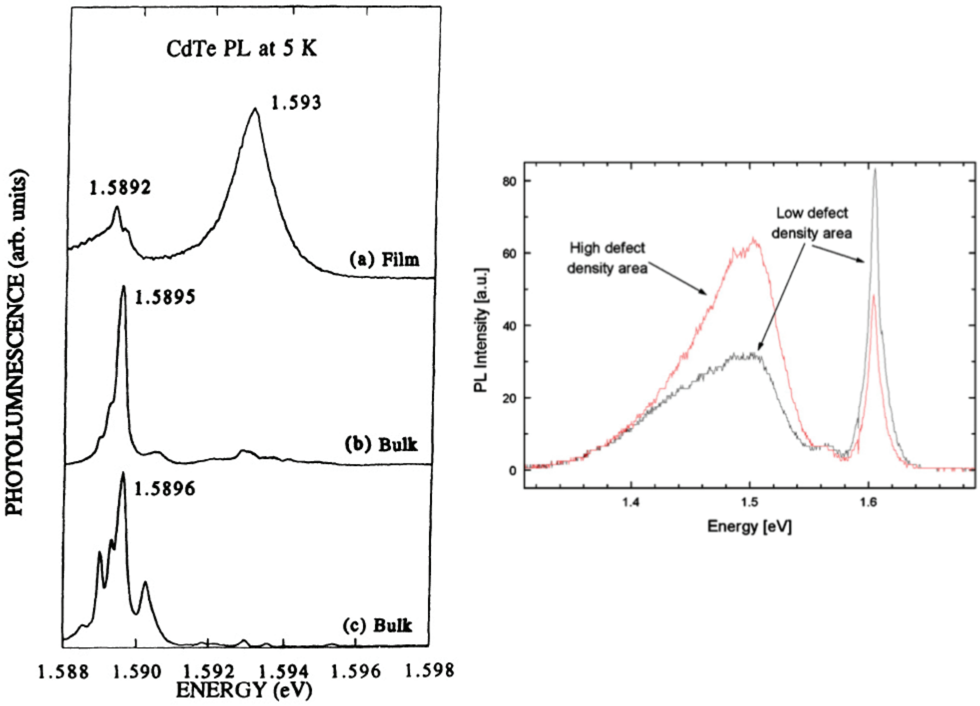

Figure 3.25.: Left: PL spectrum at 5K from (a) n-type MBE grown thin film, (b) high resistivity bulk sample, (c) as grown p-type bulk CdTe [75]. Right: PL spectrum of CdTe thin films at 77 K from areas with high and low extended defect densities. [76]

3.2.6. FTIR Transmission

To determine the thickness of the CdTe epilayers grown on GaAs(211)B substrates, FTIR transmission measurements were performed. The variation in the thickness across the epilayer was calculated by transmission measurements on different locations on the epilayer. Thickness of the epilayer was calculated from the thin-film interference fringes in the transmission spectrum of the epilayer. A sample transmission spectrum of a CdTe epilayer taken with FTIR is shown in Figure 3.26. Thickness from the transmittance can be calculated as;

$$d = \frac{1}{2\,n\,(\nu_1 - \nu_2)}$$

where ν_1 and ν_2 are the peak frequencies of the fringes in the transmission, and n is the refractive index of the material.

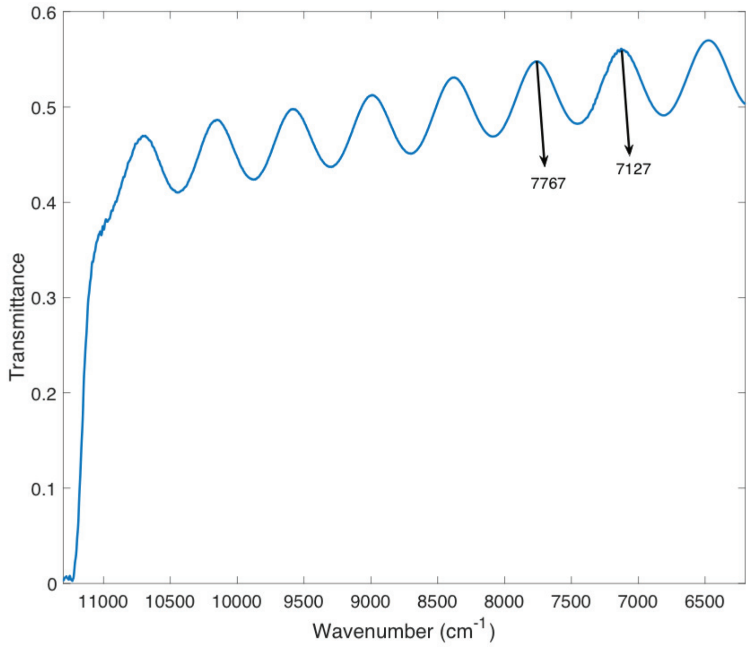

Figure 3.26.: FTIR transmission spectrum of a CdTe layer grown on GaAs(211)B.

3.2.7. Atomic Force Microscopy

The surface morphology of the epitaxial thin films can be mapped with AFM. AFM is a scanning probe microscopy technique which employs the interaction between the tip and the surface of the material to probe the surfaces. The interaction potential between the tip and material can be either exchange, Van der Waals or electromagnetic. To probe the surface morphology, the tip movement is monitored while a very small and constant force is maintained on the AFM tip. There are several operating modes of the AFM to maintain a constant force on the tip such as contact, non-contact, and tapping modes. The movement of the tip is monitored with a help of a laser which is focused on the tip cantilever (Figure 3.27). In non contact or tapping modes, the tip is stimulated with a harmonic motion. The changes in the amplitude or the frequency of the harmonic motion of the tip is then monitored. Different surface structures, valleys or hills affect the tip oscillations in different manner which allows the mapping of the material surface. AFM is capable of detection of surface features with few nanometers [77].

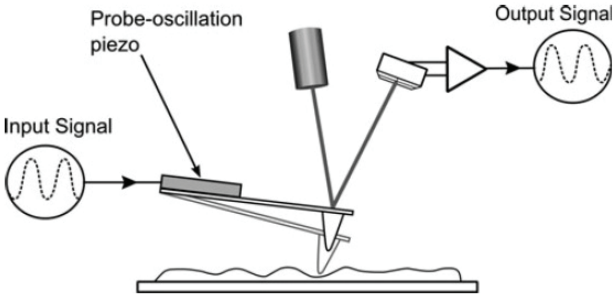

Figure 3.27.: An example AFM setup with an oscillating tip [77].

CHAPTER 4

THERMAL DEOXIDATION OF GaAs(211)B

4.1. Chemical and Physical Properties of the GaAs(211)B surface

GaAs wafer technology offers an easily prepared substrate for epitaxial growth, which is thus referred to as epiready, and is characterized by numerous advantages. On the other hand, as a by far most widely used semiconductor and substrate material, Si requires chemical preparation prior to the growth, which prolongs and complicates the growth process. Further, this chemical step might introduce contaminants to the surface, such as C, which is extremely difficult to remove. Conversely, an epiready GaAs substrate can be loaded directly to the growth chamber as received and, after protective surface oxide removal of shorter duration and at a comparatively lower temperature (thermal deoxidation) [78] , an epitaxial ready-to-grow substrate surface can be obtained. However, thermal deoxidation of both epiready and chemically prepared non-epiready GaAs wafers prior to the growth needs to be optimized, since thermal deoxidation affects the quality and nature of the consecutive epitaxial growth [79–83].

Rapid deoxidation of different oxide molecular structures from the GaAs surface occurs at different temperatures [79]. GaAs surface thermal deoxidation includes several chemical reactions [79, 84]. At low temperatures, such as 200-300°C, weakly surface-bonded O_2 molecules evaporate from the GaAs wafer surface. Following the O_2 desorption, thermal deoxidation of more complex structures such as As_2O_5, As_2O_3, and Ga_2O takes place, respectively with the following chemical reactions [79, 82, 84] :

$$3As_2O_5 + 4GaAs \rightarrow 3As_2O_3 + 2Ga_2O_3 + 2As_2(As_4) \uparrow (400^{\circ}C\ to\ 500^{\circ}C) \tag{4.1}$$

$$As_2O_3 + 2GaAs \rightarrow Ga_2O_3 + 2As_2(As_4) \uparrow (400^{\circ}C\ to\ 500^{\circ}C) \tag{4.2}$$

$$As_2O_3 + 6GaAs \rightarrow 3Ga_2O + 4As_2(As_4) \uparrow (400^{\circ}C\ to\ 500^{\circ}C) \tag{4.3}$$

$$Ga_2O \uparrow (\sim 500^{\circ}C) \tag{4.4}$$

Both As-oxide desorption reactions (first and second) produce Ga_2O_3, thus increasing the amount of the Ga_2O_3 molecules at the surface. On the other hand, third reaction generates Ga_2O. At about 500 °C, Ga_2O desorption from the GaAs surface starts, whereby only the most stable Ga-oxide molecule Ga_2O_3 resides at the GaAs surface above that temperature.

GaAs epiready substrates were characterized using XPS and grazing incidence XRR, which yielded data pertaining to the surface chemical composition. XPS measurements were performed with Al x-ray source and SPECS Phoibos 150 Hemispherical Analyzer. Large area focus and 40 eV E-pass energy was chosen to achieve the best signal to noise ratio in the XPS spectra. In Figure 4.1, complete XPS spectrum of an epiready GaAs(211)B sample is shown. Ga, As, C, O, and Mo chemical species are detected and identified from the figure. The source of the C element is believed to be due to the contamination during handling while the source of the Mo element may be coming from the sample holder of the XPS system. Ga, As, and O elements can be readily detected due to the protective oxide layer and the wafer itself from the XPS spectrum. To further investigate the oxidizing states of As and Ga, As 3d, Ga 3d, and Ga $2p_{3/2}$ regions of the XPS spectrum is collected with high resolution (≤ 1 eV). In Figure 4.2 (a), Ga 3d XPS spectrum is shown. Ga 3d XPS spectrum is deconvulated with GaAs and Ga_2O_3 chemical species with the $3d_{3/2}$ and $3d_{5/2}$ states. The XPS spectra produced by the epiready GaAs(211)B sample was simulated with 30 % Gaussian and 70 % Lorentzian

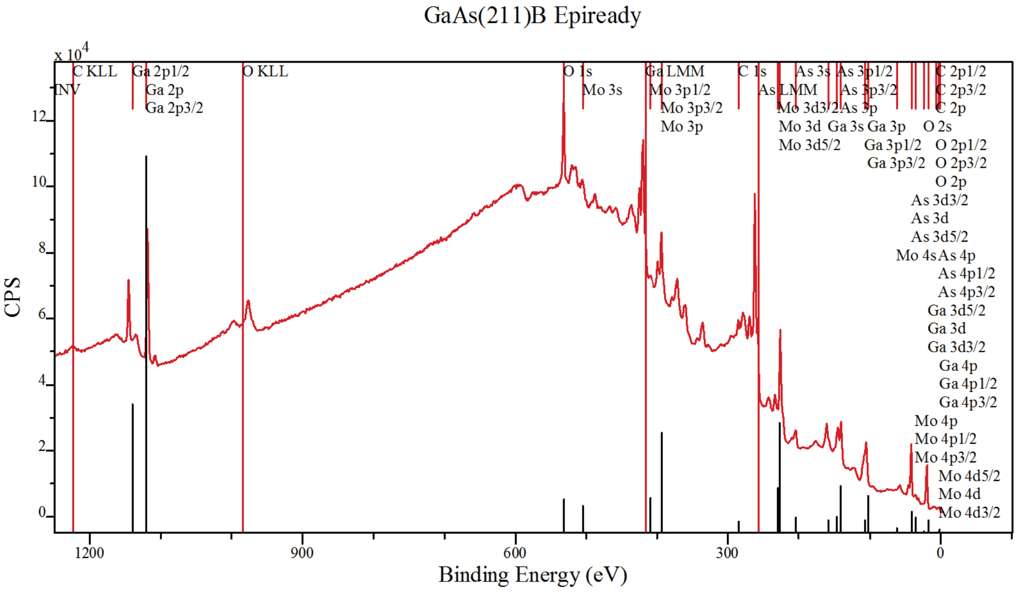

Figure 4.1.: (a) The XPS survey spectrum of an epiready GaAs(211)B wafer.

combinations of line shapes after subtracting a Shirley type background. Spin-orbit splitting energy was set to 0.695 eV and 0.453 eV for As 3d and Ga 3d spectra, respectively. Information depth of the Ga 3d and As 3d spectra is ~ 3 nm while Ga 2p3/2 signal can be collected from approximately 1 nm surface depth due to the electron mean free path differences of various orbital electrons in a highly crystalline GaAs material [85]. The Ga-oxide contribution to total Ga 3d spectrum is found as ~ 15 %. In Figure 4.2 (b), As 3d XPS spectrum is given. As 3d XPS spectrum is deconvulated with the GaAs, As_2O_5, As_2O_3, and As-As dimer chemical species with the $3d_{3/2}$ and $3d_{5/2}$ states. The As-oxide contribution in total As 3d spectrum is detected as ~ 27 %. In Figure 4.2 (c), Ga $2p_{3/2}$ XPS

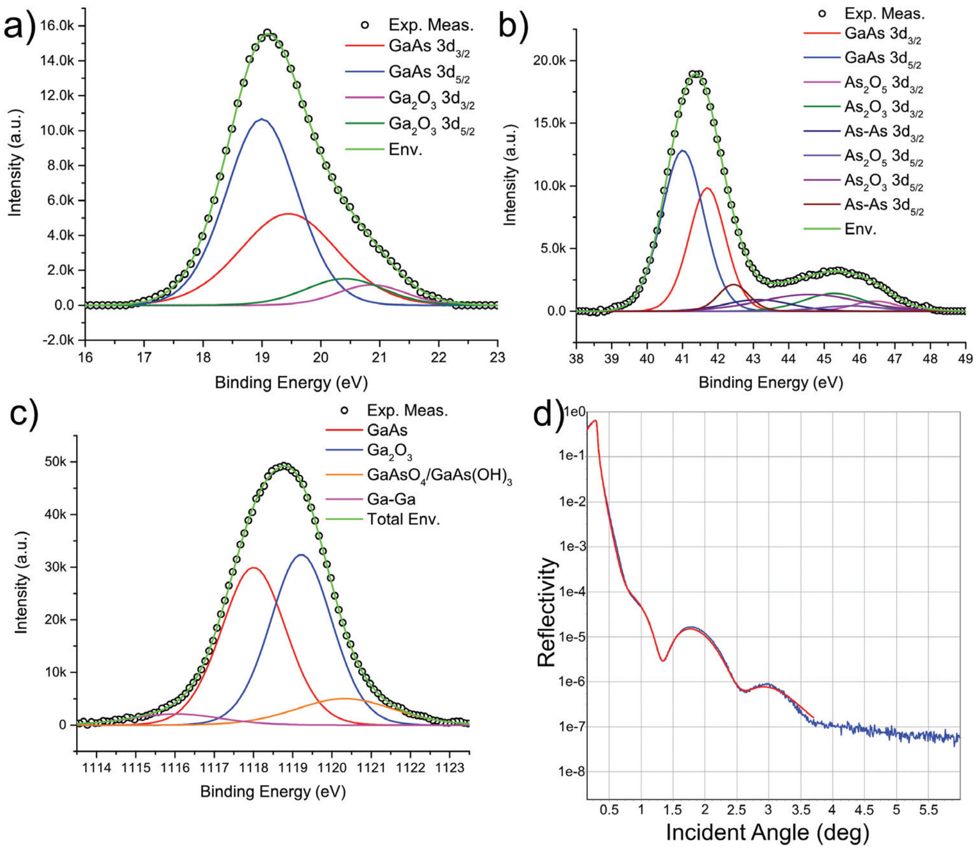

Figure 4.2.: (a) Ga 3d, (b) As 3d, (c) Ga $2p_{3/2}$ XPS spectra and deconvulated chemical species of an epiready GaAs(211)B wafer. (d) XRR spectrum from epiready GaAs(211)B wafer and fitting result with a theoretical model.

spectrum is presented. Ga $2p_{3/2}$ XPS spectrum is deconvulated with the GaAs, Ga_2O_3, $GaAsO_4/GaAs(OH)_3$, and Ga-Ga dimer chemical species. The Ga-oxide contribution in total Ga $2p_{3/2}$ spectrum is detected as ~ 53 %. The difference in the Ga-oxide contribution to Ga $2p_{3/2}$ and Ga 3d can be explained with the escape path difference of these

Table 4.1.: Results of the XRR measurements with theoretical modeling.

	Density (g/cm^3)	Thickness (nm)	Roughness (nm)
Substrate	5.3	640000	0.22
Layer 1	4.274	2.9	0.35
Layer 2	1.276	1.2	0.71
Layer 3	6.154	0.3	0.61

states. Atomic states with higher binding energy such as Ga $2p_{3/2}$ states have smaller kinetic energy compared to Ga and As 3d states since both states are knocked off from the atomic state with the same energy. Therefore, XPS spectrum of Ga $2p_{3/2}$ state is much more surface sensitive.

To analyze the chemical structure and the density values of individual layers, XRR measurement was performed at grazing incident angles for an epiready GaAs(211)B wafer. The reflectivity measurement was modeled with the Fresnel equations. The optical constants were taken from the classical theory of dispersion [69]. The XRR measurement data and theoretical model is given in Figure 4.2 (d). The layered structure was modeled with one substrate and three layers. Results from the theoretical modeling of the XRR measurement is summarized in Table 4.1. Density of Layer 1 was calculated as 4.274 g/cm^3 which suggest this layer may contain Ga_2O (4.77 g/cm^3), As_2O_3 (3.74 g/cm^3), and As_2O_5 (4.32 g/cm^3). It was detected from the XPS measurements that there was no contribution from the Ga_2O to the oxide layer. Therefore, Layer 1 should consist of As_2O_3 and As_2O_5. Density of Layer 2 was found as 1.276 g/cm^3 which should consist mostly of O_2. Finally, density of Layer 3 was calculated as 6.154 g/cm^3 which is very close to the density of Ga_2O_3. Contribution to the total oxide layer thickness from Ga_2O_3, O_2, and As_2O_5+As_2O_3 were calculated as 7.5 %, 26.8 %, and 65.7 %, respectively.

Surface morphology of the epiready GaAs samples was investigated by employing AFM method. More specifically, AFM surface topography image was taken with a Si tip in tapping mode. Figure 4.3 (a) provides AFM topography images of a 5 μm × 5 μm area for an epiready GaAs sample. To gain a better understanding of the surface morphology, statistical analysis of the AFM image pertaining to the epiready sample was performed. Peak-to-peak, root mean square (RMS) roughness, and skewness values were calculated as 4.76 nm, 0.42 nm, and 0.23, respectively. In Figure 4.3 (b), the SEM image of epiready

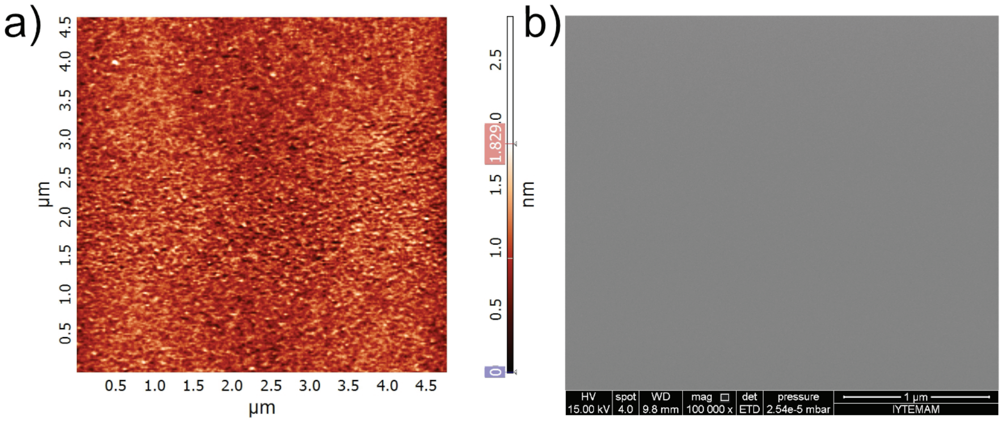

Figure 4.3.: (a) AFM height image and (b) SEM image of an epiready GaAs(211)B wafer surface.

GaAs(211)B is given. It is seen from this figure that, the surface of the epiready GaAs sample is featureless and smooth.

The optical properties of the epiready GaAs(211)B wafer was investigated with SE method. In Figure 4.4, the measured SE data and fitting with the theoretical model is represented. The theoretical model was constructed with a substrate and GaAs-oxide layer. The GaAs substrate is modeled with multiple oscillators while the oxide layer is modeled with the dielectric function from [86]. The roughness and the thickness of the layer was calculated as 0.3±0.1 nm and 3±0.3 nm, respectively. The mean square error (MSE) of the fit was below 2.5. The measured roughness and thickness values from the SE measurement was very similar to those obtained with both AFM and XRR. Therefore, the oxide layer of the epiready GaAs(211)B wafer was characterized with a thickness layer of 3.7±0.7 nm and with a surface roughness of 0.32±0.1 nm.

The crystal quality of the epiready GaAs crystal was determined with XRD from GaAs(422) reflection. RC measurement was performed around GaAs(422) reflection and the results are shown in Figure 4.5. The measured RC spectra was fit with a Pseudo-Voigt model which is a linear combination of Lorentz and Gaussian functions. The FWHM of the RC was found to be 18.2 arc-s which suggest that GaAs wafer has superior crystal quality with a very low level of defect density.

Deoxidation dynamics and the resulting surface morphology of epiready GaAs wafers have mostly been studied in (100), (110) and (111) surface orientations [81–83, 87–91]. However, GaAs (211) surface plays an important role in hetero-epitaxy of CdTe,

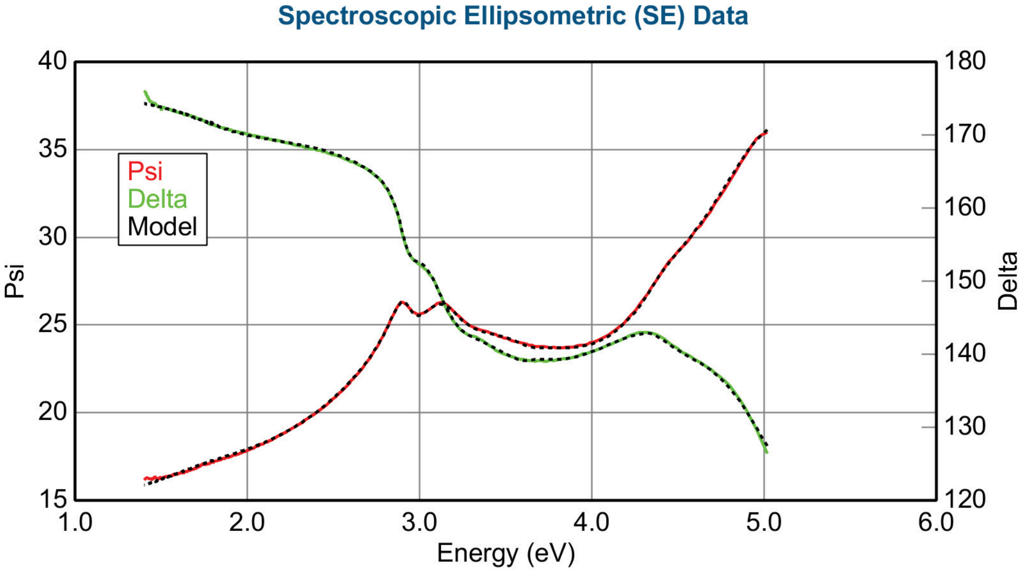

Figure 4.4.: (a) The measured SE data from an epiready GaAs(211)B wafer and fit with theoretical model which involves a GaAs substrate and a GaAs-oxide layer with roughness.

ZnTe, CdZnTe and similar compound II-VI semiconducting layers over these surfaces [23, 53, 92]. In addition, (211) termination of the GaAs surface creates step-like structures at its top layer. Moreover, this surface provides dangling bonds with one and two missing electrons. These features improve the sticking coefficient of Hg, in HgCdTe growth in particular [28]. Surface reconstruction and its Ga or As termination also affect the surface morphology and chemical nature of the protective oxide layers of the epiready wafers.

4.2. Arsenic Assisted Thermal Deoxidation

In general, GaAs surface deoxidation is carried out under As_4 fluxes [79, 80, 82] to preserve As and Ga atoms located on the surface. However, the loss of Ga atoms from the crystal surface is unavoidable when As_4 overpressure method is employed since Ga and As atoms are consumed during Ga_2O_3 desorption from surface while missing Ga atoms can not be compensated with As_4 flux. Thermal deoxidation of epiready GaAs wafer proceeds with the chemical reactions given in the introduction section of this chapter. Thermal deoxidation of the species As_2O_5, As_2O_3, and Ga_2 are completed during heating of the substrates up to 500 °C. However, non-volatile Ga_2O_3 molecule is stable

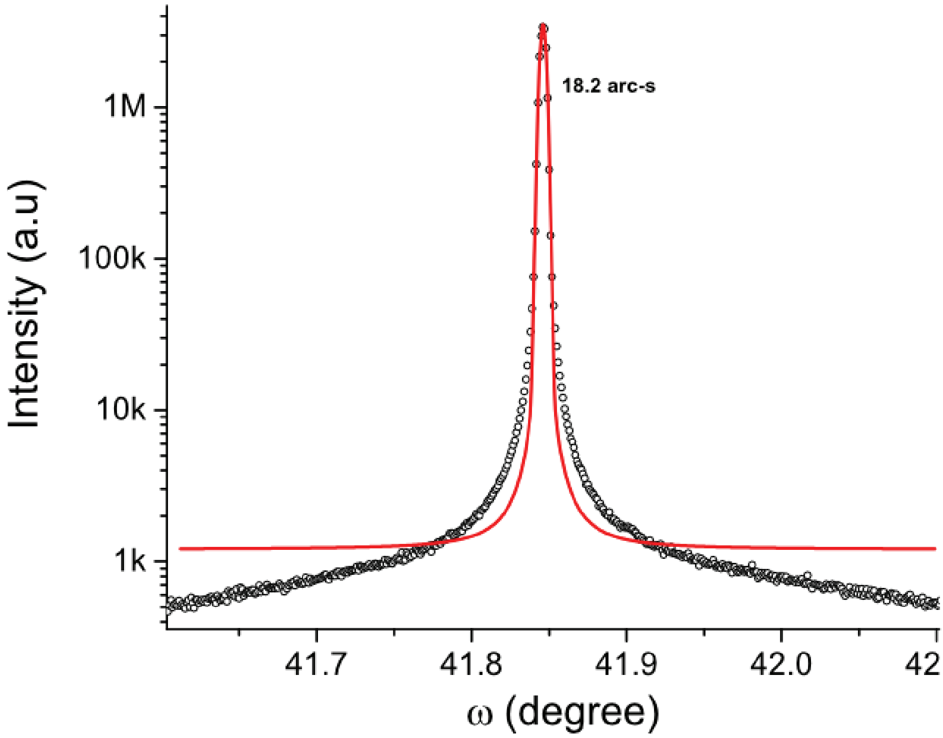

Figure 4.5.: XRD RC spectrum from (422) reflection of an epiready GaAs(211)B wafer.

at temperatures of up to 1000 °C [82, 93]. Fortunately, Ga_2O_3 desorption from the GaAs surface can be accomplished with the help of GaAs molecules at the surface temperature of 585 °C, through the following reaction [80]:

$$Ga_2O_3 + 4GaAs \rightarrow 3Ga_2O \uparrow +2As_2(As_4) \uparrow (585^{\circ}C). \tag{4.5}$$

Furthermore, the deoxidation duration of Ga_2O_3 at 585 °C depends on the oxide thickness and oxide composition of the GaAs substrate. However, the thermal desorption is hindered by the fact that Ga consumption during Ga_2O_3 desorption creates pits 50-200 nm in size and 5-40 nm in depth on the GaAs surface, which may reduce the interface and compromise the overall quality of the consecutively grown CdTe layer [82, 93].

Figure 4.6 shows a high-resolution electron micrograph of a pit region of CdTe/GaAs(211)B interface. Interface region consists of a pit at the GaAs substrate surface. The image shows that several dislocations in the CdTe layer were originating from the interface. Therefore, the pits originating during the deoxidation process can be detrimental to the crystal quality of CdTe epilayers grown on GaAs substrates.

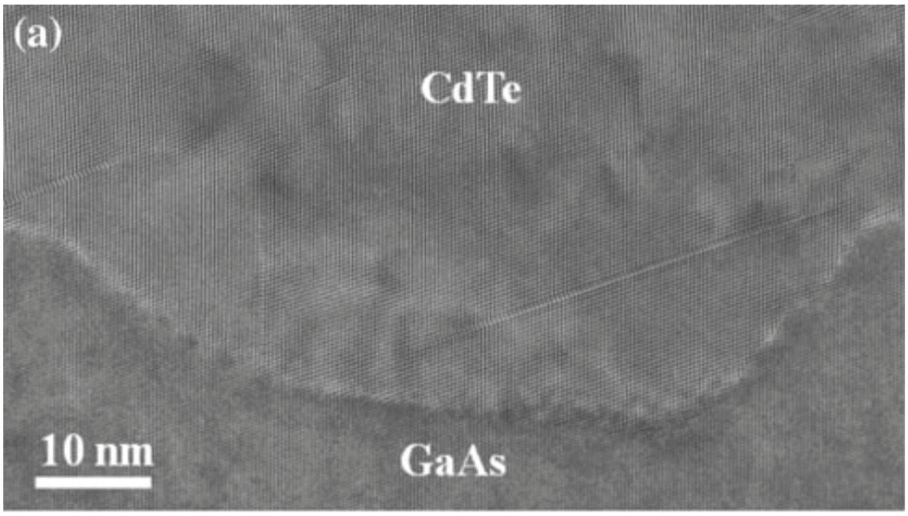

Figure 4.6.: High-resolution electron micrograph of pit region of the CdTe/GaAs(211)B interface which was taken with TEM [94].

The reaction rate of the thermal oxide desorption process under As_4 flux depends strongly on substrate temperature which is given by the Arrhenius relation [95];

$$A = A_0 e^{(-E_a/kT)} \tag{4.6}$$

where, k is Boltzmann constant, T is temperature, and E_a is the activation energy of the chemical reaction. The activation energy of the thermal deoxidation of GaAs-oxide from GaAs wafer has been calculated to be 2.0 eV [96].

4.2.1. Effect of the Deoxidation Duration

The GaAs substrates were deemed "epiready" and no pre-chemical treatment was applied prior to the thermal deoxidation. Epiready GaAs substrates were loaded into load lock chamber and baked at 200 °C for 6 hours to remove moisture from the samples. Temperature measurements during oxide desorption process were performed using calibrated band-edge detection system. GaAs substrates were heated from room temperature to 585±2 °C with 27±3 °C/min. ramp rate. At 300 °C, As_4 flux with 2.5×10^{-6} Torr beam equivalent pressure was directed to the substrates from a valve-controlled solid-source effusion cell. As_4 flux was remained directed to the samples after deoxidation until sample surface temperature decreased to 400 °C, after which the samples were cooled to room temperature without any molecular flux. Deoxidation of the GaAs(211)B surface was conducted at 582±2 °C and monitored *in situ* via RHEED. Evolution of the RHEED pattern during deoxidation was obtained from [01-1] azimuth [97] in order to ensure consistency between deoxidation runs. The RHEED patterns and diffraction spot intensities were recorded using a CMOS detector-based system. Details of the CMOS based RHEED pattern detection system are given in Appendix A. To investigate chemical structure differences of thermally deoxidized and epiready GaAs(211)B wafer surfaces, XPS technique was employed. Following thermal deoxidation, samples were transferred to XPS chamber under atmospheric conditions, ensuring that the transfer time did not exceed 5 minutes in order to prevent further contamination and re-oxidation of the GaAs surface.

RHEED pattern of the GaAs surface at 30 °C surface temperature before deoxidation is shown in Figure 4.7. As evident from Figure 4.7 (a), epiready GaAs surface exhibits a RHEED pattern related to amorphous surface structure due to the presence of oxide molecules at the surface. However, as can be seen from Figure 4.7 (c), after the surface temperature reaches 585 °C, the diffraction spot intensity in the RHEED pattern increases and the spot boundaries become sharper. This behavior is related to the sequential desorption of As_2O_3, As_2O_5 and Ga_2O from the surface. Removal of more stable and non-volatile Ga_2O_3 molecules from the GaAs surface was completed after 300 seconds at the surface temperature of 585 °C (Figure 4.7 (d)). Additionally, increase in diffraction spot intensity continues after waiting at the surface temperature of 585 °C for 600 seconds and 900 seconds (Figure 4.7 (e) and (f)). In order to understand surface crystallinity changes during deoxidation, RHEED spot intensity of the surface with [0-11] azimuth was analyzed in consecutive experiments using the progressively longer deoxidation phase. The circular shape in Figure 4.7 shows the region used for the recording the RHEED intensity.

Intensity of the diffraction spot during heating of epiready samples were recorded. Figure 4.8 shows normalized RHEED spot intensity variations observed in three thermal deoxidation experiments in which deoxidation of different durations took place about 585 °C. All deoxidation experiments have yielded similar trends in terms of RHEED pattern spot intensity. The first abrupt change in spot intensity was observed as a result of the surface temperature increase from 400 °C to 585 °C, during which As_2O_3, As_2O_5, and Ga_2O desorption took place. Second intensity change with higher slope was observed

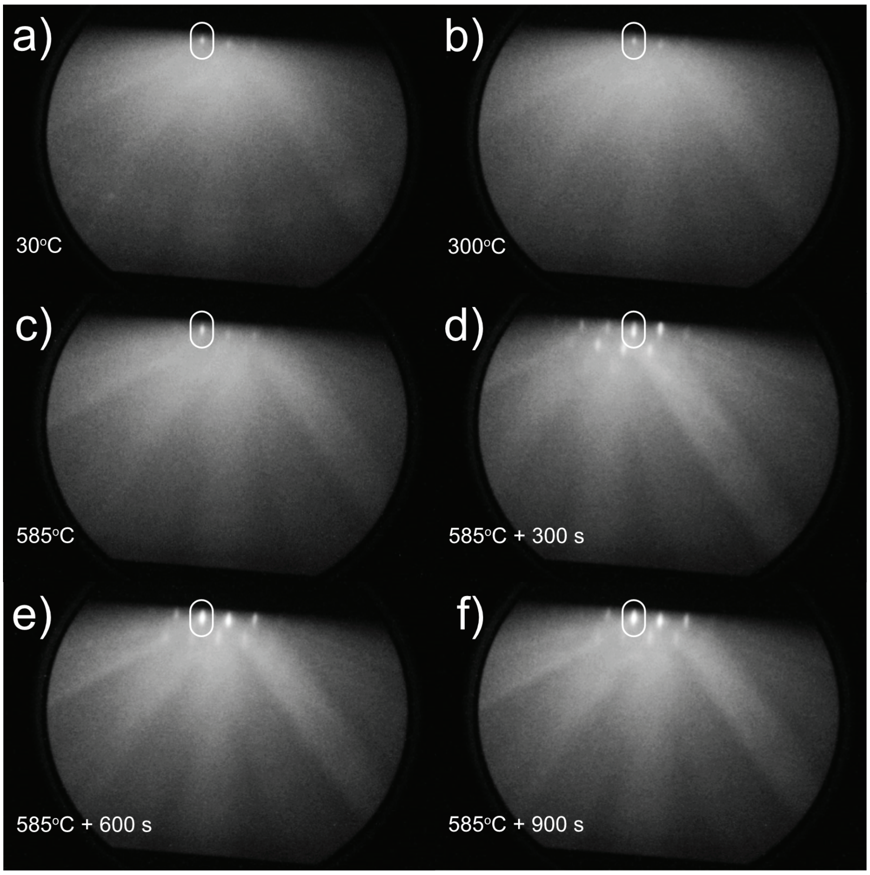

Figure 4.7.: RHEED patterns of GaAs(211)B surface which were taken from [01-1] azimuth; (a) at 30 °C, (b) at 300 °C and during heating, (c) just after surface temperature has reached 585 °C, (d),(e), and (f) after waiting at 585 °C for 300 s, 600 s, and 900 s, respectively. The circular shape shows the region used for the recording the RHEED intensity.

at the surface temperature of 585 °C, which lasted 300 seconds. However, increment in the spot intensity with smaller slope was observed from 600 seconds to 900 seconds. The observed spot intensity stability beyond this point suggests that the GaAs surface matrix was completely free of oxide molecules. In summary, the RHEED pattern and spot intensity analysis has shown that 600 seconds to 900 seconds at 585 °C is required for the thermal deoxidation process completion under As_4 overpressure.

Four samples with different deoxidation durations were chosen for XPS analysis. The XPS spectra of Ga 3d, As 3d and Ga $2p_{3/2}$ for epiready and thermally deoxidized samples for 215 s, 325 s, 410 s, and 626 s are shown in Figure 4.9 and Figure 4.10. The XPS spectra produced by the GaAs samples were simulated with 30 % Gaussian and 70 % Lorentzian combinations of line shapes after subtracting a Shirley type back-

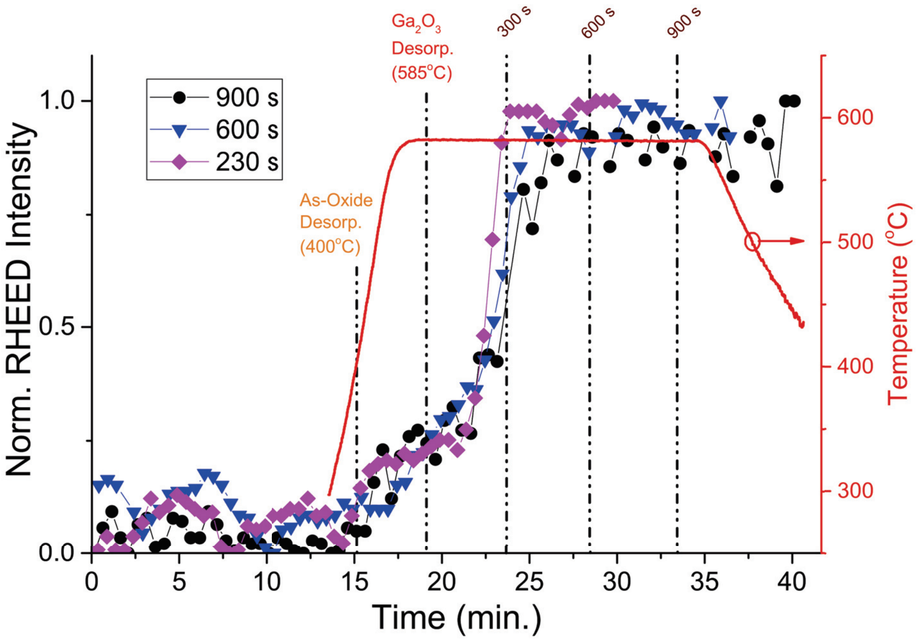

Figure 4.8.: RHEED spot intensities from deoxidation processes with three different durations. Dashed lines indicate surface temperature and desorption of different chemical species found at the sample surface. Temperature profile of the deoxidation process with 900 s duration at constant temperature is also shown.

ground. Spin-orbit splitting energy was set to 0.695 eV and 0.453 eV for As 3d and Ga 3d spectra, respectively. The XPS spectra pertaining to all samples were deconvoluted with GaAs, dimers of Ga-Ga and As-As, elemental As^0, oxide species of Ga_2O_3, Ga_2O, As_2O_5, As_2O_3, $GaAsO_4$, $GaAs(OH)_3$ [78, 85, 98–101]. $GaAsO_4$/$GaAs(OH)_3$, Ga_2O_3 and Ga_2O oxide formations on the GaAs epiready substrate are readily seen on the epiready Ga 3d and Ga $2p_3/2$ spectra, whereby $GaAsO_4$/As_2O_5 and As_2O_3 oxide formations are visible on the As 3d spectrum produced by the epiready substrate. Spontaneous Ga_2O_3 oxidation process under atmospheric conditions was reported as a bulk solid state reaction, which typically takes place over a period of several months with As_2O_3-rich surface [78]. Similarly, As_2O_5 formation on a GaAs surface is very slow [78] and, after exposure to the atmosphere for several weeks, only a small percentage of As_2O_5 may be produced in the surface oxide composition. On the other hand, GaAs surface oxidation through As_2O_3 is rapid under ambient conditions [78]. However, this oxidation reaction is self-limiting and ceases once an oxide of 1-2 nm thickness is formed [78]. Therefore, oxide layer desorption from the GaAs surface was determined based on the As_2O_5, As_2O_3, and Ga_2O_3 deficiency in the relevant As and Ga spectra. As_2O_5 and Ga_2O_3 peaks pertain-

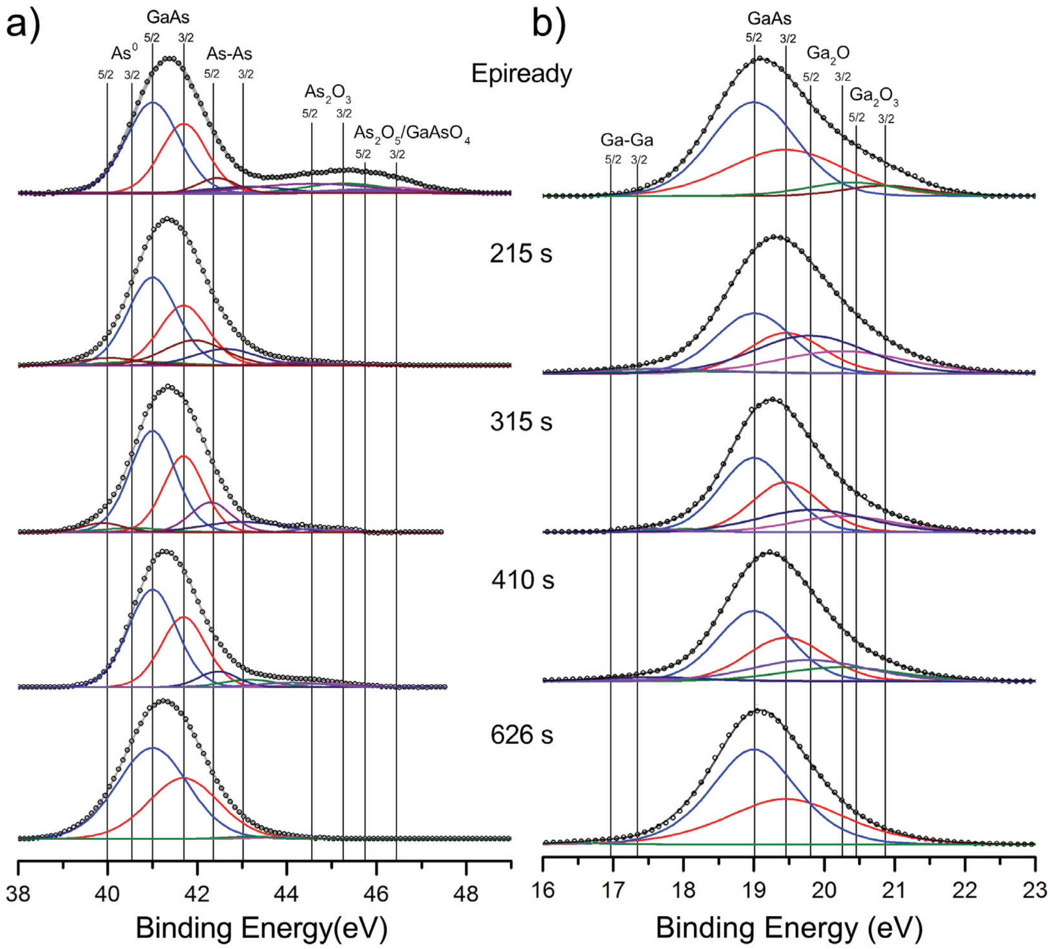

Figure 4.9.: (a) As 3d and (b) Ga 3d XPS spectra of epiready and thermally deoxidized samples at 585 °C for 215 s, 315 s, 410 s, and 626 s.

ing to molecular species were not detected in the As 3d and Ga 3d XPS spectra while a peak with core level shift (CLS) of +1.55 eV was detected in the Ga $2p_{3/2}$ XPS spectra of thermally deoxidized sample for 626 s.

CLS energies of relevant deconvoluted peaks in Ga 3d, As 3d, and Ga $2p_{3/2}$ spectra are summarized in Table 4.2. Average CLS energies and the associated standard deviations and with respect to the As 3d peak were calculated as +4.74±0.001 eV and +3.35±0.225 eV for As_2O_5 and As_2O_3 species, respectively. Additionally, As-As dimer CLS energies were found to range from +0.94 eV to +1.46 eV, while elemental As^0 CLS energies ranged from -0.95 eV to -1.11 eV. However, the peak formed from As-As dimer and As_2O_3 in As 3d spectrum of thermally deoxidized sample for 626 s could not be deconvoluted into components with an average CLS energy of +2.23 eV. This peak will be considered as As-As dimer for determination of the atomic concentrations since the posi-

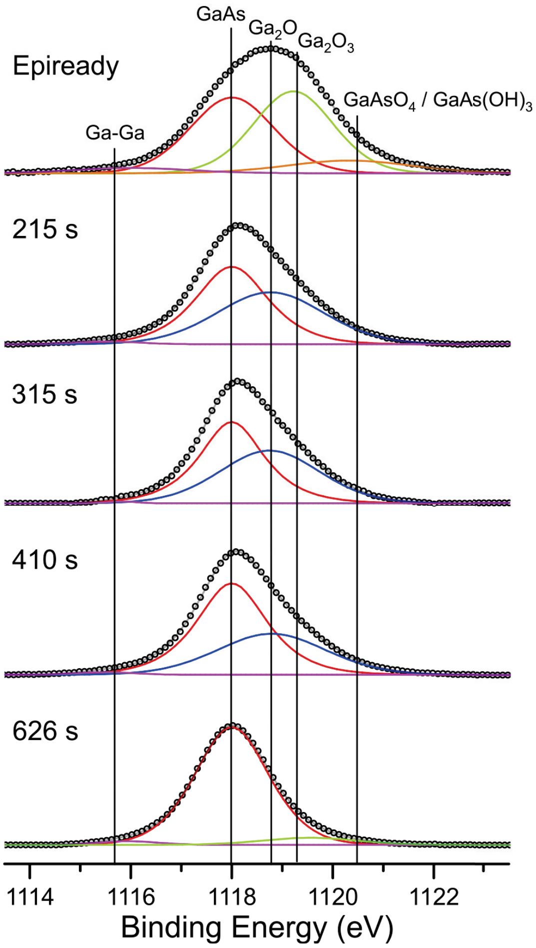

Figure 4.10.: Ga $2p_{3/2}$ XPS spectra of epiready and thermally deoxidized samples at 585 °C for 215 s, 315 s, 410 s, and 626 s.

tion of the peak is closer to the average As-As dimer CLS energy. The Ga_2O_3 and Ga_2O CLS energies were determined to be 1.385±0.165 eV and 0.79±0.04 eV, respectively, while that of the Ga-Ga dimer ranged from -2.51 eV to -1.33 eV.

To determine contribution of different chemical species to the As 3d, Ga 3d and Ga $2p_{3/2}$ XPS spectra, areas of all deconvoluted peaks were calculated and the obtained values are plotted in Figure 4.11. An enrichment of GaAs in GaAs(211)B surface was detected with respect to the increased deoxidation duration. Ga_2O_3 (43 %) and $GaAsO_4$/$GaAs(OH)_3$ (11 %) presence in the Ga $2p_{3/2}$ and Ga_2O_3 (14 %) presence in the Ga 3d XPS spectra of the epiready sample declines to zero after 215 s deoxidation. Ga_2O becomes detectable after 215 s deoxidation with the contribution of 45 % and 48 % to the Ga 3d and Ga $2p_{3/2}$ XPS spectra, respectively. Simultaneous disappearance of Ga_2O_3 and appearance of Ga_2O in the Ga 3d and Ga $2p_{3/2}$ XPS spectra of 215 s deoxidized sample suggest that

Table 4.2.: Surface composition of epiready and thermally deoxidized samples at 585 °C for 215 s, 315 s, 410 s, and 626 s

Deox. Time (s)	**As 3d**		**Ga 3d**		**Ga 2p$_{3/2}$**	
	CLS (eV)	**CLS Type**	**CLS (eV)**	**CLS Type**	**CLS (eV)**	**CLS Type**
Epiready	+4.74/+3.58/ +1.44	($GaAsO_4$)As_2O_5/ As_2O_3/As-As	+1.41	Ga_2O_3	+2.32/+1.22/ -1.98	$GaAsO_4$($GaAs(OH)_3$)/ Ga_2O_3/Ga-Ga
215	+3.2/+0.94/ -0.95	As_2O_3/As-As/ As^0	+0.8/ -1.33	Ga_2O/ Ga-Ga	+0.76/-2.5	Ga_2O/Ga-Ga
325	+3.51/+1.3/ -1.11	As_2O_3/As-As/ As^0	+0.83/ -1.44	Ga_2O/ Ga-Ga	+0.75/-2.17	Ga_2O/Ga-Ga
410	+3.13/ +1.46	As_2O_3/As-As	+0.79/ -1.45	Ga_2O/ Ga-Ga	+0.79/-2.51	Ga_2O/Ga-Ga
626	+2.24	(As_2O_3)As-As	-2.57	Ga-Ga	+1.55/-2.06	Ga_2O_3/Ga-Ga

Ga_2O_3 in the GaAs(211)B surface was probably transformed to the Ga_2O with the chemical reaction given in the introduction. As a final product of chemical reaction, Ga_2O presence decreases with increasing deoxidation duration which completely disappears in the Ga 3d and Ga 2p$_{3/2}$ XPS spectra of 626 s deoxidized sample. Similar to the desorption of the Ga-oxide species, As_2O_5 (16 %) and As_2O_3 (7 %) presence in the As 3d XPS spectra of the epiready sample declines to nearly zero after 215 s deoxidation. Additionally, 13 % and 7 % increase in the As-As and As^0 contribution to As 3d XPS spectra of the 215 s deoxidized sample was observed. The increment in elemental (or dimer) As concentration on GaAs(211)B surface was probably due to the production of As from the deoxidation reactions during heating of the epiready sample. As-As and As^0 presence in the As 3d XPS spectra of 215 s deoxidized sample completely disappear after additional 411 s deoxidation. Finally, GaAs concentration in the XPS spectra of the samples reach to range of 91 % - 99 % after 626 s deoxidation which confirms that the thermal deoxidation process was completed approximately 626 s at 585 °C.

Surface morphology of the epiready and deoxidized GaAs samples was investigated by employing the AFM method. More specifically, all AFM surface topography images were taken with a Si tip in tapping mode. Figure 4.12 provides AFM topography images of a 5 µm × 5 µm area for 215 s, 410 s, 626 s, and 800 s deoxidized samples. The AFM topography image height scale was adjusted to enhance the contrast between the GaAs surface and the pits. A gradual transition to a pit-decorated surface can be seen in Figure 4.12 (a)-(c). A very smooth surface was obtained from the 626 s deoxidized sample (Figure 4.12 (c)). In addition, Figure 4.12 reveals that thermal deoxidation duration is

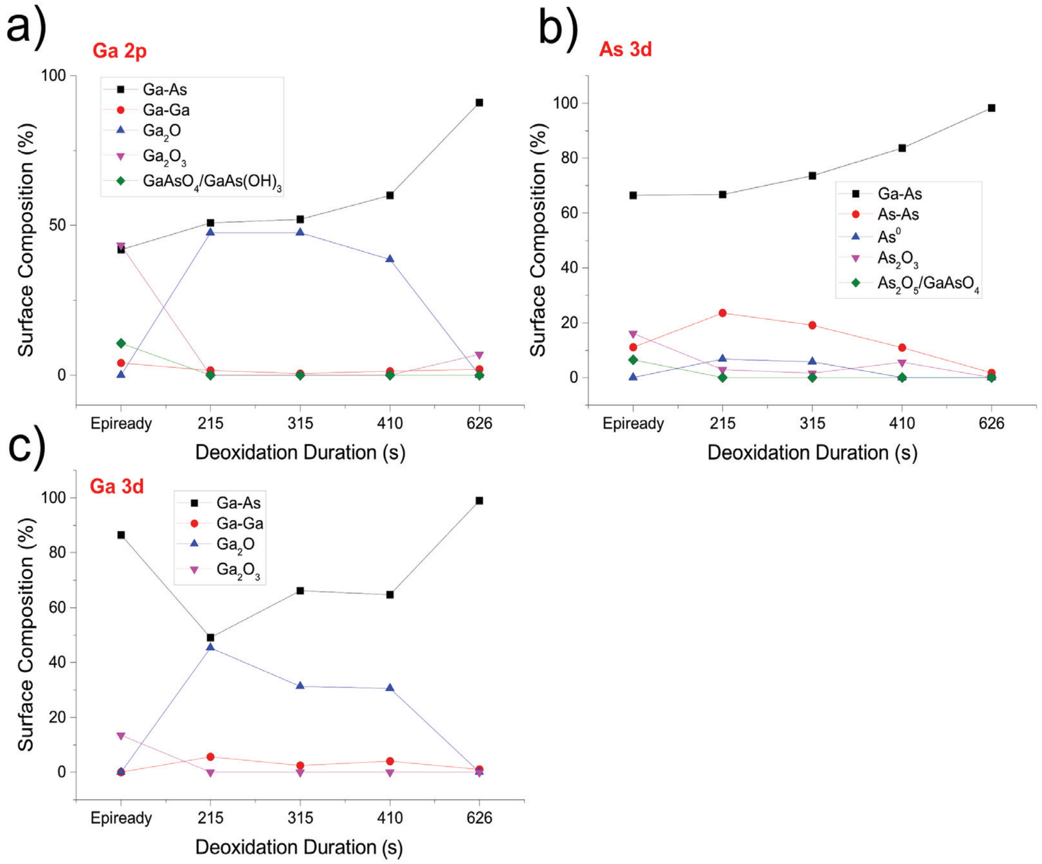

Figure 4.11.: Calculated intensity contribution of different chemical species to the As $3d_{3/2}$, Ga $3d_{3/2}$, and Ga $2p_{3/2}$ XPS spectra.

positively related to both the pit size and number density. To gain a better understanding of the surface changes during the deoxidation, AFM images were recorded from seven different zones of 10 μm × 10 μm, 5 μm × 5 μm, and 2 μm × 2 μm areas. Pit size, pit number density, and maximum detected pit size parameters were determined, along with the conventional peak-to-peak, RMS roughness, and skewness values with the statistical analysis. Statistical results obtained by analyzing the AFM images of the epiready and thermally deoxidized samples are given in Table 4.3.

For epiready GaAs wafer, an RMS roughness of 0.42 nm was obtained. Surface RMS roughness remained relatively constant at 0.35 nm and 0.37 nm after 215 s and 315 s deoxidation, respectively. However, after 410 s deoxidation, the RMS roughness increased to 0.74 nm, suggesting a dramatic change in surface morphology. Further increase in deoxidation duration from 626 s to 800 s resulted in a decrease in the surface RMS roughness, which stabilized at 0.54±0.1 nm. A similar trend in peak-to-peak values

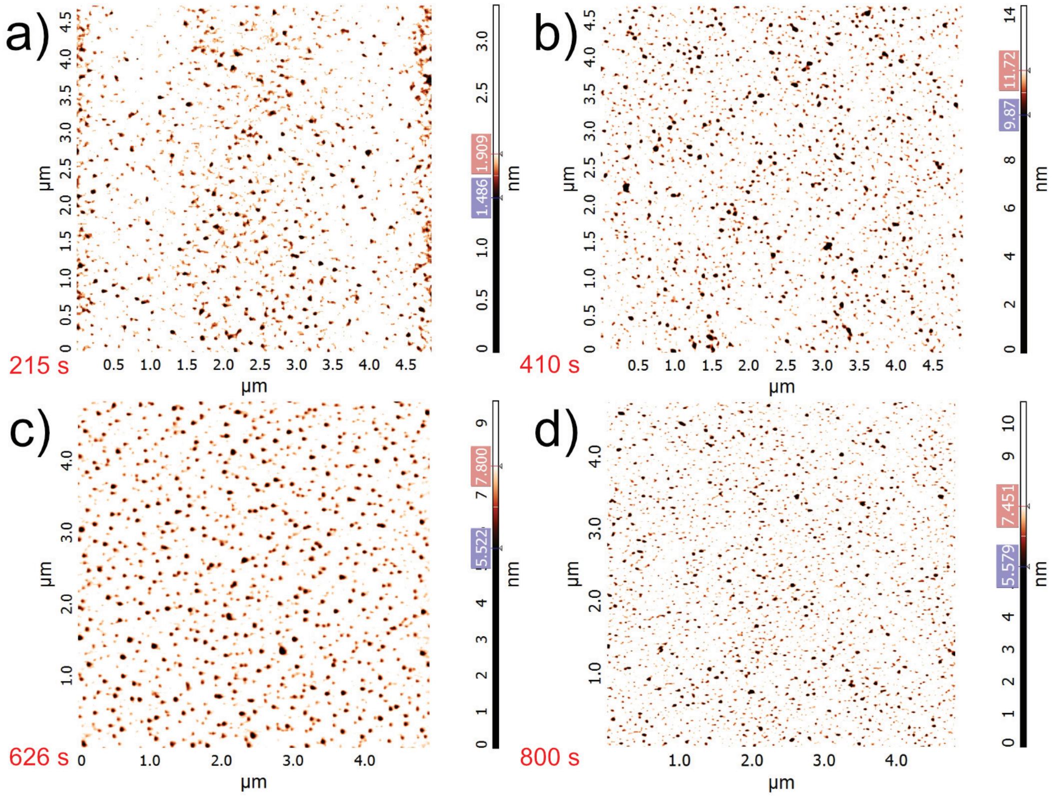

Figure 4.12.: AFM topography images of (a) 215 s, (b) 410 s, (c) 626 s, and (d) 800 s deoxidized samples from a 5 µm × 5 µm area

of epiready and 215 s and 315 s deoxidized samples was observed. Again, similar to RMS roughness values, peak-to-peak value of a sample deoxidized for 410 s reached a maximum of 13.65 nm before declining to 8-11 nm range when the deoxidation process duration was extended. Epiready surface skewness was measured at 0.23, indicating a slightly hill-decorated surface morphology. These findings suggest that the surface morphology of GaAs samples was transformed by the deoxidation process from hill-rich to pit-decorated. Additionally, the skewness of the thermally deoxidized GaAs sample surfaces decreased from -0.08 to -2.47 as the deoxidation duration increased. Finally, the skewness of a sample thermally deoxidized for 800 s decreased to -1.65. Large peak-to-peak values of thermally deoxidized samples with pit-decorated surfaces can be interpreted as an increase in pit population due to the deoxidation process.

In extant literature, surface dimension and depth of the Ga_2O_3 deoxidation-related Ga-deficiency pits have been reported to reach 50-200 nm and 5-20 nm, respectively [82, 93]. To investigate the deoxidation effects on the surface pit population and features, pit population analysis was conducted. Pit number density at the sample surfaces was

Table 4.3.: Statistical analysis results from AFM images of epiready and deoxidized samples (Pit sizes were calculated with 0.05 nm accuracy).

Deox. Time (s)	**Peak-Peak (nm)**	**RMS Roughness (nm)**	**Skewness**	**Percentages of Pits**					**Max. Pit Size (nm)**
				35.7 nm	**50.5 nm**	**61.8 nm**	**71.4 nm**	**Total (%)**	
-	4.76	0.42	0.23	17	6	-	-	23	61.8
215	5.12	0.35	-0.08	22	15	-	-	37	71.4
315	5.15	0.37	-0.29	22	10	5	3	40	133.5
410	13.65	0.74	-2.38	23	16	7	-	46	107
626	8.81	0.53	-2.47	15	26	21	11	73	128.6
800	10.56	0.55	-1.65	27	14	-	-	41	111.2

calculated by subjecting the AFM images to particle and discrete frequency analysis. The findings revealed that the pit number density ranged from the minimum of 25 nm to the maximum detected pit size for each sample. Size of the maximum detected pit on the epiready sample was 61.8 nm, which increased to 71.4 nm and 133.5 nm after 215 s and 315 s thermal deoxidation, respectively. Moreover, further increases in deoxidation duration did not result in an increase in the maximum detectable pit size, which ranged from 107 nm to 128.6 nm. Total pit percentage of epiready surface was calculated at 23 %, comprising predominantly of 35.7 nm-sized pits. After 215 s deoxidation, total pit percentage increased to 37 %, whereby 35.7 nm and 50.5 nm pits prevailed. AFM image of deoxidized additional 100 s revealed that pit percentage reached 40 %, whereby 50.5 nm pits were mostly transformed to larger pits. Further deoxidation of the epiready sample (626 s) created a pit-rich surface, with 73 % of the observed pits exceeding 35.7 nm in size. Finally, after 800 s deoxidation, pit population decreased to 41 %. In summary, thermal deoxidation duration between 626 s to 800 s created a smooth surface with lower percentage of pits not exceeding 35.7 nm in size.

To determine the effect of the As_4 assisted deoxidation to the heteroepitaxy of CdTe, three epiready GaAs(211)B substrates were deoxidized at 582 °C for 240 s, 600 s, and 900 s. A thin layer of CdTe was grown at 203±3 °C for 10 min. to suppress the formation of twins. The thin layer was annealed at 383±2 °C for 4 minutes to improve crystal quality. A thick CdTe layer was grown following the annealing step at 303±1 °C for 70 minutes. Thickness of the layers were 2.49±0.05 µm.

The crystal quality of CdTe layers grown on the the three deoxidized substrates were investigated with the XRD surface symmetric high-resolution four-crystal (Ge) RC

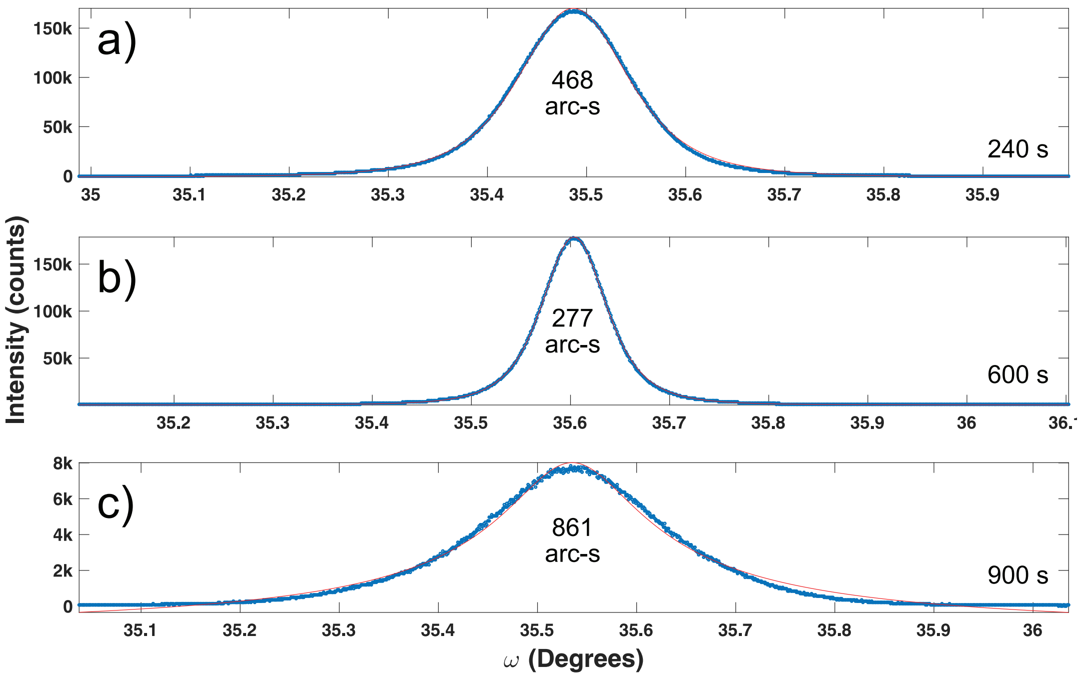

Figure 4.13.: XRD RC (blue dots) of the (422) reflection from the CdTe epilayers grown on GaAs substrates deoxidized at 582 °C for (a) 240 s, (b) 600 s, (c) and 900 s and the fit of the RCs with PearsonVII function (red line). Calculated values of FWHM from the RC of epilayers.

measurements. XRD RC scans were performed from the [0-11] azimuth. In Figure 4.13, RC of CdTe(422) surface symmetric reflection for CdTe epilayers grown on deoxidized substrates under As_4 flux at 582 °C for (a) 240 s, (b) 600 s, (c) and 900 s are shown. The RCs from the CdTe(422) reflection has a symmetric shape indicating a uniformly distributed lattice structure in the direction of surface normal. Nonperiodic imperfections in the crystal lattice and their strain fields (such as dislocations) randomly scatter the diffracted x-ray beam, resulting in broadening of the RC FWHM. This broadening of the RC FWHM due to crystal imperfections can be used as an indirect measure of the defect level in the epitaxial film [102]. The CdTe(422) RC of epilayers were fit using a PearsonVII function (the details are given in Chapter 5). RC FWHM was 468 arc-s for epilayer with 240 s deoxidation which was decreased to 277 arc-s after 600 s. The epilayer grown after 900 s deoxidation resulted in a layer with a very broad RC with a FWHM of 861 arc-s indicating a poor crystal quality.

There was a non-linear relationship between the deoxidation duration and the RC FWHM of the CdTe epilayers where the layer with minimum RC FWHM was obtained

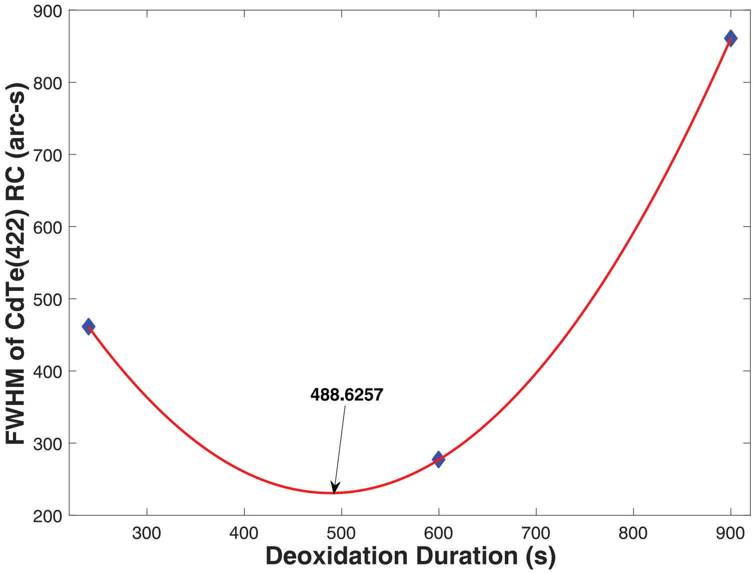

Figure 4.14.: XRD RC (blue dots) of the (422) reflection from the CdTe epilayers grown on GaAs substrates deoxidized at 582 °C for (a) 240 s, (b) 600 s, (c) and 900 s and the fit of the RCs with PearsonVII function (red line). Calculated values of FWHM from the RC of epilayers.

with the epilayer growth on a 600 s deoxidized substrate. To calculate the optimum deoxidation for the CdTe epilayer with the highest crystal quality, RC FWHM of epilayers were plotted as a function of deoxidation time and fitted with second order polynomial (Figure 4.14). The lowest FWHM of 231 arc-s with a CdTe layer (with the specific growth parameters mentioned above) grown on a deoxidized substrate at 582 °C for ~ 489 s under the As_4 flux was calculated. The optimum deoxidation duration of 489 s is in well agreement with the results of the RHEED, XPS, and AFM measurements.

4.2.2. Effect of the Deoxidation Temperature

Epiready GaAs substrates were loaded into load lock chamber and baked at 200 °C for 6 hours to remove moisture from the samples. Temperature measurements during oxide desorption process were performed using calibrated band-edge detection system. GaAs substrates were heated from room temperature to deoxidation temperature with 27±3 °C/min. ramp rate. At 300 °C, As_4 flux with 2.3×10^{-6} Torr beam equivalent pressure was directed to the substrates from a valve-controlled solid-source effusion cell. As_4 flux was remained directed to the samples after deoxidation until sample surface temperature decreased to 400 °C, after which the samples were cooled to room temperature without any molecular flux. Deoxidation of the GaAs(211)B surface was conducted at 546±2 °C and 563±2 °C and monitored *in situ* via RHEED which was analyzed with the same setup as described in previous section. To investigate chemical structure differences of thermally deoxidized and epiready GaAs(211)B wafer surfaces, XPS technique was employed. Following thermal deoxidation, samples were transferred to XPS chamber under atmospheric conditions, ensuring that the transfer time did not exceed 5 minutes in order to prevent further contamination and re-oxidation of the GaAs surface.

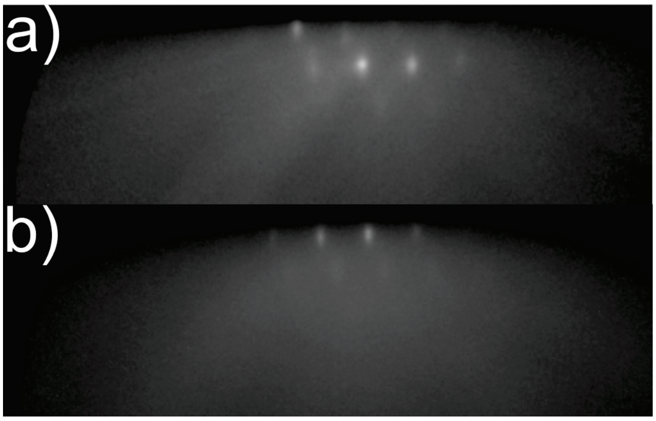

Figure 4.15.: RHEED patterns of GaAs(211)B surface which were taken from the [0-11] azimuth; (a) 21 minutes of deoxidation at 563 °C, (b) 34 minutes of deoxidation at 546 °C.

RHEED pattern of the GaAs surfaces for the deoxidation processes 21 minutes of deoxidation at 563 °C and 34 minutes of deoxidation at 546 °C are shown in Figure 4.15 (a) and (b), respectively. The RHEED pattern was recorded during cooldown at 400 °C. The RHEED patterns in the figure displays less streaky and bright spots compared to the RHEED images in Figure 4.7 which was taken after deoxidation temperature of 582 °C. As evident from both images that the deoxidation process was not completed. Probably, the removal of more stable and non-volatile Ga_2O_3 molecules from the GaAs surface was not completed. In order to understand surface changes during constant temperature deoxidation, RHEED spot intensity of the surface with [0-11] azimuth was recorded and is shown in Figure 4.16. This figure presents the change in the RHEED spot intensity during the deoxidations at 563 °C and 546 °C. Both deoxidation experiments have yielded similar trends in terms of RHEED pattern spot intensity compared to deoxidation process at 582 °C, where the abrupt change in spot intensity change with higher slope (24.2 int./min) was

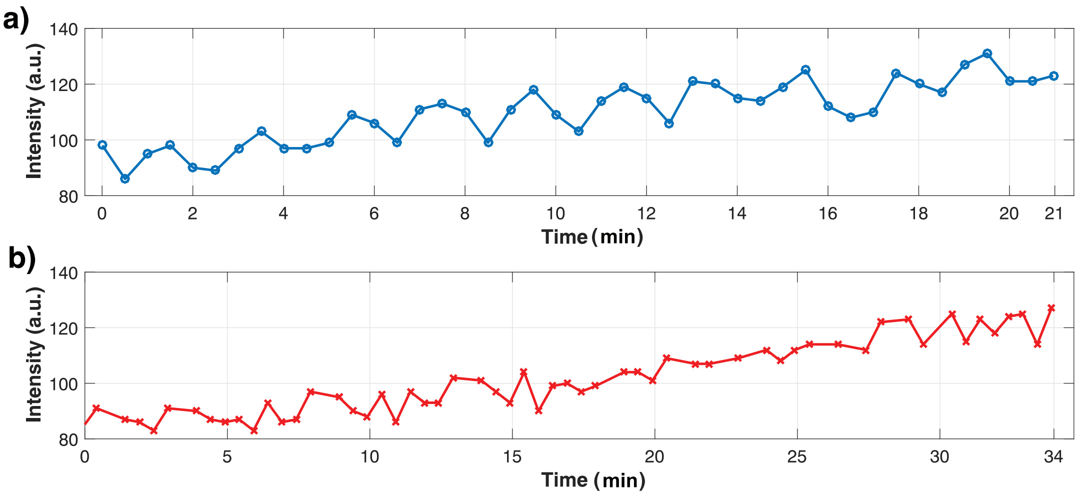

Figure 4.16.: RHEED spot intensities during constant deoxidation phase for two different processes ; (a) 21 minutes of deoxidation at 563 °C, (b) 34 minutes of deoxidation at 546 °C .

not observed which was correlated with the Ga_2O_3 desorption reaction for deoxidation process at 582 °C (Figure 4.7). Increments in the spot intensity were 1.76 int./min and 1.05 int./min for the deoxidation processes with temperatures of 563 °C and 546 °C, respectively.

To understand deoxidation reaction dynamics, the reaction rate of the change in the Ga_2O_3 desorption reaction, are calculated for the different deoxidation temperatures with the Arrhenius relation given above with the activation energy of 2.0 eV [95]. The Ga_2O_3 desorption process was ~ 1.8 times faster for the reaction at temperature of 582 °C compared to 563 °C. The Ga_2O_3 desorption rate was ~ 3.1 times faster for the reaction at temperature of 582 °C compared to 546 °C. The Ga_2O_3 desorption rate was ~ 1.72 times faster for the reaction at temperatures of 563 °C compared to 546 °C. The RHEED intensity change rate was ~ 13.6 times faster for the reaction at temperatures of 582 °C compared to 563 °C while it was ~ 23.3 times faster for the reaction at temperatures of 582 °C compared to 546 °C. The ratio of RHEED intensity change rate was ~ 1.71 times faster for the reaction at temperatures of 563 °C compared to 546 °C. The ratio of the reaction rates was ~ 7.52 times higher compared to the ratio of RHEED intensity change for the Ga_2O_3 desorption reaction at temperature of 582 °C compared to those at 563 °C and 546 °C. On the other hand, the ratio of the reaction rates was estimated as ~ 1.72 while the ratio of RHEED intensity change was ~ 1.71 for the Ga_2O_3 desorption reaction at temperatures of 563 °C to 546 °C. Inconsistency for the reaction rates and the RHEED intensity changes for the same reaction may be related to the differences of the activation energy of the As_4 and H assisted desorption processes. However, a change in the activation energy should also alter the ratio of the reaction rates at 582 °C to those at 563 °C and 546 °C while both was nearly identical. Another explanation for this difference might be the Ga_2O_3 desorption reaction itself. Complete desorption of the oxide layer from the GaAs surface involves several reactions at different temperatures, which were explained in earlier sections of this chapter. The final reaction, the Ga_2O_3 desorption reaction, involves a chemical and a physical process which are the decomposition of Ga_2O_3 molecule to the Ga_2O and the evaporation of the Ga_2O. If the Ga_2O_3 desorption process is considered as a two step process, the effect of the temperature on these two reactions will be different. Therefore, the reaction constants and thus the reaction rates will be different for these two reactions. The chemical reaction of the Ga_2O_3 decomposition will be faster at temperature ~ 582 °C while it will be slower at 563 °C and 546 °C. The inconsistency between the reaction rates and the RHEED intensity changes can be explained with this two step process.

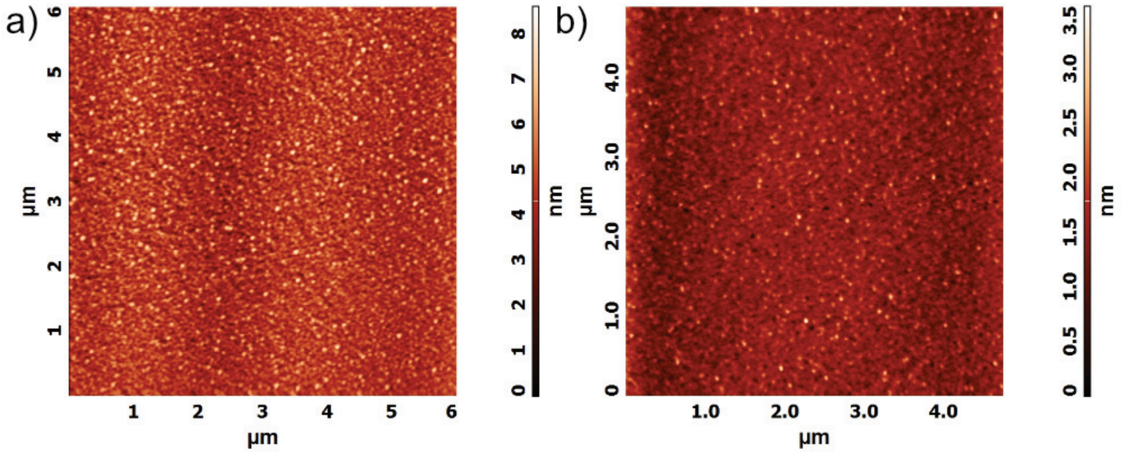

Figure 4.17.: AFM topography images from the samples which were deoxidized (a) 21 minutes at 563 °C, (b) 34 minutes at 546 °C.

Surface morphology of the epiready and deoxidized GaAs samples was investigated by employing the AFM method. Figure 4.17 provides AFM topography images of a 5 µm × 5 µm area of the samples which were deoxidized 21 minutes at 563 °C, 34 minutes at 546 °C. Both AFM images represent smooth but hill decoreated surfaces with no specific features. The statistical analysis was performed for the AFM images in Figure

4.17. RMS roughness was calculated as 0.29 nm and 0.61 nm for the samples deoxidized at 546 °C and 563 °C, respectively. Peak-to-peak distances were 3.93 nm and 6.17 nm for the samples deoxidized at 546 °C and 563 °C, respectively. Finally the calculated skewness (SK) values were 0.846 and 0.712. The SK of the deoxidized GaAs samples did not decrease which was expected to change from the hill decorated (SK>0) to pit decorated (SK<0) feature as was explained in the previous chapter. The RMS roughness and the peak-to-peak values of the deoxidized surfaces with the positive and high SK values suggest that the surfaces of the samples were covered with possibly As and oxide species. The analysis of the AFM measurements suggests that the deoxidation process was interrupted before completion and the surface of the deoxidized samples ended up with a non-crystalline structure.

A high temperature deoxidation process was found to be required for the completion of both steps of the Ga_2O_3 desorption. The ideal deoxidation duration was determined to be about 489 s at 582 °C in previous section. However, idling at high surface temperatures for long durations may enable the desorption of the Ga/As atoms or GaAs molecules from the surface lattice. Especially, Ga atoms have a high tendency to evaporate from the As (B) terminated surfaces since the Ga atoms loosely bounded to the GaAs surface. To the reduce deoxidation time at high temperatures, a high temperature thermal deoxidation of GaAs (211)B substrate at 607 °C was performed. In Figure 4.18, the RHEED pattern of the deoxidized GaAs (211)B substrate at 607 °C for 270 s is given. The long and bright streaks are visible in the figure indicating a highly crystalline surface. The deoxidation process was terminated after the RHEED pattern from the surface was obtained. To investigate the effect of the deoxidation at 607 °C, a CdTe layer was grown. The CdTe growth was initiated at a low temperature of 215±1 °C to suppress formation of twins. After the

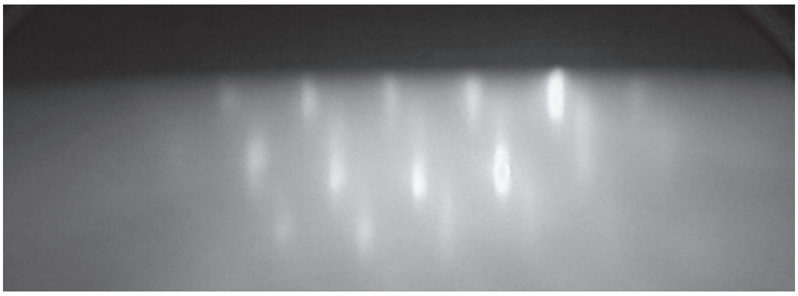

Figure 4.18.: RHEED pattern from the GaAs(211)B surface taken from the [0-11] azimuth after 270 s deoxidation at 607 °C.

nucleation, the substrate temperature was increased to 297±1 °C with a slow ramp and kept constant till the growth was completed. Thickness of the layer was determined by SE and FTIR measurements by 2.69±0.06 µm. The crystal quality of the CdTe layer was investigated with the XRD surface symmetric high-resolution four-crystal (Ge) RC measurements. XRD RC scan was performed from the [0-11] azimuth. In Figure 4.19, RC of CdTe(422) surface symmetric reflection from the CdTe epilayer which was grown on the deoxidized GaAs(211)B substrate under As_4 flux at 607 °C for 270 s is shown. The RC from the CdTe(422) reflection has a symmetric shape indicating a uniformly distributed lattice structure in the direction of surface normal. The CdTe(422) RC of epilayer was fit using a PearsonVII function. The RC FWHM was calculated as 138 arc-s which is remarkably lower than the theoretical FWHM value (238 arc-s) from the CdTe layer grown on a deoxidized GaAs substrate at 582 °C for 489 s even when the thickness dependence of the FWHM of RC was considered [28].

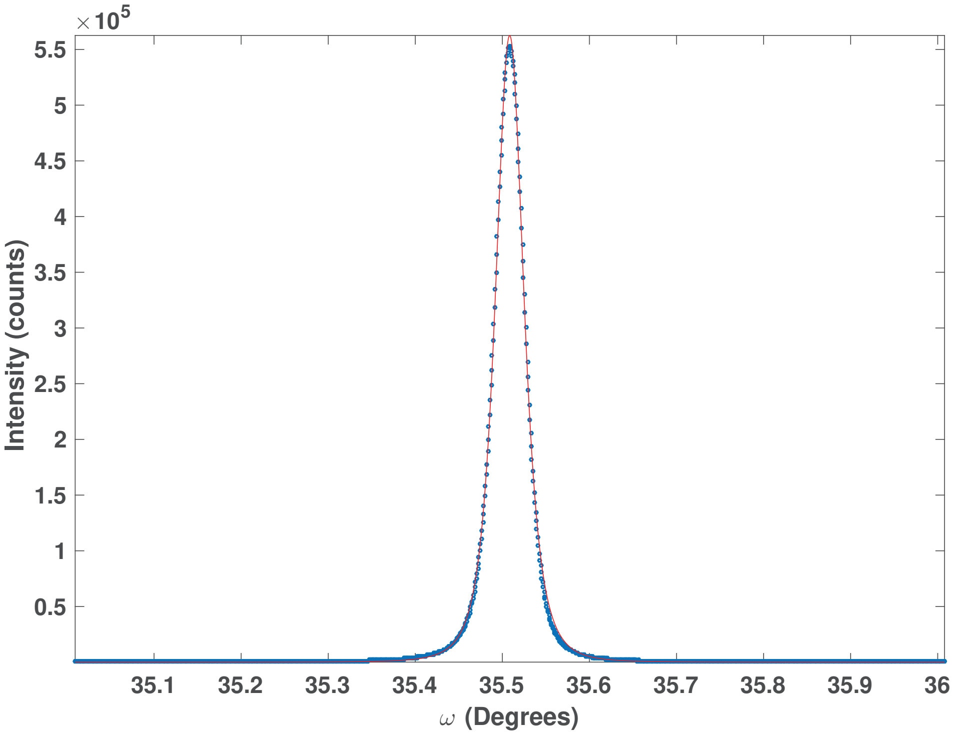

Figure 4.19.: XRD RC (blue dots) of the (422) reflection from the CdTe epilayer grown on GaAs substrates deoxidized at 607 °C for (a) 270 s and the fit of the RCs with PearsonVII function (red line).

4.3. Indium Assisted Thermal Deoxidation

Thermal deoxidation of the oxide layer from the epiready GaAs wafers under As_4 overpressure tends to result in a pitted surface as shown in previous sections. To overcome this problem, H-assisted [90], Ga-assisted [103, 104] and more recently In-assisted [87, 89] deoxidation process were suggested for the GaAs substrates. Hydrogen usage in the MBE system may result in the deposition of the H in metal panels of the growth chamber. Effective pumping of the H atom or H_2 molecule requires ion pumps since He-cyropumps can not trap or slow down H atom to pump off. On the other hand, Ga-assisted oxide desorption technique is very sensitive to the precise amount of oxides on the surfaces for which the sub-monolayer control of the Ga flux is required to remove oxides effectively. The droplet formation and the infill of pre-patterns (due to Ga-droplet etching) are unavoidable with the high Ga flux [91, 103, 105].

Compared to Ga atom, In atom has a larger atomic radius which allows In to react with non-volatile Ga_2O_3 more effectively than Ga. The interaction of the In atoms with the Ga_2O_3 may be given with the chemical reaction;

$$Ga_2O_3 + 4In \rightarrow Ga_2O \uparrow + 2In_2O \uparrow \tag{4.7}$$

The products of this reaction, Ga_2O and In_2O, can be easily desorbed from the GaAs surface at temperatures above $\sim$ 500 °C [106, 107]. Therefore, In-assisted thermal deoxidation of the epiready high index GaAs(211)B surface was investigated to obtain a smooth interface between the epilayer and the substrate.

In-assisted thermal deoxidation was carried out with Veeco Mark V 500 As (7 N) valved cracker and atomic source In (7 N, purity of 99.99999 %). Thermal deoxidation and growth was monitored *in situ* RHEED, which yielded data pertaining to surface crystal quality. In-assisted deoxidation was carried out in three steps, commencing with (1) increasing the GaAs substrate temperature to a constant deoxidation temperature without any flux, followed by (2) supplying In flux to the surface for a predefined period, and culminating in (3) increasing the temperature to a constant In-desorption temperature, which was maintained for a duration for In-related material (InAs, InO_2) desorption (Figure 4.20). Next, the epiready GaAs substrates were cooled under As_4 flux with 2.5×10^{-6} Torr BEP to ensure B polarity of the GaAs substrate. The GaAs substrates were characterized using XPS, which yielded data pertaining to the surface chemical composi-

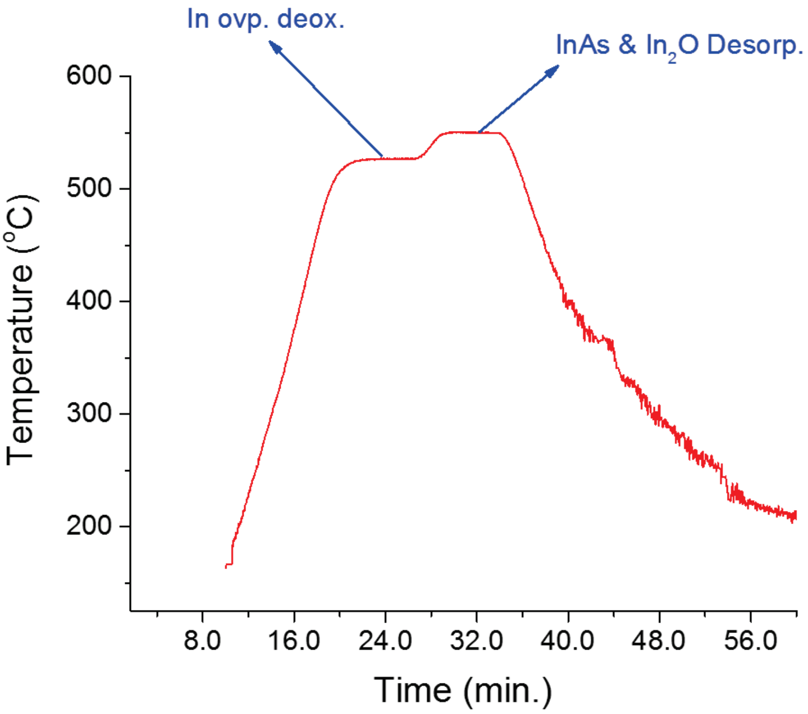

Figure 4.20.: Temperature profile of the In-assisted thermal deoxidation process and relevant steps.

tion. The XPS measurements were performed with Al x-ray source and SPECS Phoibos 150 Hemispherical Analyzer. Large area focus and 40 eV E-pass energy was chosen to achieve the best signal to noise ratio in the XPS spectra. Surface morphology of GaAs substrates was characterized using AFM.

Typical RHEED patterns along the [01-1] azimuth from the epiready GaAs(211)B surface at different deoxidation stages are shown in Figure 4.21. At 210 °C, a diffuse RHEED pattern is observed, indicating that the GaAs surface is covered with amorphous protective oxide layer (Figure 4.21 (b)) . Once the surface temperature has reached to 525 °C, bulk diffraction spots becomes visible (Figure 4.21 (c)) due to desorption of volatile As-oxide and Ga_20 species. After 3 minutes of In irradiation to the GaAs surface, a streaky diffraction pattern was observed (Figure 4.21 (d)). Without In flux directed to the surface, there was no visible change in the RHEED pattern which confirms the role of the In flux in the removal of the GaAs surface oxides. At higher temperature and before As_4 flux was sent to the GaAs surface, streaks became sharper and more visible, indicating that the removal of oxides (Figure 4.21 (e)). After the As_4 was sent to surface and at temperature of ~ 420 °C, overall RHEED pattern did not change while the spots become more rounded, indicating an increase in the surface roughness. This is consistent with the As coverage of the GaAs(211)B surface.

Figure 4.21 (a) shows RHEED intensity as a function of time with temperature profile of the deoxidation process. The RHEED intensity was recorded from a bulk diffraction spot which was observable along the [01-1] azimuth at low temperatures. As the In flux time increases, the RHEED intensity increases and decreases following the interruption of In flux. The intensity increase indicates a reduction of the oxide layer as shown in As assisted deoxidation process. The second intensity increase was readily observed at ~ 550 °C which was related to the desorption of InO_2 and InAs from the surface.

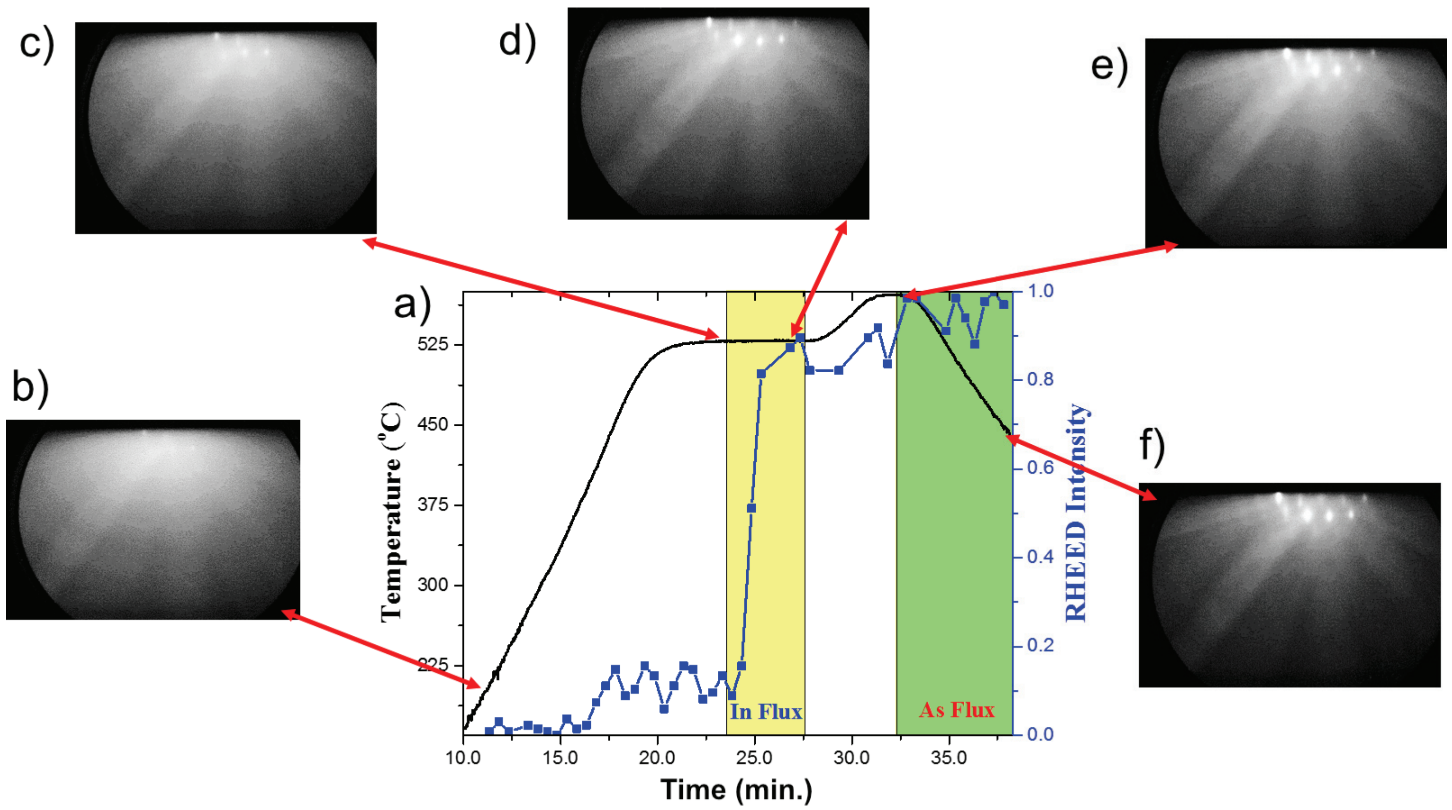

Figure 4.21.: (a) Temperature measurements and recorded RHEED spot intensities from the In-assisted thermal deoxidation processes. RHEED patterns of GaAs(211)B surface which were taken from the [01-1] azimuth; (b) at 210 °C, (c) at 525 °C before In flux was introduced, (d) at 525 °C after In shutter was closed, (e) at ~ 550 °C which was InAs and InO_2 desorption completed,(f) at 400 °C after sample was cooled down under As_4 flux.

4.3.1. Effect of the Deoxidation Temperature

To determine the effect of the deoxidation temperature on the In assisted thermal deoxidation process, four experiments were performed with constant In flux of 4.4×10^{-8} Torr BEP at four different temperatures, 485 °C, 510 °C, 530 °C, and 548 °C. In-desorption temperatures for these experiments were 530 °C, 570 °C, 570 °C, and 571°C, respectively. The soak time at constant temperature process for the desorption of the In-related species from the surface was chosen as 120, 30, 60, and 40 s for the deoxidation temperatures 485 °C, 510 °C, 530 °C, and 548 °C, respectively. A longer period for the In desorption process was chosen for the deoxidation process at 485 °C since the In desorption temperature of this process was 530 °C. Duration of the constant temperature In assisted deoxidation process was determined with the RHEED spot intensity values from the RHEED patterns. The constant temperature In assisted deoxidation step was considered as completed when the RHEED spot intensity was approximately two times brighter compared to the value which In irradiation was not directed to the substrate with exception of the experiment at the temperature of 485 °C. There was not any increase in the RHEED spot intensity for the deoxidation process with the temperature of 485 °C for the duration of 300 s. The constant temperature deoxidation durations were chosen as 300 s, 240 s, 240 s, and 210 s for the deoxidation temperatures 485 °C, 510 °C, 530 °C, and 548 °C, respectively.

Temperature measurements and recorded RHEED spot intensities with the RHEED patterns obtained after the As_4 shutter closed from the In-assisted thermal deoxidation processes at 485 °C is given in Figure 4.22 (a). The RHEED spot intensity remains constant during the constant temperature deoxidation process at 485 °C, indicating that the reaction rate is very low and could not be determined from the RHEED intensity. As the temperature is increased to the In desorption temperature of 530 °C, the RHEED intensity increases which may suggest that the deoxidation reaction was increased. Furthermore, irradiating the sample with As_4 flux results in a decrease in the RHEED intensity (Figure 4.22 (a)) suggesting growth of the (3D) InAs islands.

Temperature measurements and recorded RHEED spot intensities with the RHEED patterns obtained after the As_4 shutter closed from the In-assisted thermal deoxidation processes at 510 °C and 530 °C are given in Figures 4.22 (b) and 4.23 (a), respectively. As In irradiation was directed to the substrate, a sharp increase was observed in the RHEED intensities of both samples suggesting the desorption of the Ga_2O_3 molecules from the surface. The RHEED intensity remains unchanged during the heating of the substrate to

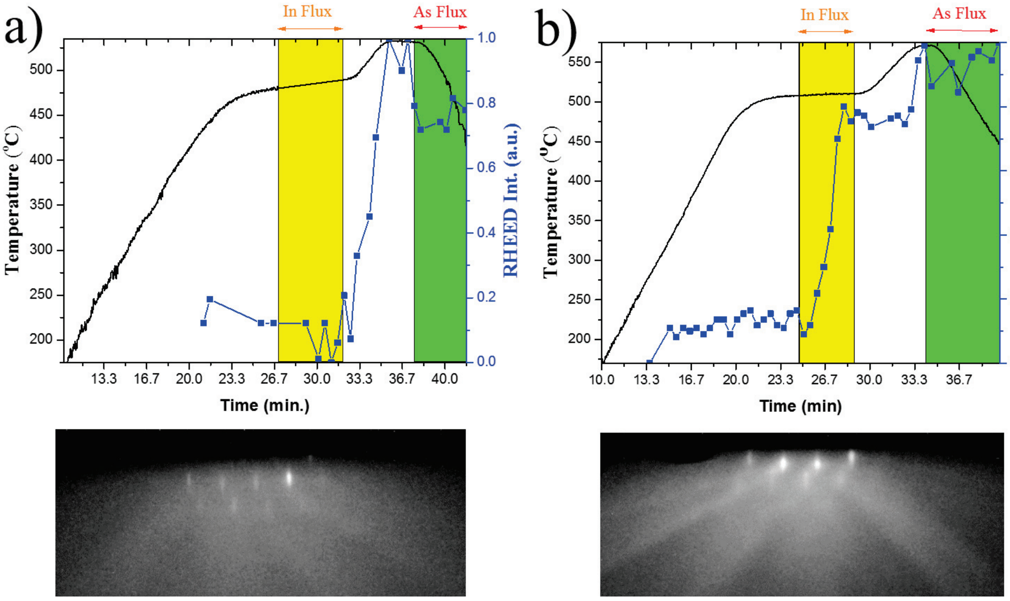

Figure 4.22.: Temperature measurements and recorded RHEED spot intensities with the RHEED patterns obtained after the As_4 shutter closed from the In-assisted thermal deoxidation processes at; (a) 485 °C and (b) 510 °C.

the In desorption temperature. As the surface temperature reaches In desorption temperature, sharp increases observed in the RHEED intensity diagrams of both samples confirming the In desorption process. The intensity was increased 8 and 9 times compared to the the RHEED intensity before the In irradiation was directed to the surface for deoxidations performed at 510 °C and 530 °C, respectively. Small oscillations in the RHEED intensities of both samples were observed following the opening of the As shutter, suggesting a change in the surface morphology which was possibly due to re-termination of the GaAs surface with the As.

Temperature measurements and recorded RHEED spot intensities with the RHEED patterns obtained after the As_4 shutter closed from the In-assisted thermal deoxidation processes at 548 °C is given in Figure 4.23 (b). As the In irradiation was directed to the substrate, a sharp increase was observed in the RHEED intensity similar to those of experiments at 510 °C and 530 °C, suggesting the desorption of the Ga_2O_3 molecules from the surface. The change in the ratio of intensity was one order of the magnitude. Following the deoxidation process, during the heating of the substrate to the In desorption temperature, the RHEED intensity remains unchanged. As the surface temperature has reached In desorption temperature, a gradual increase was observed in the RHEED

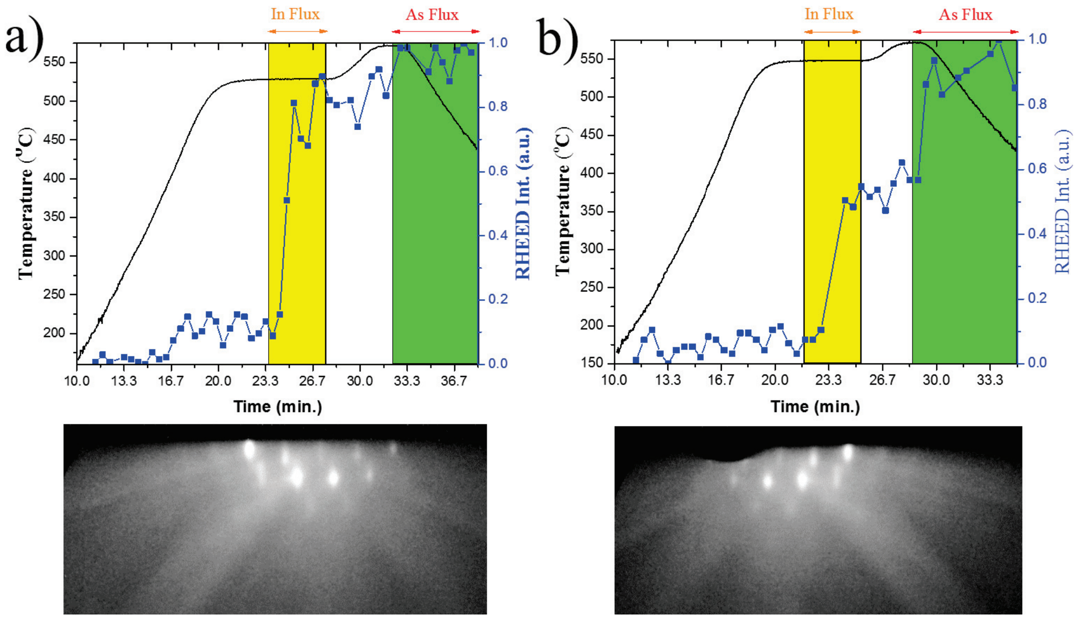

Figure 4.23.: Temperature measurements and recorded RHEED spot intensities with the RHEED patterns obtained after the As_4 shutter closed from the In-assisted thermal deoxidation processes at; (a) 530 °C and (b) 548 °C.

intensity, confirming the In desorption process. A sharp increase was observed following the opening of the As shutter, suggesting a dramatic change in the surface morphology which was possibly due to compensation of As on the GaAs surface. This behavior may be explained with the great loss of the As atoms during the deoxidation process since the temperature of the deoxidation process was 18 °C higher compared to the same process in Figure 4.23 (a). Re-termination of the GaAs surface with the As atoms might increase the surface roughness thus the overall RHEED intensity.

XPS analysis of the same samples were performed. The XPS spectra of Ga 3d with In 4d, Ga $2p_{3/2}$, and As $2p_{3/2}$ for epiready and thermally deoxidized samples at 485 °C, 510 °C, 530 °C, and 548 °C are shown in Figure 4.24, Figure 4.25, and Figure 4.26, respectively. The XPS spectra produced by the GaAs samples were simulated with 30 % Gaussian and 70 % Lorentzian combinations of line shapes after subtracting a Shirley type background. Spin-orbit splitting energy was set to 0.453 eV for Ga 3d spectra. The XPS spectra pertaining to all the samples were deconvoluted with GaAs, dimers of Ga-Ga and As-As, elemental As^0, oxide species of Ga_2O_3, Ga_2O, As_2O_5, As_2O_3, $GaAsO_4$, $GaAs(OH)_3$ [78, 85, 98–101]. $GaAsO_4$/$GaAs(OH)_3$, Ga_2O_3 and Ga_2O oxide formations on the GaAs epiready substrate are readily seen on the epiready Ga 3d and Ga $2p_3/2$

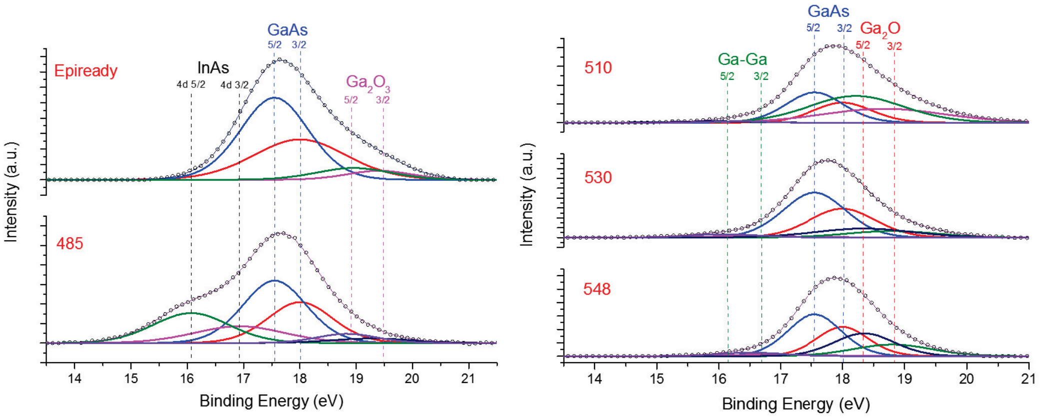

Figure 4.24.: Ga 3d XPS spectra of epiready and thermally deoxidized samples at 485 °C, 510 °C, 530 °C, and 548 °C.

spectra, whereby As_2O_5 and As_2O_3 oxide formations are visible on the As $2p_{3/2}$ spectrum produced by the epiready substrate. Average CLS energies and the associated standard

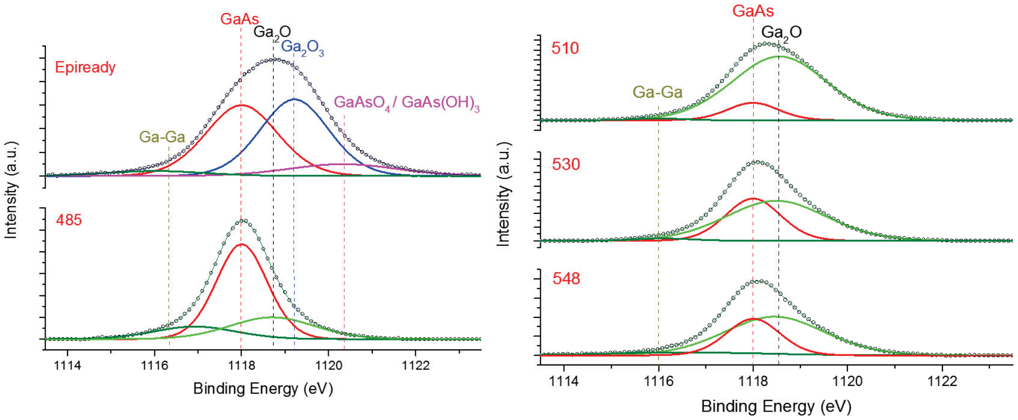

Figure 4.25.: Ga $2p_{3/2}$ XPS spectra of epiready and thermally deoxidized samples at 485 °C, 510 °C, 530 °C, and 548 °C.

deviations and with respect to the As $2p_{3/2}$ peak were calculated as +3.25±0.26 eV and +4.85±0.01 eV for As_2O_3 and As_2O_5 species, respectively. Additionally, As-As dimer CLS energies were found to range from +1.68 eV to +1.52 eV, while elemental As^0 CLS energies ranged from -1.51eV to -2.07 eV. The Ga_2O_3 and Ga_2O CLS energies were determined to be 1.32±0.1 eV and 0.6±0.15 eV, respectively, while that of the Ga-Ga dimer ranged from -2.03 eV to -1.04 eV. The oxide layer desorption from the GaAs surface was

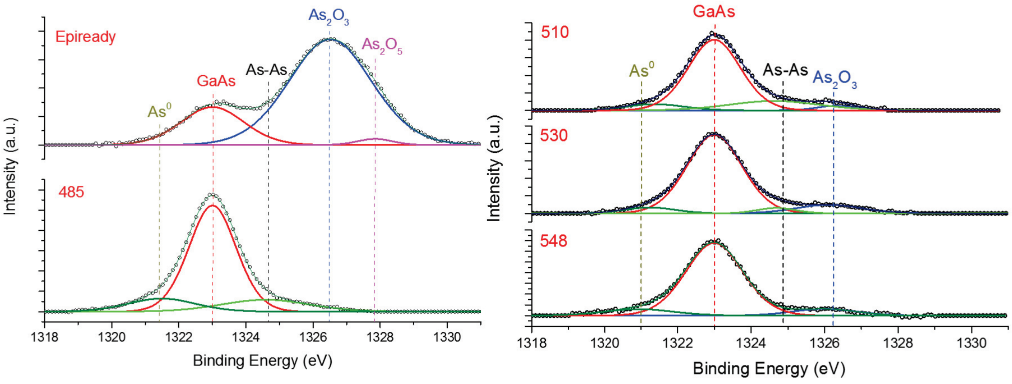

Figure 4.26.: As $2p_{3/2}$ XPS spectra of epiready and thermally deoxidized samples at 485 °C, 510 °C, 530 °C, and 548 °C.

determined based on the As_2O_5, As_2O_3, and Ga_2O_3 deficiency in the relevant As and Ga spectra. Additionally, to check the possibility of the formation of the InO_2 and InAs, the In 4d XPS spectra of the samples were investigated which is separated from the Ga 3d XPS spectra by only ~ 1 eV. As_2O_5 and Ga_2O_3 peaks pertaining to molecular species were not detected in the As $2p_{3/2}$, Ga 3d, Ga $2p_{3/2}$ XPS spectra of the samples deoxidized at 510 °C, 530 °C, and 548 °C while Ga_2O_3 in the Ga 3d and InAs in the In 4d XPS spectra of the sample deoxidized at 485 °C were detected, indicating an incomplete deoxidation process and InAs formation.

To determine the contribution of different chemical species to the Ga $3d_{3/2}$, As $_{3/2}$, and Ga $2p_{3/2}$ XPS spectra, the areas of all deconvoluted peaks were calculated and the obtained values are plotted in Figure 4.27. In general, an enrichment of GaAs in GaAs(211)B surface with increasing deoxidation temperature can be deduced from the linear increase in percentages of GaAs-related peaks in the As $2p_{3/2}$ XPS spectra yielded by the samples. On the other hand, the contribution of the GaAs-related peaks in the Ga $2p_{3/2}$ and Ga $3d_{3/2}$ XPS spectra tends to decrease after the deoxidation and it is well below the values deduced from the As $2p_{3/2}$ XPS spectra. Simultaneous disappearance of Ga_2O_3 and appearance of Ga_2O in the Ga 3d and Ga $2p_{3/2}$ XPS spectra of deoxidized samples at 510 °C and higher temperatures suggest that Ga_2O_3 in the GaAs(211)B surface had been probably transformed to the Ga_2O with the chemical reaction given in Eq. 4.7. The Ga_2O formation on the GaAs surface after In assisted deoxidation may be related to the uncompleted Ga_2O desorption from the surface. Ga_2O presence are readily seen from the Ga $3d_{3/2}$ and Ga $2p_{3/2}$ XPS spectra of the samples deoxidized at 510 °C, 530 °C, and 548 °C. The highest and lowest concentration of the Ga_2O in the Ga $2p_{3/2}$ and

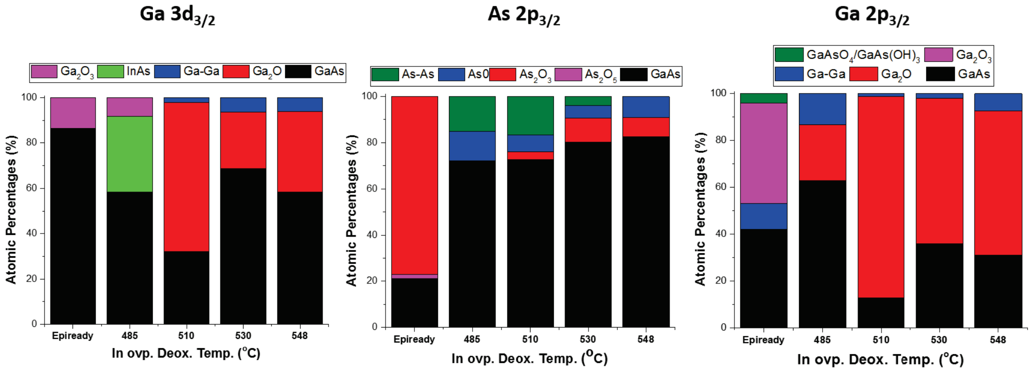

Figure 4.27.: Calculated areal contribution of different chemical species to the Ga $3d_{3/2}$, As Ga $2p_{3/2}$, and Ga $2p_{3/2}$ XPS spectra.

Ga $3d_{3/2}$ XPS spectra are detected after the deoxidation processes at 510 °C and 548 °C, respectively. This trend in Ga_2O concentration seems to be related with the In desorption times of the samples, suggesting a longer desorption duration is required to get rid of the Ga_2O molecules from the GaAs surface. Considering the XPS spectra of the deoxidized samples at 510 °C and 530 °C, the minimum time required for the desorption of the Ga_2O can be calculated as $\sim$ 120 s. Additionally, Ga_2O concentrations from the Ga $3d_{3/2}$ and Ga $2p_{3/2}$ XPS spectra were found to be well correlated with the information depth of these atomic orbitals in the XPS experiment.

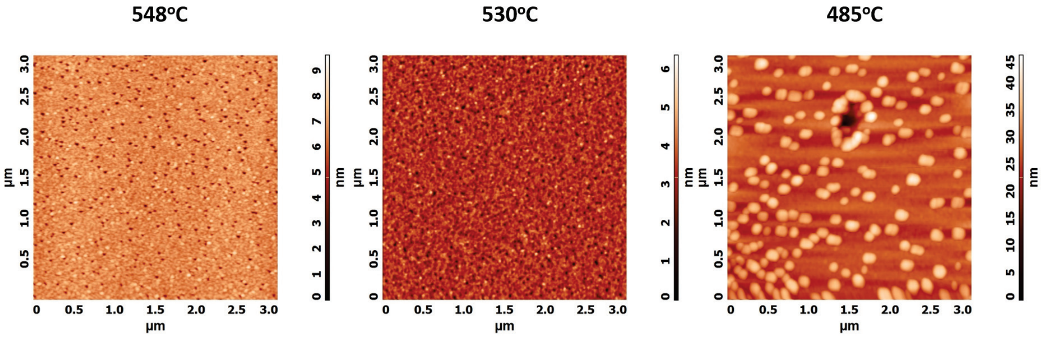

Figure 4.28.: AFM topography images from the samples which were deoxidized at 548 °C, 530 °C, and 485°C.

Surface morphology of the epiready and deoxidized GaAs samples was investigated by employing the AFM method. Figure 4.28 provides AFM topography images of a 3 µm × 3 µm area for the deoxidized samples at 485 °C, 530 °C, and 548 °C. A gradual increase in the average pit population at the GaAs surface can be seen from the deoxidized samples at 530 °C and 548 °C. In addition, Figure 4.28 reveals that thermal deoxidation at 485 °C created dot like structures and large holes on the GaAs surface. To gain a better understanding of the surface transition mechanism, the AFM images were obtained from five different zones of 3 µm × 3 µm and 2 µm × 2 µm areas. Pit size, pit number density, and maximum detected pit size parameters along with the conventional peak-to-peak, root mean square (RMS) roughness, and skewness values were determined with a statistical analysis. To investigate the deoxidation effects on the surface pit population and features, pit population analysis was conducted. Pit number density at the sample surfaces was calculated by subjecting the AFM images to particle and discrete frequency analysis. The findings revealed that the pit number density ranged from the minimum of 25 nm to the maximum detected pit size for each sample. Size of the maximum detected pit on the deoxidized sample at 548 °C has the same value as that of the epiready sample's which was 61.8 nm. The maximum detectable pit size was 71.4 nm for the deoxidized sample at 530 °C. Total pit percentage of the epiready surface was calculated at 23 %, comprising predominantly of 35.7 nm-sized pits. After deoxidation at 530 °C, total pit percentage increased to 24 %, whereby no larger pits prevailed. The AFM image of deoxidized sample at 548 °C revealed that the pit percentage decreased to 20.5 %, whereby 35.7 nm pits highly prevailed. Thermal deoxidation at temperatures from 530 °C to 548 °C created a smooth surface with lower percentage of pits without exceeding 35.7 nm in size.

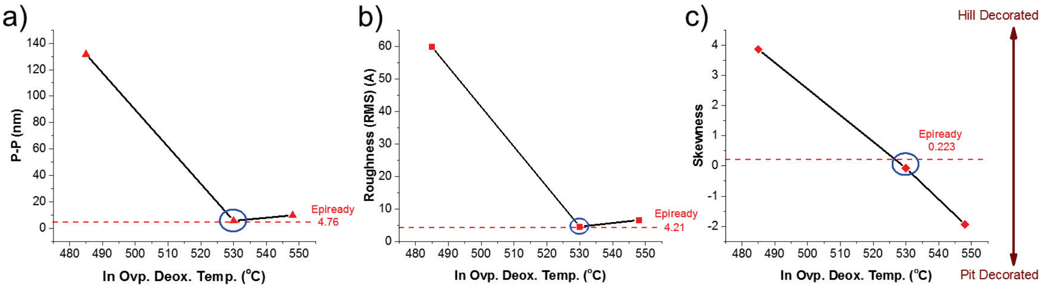

Figure 4.29.: The results of the statistical analysis on the deoxidized and epiready samples; (a) Peak-to-Peak, (b) RMS Roughness, and (c) Skewness as a function of deoxiadation temperature.

RMS roughness of the epiready GaAs wafer was 0.42 nm. Calculated surface RMS roughness, peak-to-peak, and SK values are plotted in Figure 4.29 for the deoxidized samples and epiready sample. The surface morphology of the deoxidized sample at 485 °C is found to be separated from the other samples which have ~ 130 nm peak-to-peak, ~ 6 nm RMS roughness, and ~ 3.86 SK values. Statistical results of the AFM image and the XPS results of this sample indicate that large InAs islands were formed during the process. The surface RMS roughness was increased to 0.46 nm after the deoxidation at 530 °C. The deoxidation of the GaAs surface at 548 °C resulted in a surface with the surface RMS roughness of 0.66 nm. On the other hand, the deoxidation at 548 °C crated a surface with a larger SK value indicating the depth of the pits are much larger compared to the deoxidized sample at 530 °C. In summary, the best surface morphology was obtained with the deoxidized sample at 530 °C.

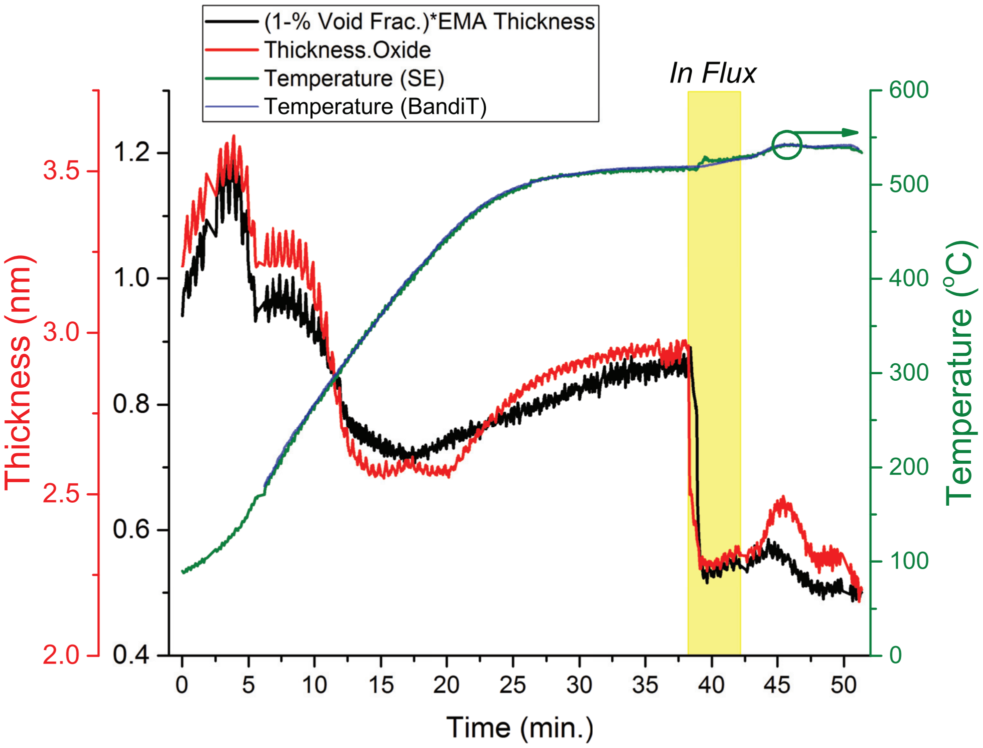

Figure 4.30.: The oxide thickness values of a GaAs substrate during oxide desorption under In flux from two different dielectric models. Surface temperature from the SE model and band-edge measurements are also plotted.

To investigate the change in the dielectric function of the GaAs substrate, *in situ* SE measurements were recorded during heating and the thermal deoxidation processes. The implementation of SE during oxide desorption facilities monitoring of both the overlayer conditions and substrate temperature. The SE data were fit by two different substrate-layer models. First model has an EMA overlayer which contains the components from the void and GaAs. The GaAs optical constant library was supplied by J.A. Woollam, Inc. The protective oxide layer and surface roughness could be modeled sufficiently enough by a two-component EMA layer consisting of variable parts of void and GaAs. Surface temperature, overlayer thickness, void fraction, and angle of incidence were varied as fit parameters within the model. The oxide thickness was extracted from this model as [(1-Void Fraction (%)) × Overlayer thickness]. The second model has a GaAs-Oxide overlayer[86]. Surface temperature, overlayer thickness, and angle of incidence were varied as fit parameters within this model. Both model included a temperature-dependent model consisting of an optically thick GaAs substrate which was constructed by the individual SE measurements at different temperatures (band-edge measurements). GaAs(211)B substrate was deoxidized at 524 °C for 240 s under In flux of 4.4×10^{-8} Torr BEP. In desorption process was performed at 541 °C for 300 s. The evolution of GaAs surface temperature from both SE and band-edge measurements and oxide thicknesses from both SE models are shown in Figure 4.30. The temperature-dependent model was able to reproduce the band-edge measurements accurately. An initial decrease in oxide thickness from both models is attributed to the loss of volatile As_2O_x species. An abrupt decrease in oxide thickness was observed following In irradiation to the GaAs surface which is coincident with an observed GaAs RHEED pattern transiton to that of a bare GaAs surface (Figure 4.21). The model constructed with the GaAs-Oxide layer[86] has over estimated the total thickness value while the reduction in the oxide layer thickness was captured. On the other hand, EMA model has estimated the oxide thickness more accurately. The change in the oxide layer thickness during desorption of the protective oxide layer under In flux is in excellent agreement with previously published data for the deoxidation process under As_4 flux [108].

4.3.2. Effect of the In Flux

Effect of the In flux to the RHEED intensity was studied by changing In effusion cell temperature by Li et al [89]. It has been shown by Li et. al., AFM measurements that the effect of the high In flux was not detrimental to the GaAs(100) surface. However, the authors performed growth of the quantum dots following In assisted deoxidation of the GaAs substrate. The effect of the In flux to the epilayer was not discussed.

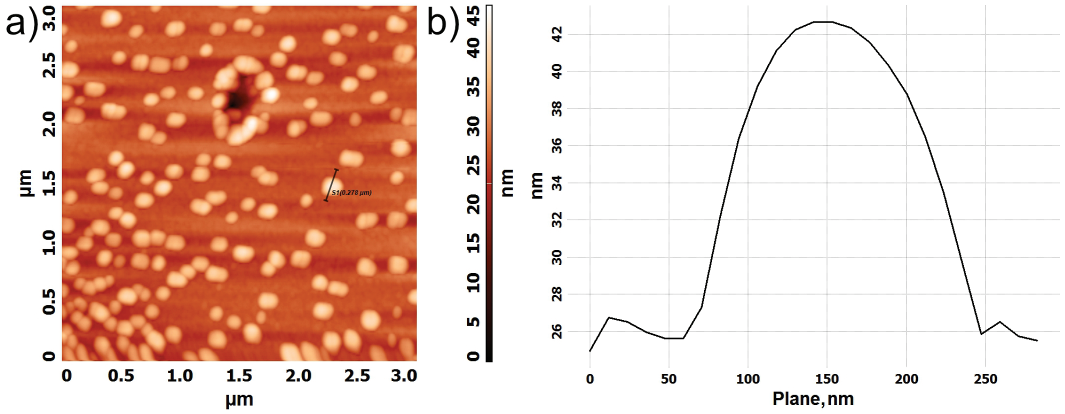

Figure 4.31.: (a) AFM topography images from the deoxidized sample under In flux at 485°C, (b) height profile of the one of the hill type feature from the AFM image.

The indium droplet formation on the GaAs surface is shown at temperature of 500 °C by AFM measurements [109]. The average radius and the height of the droplets were 90 nm and 30 nm, respectively [109]. In Figure 4.31 (a), the AFM image of the deoxidized sample with hill type defects are shown. The height profile of the one of the hill type defects are shown in Figure 4.31 (b). Size and surface dimension of the defect was similar to In droplets formed on the GaAs surface [109]. Similarly, the droplet formation of Ga atoms during oxide desorption due to excess Ga atoms with Ga assisted deoxidation process was also reported [91]. The migration of the excess In atoms might form the In droplets on the GaAs surface. These droplets then can become inter-diffusion centers for Ga atoms of the surface lattice, or etching centers for Ga_2O_3 molecules. Either way, a non-isotropic change in the surface structure becomes possible leading to surface pits. These surface pits, on the other hand, were not observed in the AFM images of the deoxidized sample under In flux at 530 °C (see Figure 4.28). The surface pits might be infilled during cooldown of the deoxidized samples under As_4 flux. Another mechanism for the infilling of these surface pits might be oxidation of the surface under air exposure.

To determine the effect of the In flux on the GaAs surface, CdTe layers were grown on the deoxidized GaAs(211)B surface. CdTe layers were not annealed since this might affect the surface of the CdTe layers. The GaAs(211)B substrates were deoxidized at 520 °C for 240 s under In flux of 4.4×10^{-8} Torr BEP. In desorption process was performed at 541 °C for 240 s. A 2.8 ±0.1µm thick CdTe layer was grown on deoxidized substrate which was measured with SE and FTIR measurements. The optical image of the CdTe

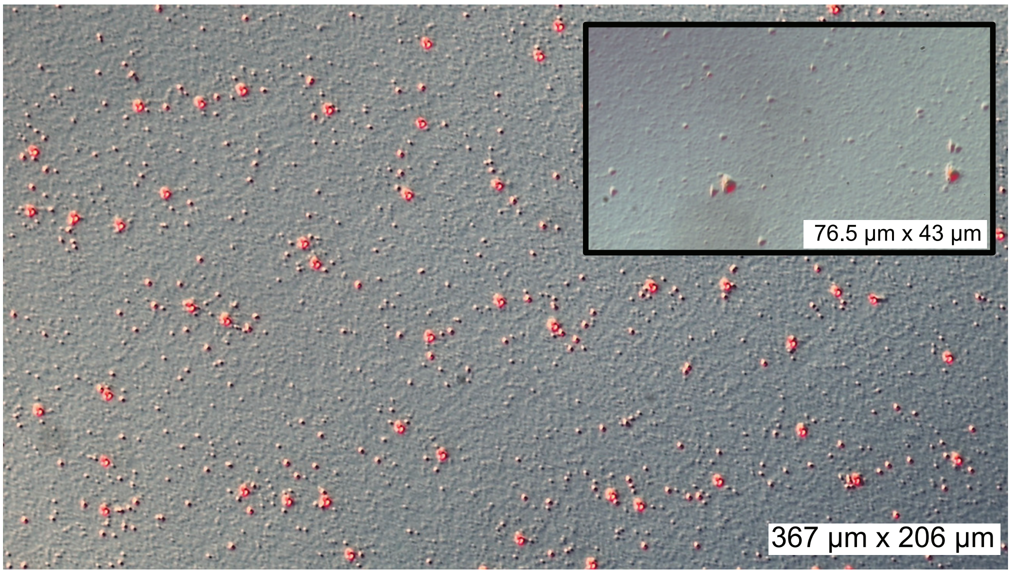

Figure 4.32.: Nomarski optical image of the CdTe layer grown on GaAs substrate which was deoxidized at 520 °C for 240 s under In flux of 4.4×10^{-8} Torr BEP. Inset: Nomarski optic image of the same surface with higher magnification.

layer taken by Nomarski microscope is shown in Figure 4.32. Two type of defects with different sizes are readily observed from the figure. The density of the larger defects calculated as 7.16×10^{4} cm^{-2}. In the inset of the figure, a surface image with increased magnification is shown. It is seen from the inset, the larger defects has a triangular or pyramidal structure which are directed to [1-1-1] direction. An AFM height image of the CdTe layer is shown in Figure 4.33 with the surface crystal orientations. It is seen from the figure that, the flat or back plane of the "triangular" shaped defect is parallel to the [0-11] direction while the "triangle" is directed to the [1-1-1]. Similar type of defects were observed from the CdTe layers grown on GaAs substrates [110], which were originating from improper growth temperature. On the other hand, over 30 CdTe layers grown in this study had the same type of surface defect where only the density of the defects was varied individually. The growth and the annealing parameters might affect the density of the surface defects while the origin of the surface defects should be different.

To investigate the origin of the surface defects, thermal deoxidation process under In flux was altered to the heating of the substrate under As_4 irradiation. As_4 shutter was closed ~ 20 s before introducing In flux to the GaAs surface. And a 2.8 ±0.1µm thick CdTe layer was grown on the deoxidized substrate. The optical image of the CdTe layer taken by Nomarski microscope is shown in Figure 4.34. Similar type of defects were ob-

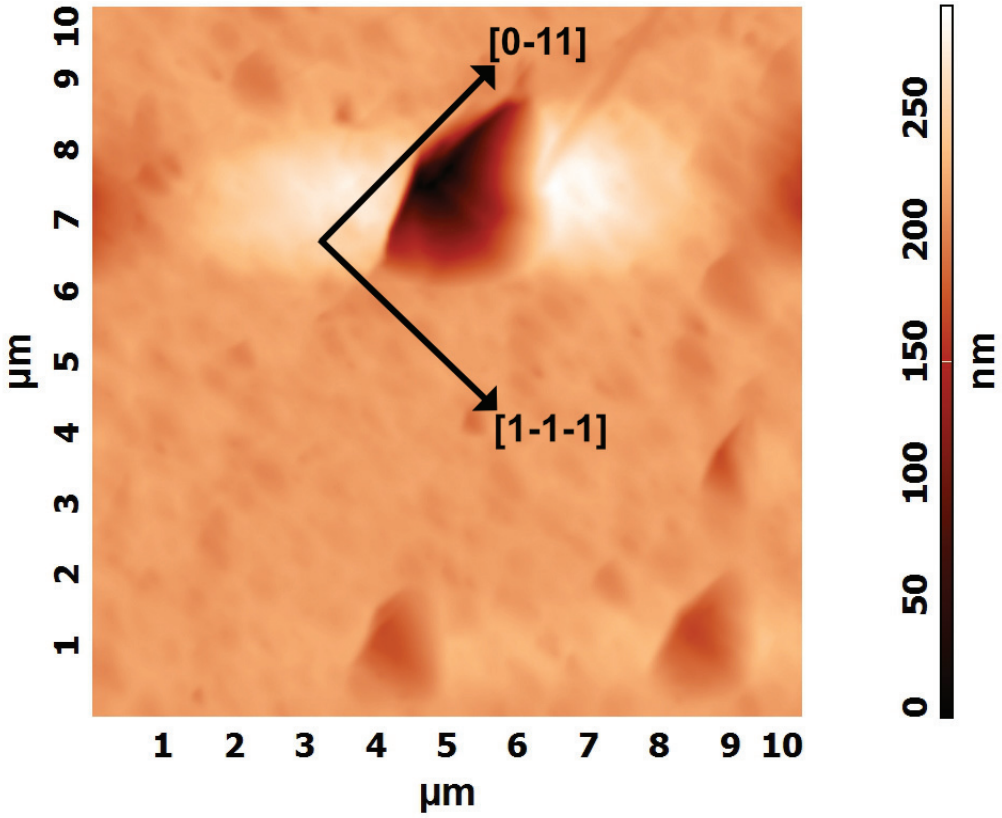

Figure 4.33.: AFM height image of the CdTe layer grown on GaAs substrate which was deoxidized at 520 °C for 240 s under In flux of 4.4×10^{-8} Torr BEP.

served on the surface of the CdTe layer for which the density of the defects was increased to 1.59×10^5 cm^{-2}. The shape of the defects was appeared to be similar to those of on the CdTe layer grown on deoxidized GaAs substrate without a pre-As_4 irradiation step. Therefore, the pre-As_4 irradiation during heating of the GaAs substrate to the deoxidation was eliminated.

Next, the duration of the In assisted deoxidation step was studied. If the total Ga_2O_3 content in the oxide layer was considered as reaction limiting factor of the deoxidation process, then the total amount of the In atoms required for this reaction is a fixed value. The total amount of the In atoms delivered to the surface then is a function of the flux and the duration of In irradiation. If the total amount of the In atoms on the GaAs surface is greater than the amount required for the chemical reaction of the Ga_2O_3 decomposition, In atoms can migrate on the surface and form droplets. To reduce the amount of the total In atoms on the GaAs surface during the In assisted deoxidation process,the duration of the In irradiation time was decreased. GaAs(211)B substrate was deoxidized

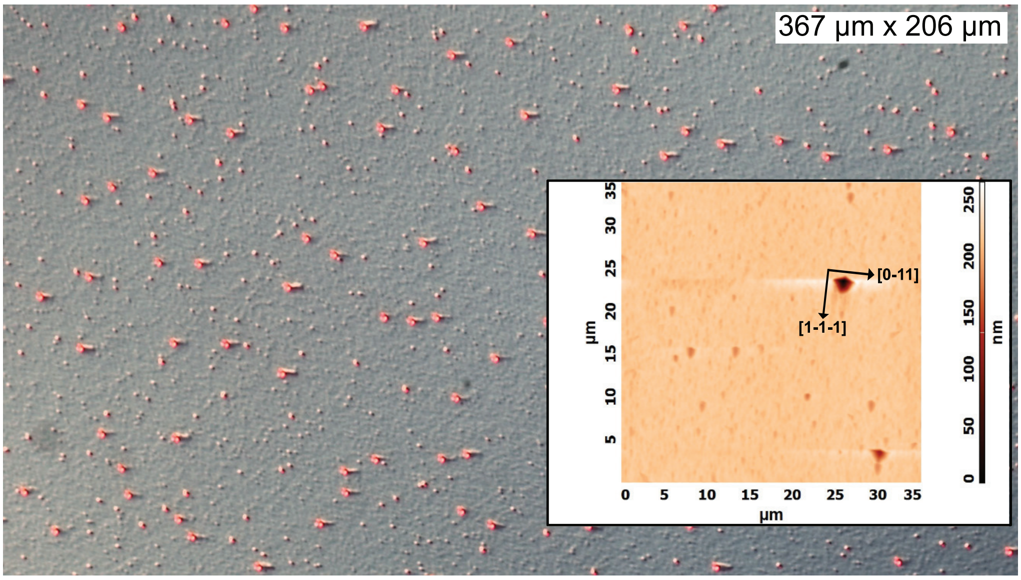

Figure 4.34.: Nomarski optical image of the CdTe layer grown on GaAs substrate which was deoxidized at 520 °C for 240 s under In flux of 4.4 × 10^{-8} Torr BEP while heating of the GaAs substrate to the deoxidation temperature was carried out under As_4 flux. Inset: AFM height image of the same CdTe layer.

at 520 °C for 120 s under In flux of 4.4 × 10^{-8} Torr BEP. In desorption process was performed at 541 °C for 180 s. A 2.8 ±0.1µm thick CdTe layer was grown on the deoxidized substrate. The optical image of the CdTe layer taken by Nomarski microscope is shown in Figure 4.35. The great reduction in the density of the surface defects can be seen from the figure. The density of the surface defects was reduced to 4.77 × 10^4 cm^{-2}. Additionally, the density of the defects with smaller size was dramatically reduced. The shape of the larger defects with a triangular shape can be seen from the inset of Figure 4.35.

The reduction in the density of the defects with a triangular shape suggests that additional In atoms which not participating to the Ga_2O_3 decomposition reaction was creating the In droplets on the surface. On the other hand, the spontaneous change in the density of the In atoms on the GaAs surface might also affect the droplet formation. If the In atoms delivered to surface faster than the reaction rate of the Ga_2O_3 decomposition, the density of the In atoms will increase in time therefore allowing In atoms to form droplets. To study the effect of the spontaneous change in the In flux, the BEP flux of the In irradiation was decreased to 1.6 × 10^{-8} Torr BEP. However, to preserve the reaction rate, the desorption temperature was increased to 535 °C. In desorption process was performed at 550 °C for 240 s. A 2.8 ±0.1µm thick CdTe layer was grown on the

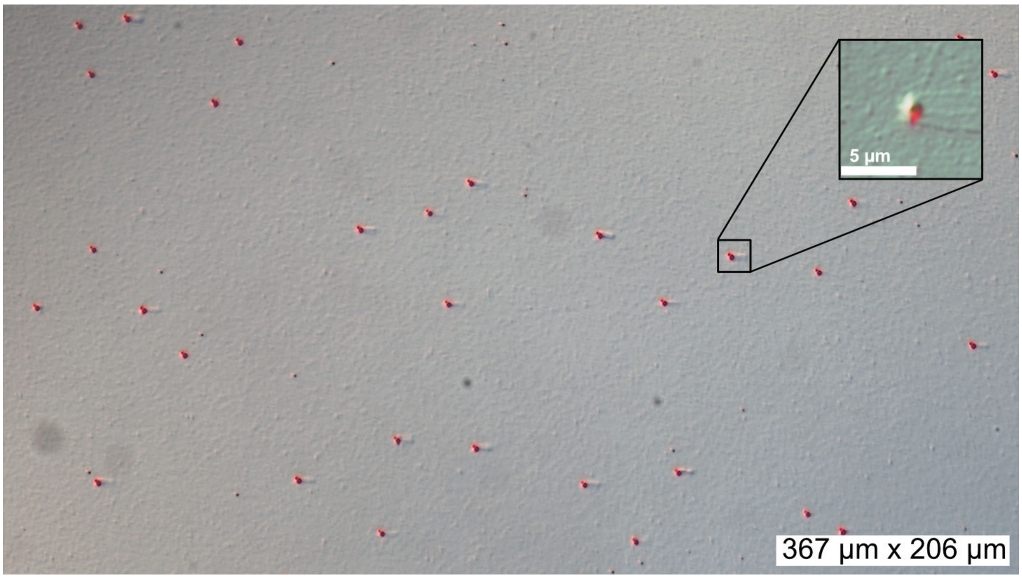

Figure 4.35.: Nomarski optical image of the CdTe layer grown on GaAs substrate which was deoxidized at 520 °C for 120 s under In flux of 4.4×10^{-8} Torr BEP. Inset: Nomarski optical image of the same surface with higher magnification.

deoxidized substrate.

The optical image of the CdTe layer taken by Nomarski microscope is shown in Figure 4.36 (a). The surface of CdTe layer is featureless and without any triangular defects which indicates that the dominant factor of the In droplet formation is the spontaneous density during the In assisted deoxidation. AFM height image of the same layer is shown in Figure 4.36 (b). The surface morphology is similar to the previously reported AFM images of the high quality CdTe layers grown on GaAs [111]. The RMS roughness of the CdTe layer calculated from the AFM image is 1.74 nm indicating a smooth surface.

To study the effect of the In flux at optimum deoxidation temperature, the growth of the CdTe epilayer was performed on the deoxidized GaAs (211)B under In fluxes of 1.6×10^{-8} and 4.4×10^{-8} Torr BEP. CdTe growth was initiated at a low temperature of 216±1 °C to suppress the formation of twins. Following the nucleation, the substrate temperature was increased to 296±2 °C with a slow ramp and kept constant till the growth was completed. Thickness of the layers was 2.85±0.1 µm. The crystal quality of the CdTe layer was investigated with the XRD surface symmetric high-resolution four-crystal (Ge) RC measurements. XRD RC scan was performed from the [0-11] azimuth. The CdTe(422) RC of epilayer was fit using a PearsonVII function. The RC FWHM was calculated as 125 arc-s and 118 arc-s for the CdTe epilayers grown on the eoxidized GaAs

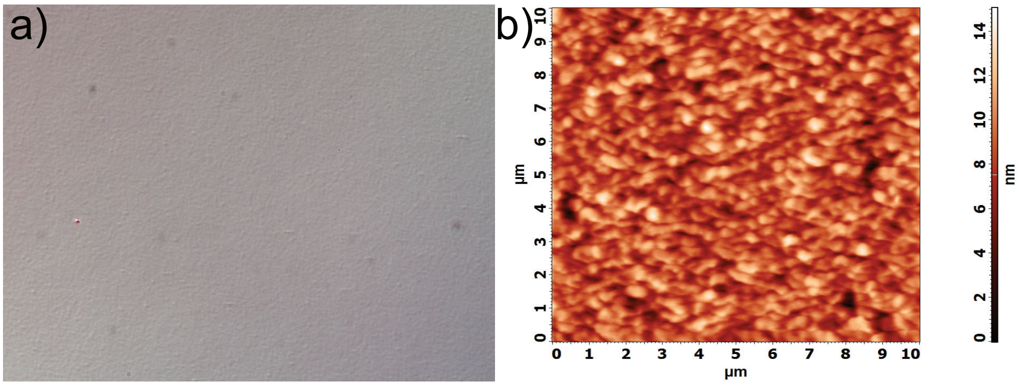

Figure 4.36.: Nomarski optical image of the CdTe layer grown on GaAs substrate which was deoxidized at 535 °C for 120 s under In flux of 1.6×10^{-8} Torr BEP. Inset: AFM height image of the same CdTe layer.

substrates under In fluxes of 1.6×10^{-8} and 4.4×10^{-8} Torr BEP, respectively. The XRD RC FWHM values of the epilayers suggest that the CdTe layer grown on the deoxidized GaAs under high In flux has a better crystal quality conflicting with the previously given results. Therefore, the crystal quality of the epilayers were characterized additionally with the defect decorative etching method. The dislocation density of CdTe layers were determined with defect selective 30 s (1HF:4HNO_3:25H_2O) etching [112] which reveals EPD. The detection of the triangular pits were carried out with the surface SEM images. EPD of the CdTe layers grown on deoxidized GaAs substrates under high and low In flux were 1.96×10^6 cm^{-2} and 4.86×10^7 cm^{-2}, respectively. The results of the XRD RC and defect decorative etching measurements does not correlate well. The discrepancy between the results points out to a problem with the calculation of the EPD of the epilayers. In Figure 4.37, the SEM images of the etched CdTe layers grown on the deoxidized GaAs substrates under the two different In flux are shown. In Figure 4.37 (a), the SEM image of the CdTe layer grown on deoxidized GaAs substrate under high In flux shows that the surface is rough. Additionally, triangular shaped defects due to defect decorative etching were strictly localized near the surface defects which was related to the In droplets. An etched epilayer with high surface roughness and high pit population reduces the visibility of the triangular defects which introduces an uncertainty to the counting process. The SEM image of the CdTe layer grown on the deoxidized GaAs substrate under low In flux (Figure 4.37 (b)) shows that triangular defects related to the etching are well separated and easily detectable for counting. Therefore, EPD value of the CdTe layer grown on the deoxidized GaAs substrate under high In flux was not reliable for evaluation of the crystal

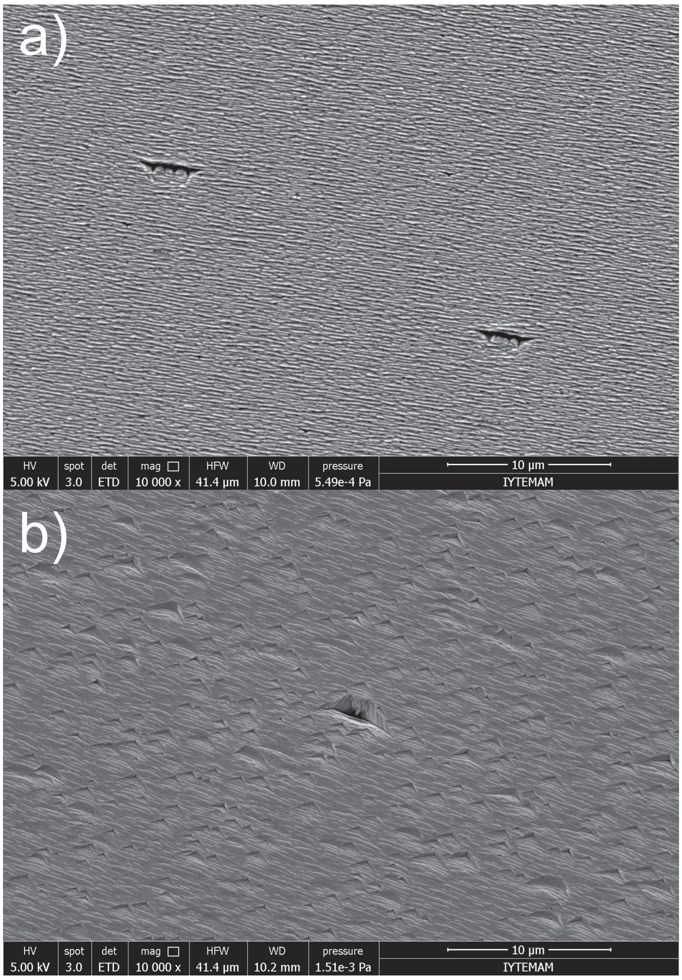

Figure 4.37.: SEM images of the etched CdTe layers grown on deoxidized GaAs(211)B substrates under In fluxes of (a) 1.6×10^{-8} Torr BEP and (b) 4.4×10^{-8} Torr BEP.

quality. The characterization results of the CdTe layers suggest that a highly crystalline CdTe layer can grown on the deoxidized GaAs(211)B substrate under In flux of 1.6×10^{-8} Torr BEP.

4.4. Conclusions

A systematic study of thermal deoxidation of GaAs(211)B surfaces under As_4 overpressure has been carried out at a constant deoxidation temperature. By using *in situ* RHEED and *ex situ* XPS and AFM, it has been shown that, for a GaAs(211)B surface, approximately 626 s to 800 s is the optimal deoxidation duration under 2.5×10^{-6} As_4 Torr BEP and 582 °C surface temperature. It has been observed that RHEED spot intensity was saturated after 600 s of deoxidation. Extending the deoxidation duration further did not result in a notable increase in the RHEED intensity. By XPS analysis, it has been shown that oxide desorption for 215 s duration has completely removed Ga_2O_3 and As_2O_5 molecular species from the surface. However, as product of Ga_2O_3 thermal deoxidation process, Ga_2O did not desorb from the surface until 626 s. Similarly, excess As-As and As^0 did not evaporate from the GaAs surface until 626s. Detection of the GaAs concentration with a high value (over 90 %) in the XPS spectra of the sample with 626 s deoxidation suggesting that the deoxidation process was completed. Moreover, the AFM measurements of the deoxidized samples under different oxide desorption durations revealed that 626 s deoxidation has yielded the compatible morphology with the deoxidized Ga-deficient surface, characterized by 0.53 nm RMS roughness and a 50 % increase in deoxidation-related pit population. Abrupt changes in surface roughness, peak-to-peak, and skewness values related to the Ga and As matrix disruption were observed when the deoxidation duration exceeded 626 s, which was in good agreement with the XPS results. The effect of the deoxidation duration the CdTe epilayer crystal quality was carried out by the growth of CdTe layers on the deoxidized GaAs substrates. The relation between the XRD RC FWHM from the epilayers with the deoxidation duration was non-linear which was fit with a second-order polynomial. It was shown that the lowest FWHM can be obtainable with 489 s deoxidation.

The effect of the deoxidation temperature on GaAs surface under As_4 flux was studied. *in situ* RHEED characterization of the temperature-dependent deoxidation experiments under As_4 flux has shown that desorption of the Ga_2O_3 from the GaAs surfaces may be a two step process; decomposition of the Ga_2O_3 and desorption of the Ga_2O. The reaction rates and constants of both processes may be quite different. The reaction rate of the decomposition of the Ga_2O_3 was determined to be small during the deoxidation at 546 °C and 563 °C. Both RHEED and AFM measurements confirmed that thermal deoxidation processes at 546 °C for 34 minutes and at 563 °C for 21 minutes was not enough for the completion of the desorption of the oxide layers. Additionally, to reduce the Ga desorption due to non-deoxidation mechanisms, the deoxidation of the GaAs substrate was performed at a high temperature of 607 °C. The deoxidation duration was determined with the RHEED spot intensity saturation which was obtained after 270 s. The RHEED pattern from the GaAs substrate following the deoxidation process was streaky and bright indicating a highly crystalline and oxide-free surface. To study the effect of high temperature deoxidation on to the CdTe epilayer crystal quality, a thick CdTe layer was grown. XRD RC FWHM value of the layer was 138 arc-s which was remarkably lower than that of the theoretical FWHM value obtained with the deoxidation at 582 °C.

Thermal deoxidation of GaAs(211)B surfaces under In overpressures has been studied extensively for four different process with three steps. By using AFM and XPS techniques, it has been shown that the low temperature (485 °C) In-assisted deoxidation resulted in a very rough surface with InAs islands and as well as Ga_2O_3 molecules while the high temperature In assisted deoxidation created a surface with deep pits. The best surface morphology was obtained with the In assisted deoxidation at 530 °C. In addition, it has been found that at least 120 s was required for the desorption of the Ga_2O from the surface which is a product of the reaction of the Ga_2O_3 decomposition under In flux.

The effect of the In flux on to the GaAs surface morphology could not be determined with ex situ AFM and XPS measurements from the GaAs substrates. Therefore, CdTe epilayers were grown on the deoxidized substrates. It has been shown that, the In flux has a great impact on the surface quality of the CdTe layers. The In atoms not participating in the reaction of the Ga_2O_3 decomposition, may create In droplets on the GaAs surface. In addition, the In droplets can create inter-diffusion centers or etching zones on the GaAs surface. CdTe layers grown on the deoxidized GaAs substrates under high In flux (4.4×10^{-8} Torr BEP) had a surface with triangular defects. Similarly, CdTe layers grown on the deoxidized GaAs substrates under In flux with extended duration had a surface with triangular defects. The total amount of the In atoms and the spontaneous In flux is found to be critical to obtain defect free GaAs and therefore CdTe surfaces. By adjusting the reaction temperature with the In flux, a CdTe layer on the deoxidized GaAs substrate was grown without any major surface defects. To investigate the effect of the thermal deoxidation under In flux on to the CdTe epilayer crystal quality, thick CdTe layers were grown. The characterization of the crystal quality of the epilayers has shown that a highly crystalline CdTe was grown on the deoxidized GaAs(211)B substrate under low (1.6×10^{-8} Torr BEP) In flux. The RC FWHM of this layer was 125 arc-s. In addition, the SEM images of CdTe layers following defect decoration etching have shown that the structural defects were densely packed at the surface defects due to the In droplets. The rough surfaces related to the defect decorative etching process complicated the counting of the pits on the CdTe layer grown on the deoxidized GaAs substrate under the high In flux.

The comparison of the surface characterization of both In and As_4 assisted deoxidation process has shown that the In assisted deoxidation process has a great potential to produce GaAs substrates with a smooth and nearly Ga-related pit free surface.

To compare the characterization results of the As_4 and In assisted deoxidation processes, the deoxidized samples with the best surface morphology and chemical structure are determined as 626 s deoxidation at 582 °C under As_4 overpressure, and 240 s deoxidation at 530 °C under In overpressure. From this point, the characterization results of these samples will be compared.

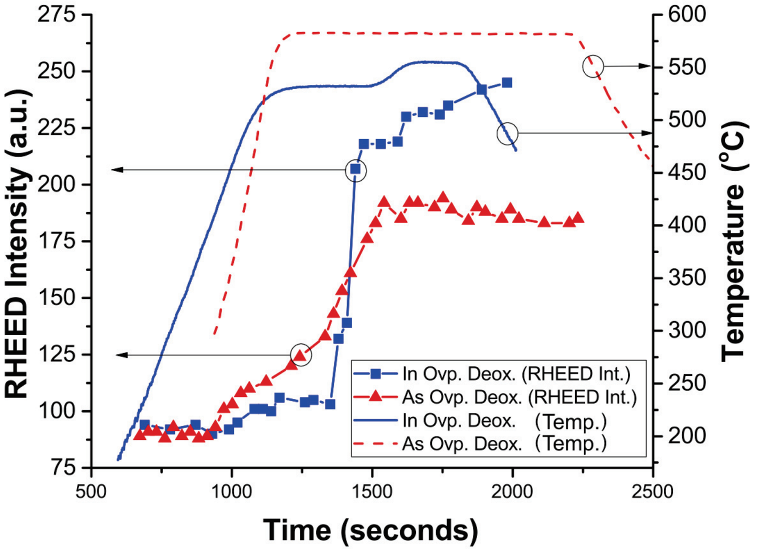

Figure 4.38.: RHEED spot intensity and surface temperature change during deoxidation. Blue (red) lines corresponds to the In-(As-)assisted deoxidation.

RHEED spot intensity and surface temperature change during the deoxidation processes are shown in Figure 4.38. It should be noted that the ratio of intensity change with respect to that noted at the beginning of deoxidation is ~ 1.33 times higher for In-assisted deoxidation relative to As_4 assisted desorption. The RHEED patterns of the deoxidized samples under As_4 and In overpressure are given in Figures 4.7 (e) and 4.23 (a). The appearance of brighter RHEED spots and streakier RHEED patterns after In-assisted deoxidation might be an indication of an atomically smoother surface compared to that achieved by As_4 assisted deoxidation. On the other hand, the brighter RHEED patterns might be related to the surface roughness.

AFM height images of thermally deoxidized samples under As_4 and In overpressures are given in Figures 4.12 and 4.28. These figures show that the thermal deoxidation under As_4 overpressure created large pits on the surface of GaAs substrates compared to the In assisted deoxidation process. The RMS roughness of the epiready wafer surfaces was altered slightly after thermal deoxidation under In and As_4 fluxes. It is seen from the

Peak-to-Peak and SK values of the deoxidized samples, the In-assisted desorption created a smooth surface with shallower pits. Additionally, the In assisted deoxidation resulted in to a surface with a $\sim$ 13 % less pit number density compared that of the GaAs surface deoxidized under As_4 irradiation. Occurrence of fewer pits on the thermally deoxidized samples under In overpressure is in agreement with the RHEED results. Furthermore, the absence of As_2O_5 and Ga_2O_3 states in relevant XPS spectra suggests the completion of deoxidation processes in both cases. However, Ga_2O desorption process was not completed for the In assisted deoxidation.

The crystal quality of CdTe epilayers grown on GaAs(211)B substrates under In and As assisted deoxidation process with optimized deoxidation parameters were characterized using XRD RC and defect decorative etching. The results have shown that highly crystalline CdTe epilayers with XRD RC FWHM of 138 arc-s and 125 arc-s could be achieved employing As and In assisted deoxidation, respectively. Highest crystal quality was obtained with the CdTe layer grown on the deoxidized GaAs(211)B under In flux.

CHAPTER 5

EPITAXIAL GROWTH OF CdTe

The (211) orientation of zinc-blende crystals has a number of beneficial properties. Of most relevance to the epitaxy of thin films is the tendency of the (211)B orientations of Te-terminated substrates to suppress twin formation on (111) planes [113]. The critical dimension of a twin nucleus in (111) plane can be reached within a single monolayer whereas that in the (211) direction is much larger [113]. Thin films grown on (211) substrates have a tilted epilayer orientation relative to the substrate [51, 114–117]. The tilt phenomenon has been attributed to a number of causes by different authors including the glide and interactions of misfit dislocations [118–121] and localized distortion of the lattice at the interface [122]. The mismatched CdTe on GaAs(211) epitaxy can result in films growing in a twinned orientation such that the (133) planes make up the epilayer surface and are parallel to the substrate (211) planes [51, 114, 123]. However, with the [111] as the mirror plane, [255] is the exact twin of [211] [52]. The x-ray diffraction from the [255] peak is forbidden where the closest lower plane index with allowed reflection is (133).

In summary, nonpolar surface of low symmetry of the (211) surface is ideal for MBE growth of CdTe. On the other hand, such high-index surfaces are not as flat in atomic scale as low-index surfaces. (211) surfaces have a double dangling bond on top surface layer [124]. This would make (211) surfaces more chemically active and thus more attractive to impurities than low-index surfaces like (001).

5.1. Nucleation

The initiation of the growth is a critical step in the heteroepitaxy of CdTe layers on high index GaAs(211)B substrates as mentioned above. The growth of the CdTe epilayer starts with the nucleation step which can result in a highly twinned layer. To investigate the effect of the nucleation process to CdTe crystal quality, the nucleation temperature and the nucleation procedure were studied. The localized distortion of the lattice at the interface between CdTe and GaAs(211)B may enable twinned growth as suggested above. The strain on CdTe layer at the nucleation step originates from the lattice constant and thermal expansion difference of those structures. The thermal expansion constant of the materials is a function of temperature. The difference between the thermal expansion constants of the CdTe and GaAs has the lowest value around 50 °C while it gets larger with increasing temperature. Nucleation of the CdTe on GaAs is favorable at low temperatures. On the other hand, the low temperature nucleation can restrain the migration of Cd and Te atoms on the GaAs surface. Therefore, a relatively high temperature is required to preserve (211) crystal orientation while improving the mobility of the adatoms on the surface.

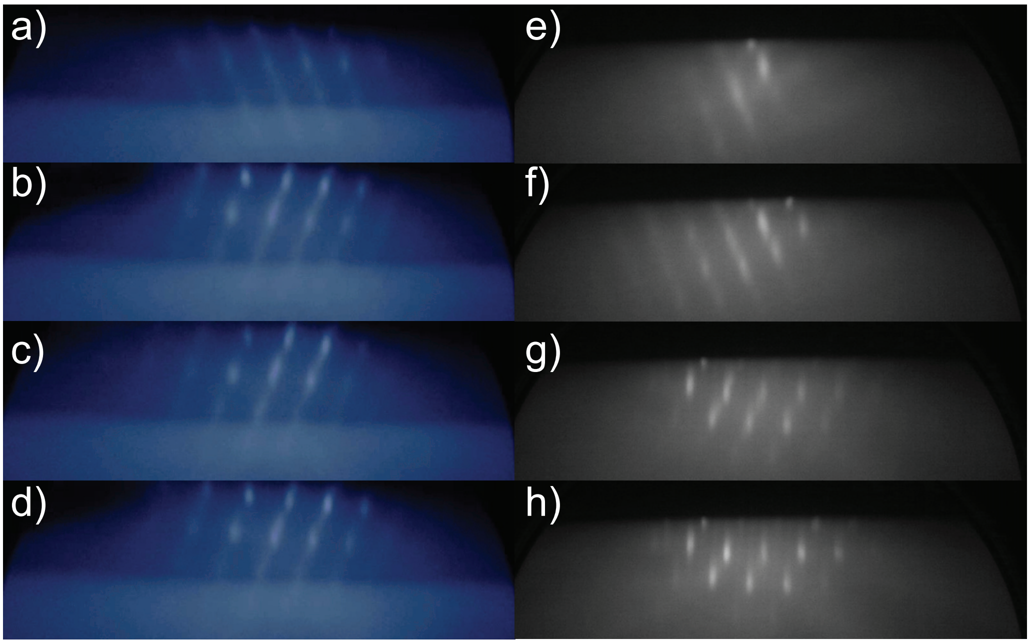

Figure 5.1.: RHEED patterns of CdTe epilayers nucleated at 233 °C; after nucleation started (a) 15 s, (b) 30 s, (c) 120 s, and (d) 300 s. RHEED patterns of CdTe epilayers nucleated at 215 °C; after nucleation started (a) 15 s, (b) 30 s, (c) 120 s, and (d) 300 s.

Thermal deoxidation and CdTe growth were performed in Veeco GEN20MZ MBE system using 3-inch GaAs(211)B epiready substrates. The thermal deoxidation was carried out with Veeco Mark V 500 As (7 N) valved cracker, whereas CdTe growth was performed with Veeco Mark V 200 CdTe (7 N) and Te (7 N) valved crackers. The thermal deoxidation and growth was monitored in situ through RHEED, which yielded data pertaining to surface crystal quality. In addition, calibrated band-edge detection system was used for temperature measurements. GaAs substrates were heated from room temperature to 585 °C and were kept at this temperature for ~ 10 min under As_4 flux with 2.5×10^{-6} Torr BEP, which was initiated at the surface temperature of 300 °C for As_4-

assisted deoxidation procedure. Next, GaAs substrates were cooled under same As_4 flux to ensure B polarity of the GaAs substrate. Growth of the CdTe epilayers was initiated at temperatures from 215 °C to 233 °C.

In Figure 5.1, RHEED patterns taken after the nucleation of CdTe epilayers at the temperatures from 215 °C to 233 °C are shown. After initiation of the growth at 15 s, spots in the RHEED pattern of the CdTe layer nucleated at 215 °C already begun to transform into streaks (Figure 5.1 (e)). At 30 s, both RHEED patterns become brighter while the streaks from the layer nucleated at 215 °C are longer (Figure 5.1 (f)). The streaks from the layer nucleated at 233 °C did not get longer and remained nearly the same following 2 minutes after the initiation of the CdTe growth indicating a twinned growth (Figure 5.1 (c) and (d)). Through 5 minutes after the nucleation at 215 °C, the RHEED patterns exhibit long and bright streaks indicating a high crystalline layer (Figure 5.1 (g) and (h)).

To investigate the effect of the nucleation temperature on the CdTe crystal quality, three CdTe layers were grown with the nucleation temperatures of 218 °C, 233 °C, and 270 °C. The CdTe layers were grown at the rate of ~ 1 μm/h. The Te/Cd ratio was 3 and kept constant during the growth. To ensure homogeneous distributions of the Cd and Te atoms on the surface, the samples were rotated at 4 rotations per minute (RPM). Following the nucleation, after 30 s, the growth temperatures were increased to 300±2°C with a slow ramp of ~ 3°C/min. To characterize epilayers with XRD, CdTe layers were grown with a minimum thickness of ~ 1.5 μm. Thickness of the layers were measured by FTIR transmission measurements and SE. The crystal quality of the CdTe layers were investigated with the surface symmetric ($\omega = \theta$) scans. The x-rays were generated with a Cu tube then directed to the sample surface with a half-angle slit. The reflected x-rays were collected at the detector with the help of a collimator. In Figure 5.2, the spectra from the surface symmetric Gonio scan of the CdTe layers nucleated at 218 °C, 233 °C, and 270 °C are shown. The reflections from the (211) planes of the zinc-blende crystals are not allowed, thus the XRD patterns from the (422) planes are observed. The reflections from the GaAs(422) crystal planes with Cu x-ray tube $K\alpha_1$, $K\alpha_2$, $K\beta$, and W $L\alpha$ wavelengths are detected and shown in this figure. The GaAs(422) $K\alpha_1$ and $K\alpha_2$ peaks were located at 83.88° and 84.12°, respectively. The calculation of the GaAs(422) $K\alpha_1$ and $K\alpha_2$ peaks with the Bragg equation using wavelengths of $K\alpha_1$ =1.540598 Å, $K\alpha_2$ =1.544426 Å (supplied by XRD system specification sheet) and lattice constant of 5.65 Å yields 83.82° and 84.07°, respectively.

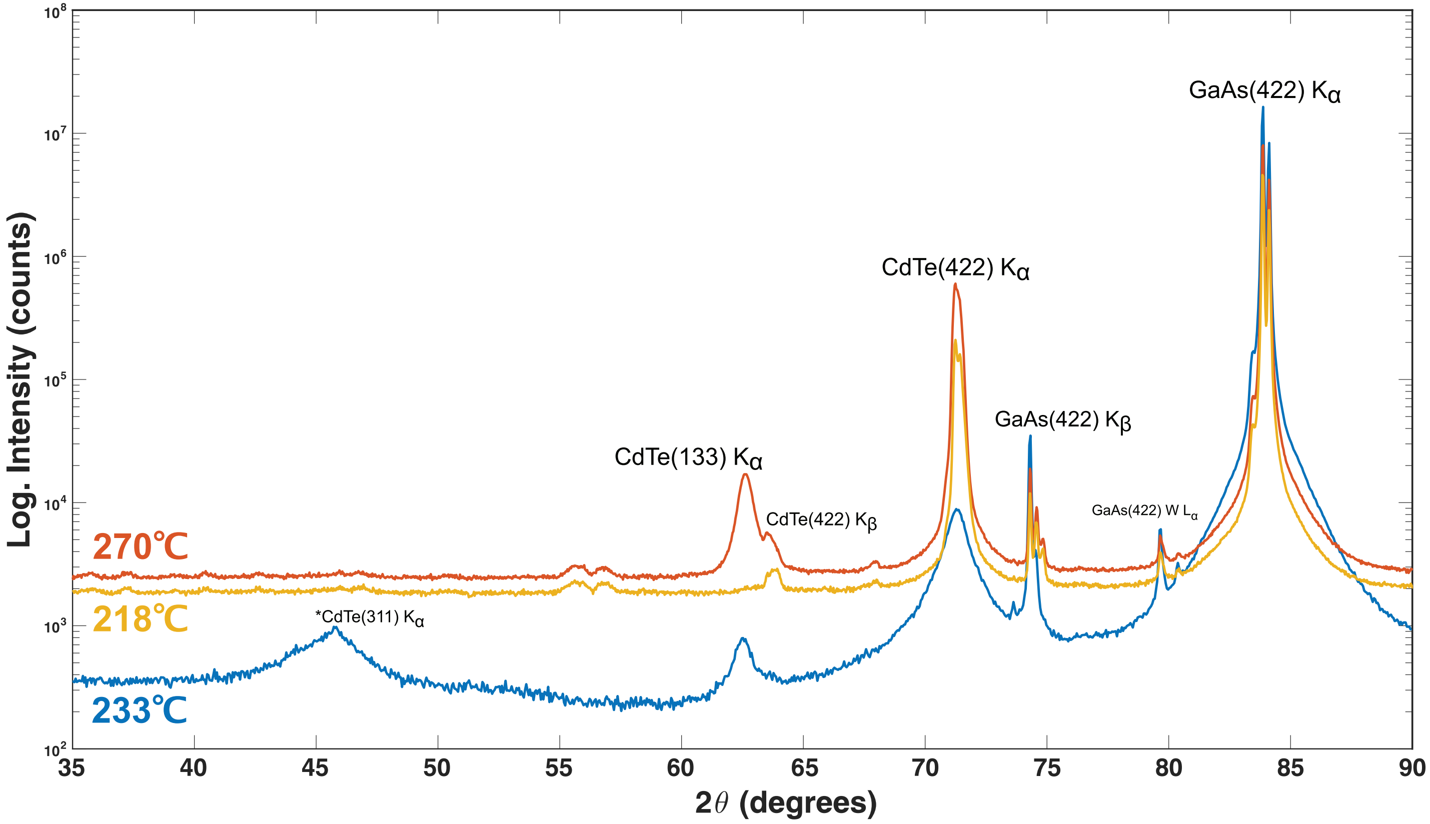

Figure 5.2.: XRD Gonio spectra of CdTe epilayers nucleated at 218 °C, 233 °C, and 270 °C.

The measured and calculated peak positions of the GaAs(422) Kα_1 and Kα_2 peaks is in agreement. The difference between the measured and estimated peak values is in the resolution limit of the XRD Gonio scan. In addition to the GaAs peaks, several peaks were located at 71.22°, 61.52°, and, 45.72° which were the reflections from the CdTe(422), CdTe(133), and CdTe(311) planes, respectively. However, CdTe(311) peak was detected only when the Gonio scan was performed from the [0-11] or [01-1] azimuths. The angle between the planes of CdTe(311) and CdTe(211) is 10.02°, with the tilting in toward [-111] direction about [0-11] axis, then the angle becomes ~ 7°. The asymmetric reflection from the CdTe(311) plane becomes detectable during a symmetric surface scan. Therefore, the reflection at 45.72° is not from a symmetrical reflection from the CdTe(311) planes, instead it is an asymmetrical reflection of the CdTe(422) planes which were parallel to the epilayer surface. Theoretical calculation of the reflections from the planes parallel to the surface of CdTe(422) and CdTe(133) with Kα_1 =1.540598 Å and lattice constant of 6.48 Å yields 71.23° and 62.42° , respectively. The difference between the theoretical calculation and experimental measurement of the reflection angle of the CdTe(422) plane is in well agreement. The angle of the CdTe(133) reflection is detected 0.9° lower than the theoretical value which might be related to the relaxation of the CdTe layer during twinned nucleation step. It is seen from the figure that the nucleation process at 218 °C created a single crystal layer without the nucleation related twins. The nucleation processes at 233 °C and 270 °C, on the other hand, created CdTe(211) layers with twinned planes of (133). The nucleation of CdTe epilayer at higher surface temperature allows twinned growth with the (133) surface orientation indicating surface energy (Φ) of the (133) surface is larger than the (211) ($\Phi_{(133)} > \Phi_{(211)}$). To determine the transition temperature, consecutive growth of the CdTe layers were performed and the nucleation of the CdTe layers were studied by RHEED. It was found that for a twin-free CdTe layer, the nucleation process must be initiated at a maximum temperature of 229°C.

The initiation of the growth of the CdTe epilayer on GaAs may continue with a low and constant growth or with a temperature ramp to the nominal growth temperature [23, 94, 125]. Both methods are frequently applied to the heteroepitaxial growth of CdTe. The low temperature growth may cause formation of an unstoichiometric epilayer. Therefore, an anneal step of the nucleation layer is required to improve crystal quality of epilayers. To investigate the effect of the nucleation method to the CdTe crystal quality, CdTe layers were grown with two different methods. In the first method, nucleation starts at 218 °C which is followed by a 3.87 °C/min. temperature ramp to the growth temperature of 276 °C where the temperature is kept constant for 65 minutes and finally a flash anneal at

404 °C is performed (Figure 5.3 b.). The second method involves, a constant temperature

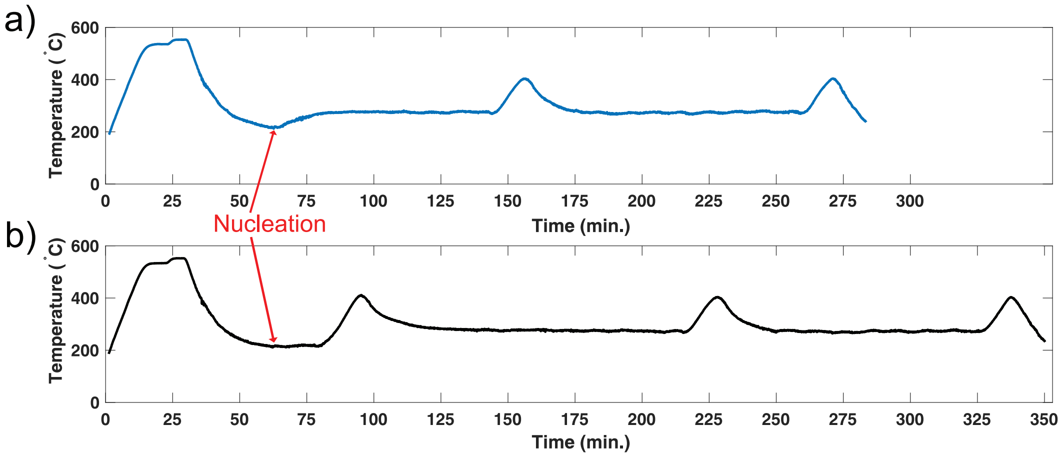

Figure 5.3.: Measured temperatures as a function of time during growth of with the two different nucleation methods; (a) nucleation was followed by a temperature ramp. (b) nucleation was performed a constant temperature and followed by anneal.

nucleation at 217 °C which is followed by a flash anneal at 406 °C (Figure 5.3 a.). For both methods, the remaining of the CdTe epilayer growth consists of a growth step at 276 °C for 80 minutes and a flash annealing step at 405 °C. GaAs substrates were deoxidized under In flux of 1×10^{-8} Torr BEP at 535 °C for 4 minutes which was followed by a 3 minute In desorption at 553 °C. Then, the GaAs substrates were cooled to nucleation temperature under 4.2×10^{-6} Torr BEP As_4 flux. The Te/Cd (VI/II) ratio was chosen as 3.45 with a $6.89 \pm 0.02 \times 10^{-7}$ Torr BEP CdTe flux.

Thickness of the CdTe layers of grown with both methods were determined from interference fringes from the FTIR transmission measurements, in situ transmission spectroscopy (band-edge detection system) and by SE as 2.74±0.06 µm and 2.66±0.04 µm, respectively. The refractive index of the CdTe layer is required for the accurate calculation of the thickness of thin films by using the interference fringes. Therefore, the calculated refractive index of the CdTe from SE measurements was used for the determination of the thickness of the epilayers. The dielectric function of the CdTe epilayers were modeled using a multi-oscillator model with a MSE of 14 which had PSemi-Tri and harmonic oscillators [73]. In Figure 5.4 (a), the results from SE measurements with the model consisting of CdTe layer and GaAs substrate is shown for the sample nucleated with the first method. The interference oscillations till the band gap of the GaAs substrate can bee seen from the figure. The real (e1) and imaginary parts (e2) of the dielectric function as a function of the photon energy are shown in Figure 5.4 (b). The energy band gap of the CdTe layer grown with first method was determined with the Psem-Tri oscillator as 1.512±0.003 eV where E_1 and $E_1+\Delta_1$ critical points are calculated as 3.28±0.01 eV and 3.829±0.014 eV, respectively. The energy band gap and the critical point energies of E_1 and $E_1+\Delta_1$ of the layer grown with second method are determined as 1.511±0.004 eV, 3.277±0.008 eV, and 3.825±0.015 eV, respectively. The difference between the critical energies of the two CdTe layers is within the error limit of the SE model, indicating that the optical properties of the layers is very similar.

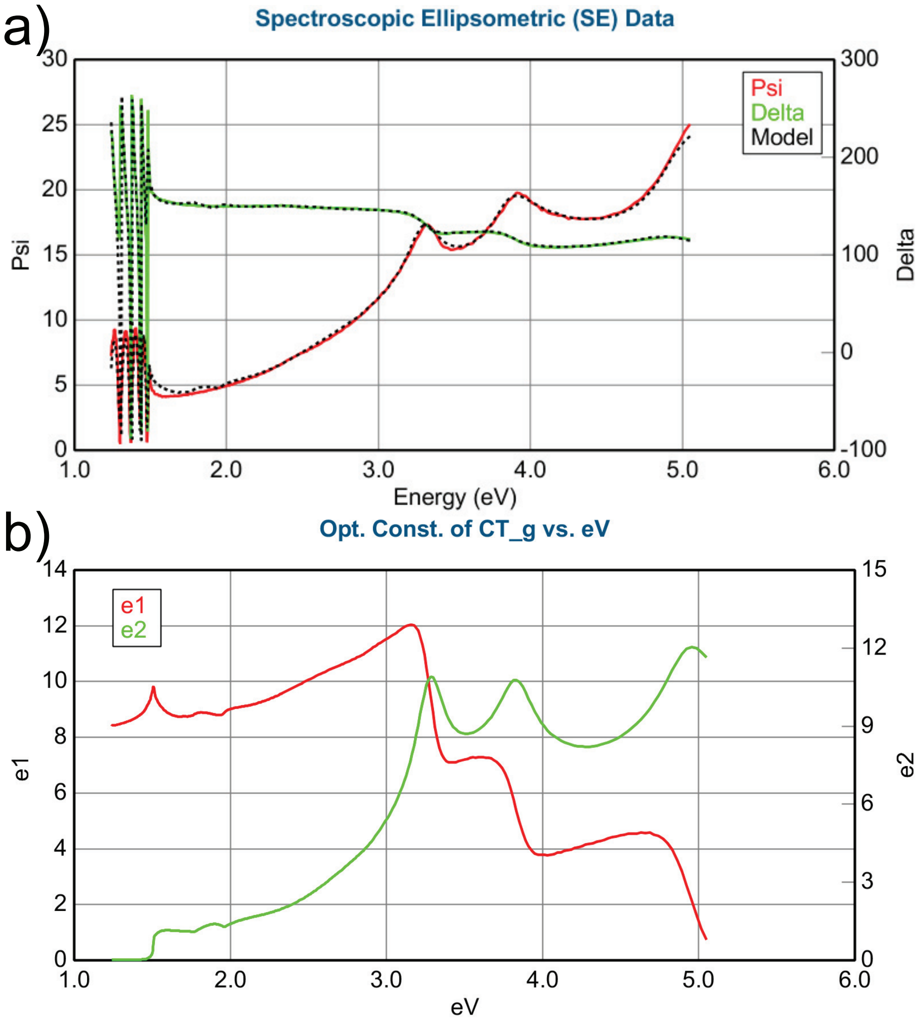

Figure 5.4.: (a) The result of SE measurent for the CdTe layer grown with the first nucleation method. (b) The real (e1) and the imaginary part (e2) of the dielectric function of the CdTe layer modeled with multi-oscilator function as a function of photon energy.

The crystal quality of the CdTe layers were investigated with the XRD surface symmetric Gonio scans and high-resolution four-crystal (Ge) RC measurements. The reflection from the (133) planes were not detected which is the twin of the CdTe(211) orientation during Gonio scans. XRD RC scans were performed from the [0-11] azimuth. The RC scans of the CdTe layers grown with the first and second method are given in Figure 5.5. The RC of the CdTe(422) reflection was fit with a PearsonVII function which is a basically a Lorentz function raised to a power m, and given as;

$$y_0 + A\frac{2\Gamma(m)\sqrt{2^{(1/m)}-1}}{\sqrt{\pi}\Gamma(m-\frac{1}{2})w}\left[1+4\frac{2^{(1/m)}-1}{w^2}(x-x_c)^2\right]^{(-m)} \tag{5.1}$$

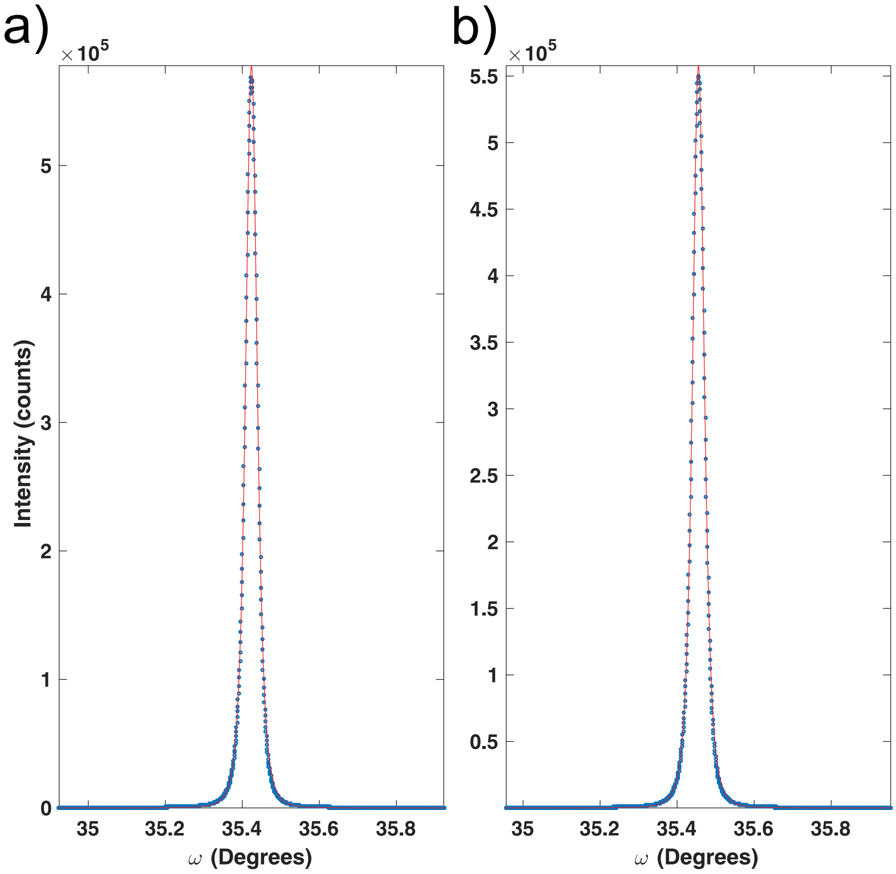

Figure 5.5.: XRD RC of CdTe layers (blue dots) nucleated with the two different nucleation methods; (a) the nucleation was followed by a temperature ramp. (b) the nucleation was performed a constant temperature and followed by anneal. RC of the samples were fit using a PearsonVII function (red line).

FWHM of the RCs were 126.81 arc-seconds and 129.29 arc-seconds while the adjusted-R^2 value of the fits were 0.999459 and 0.999651 for the epilayer grown with the first method (Figure 5.5 (a)) and second method (Figure 5.5 (b)), respectively. The dislocation density of CdTe layers were determined with defect selective 30 s (1HF: 4HNO_3: 25H_2O) etching[112] which reveals etch pit density (EPD). The observation and counting of the triangular defects to determine EPD can be performed by Nomarski, AFM, and SEM techniques. However, small pits could not resolved with the Nomarski microscopy leading to underestimation of the EPD of the epilayers [126]. Therefore, the detection of the triangular pits were carried out with the surface SEM images. In Figure 5.6, SEM image of the CdTe layer grown with the first method is shown. Several SEM images were used for the determination of the EPD. The pits were counted and the average of the pits was used to determine the EPD of the epilayers. The EPD value of CdTe layers grown with the first and second methods were 4.18×10^7 cm^{-2} and 4.54×10^7 cm^{-2}, respectively. The difference of 3.6×10^6 cm^{-2} in EPD values of the layers grown with both methods and the lower FWHM of XRD RC of the layer grown with the first method indicates that the CdTe layer grown with first method resulted in a slightly better crystal quality.

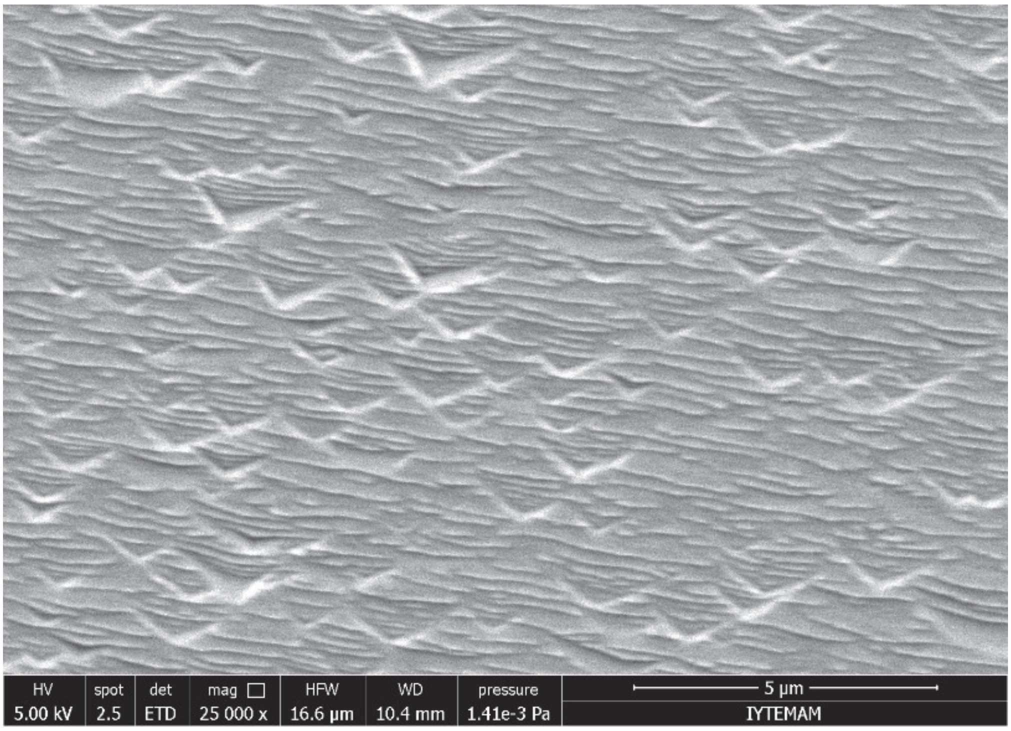

Figure 5.6.: SEM image of the CdTe layer grown with the first method which was etched to reveal dislocations (1HF:4HNO_3:25H_2O for 30 s).

Nomarski microscope surface image of the CdTe layer grown with the first method

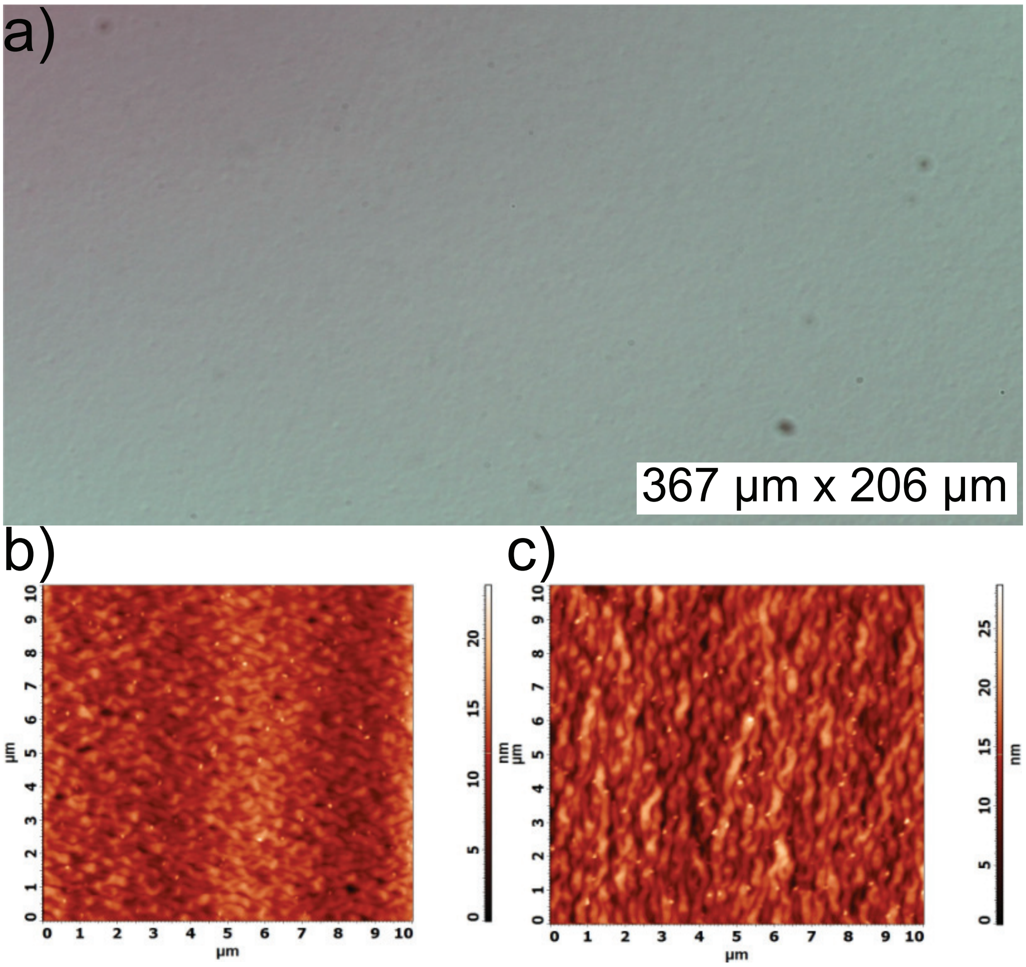

Figure 5.7.: (a) Nomarski optical image of the CdTe layer grown with the first method. AFM images of the of the CdTe layer grown with the first method (b) and the second method (c).

is given in Figure 5.7. The surface image of the other layer was similar. To probe the surface morphology of the epilayers with higher resolution, AFM technique was employed. The AFM height images of a 10 × 10 µm area representing the surface morphologies of the CdTe epilayers grown with two different nucleation methods are shown in Figure 5.7 (b) and 5.7 (c), respectively. The cross hatched lines [37] are visible on the AFM images of both samples indicating a smooth surface morphology. The AFM image of the second sample exhibit larger surface features which is not related to the step and edge formation of the (211) surface. The RMS roughness of surfaces were calculated as 1.94 nm and 3.14 nm for the CdTe layers grown with the first and the second methods, respectively. The nucleation process with first method was found to produce a smoother surface. The lower surface quality of the CdTe layer grown with the second method may be related to the involvement of the additional annealing step during growth. The additional annealing step was performed following the constant temperature growth. The SK values of the epilayers were 0.089 and -0.0017 for the epilayers grown with the first and second methods. The negative SK value indicates a change in the surface morphology due to the additional annealing step.

5.2. Te/Cd Ratio

The surface and the crystal quality of the heteroepitaxially grown layers may be greatly affected by the growth conditions such as the ratio of the atomic fluxes which are directed to the substrate during growth. Depending on the surface orientation, the stoichiometry of the crystal are greatly influenced by the ratio of the atomic fluxes [127]. In particular, Te-rich growth conditions during growth of CdTe epilayers on GaAs substrates with high index surfaces such as (211) were shown to yield higher crystal quality [128]. Additionally, the stoichiometric growth of the CdTe layer may also create an imbalance in the density of dislocation cores on the (111)A and (111)B glide planes [128]. To analyze the effect of the stoichiometry to the crystal and surface quality of the CdTe epilayers, CdTe layers were grown with different Te/Cd ratios.

Thermal deoxidation and CdTe growth were performed in Veeco GEN20MZ MBE system using 3-inch GaAs(211)B epiready substrates. Thermal deoxidation was carried out with Veeco Mark V 500 As (7 N) valved cracker whereas CdTe growth was performed with Veeco Mark V 200 CdTe (7 N) and Te (7 N) valved crackers. Thermal deoxidation and growth was monitored in situ through RHEED, which yielded data pertaining to surface crystal quality. In addition, calibrated band-edge detection system was used for temperature measurement. GaAs substrates were heated from room temperature to 605°C and were kept at this temperature for ∼ 4 min under As_4 flux with 4.01×10^{-6} Torr BEP, which was initiated at the surface temperature of 300 °C. Next, GaAs substrates were cooled under the same As_4 flux to ensure B polarity of the GaAs substrate. The growth of the CdTe epilayers was initiated at a surface temperature of 217±2 °C. To investigate the effect of the Te/Cd ratio on the CdTe crystal quality, three CdTe layers were grown at a temperature of 297±2 °C with the Te/Cd ratios of 3.45, 4.5, and 6. The growth of the epilayers were terminated by closing CdTe source shutter. The epilayers were cooled down to 240 °C under protective Te flux. CdTe layers were grown at the rate of ∼ 1 µm/h. To ensure homogeneous distributions of the Cd and Te atoms on the surface, samples were rotated at 4 RPM. In situ cyclic annealing was performed on the epilayers following 80 minutes intervals of the growth at 411±2 °C. Thickness of the layers were determined by SE and FTIR transmission measurements which was 2.66±0.05 μm.

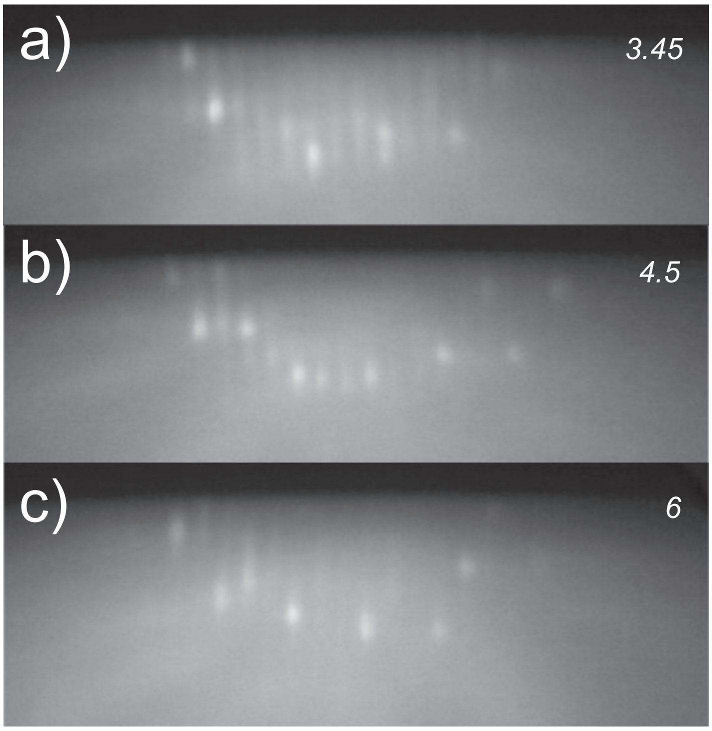

Figure 5.8.: RHEED patterns of CdTe epilayers grown with Te/Cd flux ratios of (a) 3.45, (b) 4.5, and (c) 6.

In figure 5.8, the RHEED patterns of CdTe epilayers grown with different flux ratios are shown. These patterns were recorded after the growth process and at ~ 250 °C. The RHEED pattern of Te stabilized CdTe(211)B surface [129] was obtained from all of the the CdTe layers. The RHEED pattern is indicative of the expected CdTe-like step array superimposed on the CdTe-like streaks or hybrid pattern [130]. The streaks of the CdTe layer grown with the flux ratio of 3.45 (Figure 5.8 (a)) are long and bright indicating a smooth surface morphology. By increasing the flux ratio, the RHEED patterns became less bright and some of the streaks became less visible (Figure 5.8 b. and c.).

To study the effect of atomic flux ratio on the crystal quality of the CdTe layers, the defect decorating etching for 30 s with 1HF:4HNO_3:25H_2O was applied. Several SEM images were used for the calculation of the EPD. The EPD of CdTe layers grown with the atomic flux ratios of 3.45, 4.5, and 6 was 4.21×10^7 cm^{-2}, 3.18×10^7 cm^{-2}, and 4.22×10^7 cm^{-2}, respectively. The lowest EPD value was observed for the epilayer grown with the Te/Cd ratio of 4.5. The EPD values of the other layers were similar. The disparity between the RHEED images and the EPD might be related to an imbalance in the density of dislocation cores on the (111)A and (111)B glide planes. The crystal quality of the CdTe layers were investigated with the XRD surface symmetric high-resolution four-crystal (Ge) RC measurements. XRD RC scans of the CdTe(422) reflections were performed from the [0-11] and [-111] azimuths.

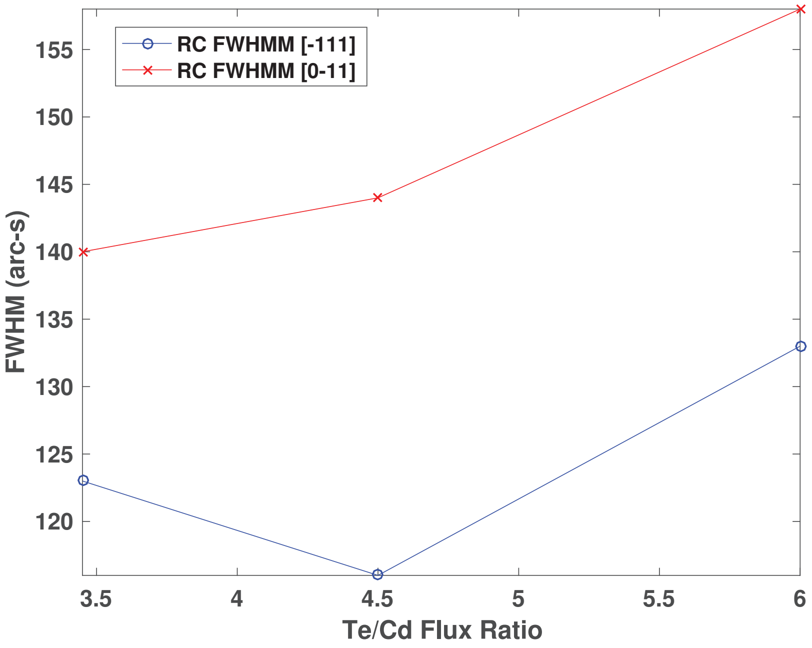

Figure 5.9.: Calculated RC FWHM values of CdTe layers grown with 3.45, 4.5, and 6 atomic flux ratios from the [0-11] and [-111] azimuths as a function of atomic flux.

In Figure 5.9, RC FWHM values of the CdTe layers grown with 3.45, 4.5, and 6 atomic flux ratios from the [0-11] and [-111] azimuths are plotted as a function of atomic flux. The RC of CdTe(422) symmetric reflection from epilayers had symmetric shapes (not shown) indicating a uniformly distributed lattice structure in the direction of surface normal. The CdTe(422) RC of epilayers were fit using a PearsonVII function. The RC FWHM from the [-111] azimuth of epilayers increases with the increasing Te/Cd ratio. On the other hand, the lowest RC FWHM from the [0-11] azimuth was observed from the epilayer grown with the flux ratio of 4.5. The discrepancy between the RC FWHM values indicates an azimuthal dependence of the FWHM broadening which it might be related to the imbalance in the dislocation populations with misfit dislocation vectors.

Extended, deep, and shallow defects can be observed in PL spectra of the semi-

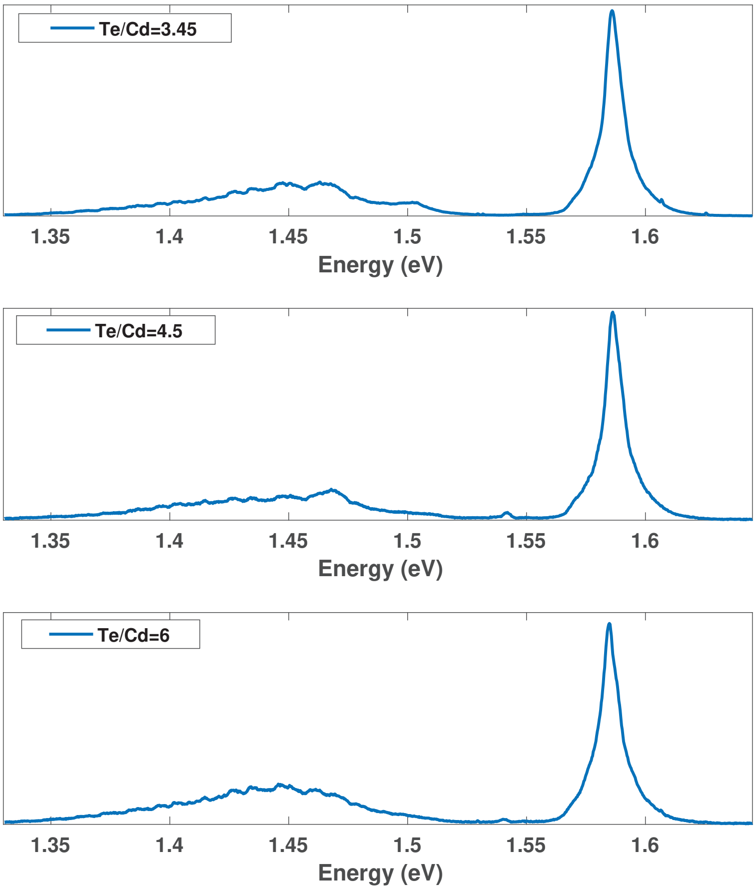

Figure 5.10.: PL spectra of CdTe layers grown with 3.45, 4.5, and 6 atomic flux ratios

conductor crystals. Point defects due to doping or unintentional contamination of the crystals are located near the band gap of the semiconductors such as CdTe [131]. On the other hand, the extended defects related to the structural defects such as Frank loops were detected at deep levels [131]. Around 1.47 eV, a strong emission band with LO-phonon replicas are expected to be observed in PL spectra from the CdTe layers with extended defects such as dislocations. It has been shown that the band at 1.47 eV behaves like a bound exciton trapped in an extended defect. To characterize dislocations in CdTe layers, low temperature micro-PL measurements were taken at a temperature of 80 K with S& I Tri Vista system consists of (Princeton Ins. Acton SP-2750) a monochromator with a 150 grating/mm and a ProEM EMCCD camera. A 488 nm laser was used as excitation source. The penetration depth of the laser was calculated as $\frac{1}{a} = \frac{1}{10.51\mu m} = 95\ nm$ where a is the absorption coefficient of the CdTe layer at 488 nm. This value was derived from the SE measurements. The resolution of the monochromator with 150 grating/mm and camera was ~ 0.8 meV around the band gap of the CdTe at 80 K (~ 782 nm). In Figure 5.10, PL spectra of the CdTe epilayers grown with different atomic flux ratios are shown. PL spectra of CdTe layers grown with the flux ratios of 3.45, 4.5, and 6 exhibit a near gap emission at 1.5859 eV, 1.5862 eV, and 1.5848 eV, respectively. At around 1.47 eV, a second peak and its phonon replicas were detected in the PL spectra due to the extended defects (dislocations). To study the correlation between the intensity of the emission around 1.47 eV (E_Y) and density of the dislocations, the intensity ratio of the emission from the extended defects to near gap emission (E_g) was calculated. The intensity ratio from PL spectra, XRD RC FWHM from [-111] azimuth, and EPD were plotted as function of atomic flux ratio and are shown in Figure 5.11. A good correlation between the RC FWHM and the PL intensity ratio of E_Y/E_g of CdTe epilayers grown with different atomic fluxes was observed. Similary, a correlation between the PL intensity ratio and the

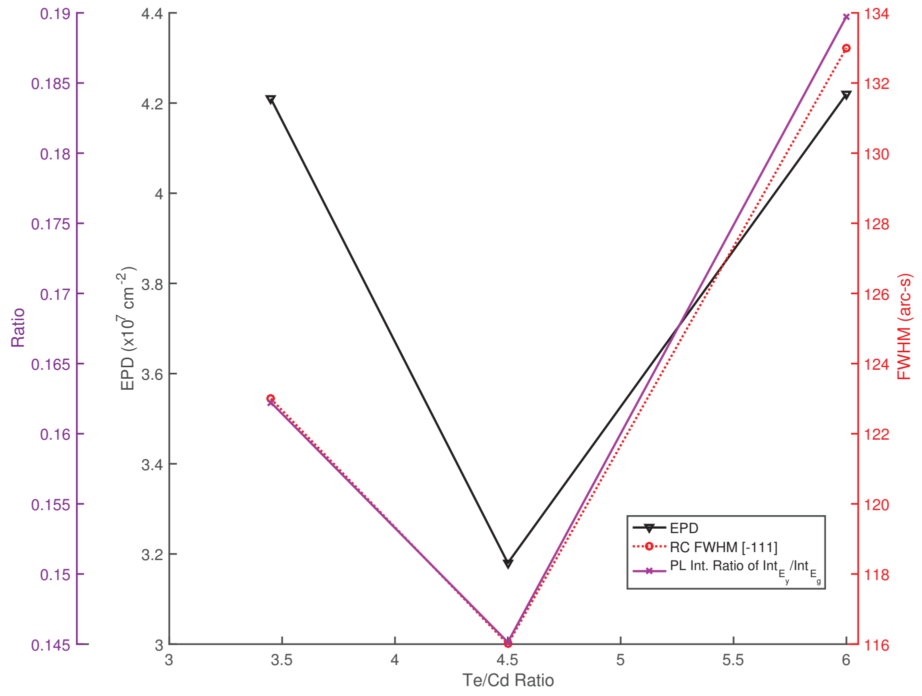

Figure 5.11.: Intensity ratio of the emission from extended defects (E_Y) to near gap emission (E_g) from PL spectra, XRD RC FWHM from [-111] azimuth, and EPD as function of atomic flux ratio.

EPD was observed which indicates that highest contribution to the E_Y emission from the extended defects was due to dislocations.

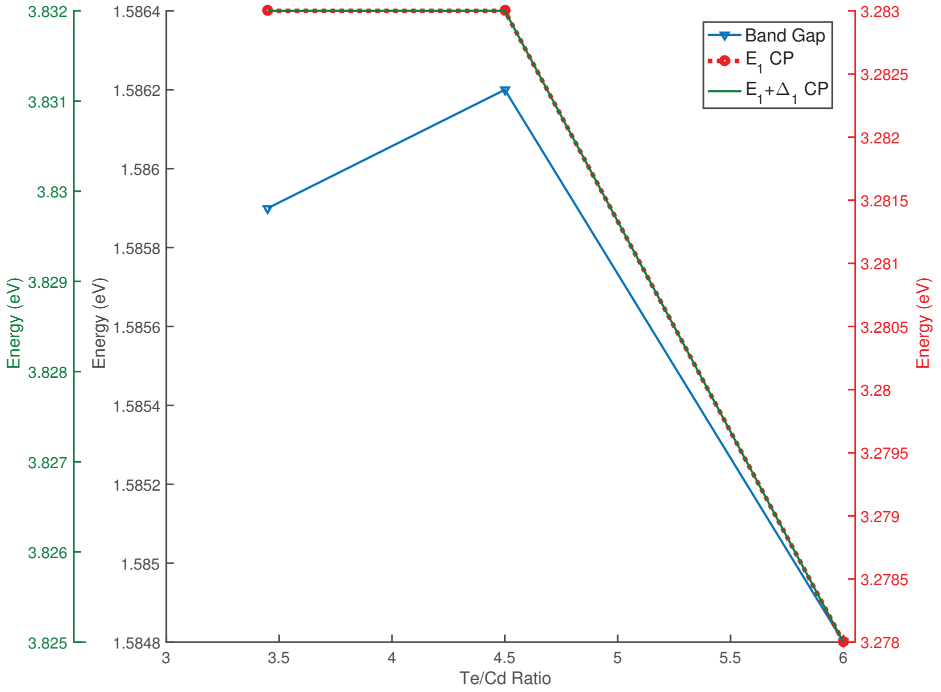

Figure 5.12.: The energies of E_g from PL (80 K), E_1 and $E_1+\Delta_1$ critical points from room temperature SE measurements as a function of Te/Cd flux.

The optical properties of the CdTe layers grown with different Te/Cd flux ratios were further investigated by room temperature SE measurements. The SE measurements were modeled with n-oscillator model with the details given in the Nucleation section. MSE of the fits were 14±0.1. The critical point energies of the E_1 and $E_1+\Delta_1$ were extracted from the model. E_1 and $E_1+\Delta_1$ critical points (CP) originate from the transitions at the L point of the Brillouin zone, which is parallel to [111]. It has been shown that the critical point energies of the dielectric function of the zinc blende crystal structures are blue or red shifted by the compressive or biaxial strain, respectively. [132, 133].

In Figure 5.12, calculated CP energies of the E_1 and $E_1+\Delta_1$ from SE measurements are shown along with the energy of the E_0 CP or E_g (band gap) from PL (80 K) measurement. A change in the flux ratio from 3.45 to 4.5 increases the CP energy of E_g although the change is within the resolution limit of the spectrometer. Similarly, the CP energies of the E_1 and $E_1+\Delta_1$ did not vary as the flux ratio increased from 3.45 to 4.5.

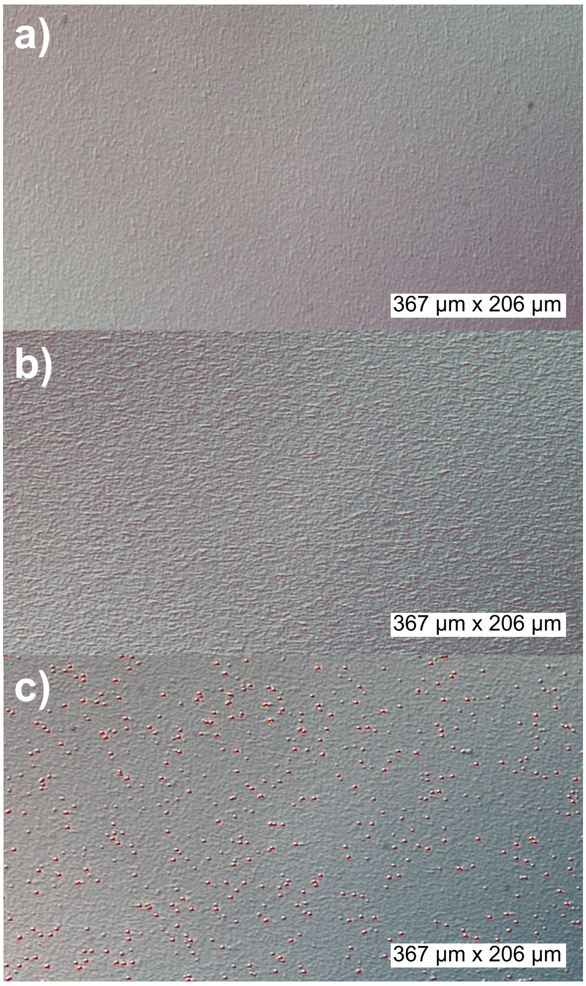

Figure 5.13.: Optical images representing the surface of the CdTe layers grown with the Te/Cd ratios of 3.45, 4.5, and 6 from areas of 367 µm × 206 µm. The optical images was obtained with a Nomarski microscope.

On the other hand, when the flux ratio was further increased to 6, the CP energies of E_0, E_1, and $E_1+\Delta_1$ was red shifted suggesting the occurrence of the biaxial strain in the CdTe layer. The biaxial strain in the CdTe layer might originate from the fact that growth of the CdTe layer with high Te/Cd ratio may introduce additional Te atoms to the epilayer which might create additional stress in the crystal lattice. In summary, the best crystal quality was obtained with the growth of the CdTe epilayer with Te/Cd ratio of 4.5.

The effect of the unstoichometric atomic fluxes of Te and Cd on the surface morphology was investigated by Nomarski microscopy. In Figure 5.13, optical images representing the surfaces of the CdTe layers grown with the Te/Cd ratios of 3.45, 4.5, and 6 from areas of 367 µm × 206 µm are given. The surface of CdTe layer grown with flux ratio of 3.45 has the smoothest surface morphology. The surface quality of the layers seems to degrade with the increasing Te/Cd ratio. Especially, large surface defects spotted in the surface image of the CdTe layer grown with the largest flux ratio might indicate the precipitation of Te atoms on the surface. Further investigation of the surface structure

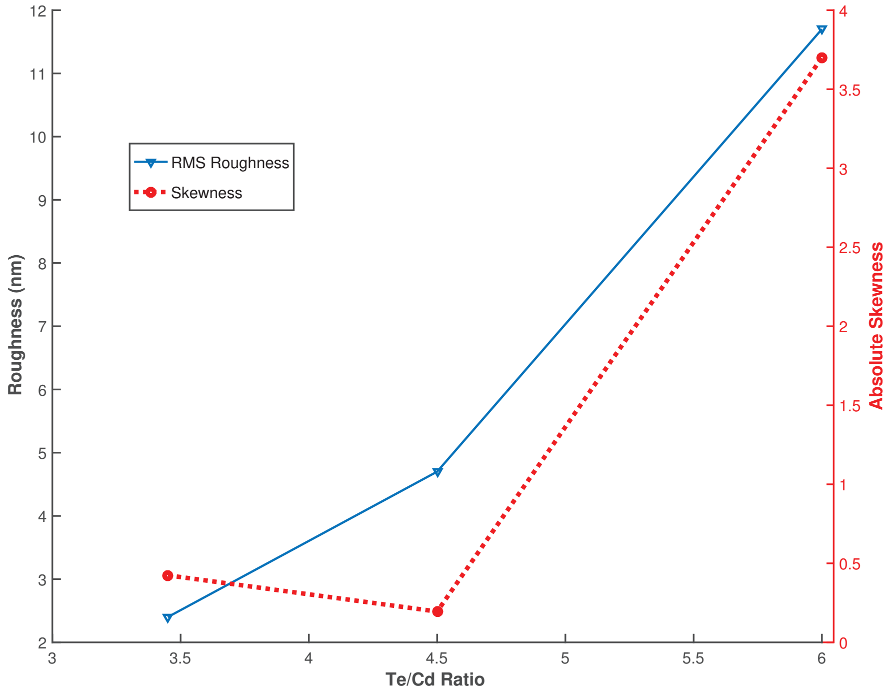

Figure 5.14.: The calculated RMS roughness and the SK of the CdTe epilayers as a functuion Te/Cd flux.

of CdTe epilayers were performed with AFM. The AFM height images from the 10 × 10 µm areas of CdTe layers were recorded and analyzed. RMS roughness and absolute SK values from the statistical analysis of the AFM height images are shown in Figure 5.14 as a function of flux ratio. All of the SK values were negative. To demonstrate the correlation between the surface roughness and SK values, absolute SK was plotted with the RMS roughness values. Surface of the CdTe layer grown with Te/Cd ratio of 3.45 has the lowest surface roughness which is in agreement with the Nomarski microscopy results. Surface roughness of CdTe epilayers increases (by order of 2) with the increasing atomic flux from 3.45 to 4.5. The surface of the CdTe epilayer grown with Te/Cd ratio of 6 was extremely rough (~ 12 nm roughness) and had a very large SK value of -3.7 indicating that the bright spots on the Nomarski image of the same sample were pits. The

SK values from the CdTe layers grown with the flux ratios of 3.45 and 4.5 are similar and very close to zero which indicates a smooth surface morphology. In summary, the best surface morphology was obtained with the growth of the CdTe epilayer with the Te/Cd flux ratio of 3.45.

5.3. Growth Temperature

The longest step during the production of the CdTe epilayers is the growth of the epilayer at a constant temperature following the initial nucleation process or following an anneal. In order to obtain a highly crystalline epilayer, the growth of the epilayers has to be performed at equilibrium conditions. The growth temperature and atomic fluxes have the highest impact on the crystal quality of the epilayer. The optimum growth temperature window to produce highly crystalline CdTe layer is larger than that of HgCdTe. On the other hand, the surface morphology of the CdTe layer is susceptible to growth temperature [134]. Therefore, the temperature during constant temperature growth step has to be optimized to obtain a highly crystalline CdTe epilayer with good surface morphology.

To study the effect of the growth temperature to the crystal and the surface morphology, three CdTe layers were grown at 275 °C, 285 °C, and 295 °C. Thermal deoxidation and CdTe growth were performed in Veeco GEN20MZ MBE system using 3-inch GaAs(211)B epiready substrates. Thermal deoxidation was carried out with Veeco Mark V 500 As (7 N) valved cracker and dual filament In effusion cell whereas CdTe growth was performed with Veeco Mark V 200 CdTe (7 N) and Te (7 N) valved crackers.Thermal deoxidation and growth was monitored *in situ* through RHEED, which yielded data pertaining to surface crystal quality. In addition, calibrated band-edge detection system was used for temperature measurement. GaAs(211)B substrates were deoxidized at 535 °C for 240 s under In flux of 1.1×10^{-8} Torr BEP. In desorption process was performed at 553 °C for 180 s. Next, GaAs substrates were cooled under As_4 of 4.24×10^{-6} Torr BEP flux to ensure B polarity of the GaAs substrate. Growth of the CdTe epilayers was initiated at a surface temperature of 216±2 °C. To investigate the effect of the growth temperature on the CdTe crystal quality, three CdTe layers were grown at the temperatures of 275 °C, 285 °C , and 295 °C with the Te/Cd ratio of 3.45. The constant temperature growth was interrupted every 80 minutes to perform annealing for the epilayers under the Te flux of 8.5×10^{-7} Torr BEP at a temperature of 403±1.5 °C. Following last anneal cycle, the epilayers were cooled down to 240 °C under protective Te flux. In Figure 5.15, the tem-

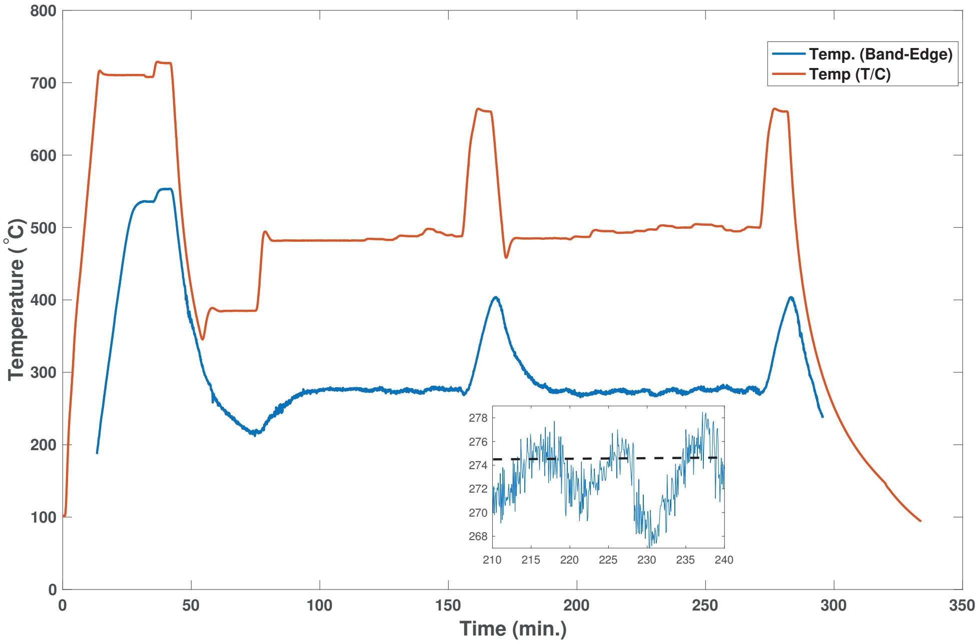

Figure 5.15.: Temperature profile of the growth process of the CdTe layer grown at 275 °C. Temperature measurements with band-edge detection and T/C system. Inset: Temperature oscillations during growth of epilayer and the average temperatures shown with a dashed black line.

perature profile of the CdTe layer grown at 275 °C is shown. In this figure, the temperature measurements with the band-edge detection (blue line) and T/C (red line) are shown. The substrate heater was controlled by a power supply and a PID (proportional integral derivative) controller. As can be seen from this figure, there is a non-monotonic off-set between the T/C and band-edge readings. The surface temperature the from band-edge system lags behind the T/C reading. Therefore, surface temperature was controlled indirectly by T/C readings and with the help of the temperature predictions from the past growth runs. Oscillations in temperature readings from the band-edge measurements were detected after the thickness of the CdTe layers has reached to ~ 1 µm. The oscillations were due to the development of constructive and destructive interference fringes from the epilayer and the substrate [135]. The oscillations in band-edge measurements introduce an uncertainty in temperature readings which may become as large as 8 °C [135]. By eliminating the effect of the oscillations, the real surface temperature can be determined. It was shown that the real temperature was not a mean value of the oscillation [135]. Instead, it was closer to the maximum value of the oscillation. By employing the same method, the surface temperature during the growth of the constant temperature phases were determined (inset of Figure 5.15). CdTe layers were grown with the rate of ~ 1 μm/h. To ensure homogeneous distributions of the Cd and Te atoms on the surface, the samples were rotated at 8 RPM. Thickness of the layers were determined by SE and FTIR transmission measurements, and was found to be 2.8±0.1μm.

Figure 5.16 shows color-mapped RHEED patterns of CdTe epilayers grown at different temperatures. The patterns were obtained during the constant temperature growth processes at 275 °C, 285 °C, 295 °C. Additionally, to investigate the streaks from the RHEED patterns, the pixel intensity of the original gray-scale RHEED patterns were extracted and plotted as a 3D surface map and are shown in Figure 5.16 for the layers grown at 275 °C, 285 °C, 295 °C. Te-stabilized smooth surface morphology was observed for all of the RHEED patterns. The longest streaks were detected from the 3D surface map of the RHEED pattern of the CdTe layer grown at 275 °C (Figure 5.16 (b)). The streaks from the RHEED pattern of CdTe layer grown at 285 °C and 295 °C were shorter but brighter (Figure 5.16 (d) and (f)) indicating a higher surface roughness compared to the one grown at 275 °C. The analysis of the RHEED patterns show that the smoothest surface was obtained for the growth at 275 °C.

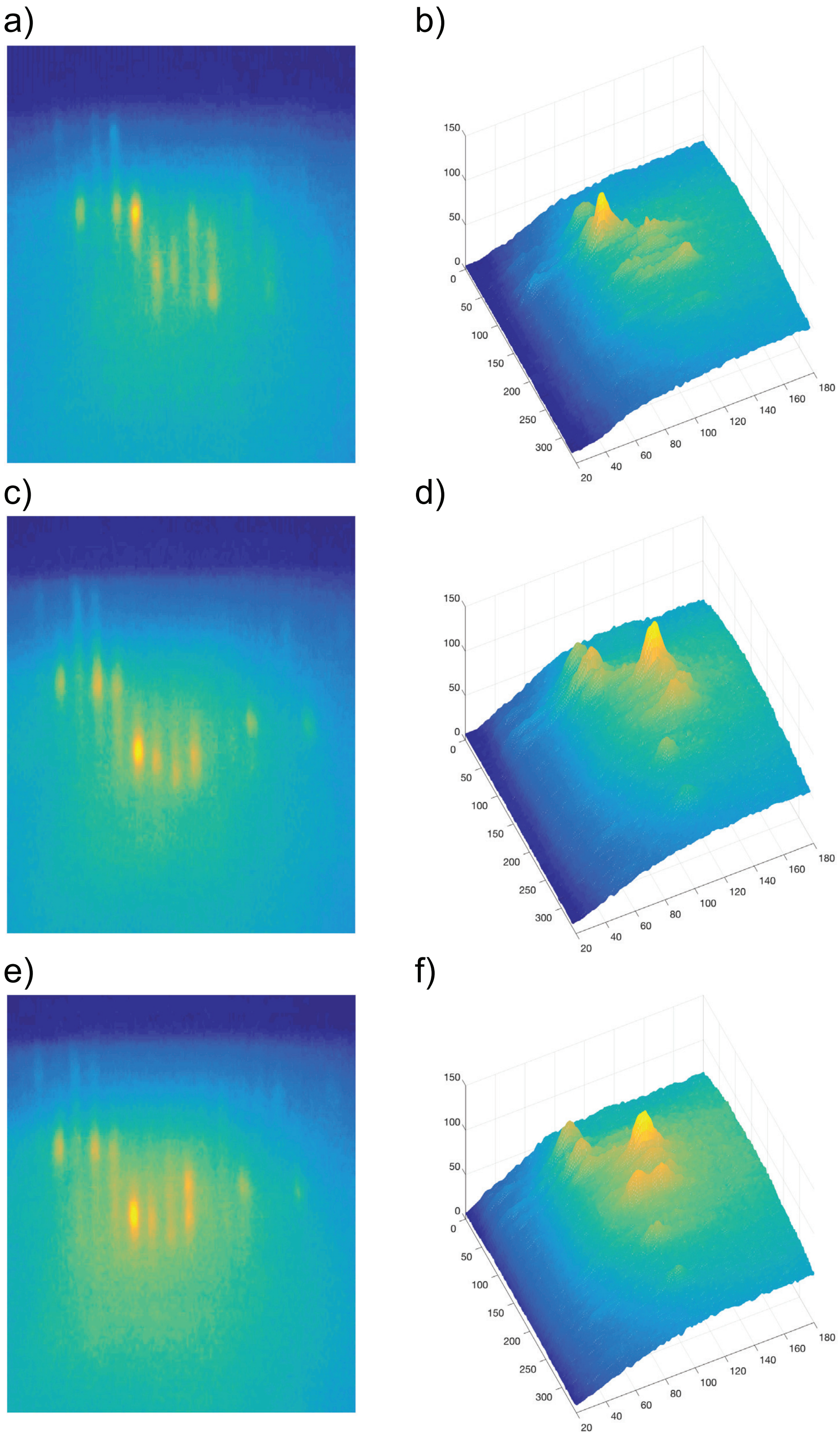

Figure 5.16.: Color-mapped RHEED patterns of the CdTe layers grown at (a) 275 °C, (c) 285 °C, (e) 295 °C. 3D surface maps of the RHEED images of the CdTe layers grown at (b) 275 °C, (d) 285 °C, (f) 295 °C.

The change in optical properties of the CdTe layers during constant temperature growth was monitored with *in situ* SE measurements. The experimental data was fitted with a model consisting of a layer and a substrate. The dielectric function of the CdTe epilayers were modeled using a multi-oscillator model with a MSE of 14 which had PSemi-Tri and harmonic oscillators [73]. The GaAs substrate was modeled with a pre-defined temperature library (details given in Chapter 4). The energies of E_0 and E_1 CP were calculated with the oscillator model. In Figure 5.17, the energies of E_0 and E_1 CP are plotted with the temperature measurements from band-edge detection system during constant temperature growth stage. Following the initiation of constant temperature growth, temperature was decreased by ~ 4 °C. A reduction in the energies of the E_0 and E_1 was observed as response to temperature decline. The detection of E_0 was difficult during the growth due to the occurrence of the interference fringes in the SE spectra. However, the E_1 was directly affected by the changes in temperature and remained constant when the temperature was constant. Additionally, the temperature and the energy of E_1 was inversely proportional.

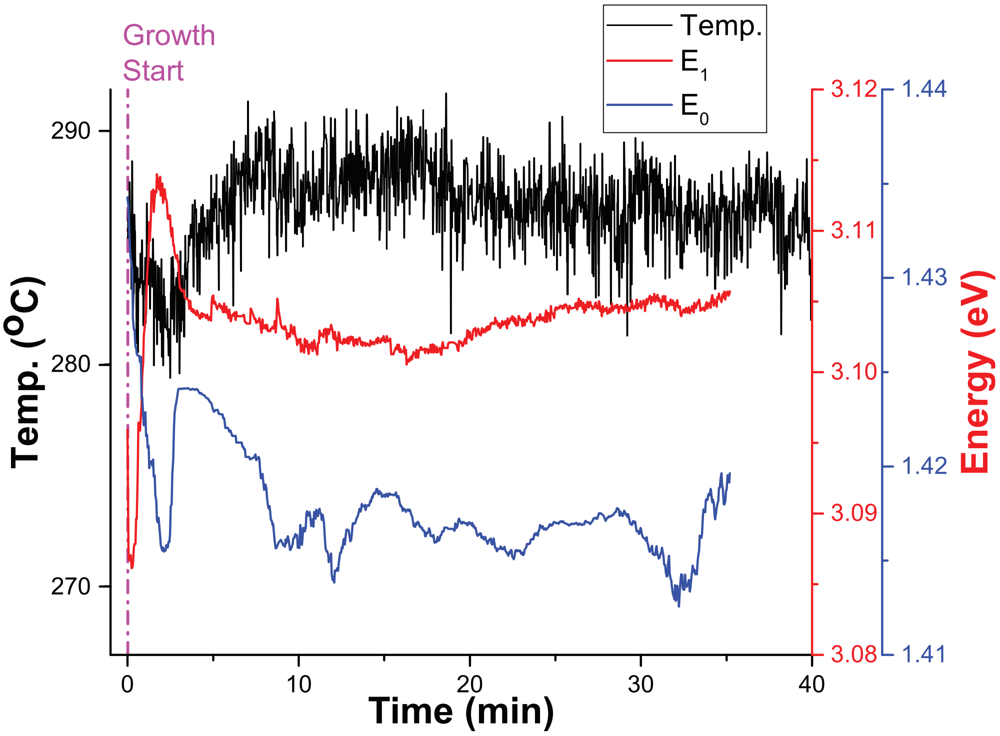

Figure 5.17.: Energies of the E_0 and E_1 CP from SE measurements and temperature measurements from band-edge detection system as a function of time.

In Figure 5.18, the relationship between the surface temperature and inverse of the energy of the E_1 CP is presented. The inverse of the E_1 energy is well correlated with the surface temperature. The change in temperature causes the expansion or shrinkage of the lattice of the CdTe layer. The shrinkage of the lattice causes a blue shift while the expansion of the lattice results in a red shift in the energy of E_1 CP. These results are in agreement with the results of the nucleation section where a red shift was observed in the presence of biaxial stress. The results suggest that the inverse of the CP energy of E_1 can be used to determine the surface temperature of the epilayers. Additionally, the results of the *in situ* SE measurements indicates that the growth was performed at equilibrium conditions.

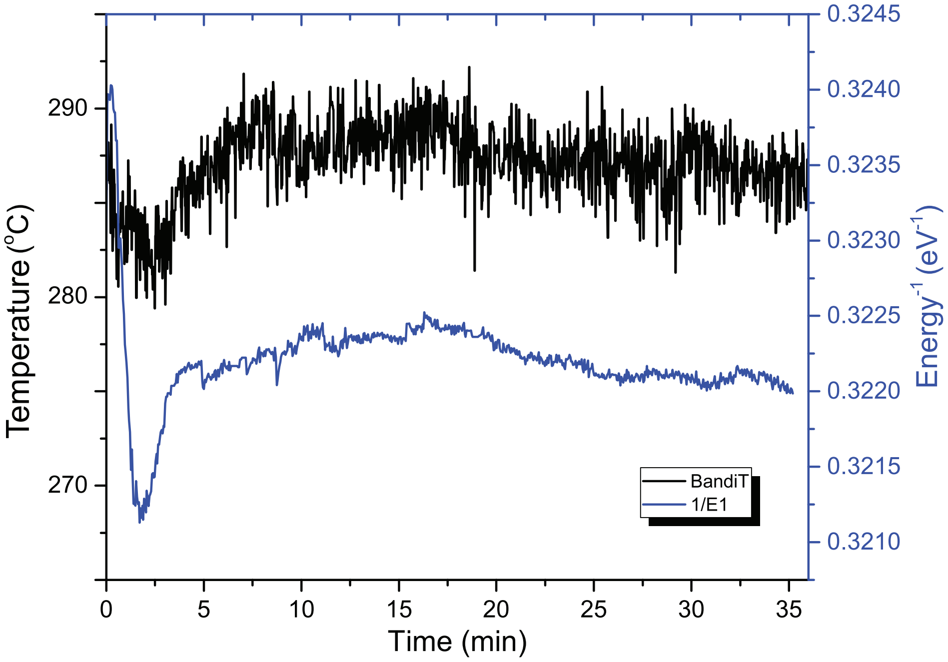

Figure 5.18.: Surface temperature with the inverse of the E_1 CP energy as a function of time.

To investigate the effect of the growth temperature to the crystal quality of the CdTe layers, defect decorating etching for 30 s with ($1HF:4HNO_3:25H_2O$) ratios was applied. Several SEM images were used to calculation of the EPD. The EPD of CdTe layers grown at temperatures of 275 °C, 285 °C , and 295 °C was 4.18×10^7 cm^{-2}, 6.25×10^7 cm^{-2}, and 5.65×10^7 cm^{-2}, respectively. A direct relation between the EPD of the layers and the growth temperature was not detected. CdTe layer with the lowest EPD was obtained from the epilayer grown at the temperature of 275 °C. The RHEED and EPD measurements of the layer grown at 275 °C suggest that a smooth surface morphology during growth results in an epilayer with high crystal quality.

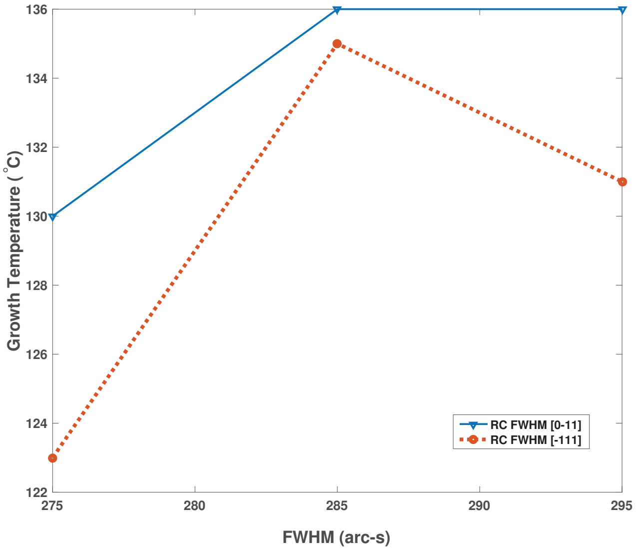

Figure 5.19.: Calculated RC FWHM values of CdTe layers grown at 275 °C, 285 °C , and 295 °C from the [0-11] and [-111] azimuths as a function of growth temperature.

In Figure 5.19, RC FWHM values of CdTe layers grown at different temperatures from the [0-11] and [-111] azimuths are plotted as a function of growth temperature. The RC of CdTe(422) symmetric reflection from epilayers had symmetric shapes (not shown) indicating a uniformly distributed lattice structure in the direction of surface normal. The CdTe(422) RC of epilayers were fit using a PearsonVII function. The layer with the lowest RC FWHM from both azimuths was that of grown at 275 °C which is in agreement with the results of the defect decorative etching. An increment in the RC FWHM of the CdTe layers was observed when the epilayers grown at higher temperatures suggesting a reduction in crystal quality. However, increase in RC FWHM was not symmetric from the measurements of both azimuths when the layer was grown at 295 °C. The inconsistency in RC FWHM values indicates an imbalance in the density of dislocation cores on the (111)A and (111)B glide planes. The correlation between the RC FWHM and EPD results can be seen from Figure 5.20. It can be seen from this figure that the methods of HRXRD RC scans and defect decorative etching probes the dislocations which have same structure (i.e. line vector).

To characterize dislocations in CdTe layers, low temperature micro-PL measurements were taken at temperature of 80 K with S& I Tri Vista system (Princeton Ins. Acton

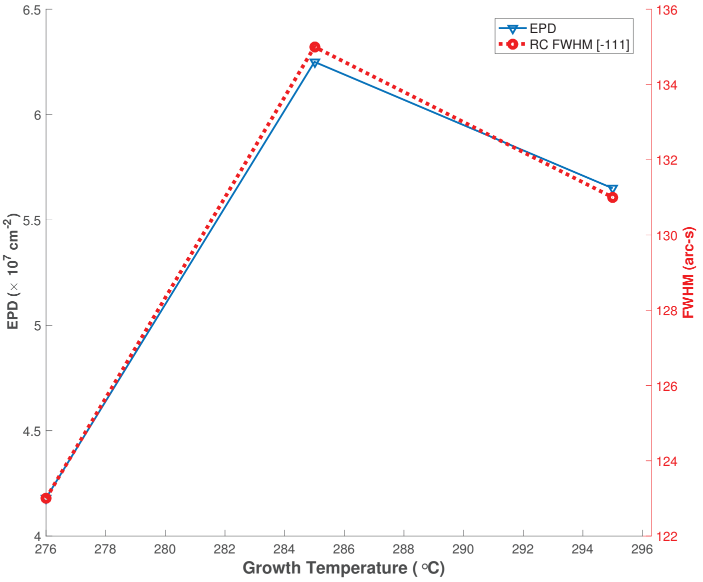

Figure 5.20.: Calculated RC FWHM values of CdTe layers grown at 275 °C, 285 °C , and 295 °C from the [-111] azimuth and EPD values as a function of atomic flux.

SP-2750) and a monochromator and a 150 grating/mm and a ProEM EMCCD camera. A 488 nm laser was used as excitation source. The penetration depth of the laser was 95 nm. The resolution of the monochromator with 150 grating/mm and camera was ~ 0.8 meV around the band gap of the CdTe at 80 K (~ 782 nm). In Figure 5.21, PL spectra of the CdTe epilayers grown at different temperatures are shown. Near gap emission from the PL spectra of CdTe layers grown at the temperatures of 275 °C, 285 °C , and 295 °C are detected at 1.5859 eV, 1.5868 eV, and 1.5859 eV, respectively.

The optical properties of the CdTe layers grown at different temperatures were further investigated by room temperature SE measurements. The SE measurements were modeled with n-oscillator model with the details given in the Nucleation section. MSE of the fits were 13.5±0.1. The critical point energies of the E_1 and $E_1+\Delta_1$ were extracted from the model. The energies of the E_1 and $E_1+\Delta_1$ CP was same for all the CdTe layers with the values of 3.28 eV and 3.829 eV, respectively. Therefore, a shift in the energies of the critical points due to the growth temperature related effects was not detected.

To investigate the possible imbalance in the density of dislocation cores on the (111)A and (111)B glide planes, the dislocation structure of the CdTe crystal structure with (211) surface orientation was studied. Two different dislocation type are possible with the cores of Cd and Te for the CdTe zinc blende crystal, as mentioned in Chapter

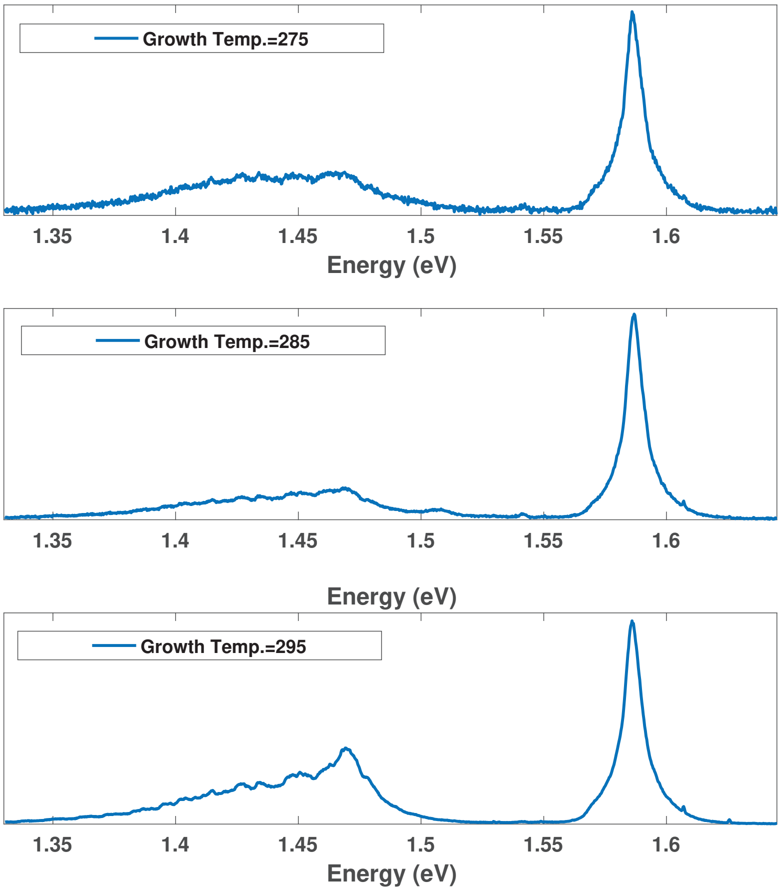

Figure 5.21.: PL spectra of CdTe layers grown at the temperatures of 275 °C, 285 °C , and 295 °C.

2. The detection of the imbalance in the dislocation populations on the two types of slip systems in a zinc blende crystal was studied for the (001) surface recently [136]. To determine the density of dislocation with the different cores, the slip systems of the zinc blende crystal with (211) surface has to be determined. During the hetereoepitaxy of the CdTe on GaAs(211)B substrate, epilayer is dominated by the strain parallel to the (211) growth plane. Depending on the angle between the strain axis and slip planes, several different slip systems can be activated. The activation of the slip system are determined with the calculation of the Schmid factor. Schmid factors of the zinc blende crystal with (211) surface orientation with the <110> Burgers vectors are calculated for the stress applied in [0-11] and [-111] directions and given in Table 5.1 and Table 5.2, respectively. The highest Schmid factor is obtained when the stress is applied in [0-11] which is 0.40825.

Table 5.1.: Active Slip Systems in Zinc-Blende Crystals with (211) surface orientation under stress applied in [0-11] direction

Slip System	MD Line Vector	Glide Plane	Burgers Vector	Schmid Factor
S_1	[01-1]	(-1-11)	$\frac{a}{2}$[101]	0.40825
S_2	[01-1]	(1-11)	$\frac{a}{2}$[10-1]	0.40825
S_3	[10-1]	(-1-11)	$\frac{a}{2}$[1-10]	0.40825
S_4	[10-1]	(1-11)	$\frac{a}{2}$[110]	0.40825

On the other hand, when stress was applied in [-111] direction, the highest Schmid factor is calculated as 0.27217. Therefore, glide motion of the dislocations in the active slip planes under the stress applied in [0-11] is considered.

The active slip systems given in Table 5.1 can be further grouped based on the orientation of the line vectors for their misfit dislocations (MD). Slip systems with the MD line vectors of the type [01-1] are considered as type A whereas those with their MD line vectors along the [10-1] are considered as type B. Furthermore, if symmetric RC is measured at a Bragg angle θ_B lower than that $\tan^2\theta_B < 5$ (~ 0.5 for the RC of CdTe(422) plane with Cu Kα_1 radiation) and dislocation density is greater than ~ 10^6 then the highest contribution to the broadening of the RC is from the angular mosaic spread introduced by dislocations [119]. The XRD RC or reciprocal space map measurements at different azimuths can detect an imbalance in the dislocation populations on the two types of slip systems. To probe the RC broadening, the RSM of the (333) and (422) reflections from [-111] azimuth and (404) and (422) reflections from [01-1] azimuth of a CdTe layer were measured. For XRD RSM measurements, a CdTe layer was grown. The growth procedure of the CdTe layer initiated by GaAs(211)B deoxidation at 527 °C for 240 s under In flux of 4.4×10^{-8} Torr BEP. In desorption process was performed at 550 °C for 240 s. Next, GaAs substrate was cooled under As_4 of 4.24×10^{-6} Torr BEP flux to ensure B polarity of the GaAs substrate. Growth of the CdTe epilayer was initiated at a surface temperature of 208 °C. The CdTe layer was grown at the temperatures of 297 °C with the Te/Cd ratio of 1. The constant temperature growth was interrupted every 40 minutes to perform annealing of the epilayers under Te flux of 3.5×10^{-7} Torr BEP and at a temperature of 404 °C. Following last anneal cycle, the epilayer was cooled down to 240 °C under protective Te

Table 5.2.: Active Slip Systems in Zinc-Blende Crystals with (211) surface orientation under stress applied in [-111] direction

Slip System	MD Line Vector	Glide Plane	Burgers Vector	Schmid Factor
S_5	[01-1]	(111)	$\frac{a}{2}$[10-1]	0.27217
S_6	[01-1]	(111)	$\frac{a}{2}$[1-10]	0.27217
S_2	[01-1]	(1-11)	$\frac{a}{2}$[10-1]	0.27217
S_7	[10-1]	(-1-11)	$\frac{a}{2}$[011]	0.27217
S_3	[10-1]	(-1-11)	$\frac{a}{2}$[1-10]	0.27217
S_8	[10-1]	(1-11)	$\frac{a}{2}$[011]	0.27217

flux.

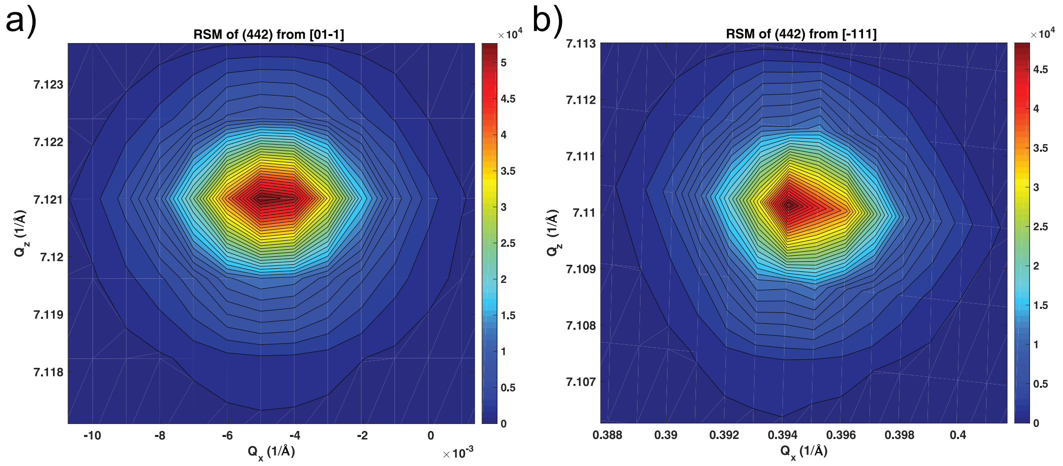

Figure 5.22.: RSM of (422) reflections from (a) [01-1] azimuth and (b) [-111] azimuth.

In Figure 5.22, the RSM of (422) reflections from [01-1] azimuth and [-111] azimuth of the CdTe layers are shown. The RSM of surface of the (422) reflections exhibit a lateral broadening indicating a mosaic spreading in the epilayer with a negligible vertical broadening. The RSM of the (422) from [-111] azimuth (Figure 5.22 b.) is tilted with an angle of 3.177° towards [-111] direction.

Any region in CdTe epilayers that is tilted (microscopically) with respect to the average will introduce a broadening to the reflections in RSM. Scattering from planes

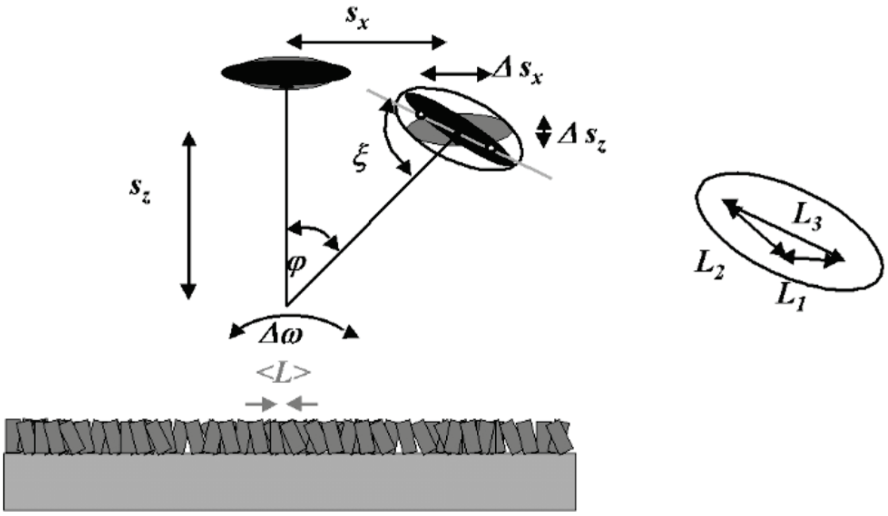

Figure 5.23.: Lateral correlation length and mosaic spreading (microscopic tilt) that rises the shape of the scattering in the RSM [68]. s_z and s_x are the reciprocal coordinates.

approximately parallel to the surface will have overlapping contributions from lateral correlation lengths and the distribution of tilts (microscopic tilts). Contributions from those planes inclined to the surface will be also inclined to each other and will rotate the the ellipsoid in the RSM. In Figure 5.23, symmetric and asymmetric RSM of an epilayer are shown. The shape of the epilayer is a dot in the ideal position of the reflection in the reciprocal space (center of the dashed lines in Figure 5.23). The effect of the mosaic broadening of the scattering from the surface planes in the asymmetric RSM is observed as tilting of the point and broadening in FWHM. The contribution from the lateral correlation length to the spreading, L_1 is parallel to the surface plane. The microscopic tilt contribution to the spreading, L_2 is normal to the radial direction. The FWHM of the ellipse is given by δs_x and δs_z. By using the trigonometric relations, the lateral correlation length can be given as [68];

$$-\frac{\sin(\psi)}{\sqrt{(\delta s_x)^2+(\delta s_z)^2}\cos(\psi+\zeta)} \tag{5.2}$$

and the microscopic tilt or mosaic spreading [68]:

$$\frac{\sqrt{(\delta s_x)^2 + (\delta s_z)^2}\cos(\zeta)}{\sqrt{s_x^2 + s_z^2}\sin(\psi)} \tag{5.3}$$

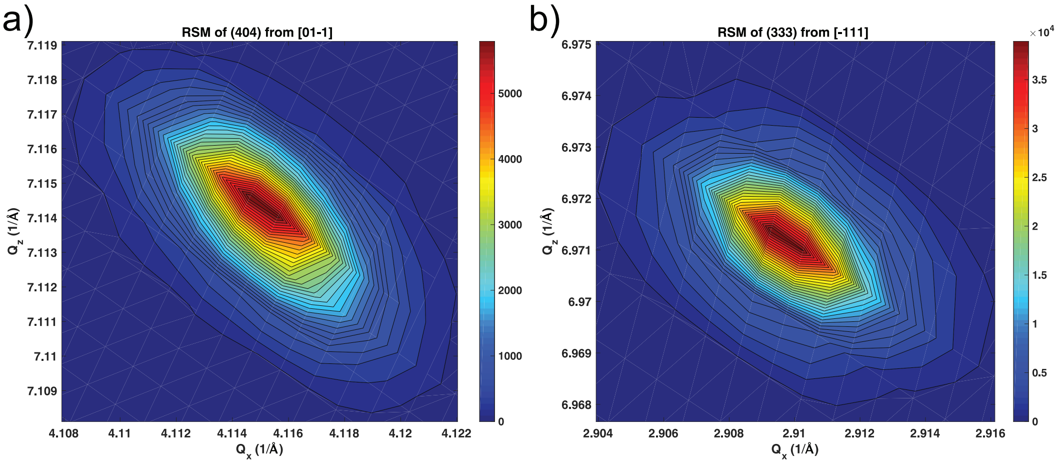

Figure 5.24.: RSM of (422) reflections from (a) [01-1] azimuth and (b) [-111] azimuth.

To calculate the mosaic spreading angle and the lateral correlation length in the CdTe layer, RSM of antisymmetric (333) and (404) reflections were measured from the [-111] and [01-1] azimuths, respectively (Figure 5.24). The RSM of the (333) from [-111] azimuth (Figure 5.24 b.) is tilted with an angle of 3.185° confirming the tilted epitaxial growth of CdTe in the [-111] direction. The lateral correlation lengths from the RSM of (333) and (404) was calculated as 1.712 µm and 1.702 µm, respectively. The mosaic spreading from the RSM of (333) and (404) were calculated as 0.054° and 0.029°, respectively. Therefore, the highest contribution to the broadening of the RC was from the angular mosaic spread introduced by dislocations.

When the incident x-ray spot is aligned with the axis of azimuthal rotation, a variation of the RC FWHM with azimuth indicates an imbalance in the dislocation populations on the different type of defects. Therefore, the individual dislocation populations of defects of type A and type B can be estimated from the RC FWHM dependence on the azimuth ψ. There are four directions parallel to the normal of the (211) surface which are [-111], [0-11], [1-1-1], and [01-1]. Considering the [0-11] direction as zero azimuth ($\psi = 0$), the $\psi = 90$ azimuth becomes parallel to the [1-1-1]. The dislocations with the cores of A and B will broaden the RC when the azimuth of the XRD RC measurement is such that the projection of the incident beam is normal to the MD line vector [136]. The mean misorientation of crystal blocks about an axis in the plane of the interface and perpendicular to the incident x-ray beam associated with dislocations on type B is $2b\sqrt{D_B}\sin(\psi - \psi_B)\cos(\gamma_B)$, where D_B is the density of the dislocations of type B, and γ_B are the angles between the Burgers vectors and diffraction vectors for dislocation on type B. XRD RC width β_B associated with dislocations on the type B slip system with a Gauissian distribution will be;

$$\beta_B^2 = 8\pi D_B \ln(2) b^2 \sin^2(\psi - \psi_B)\cos^2(\gamma_B) \tag{5.4}$$

where b is the Burgers vector. The highest value of β_B^2 could be obtained when the incident beam is aligned to the [0-11] or [01-1] direction since the angle between these directions and MD line vector of dislocation type B ([10-1]) is 90°. Therefore $\psi_B = 90°$. Similarly, for dislocations on type A slip systems,

$$\beta_A^2 = 8\pi D_A \ln(2) b^2 \sin^2(\psi - \psi_A)\cos^2(\gamma_A) \tag{5.5}$$

where $\psi_A = 0°$. The angle (γ_A) between the diffraction vector of (422) and Burgers vectors of type A dislocations [101] and [10-1] which is calculated as 120° and 60°, respectively. Similarly, the angle (γ_B) between the diffraction vector of (422) and Burgers vectors of type B dislocations [1-10] and [110] is determined as 60°. The values of the $\cos^2(\gamma_A)$ and $\cos^2(\gamma_B)$ are same and equal to 0.25. The magnitude of the Burgers vectors of both types of the defect system can be calculated as $\frac{1}{2}[110] = 0.458$ nm.

Finally, the azimuthal dependence of the RC FWHM β is given as,

$$\beta^2 = 8\pi \ln(2)\, b^2\, 0.25 \left[\sin^2(\Psi) D_A + (0.289\ \cos^2(\Psi) + 0.577) D_B\right] \tag{5.6}$$

To investigate the azimuthal dependence of the RC FWHM of CdTe layers, symmetric 422 RC were measured from [0-11] to [01-1] azimuths with the steps of 15°. In Figure 5.25, peak position of the RC and the rocking angle perpendicular to the incident beam ψ is shown as a function azimuthal angle which was obtained from the CdTe layer grown at 295 °C. At zero azimuthal angle, the tilt is zero in the direction of the measure-

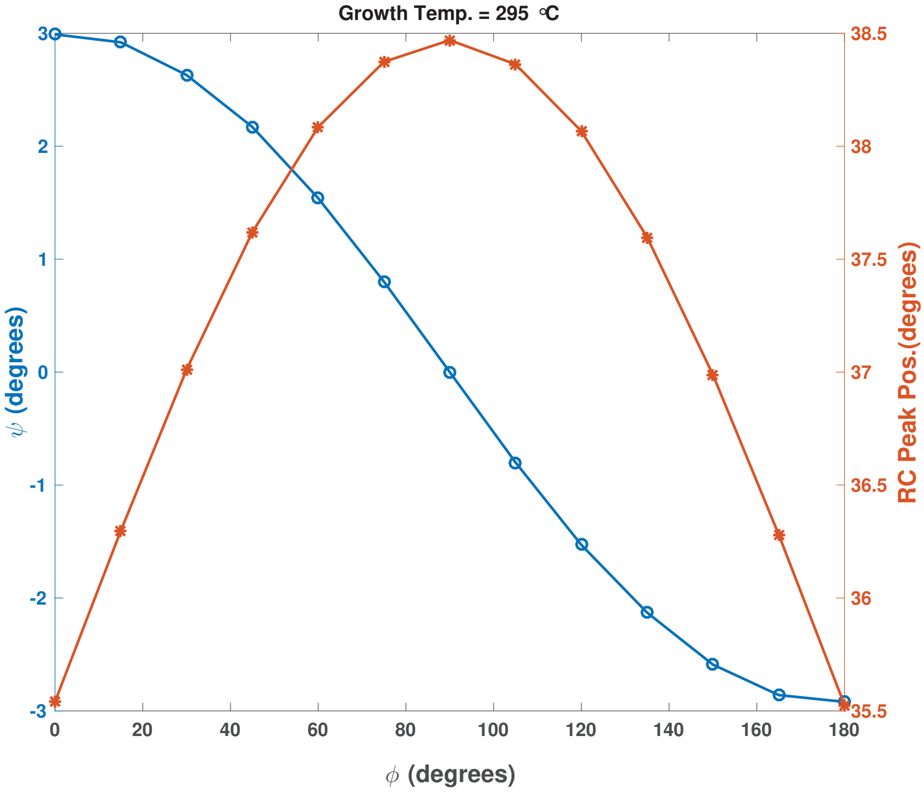

Figure 5.25.: Peak position of the RC and the rocking angle perpendicular to the incident beam ψ as a function azimuthal angle from the CdTe layer grown at 295 °C.

ment while it is ~ 3° in the direction of [-111]. When azimuthal angle increases, RC peak position increases and ψ decreases. The period of the change in RC was half of the period of the change in ψ angle. For a specific ϕ azimuthal angle RC peak position + ψ is ~ 3° confirming the tilted epitaxy of CdTe on GaAs(211)B [53].

The square of the RC FWHM from CdTe layer grown at 295 °C was plotted as a function of the azimuthal angle and is shown in Figure 5.26. The filled circles show the experimental data and the curve shows the fit to Equation 5.6 with an adjusted R^2 value of 0.9. At each azimuth, the alignment for the CdTe(422) peak was repeated prior to the RC measurement. By measuring the RC FWHM for CdTe(422) reflection at different azimuths, the azimuthal dependence of the square of the FWHM (β^2) due to the dislocations with different origins was verified. The individual dislocation densities on the two types

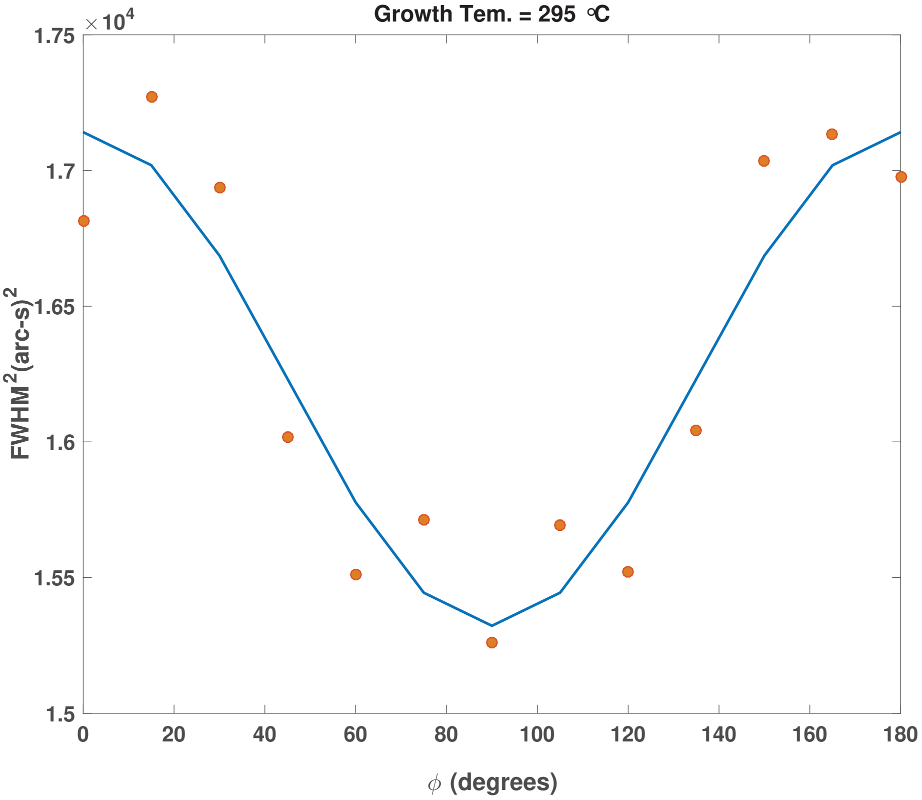

Figure 5.26.: Square of the RC FWHM as a function azimuthal angle from the CdTe layer grown at 295 °C.

of slip systems can be approximately given as;

$$D_B = \frac{\beta^2_{[0-11]}}{8\pi \ln(2)(0.458\times 10^{-7})^2(0.25)(0.886)}\, cm^{-2} \tag{5.7}$$

$$D_A = \left[\frac{\beta^2_{[-111]}}{8\pi \ln(2)(0.458\times 10^{-7})^2(0.25)} - 0.577\, D_A\right] cm^{-2} \tag{5.8}$$

The density of the dislocations of type A and type B was calculated by using Equations 5.6, 5.7, and 5.8. In Figure 5.27, the EPD, the total dislocation density, and the dislocation densities of type A and type B defects are given as function of the growth temperature. The dependency of EPD and the density of the type A dislocations on the growth temperature was similar while it was not similar for that of type B. The difference between the dislocation density from the azimuthal RC scans and the EPD might be related to the various factors. The calculation of the β parameter was carried out un-

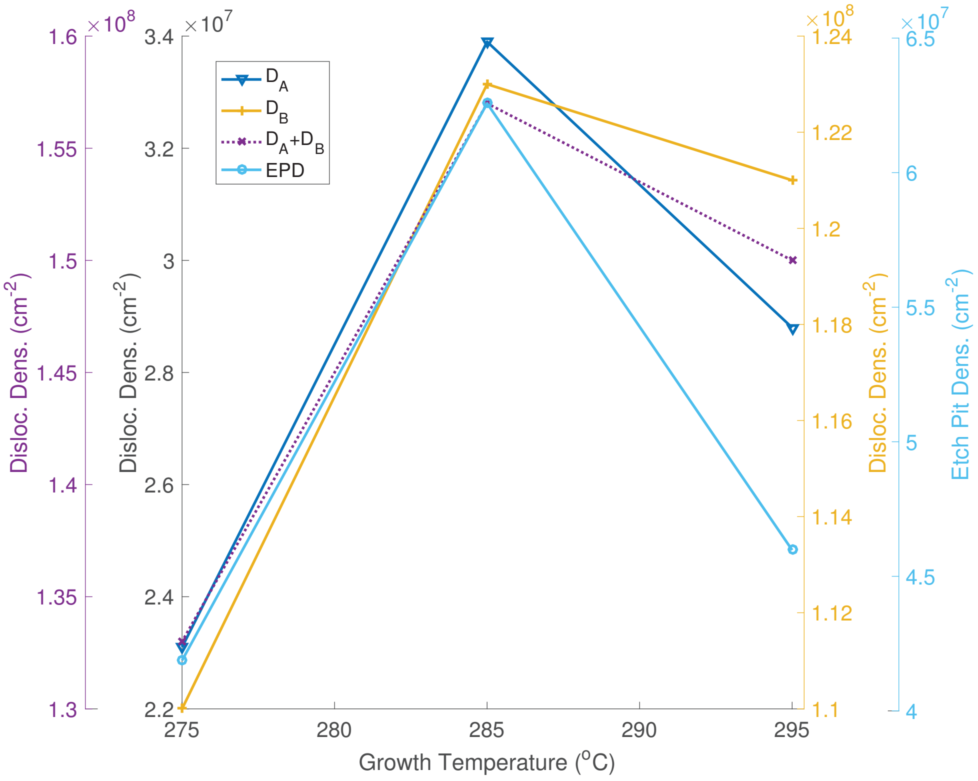

Figure 5.27.: EPD, the total dislocation density, and the dislocation densities of type A and type B defects as function of the growth temperature.

der the assumption that the RC of CdTe(422) was Gaussian while it has been fit with a Lorentzian type distribution (PearsonVII). The FWHM broadening can not be calculated by using Lorentzian distribution since second moment of the Lorentzian diverges. Therefore, using an approximate distribution to the Lorentzian fit introduced an error in the calculation of β^2.

To investigate the origin of the inconsistency between the dislocation density of the defect type B and EPD, the intensity ratio of the E_Y to E_g was calculated from PL (80 K) measurements of the CdTe layers grown at different temperatures. In Figure 5.28, difference between the dislocation density of type A and type B defects and the intensity ratio of the E_Y to E_g is shown as a function of the growth temperature. A correlation can be observed between the intensity ratio from PL measurements and the difference of the density of the dislocations for the CdTe layers grown at 285 °C and higher temperatures. Despite the difference between the results of the two measurements for the epilayer grown at 275 °C, a similar pattern for both measurements was observed. An increase in the

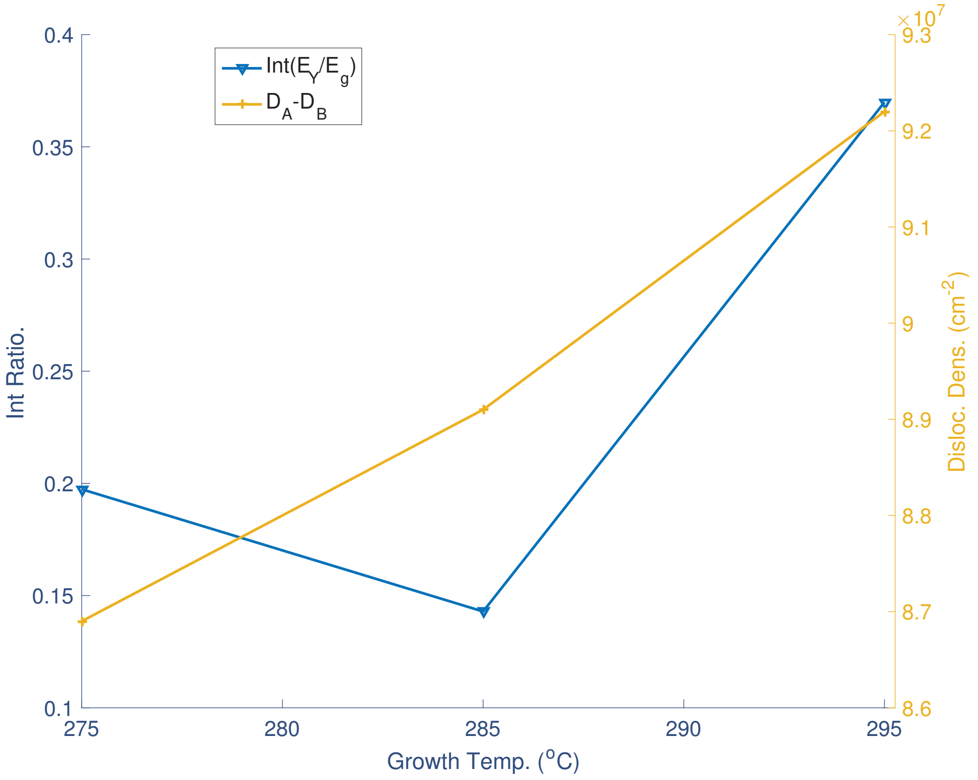

Figure 5.28.: The difference between the dislocation density of type A and type B defects and the intensity ratio of the E_Y to E_g as function of the growth temperature.

difference of the dislocation densities might be related to the generation of additional extended defects in the crystal which was observed as increase in the intensity of the E_Y emission.

The effect of the growth temperature to the surface morphology of the CdTe layers was investigated by Nomarski microscopy. In Figure 5.29, optical images representing the surface of the CdTe layers grown at 275 °C, 285 °C, and 295 °C from an area of 367 µm × 206 µm are given. The surface of CdTe layer grown at 275 °C is featureless and smooth. The surface quality of the layers seems to degrade with increasing growth temperature. Especially, diamond shaped surface defects [134] were spotted in the surface images of the CdTe layer grown at 285 °C and 295 °C. The roughness related to the surface defects were observed in the RHEED patterns. The surface morphology of the CdTe layers were further investigated by employing AFM technique. The AFM height images from the 10 × 10 µm areas of CdTe layers were recorded and analyzed. RMS roughness and absolute SK values from the statistical analysis of the AFM height images

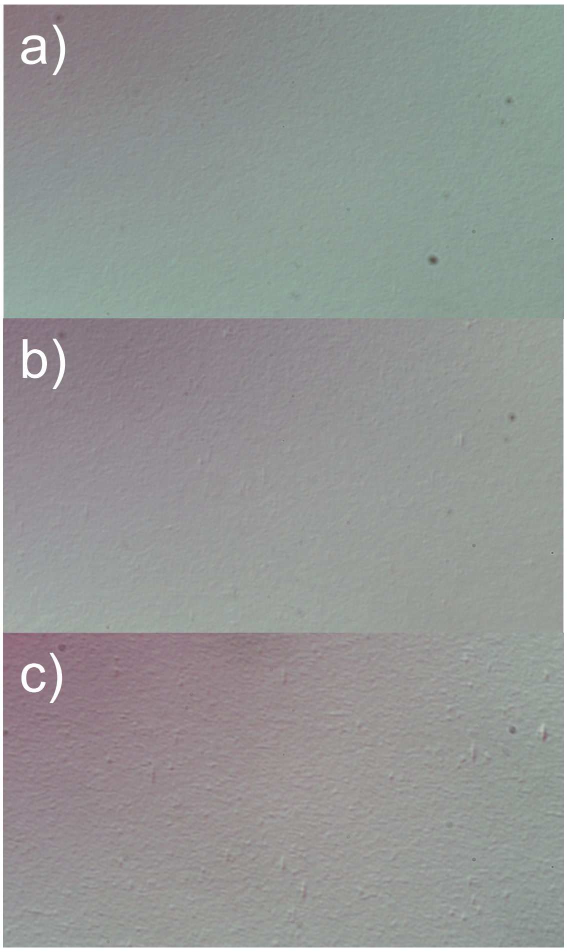

Figure 5.29.: Optical images of the CdTe layers grown at (a) 275 °C, (b) 285 °C, and (c) 295 °C taken by Nomarski microscopy.

of the CdTe layers grown at different temperatures as a function of growth temperature is shown in Figure 5.30. The SK value from the analysis of the CdTe layer grown at 295 °C was negative while the others were positive. To demonstrate the correlation between the surface roughness and SK, absolute SK was plotted with the RMS roughness. Surface of the CdTe layer grown at 275 °C has a RMS roughness of 1.94 nm and SK value of 0.089 indicating a very smooth surface which is in agreement with the Nomarski microscopy results. Surface roughness and the SK values of CdTe epilayers gradually increases with increasing growth temperature. The surface of the CdTe epilayer grown at 295 °C was rough (2.6 nm RMS roughness) and had a large SK value of -1.147 suggesting the growth of the CdTe epilayer at 295 °C was not ideal to maintain surface stoichiometry. In summary, the best surface morphology was obtained for the growth at 275 °C.

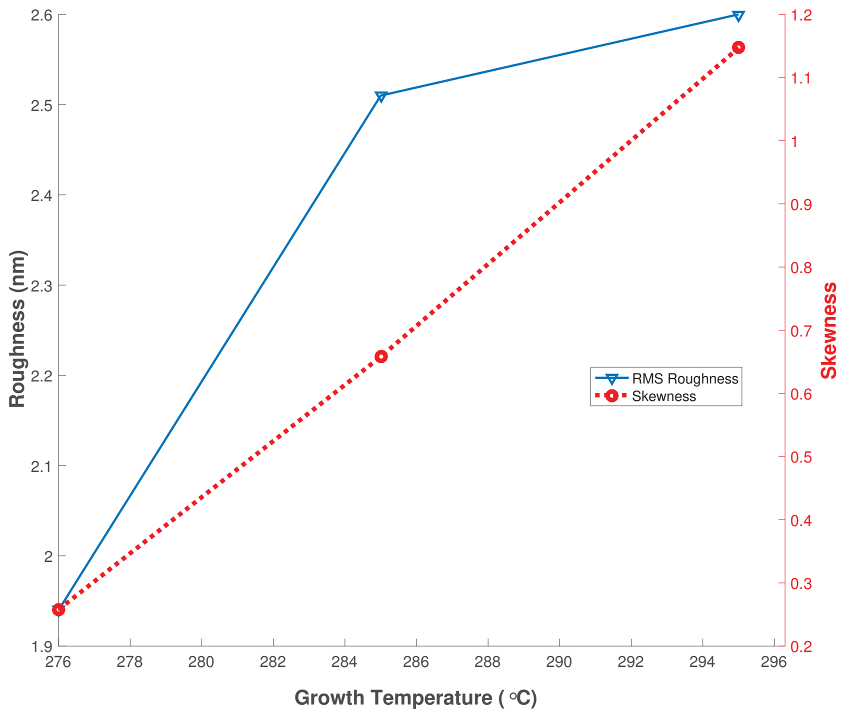

Figure 5.30.: The calculated RMS roughness and the absolute SK of the CdTe epilayers as a function of growth temperature.

5.4. Conclusions

A systematic study of the growth of the CdTe layers on the deoxidized of GaAs (211)B surfaces has been performed. Firstly, the effect of the nucleation temperatures and the nucleation methods to the surface and crystal quality of the CdTe epilayers were investigated. By using *in situ* RHEED and XRD Gonio measurements, it has been shown that when the growth of the CdTe layers were initiated at 230 °C and above, the (133) twin orientation became favorable. The occurrence of the twins was verified by RHEED and XRD Gonio measurements. Constant temperature nucleation which was followed by annealing was chosen as first method. The second method consisted of instantaneous nucleation followed by ramp of temperature to the growth window. By employing SE, HRXRD RC, defect decorative etching, Nomarski, and AFM techniques, the results of the both methods were compared. Optical properties of the layers grown with the either method were similar. The CdTe layer grown with the first method had higher crystal quality which was determined from the XRD RC and EPD results. In addition, the surface morphology of the layer grown with the first method was smoother to the layer grown with the second method. An atomically smooth surface with a RMS Roughness of 1.94 nm was obtained by employing the first method of the nucleation.

The effect of the Te/Cd flux ratio to the crystal and the surface quality of the epitaxially grown CdTe layers was studied. Te/Cd flux ratios of 3.45 and higher created a Te-stabilized surface indicating a smooth surface morphology which was observed from the RHEED patterns of the samples. The step array superimposed on the CdTe-like streaks was observed from RHEED patterns. The longest and bright streaks were obtained from the layer grown with the Te/Cd ratio of 3.45. The crystal quality of the CdTe layers grown with different atomic flux ratios were investigated by XRD RC, EPD, low temperature PL, and SE measurements. The layer with the lowest EPD was grown with the ratio of 4.5 while the lowest RC FWHM was obtained from the layer grown with the flux ratio of 3.45. The inconsistency between the results of the characterization methods was further investigated by PL and SE measurements. The results of the PL and SE have suggested an imbalance in the density of the dislocations with Te and Cd cores. Additionally, it was shown that the EPD and the RC FWHM from the [-111] azimuth with PL dislocation analysis were in good agreement suggesting that both characterization methods probes the same type of the dislocations. CdTe layers grown with a high flux ratio of 6 possibly created a biaxial strain in the layer causing a red shift in the energies of the E_1 and $E_1+\Delta_1$. Surface analysis of the CdTe layers with AFM and Nomarski has shown that the layers grown with the flux ratios of 4.5 and higher created pit decorated rough surfaces.

The last parameter studied was the temperature during the constant temperature growth step. By using the color-mapping and the 3D surface reconstruction of the RHEED images, the longest and bright streaks were detected from all the layers grown at different temperatures. The smoothest surface was predicted with the help of the RHEED images which belonged to the layer grown at 275 °C. The layers grown at higher temperatures had brighter spots and shorter streaks suggesting the layers grown at high temperatures had slightly rough surface morphology. The equilibrium growth conditions were studied with the *in situ* SE technique. The CP analysis has shown that the only factor affecting the optical properties of the layers during the growth was the expansion or shrinkage of the lattice due to the changes in temperature. It has been shown that the inverse of the E_1 CP energy can be used as an accurate surface temperature measurement tool. Crystal quality of the epilayers grown at different temperatures were investigated with XRD RC, PL, and defect decorative etching techniques. An inconsistency was detected between the XRD

RC and EPD results suggesting an imbalance in the density of the dislocations with the different cores. To investigate the possible imbalance in the density of the different type of dislocations, low temperature (80 K) PL measurements were performed. A direct correlation between the results of PL measurements with the XRD RC and EPD results were not observed. Inconsistency between the experimental measurements was theoretically studied by employing a new model [136]. To employ the model, active slip systems of (211) zinc blende crystal was calculated by using Schmid factor analysis. The broadening of the RC FWHM from the different azimuthal angles was modeled with the contribution of the two different type of active slip systems. The active slip systems are classified with the MD line vectors. The dislocations with the same line vectors might have Te or Cd atoms in their cores. The model was verified with the RC FWHM measurements from the different azimuthal angles. Densities of the different type of dislocations (D_A and D_B) were calculated by using azimuthal XRD RC scans. Correlation between the EPD and D_A has shown that the defect decorative etching might be sensitive to the dislocations with the core atoms of Te (D_A). Surface quality of the layers was further investigated with the Nomarski and AFM techniques. The growth of the layers at temperatures higher than 275 °C created diamond shaped defects on the surface of epilayers. The lowest RMS roughness and SK values were obtained with the layer grown at 275 °C, and these values were in good agreement with the results of the RHEED analysis.

CHAPTER 6

CYCLIC ANNEALING

Heteroepitaxial growth of CdTe on GaAs(211)B substrates creates a 14.6 % compressive strain ($\varepsilon_{\|}$) in the epilayer. The interface of CdTe and GaAs is rotationally commensurate and an 8-7 registry relieves the most of the strain in CdTe on GaAs [137]. The remaining strain is relaxed by forming dislocations and by the tilted epitaxy. As the thickness of the epilayer increases during growth, dislocation loops can self-annihilate and threading dislocations on the same glide plane can fuse by gliding while the threading dislocations on parallel and intersecting slip planes can fuse or annihilate by gliding or climbing. However, since the dislocations can only move under the effect of the biaxial stress, the dislocation density will be saturated as the stress in the epilayer is relieved. The glide motion of the threading dislocations can be enabled by reducing Peierls stress. Annealing CdTe epilayers above 345 °C (see Chapter 2) allows the glide motion on the threading dislocations. In this chapter, effect of the annealing to the crystal and the surface quality of CdTe layers at the temperatures above 345 °C is investigated. The results of *in situ* growth interrupted thermal cyclic annealing of CdTe on GaAs(211)B are presented.

6.1. Annealing Temperature

Thermal deoxidation and CdTe growth were performed in Veeco GEN20MZ MBE system using 3-inch GaAs(211)B epiready substrates. Thermal deoxidation was carried out with Veeco Mark V 500 As (7 N) valved cracker and dual filament In effusion cell whereas CdTe growth was performed with Veeco Mark V 200 CdTe (7 N) and Te (7 N) valved crackers. Thermal deoxidation and growth were monitored *in situ* through RHEED, which yielded data pertaining to surface crystal quality. In addition, calibrated band-edge detection system was used for temperature measurement.

GaAs(211)B substrates were deoxidized at 535 °C for 215 s under In flux of 1.1×10^{-8} Torr BEP. In desorption process was performed at 553 °C for 200 s. Next, GaAs substrates were cooled under As_4 of 4.3×10^{-6} Torr BEP flux to ensure B polarity of the GaAs substrate. Growth of the CdTe epilayers was initiated at a surface temperature of 217±2 °C. To investigate the effect of the annealing temperature on the CdTe crystal quality, CdTe layers were grown at temperature of 295±1 °C with the Te/Cd ratio of 3.45. The constant temperature growth was interrupted every 80 minutes to perform annealing on the epilayers under Te flux of 8.5×10^{-7} Torr BEP. Three CdTe layers were annealed instantaneously (flash anneal) at temperatures of 403 °C, 411 °C, and 419 °C. Following last anneal cycle, the epilayers were cooled down to 240 °C under protective Te flux. CdTe layers were grown at the rate of ~ 1 µm/h. To ensure homogeneous distributions of the Cd and Te atoms on the surface, the samples were rotated at 8 rotations per minute (RPM). Thickness of the layers were determined by SE and FTIR transmission measurements. The thicknesses of the CdTe layers annealed at 403 °C, 411 °C, and 419 °C were measured as 2.76 µm, 2.65 µm, and 2.55 µm, respectively. A reduction in the thickness of the epilayers annealed at 403 °C, 411 °C, and 419 °C was detected as 80 nm, 135 nm, and 185 nm per annealing cycle, respectively.

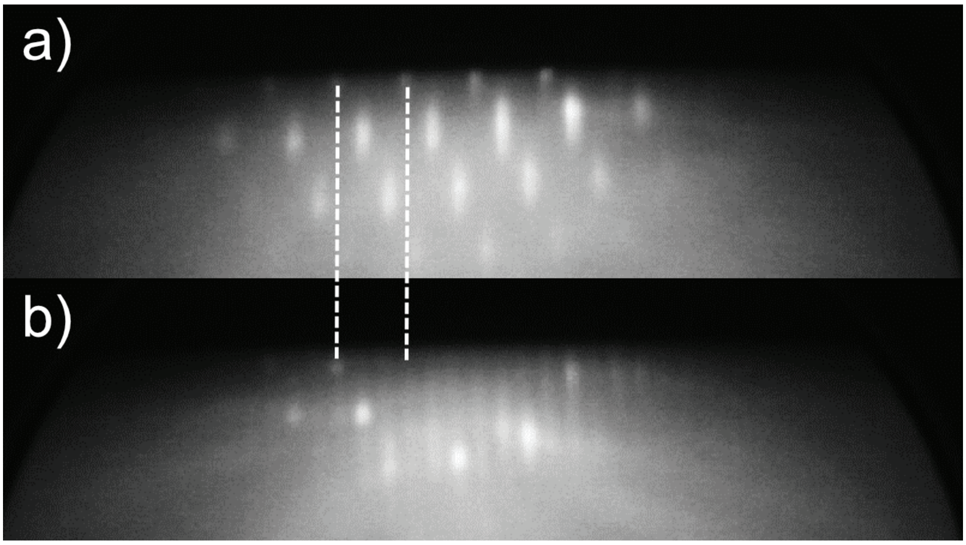

Figure 6.1.: RHEED patterns of the CdTe layers taken during growth at (b) 295 °C and during heating to the annealing at a temperature of (a) 355 °C. Dashed lines for the comparison of the periodicity of two RHEED patterns.

The CdTe epitaxial growth was carried under Te-stabilized surface conditions. The RHEED pattern taken during the growth of an epilayer is shown in Figure 6.1 (b). The RHEED pattern consists of two different periodic patterns of which the first one belongs to the (211) surface while the other one is due to the reconstruction of (111) planes from Te-stabilization [126]. The RHEED pattern due to the step structure is shown with the dashed lines in the figure. By comparing the patterns between the dashed lines, the RHEED pattern of a non Te-stabilized (211) surface can be detected from both images.

In Figure 6.1 b), additional less bright streaks were detected in the RHEED pattern which was due to the Te-stabilized (111) surface. Following the termination of growth cycle and during heating to the annealing temperature, the RHEED pattern was changed from Te-stabilized (211) surface to bare (211) surface. In Figure 6.1 (a), a RHEED pattern taken at a temperature of 355 °C is shown. The RHEED pattern exhibit clear, bright and long streaks indicating a smooth surface morphology. The RHEED pattern of the surface was returned to the Te-stabilized (211) structure during cooling down after the annealing process. The Te-stabilized (211) to bare (211) surface reconstruction was observed at a temperature of 335±2 °C.

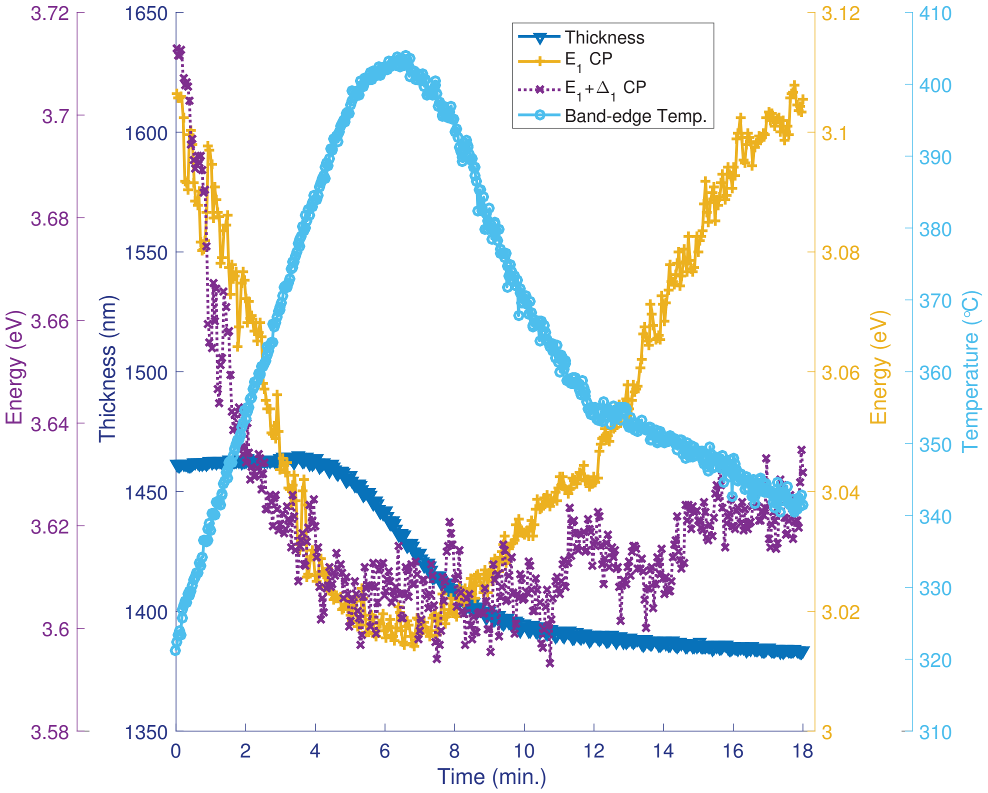

Figure 6.2.: Epilayer thickness and the energies of E_1 and $E_1+\Delta_1$ CP from SE measurements with temperature measurements from band-edge detection system as a function of time.

The change in optical properties of the CdTe layers during flash annealing process was monitored with *in situ* SE measurements. The experimental data was fitted a model consisting of a dielectric layer and a substrate. The layer thickness was monitored

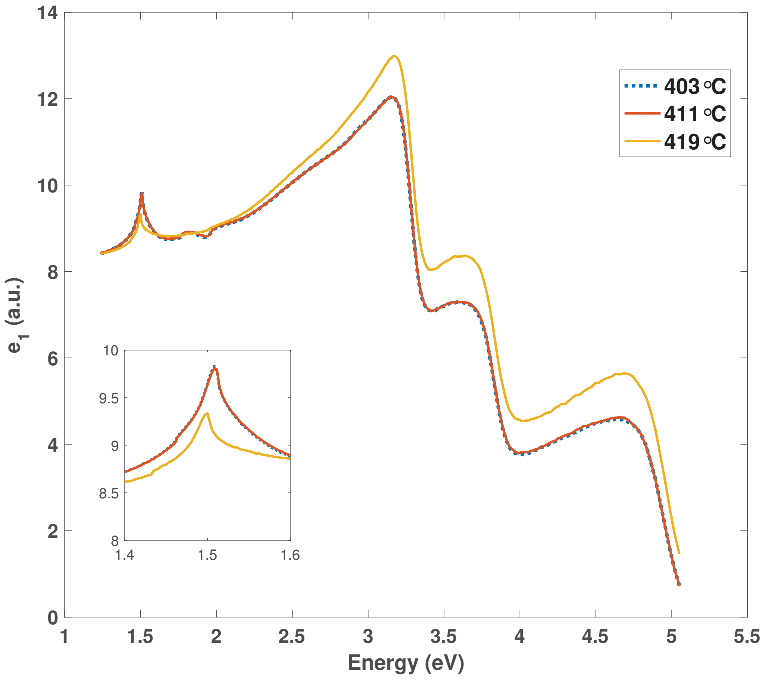

Figure 6.3.: Real (e_1) part of the dielectric function of the CdTe layers annealed at 403 °C, 411 °C, and 419 °C.

during annealing. The dielectric function of the CdTe epilayers were modeled using a multi-oscillator model with a MSE of 13.5 which had PSemi-Tri and harmonic oscillators [73]. GaAs substrate was modeled with a pre-defined temperature library (details given in Chapter 5). The energies of E_1 and $E_1+\Delta_1$ CP were calculated with the oscillator model. In Figure 6.2, change in the thickness, energies of the E_1 and $E_1+\Delta_1$ CP with temperature measurements from band-edge detection system were plotted during heating to the annealing and cooling down to growth temperature. The annealing process was initiated with a temperature ramp to 403 °C. A decrement in the energies of the E_1 and $E_1+\Delta_1$ CP was simultaneously observed which was related to the response of lattice parameter change due to the temperature decline. The response of the E_1 and $E_1+\Delta_1$ CP was not similar during cooling down to the growth temperature. The E_1 CP energy was higher compared to initial value before annealing which indicates a reduction in the biaxial stress. $E_1+\Delta_1$ CP gap slowly increased to 3.63 eV when the surface temperature has reached 340 °C. The energy of the $E_1+\Delta_1$ was 0.03 eV lower compared to the same temperature value before annealing. The inhomogenous broadening of the E_1 and $E_1+\Delta_1$ gaps after annealing process indicates a change in the electronic structure. The loss of the

CdTe molecules was detected after the surface temperature has reached to ~ 375 °C. A total 80 nm thickness of the epilayer was lost during the annealing process.

To investigate the effect of the annealing temperature on the crystal quality of the CdTe layers, defect decorating etching for 30 s with (1HF:4HNO_3:25H_2O) ratios was applied. Several SEM images were used for the calculation of the EPD. The pits were counted and the average of the pits was used to determine EPD of epilayers. The EPD values of CdTe layers annealed at temperatures of 403 °C, 411 °C, and 419 °C were 4.59 $\times 10^7$ cm^{-2}, 4.09 $\times 10^7$ cm^{-2}, and 3.73 $\times 10^7$ cm^{-2}, respectively. A reduction in the dislocation density of the CdTe layers was detected with increasing annealing temperature. CdTe layer with the lowest EPD was obtained from epilayer annealed at temperature of 419 °C.

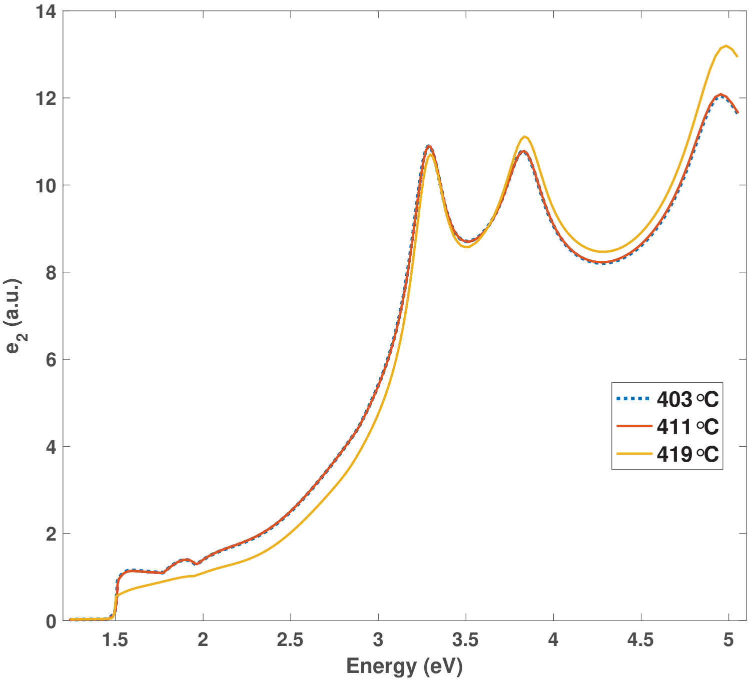

Figure 6.4.: Imaginary (e_2) part of the dielectric function of the CdTe layers annealed at 403 °C, 411 °C, and 419 °C.

The optical properties of the CdTe layers annealed at different temperatures were further investigated with room temperature SE measurements. The SE measurements were modeled with n-oscillator model with the details given in the Nucleation section of Chapter 5. MSE of the fits were 13.3±0.1. In Figures 6.3 and 6.4, real (e_1) and the imaginary (e_2) parts of the dielectric function of the CdTe layers annealed at 403 °C, 411

°C, and 419 °C are shown, respectively. Real and the imaginary parts of the dielectric function of CdTe layers annealed at 403 °C and 411 °C exhibit a similar behavior (i.e. energy of CP) in terms of energy. On the other hand, spectral shape of the dielectric functions of the CdTe layer annealed at 419 °C is blue shifted suggesting an improvement in the crystal quality which can be observed from Figures 6.3 and 6.4. A red shift in the energy of the E_0 was also observed indicating an increase in the density of electronically active point defects.

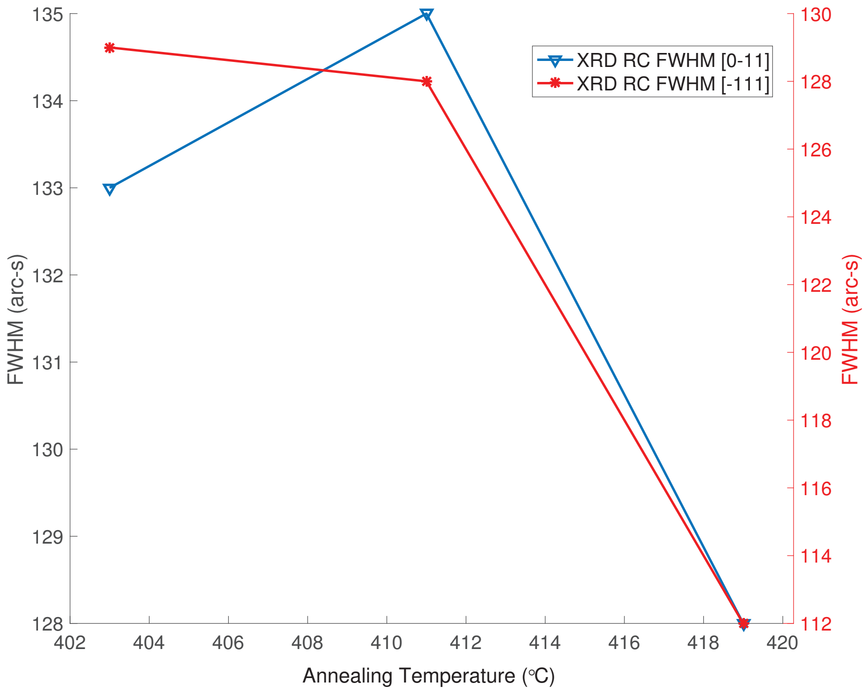

Figure 6.5.: Calculated RC FWHM values of CdTe layers annealed at 403 °C, 411 °C, and 419 °C from the [0-11] and [-111] azimuths as a function of annealing temperature.

To characterize dislocations in CdTe layers, low temperature micro-PL measurements were taken at a temperature of 80 K and with S& I Tri Vista system with Princeton Ins. Acton SP-2750 monochromator with 150 grating/mm and ProEM EMCCD camera. A 488 nm laser was used as excitation source. The penetration depth of the laser was 95 nm. The resolution of the monochromator with 150 grating/mm and camera was ~ 0.8 meV around the band gap of the CdTe at 80 K (~ 782 nm). Near gap emission from the PL spectra of CdTe layers annealed at the temperatures of 403 °C, 411 °C, and 419 °C are detected at 1.5859 eV, 1.5856 eV, and 1.5854 eV, respectively. To study the correlation between the intensity of the emission around 1.47 eV (E_Y) and density of the dislocations, the intensity ratio of the emission from the extended defects to near gap emission (E_g) was calculated (Figure 6.7).

In Figure 6.5, RC FWHM values of CdTe layers annealed at different temperatures from the [0-11] and [-111] azimuths are plotted as a function of annealing temperature. The RC of CdTe(422) symmetric reflection from epilayers had symmetric shapes (not shown) indicating a uniformly distributed lattice structure in the direction of surface normal. The CdTe(422) RC of epilayers were fit using a PearsonVII function. The layer with the lowest RC FWHM from both azimuths was that of annealed at 419 °C which is in agreement with the results of the defect decorative etching. An increment in the RC FWHM of the CdTe layers was observed when the epilayers annealed at lower temperatures suggesting a reduction in the crystal quality. However, increase in RC FWHM was not symmetric from both the azimuths when the layer was annealed at 403 °C suggesting an imbalance in the density of dislocation cores on the (111)A and (111)B glide planes. As mentioned in Chapter 2, dislocations with the cores of Te and Cd atoms may have different mobility values thus may glide with different velocities during annealing. The difference in the mobility might cause an imbalance in the reduction of the threading dislocation density due to annealing. The possible imbalance in the density of dislocation cores was further investigated with the azimuthal RC scans of CdTe(422) reflections.

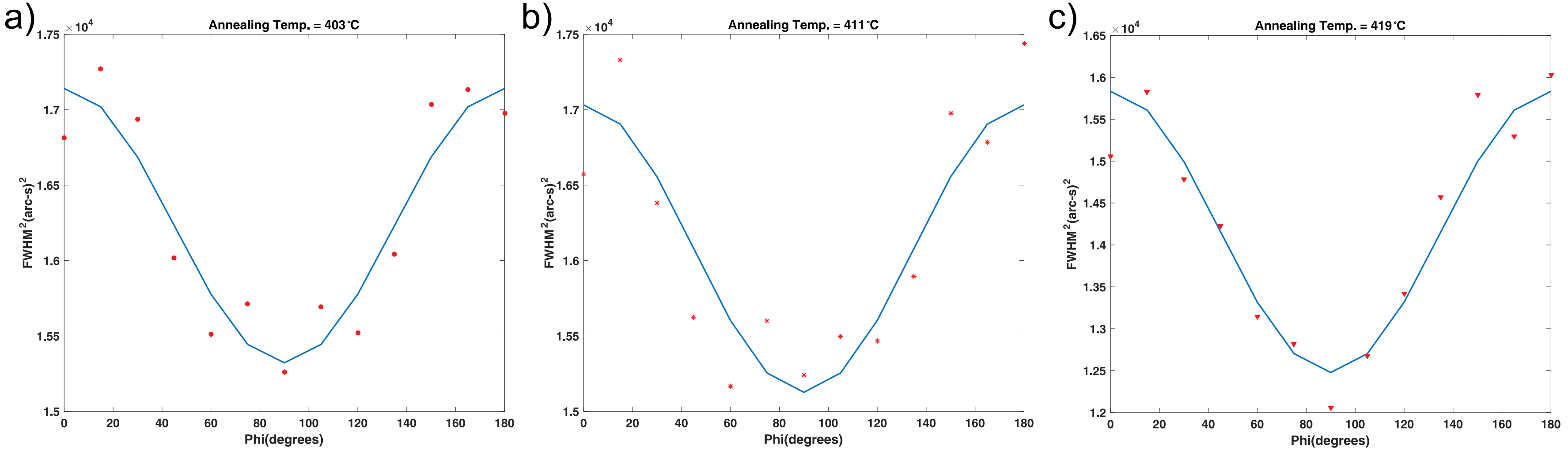

Figure 6.6.: Square of the RC FWHM values of CdTe layers annealed at (a) 403 °C, (b) 411 °C, and (c) 419 °C as a function of azimuthal angle.

The square of the RC FWHM from CdTe layers annealed at 403 °C, 411 °C, and 419 °C were plotted as a function of the azimuthal angle and the plots are shown in Figure 6.6. The filled circles, stars and triangles correspond to the experimental data and the line curves show the fits to Equation 5.6 with an average adjusted R^2 value of 0.9±0.02. At each azimuthal angle, the alignment for the CdTe(422) peak was repeated prior to the RC measurement. By measuring the RC FWHM for CdTe(422) reflection at different azimuths, the azimuthal dependence of the square of the FWHM (β^2) due to the dislocations with different origin was presented.

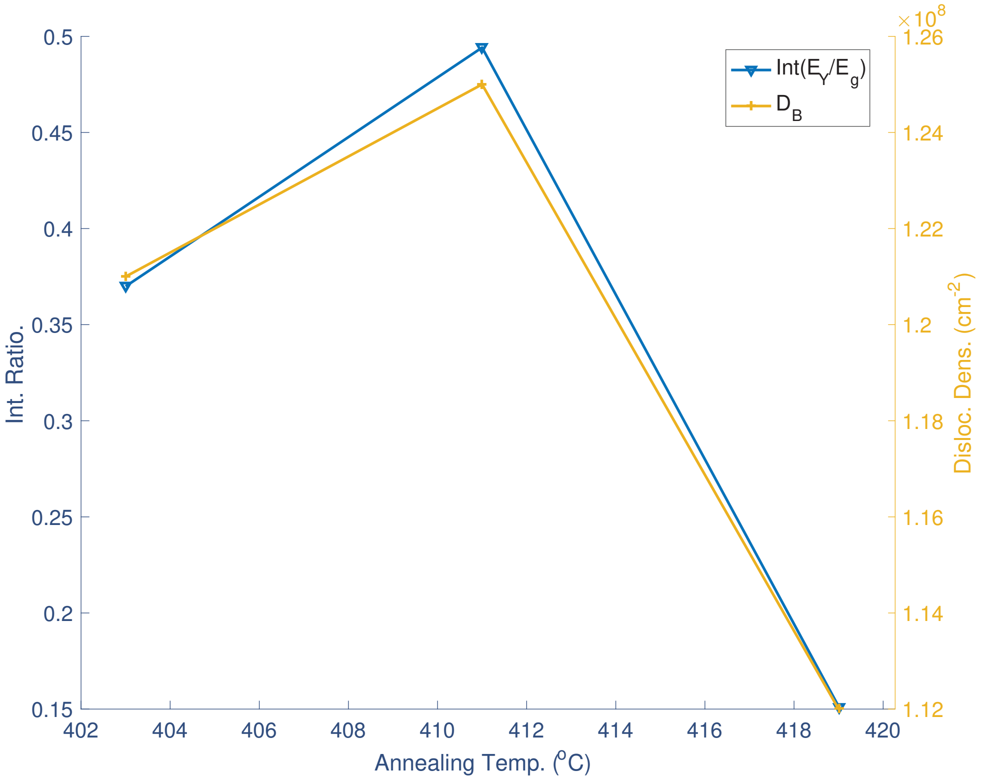

Figure 6.7.: The dislocation density of type B defects and intensity ratio of E_Y/E_g as function of the annealing temperature.

The density of the dislocations of type A and type B was calculated by using Equations 5.6, 5.7, and 5.8. In Figure 6.7, the density of the dislocations of type B and the intensity ratio of the E_Y emission to E_g emissions are given as a function of the annealing temperature. An increase in the density of the dislocations of type B was accompanied with the increase in the intensity ratio of E_Y/E_g which was proportional to the change in the annealing temperature. Correlation between the dislocation density of type B defects and the PL intensity ratio suggest that the E_Y emission might be originating from the type B defect centers. The increase in the dislocation density of type B defects contradicts the change in EPD indicating that defect decorative etching is not sensitive to the defects of type B.

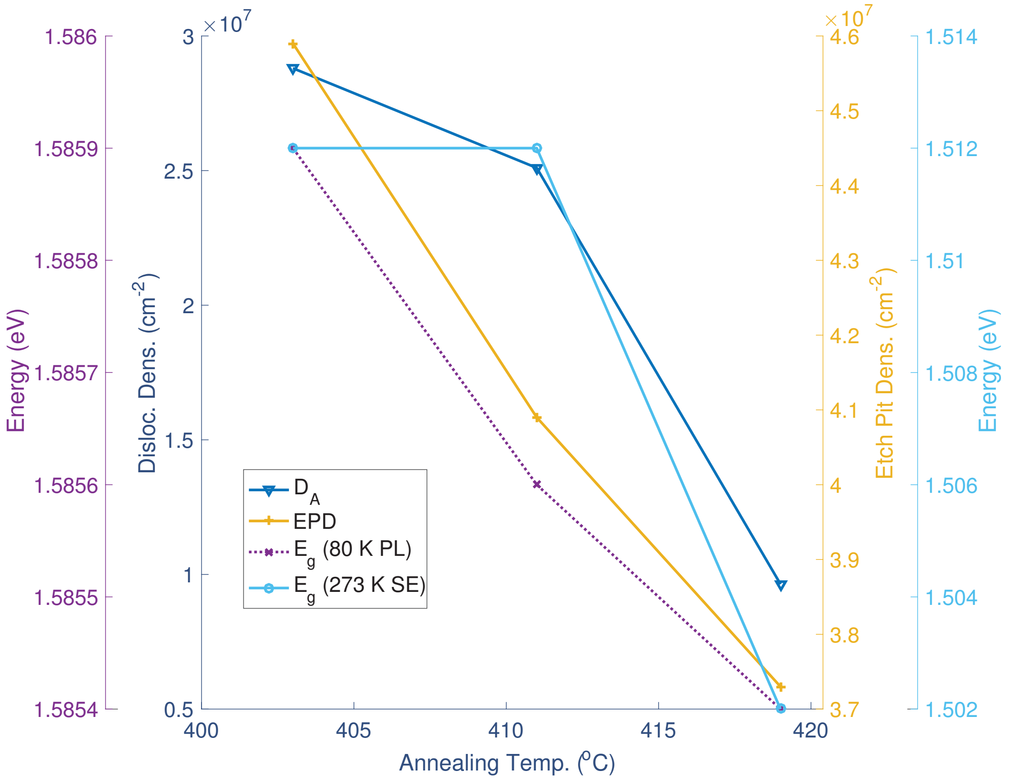

Figure 6.8.: EPD, dislocation density of type A defects, E_g from SE (297 K) and PL (80 K) measuremenets as function of the annealing temperature.

In Figure 6.8, EPD, density of the dislocation of type A defects and band gap energies at 297 K from SE measurements and 80 K PL measurements are shown as a function of the annealing temperature. The results of the EPD and the density of dislocations with the type A core are in well agreement, both exhibiting a reduction with the increase in the annealing temperature. The energy of the E_g got narrowed inversely proportional to the annealing temperature suggesting an increase in density of the point defects. The increase in the defect density may be related to the loss of the Cd and Te atoms during annealing. The most dramatic loss of atoms was observed after the annealing of CdTe layer at 419 °C. The lowest total dislocation density was obtained from the CdTe layer annealed at 419 °C. In summary, CdTe layer with the highest crystal quality was obtained with the annealing process at a temperature of 419 °C.

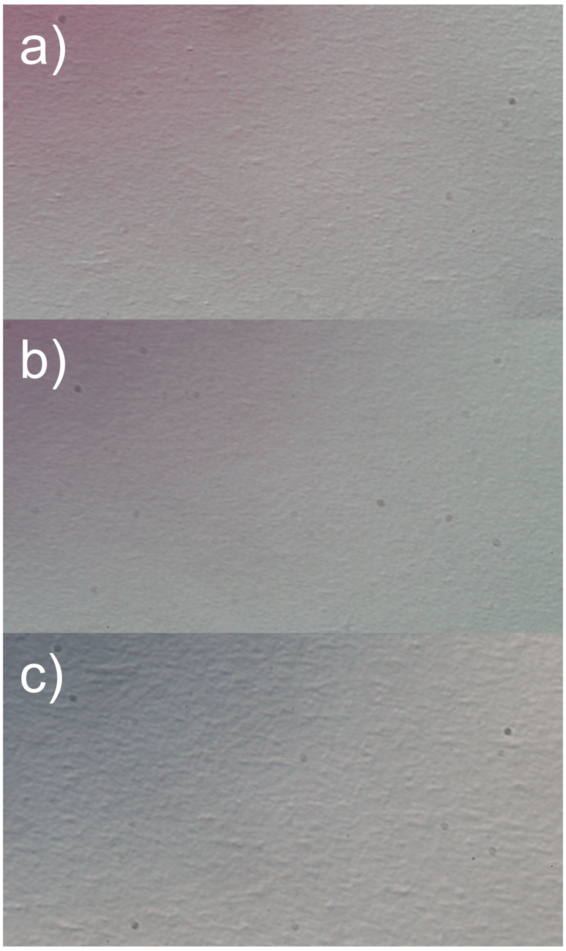

Figure 6.9.: Optical images of the CdTe layers annealed at (a) 403 °C, (b) 411 °C, and (c) 419 °C taken by Nomarski microscopy.

The effect of the annealing temperature on the surface morphology of the CdTe layers was investigated by Nomarski microscopy. In Figure 6.9, optical images representing the surface of the CdTe layers annealed at 403 °C, 411 °C, and 419 °C from an area of 367 µm × 206 µm are given. The surface of CdTe layer annealed at 411 °C is featureless and smooth. The surface images of the other layers exhibit large defects.

The surface morphologies of the CdTe layers were further investigated by employing AFM technique. The AFM height images from 10 × 10 µm areas of CdTe layers were recorded and analyzed. In Figure 6.10, the AFM height images of the CdTe layers annealed at 403 °C, 411 °C, and 419 °C are shown. Deep surface pits were observed from the AFM height images of the CdTe layer annealed at 403 °C. The smoothest surface morphology was observed from the surface of the CdTe layer annealed at 411 °C. Addi-

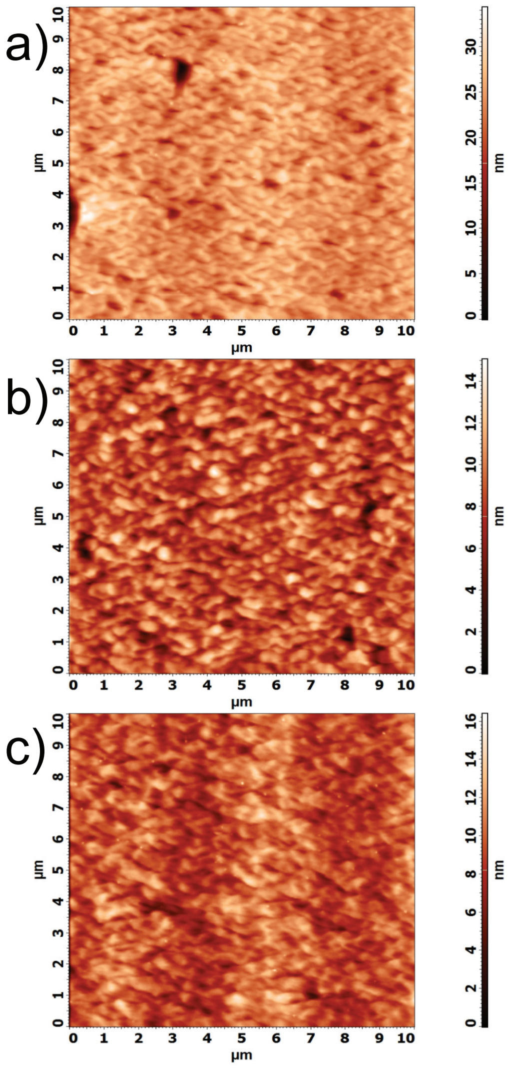

Figure 6.10.: AFM height images of the CdTe layers annealed at (a) 403 °C, (b) 411 °C, and (c) 419 °C.

tionally, cross hatches of the (211) surface was also observed from the AFM height image indicating a very smooth surface morphology. The surface of the CdTe layer annealed at 419 °C seems to be degraded after high loss of the Cd and Te atoms from the surface. RMS roughness and absolute SK values from the statistical analysis of the AFM height images of the CdTe layers annealed at different temperatures as a function of annealing temperature are shown in Figure 6.11. The SK values of all the CdTe layers were negative. To demonstrate the correlation between the surface roughness and SK, absolute SK was plotted with the RMS roughness. The figure suggests that the surface roughness of the epilayers originate from the SK. Surfaces of the CdTe layer annealed at 411 °C and 419 °C have the RMS roughnesses of 1.73 nm and 1.64 nm, respectively. SK values of the same surfaces were -0.012 and -0.074, respectively. Therefore, the degradation of surface quality due to the annealing at a high temperature of 419 °C was verified. Surface roughness values of CdTe epilayers gradually increases with increasing annealing temperature. The surface of the CdTe epilayer annealed at 403 °C was rough (2.6 nm RMS roughness) and had a large SK value of -1.147 suggesting the annealing of the CdTe epilayer at 403 °C was not ideal to maintain surface stoichiometry. In summary, the best surface morphology was obtained with the annealing at 411 °C.

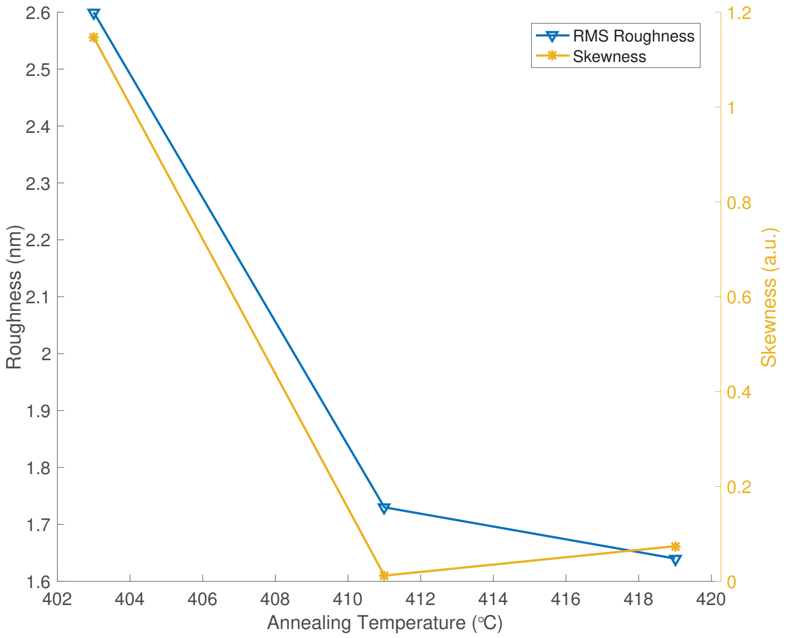

Figure 6.11.: The calculated RMS roughness and the absolute SK of the CdTe epilayers as a function of annealing temperature.

6.2. Temperature Uniformity

The effects of the growth and the annealing temperature on the surface and the crystal quality of the epilayers were investigated in Chapter 5 and Chapter 6, respectively. The epitaxial growth of CdTe layers are usually carried out on large area (3"-6") substrates. Therefore, temperature uniformity is desired during the growth and annealing processes. Large area substrates are heated with two different heating zones. The heating power of the two zones might be proportional to each other or completely independent.

The radiation from the substrate heaters usually have rotational symmetry up to certain radius. The substrates are either stick to the blank holders by In or are hanged to the hollow holders. The edge of the substrates are additionally heated due to the heat transfer from the holders.

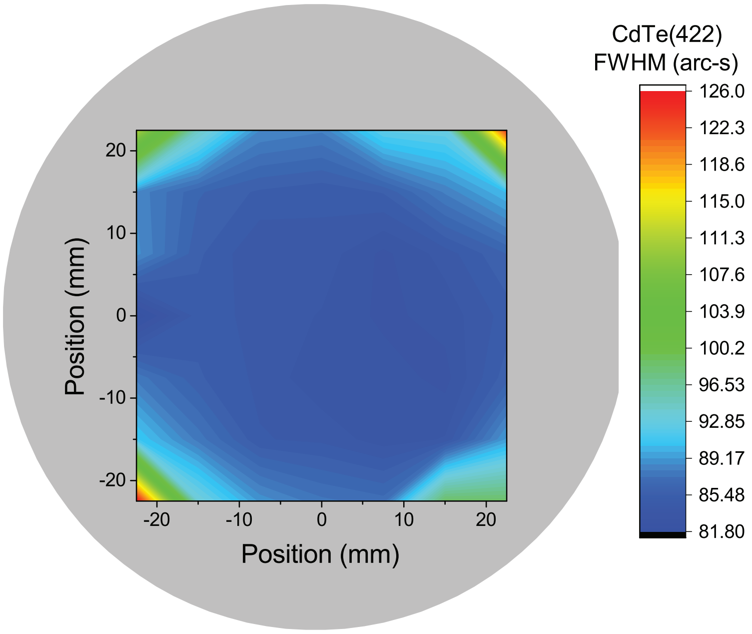

Figure 6.12.: XRD RC FWHM Map from a 52.5 mm × 52.5 mm area with 7 × 7 grid.

A 3 inch and a 20 × 20 mm CdTe layers were grown on the deoxidized GaAs(211)B substrates with the optimized parameters given in previous chapters. To study the uniformity of the crystal quality across the epilayers, series of XRD RC scans of CdTe(422) reflections were performed on the different positions of 3 inch CdTe layer. In Figure 6.12, XRD RC FWHM Map from a 52.5 mm × 52.5 mm area with 7 × 7 grid was shown. Distributions of RC FWHM across the wafer has a rotational symmetrical shape. The middle area has an average FWHM of 83 arc-s while FWHM of the areas closer to the edges reduces to a value of 126 arc-s.

To determine the change in the RC FWHM near the edges of the 3 inch CdTe layer, FTIR transmission measurements were performed on a 38 mm × 42 mm area with a 10 × 10 grid (Figure 6.13) . The change in the overall thickness of the CdTe layer was 4 %. The thickness distribution across the epilayer is found to have rotational symmetry.

To confirm the temperature related edge effects to the crystal quality, a 20 mm × 20 mm CdTe layer was grown and annealed. The crystal quality of the layer were investigated with 80 K PL measurements. The PL measurements were performed on a

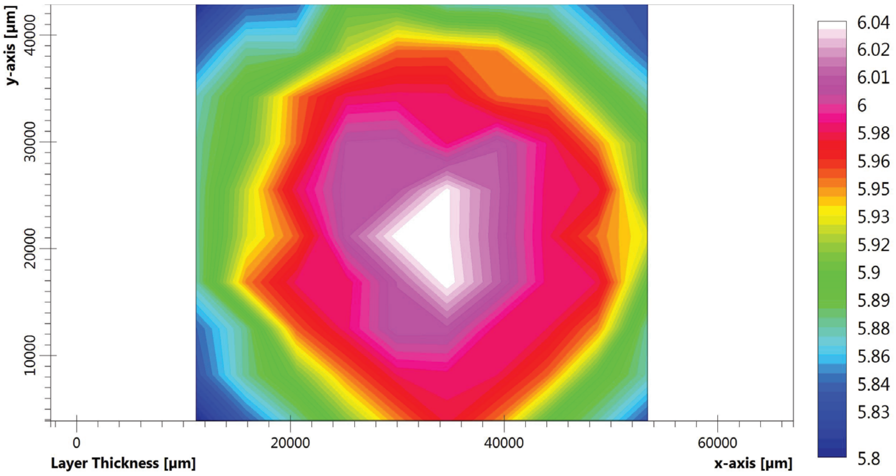

Figure 6.13.: Thickness map from the FTIR transmission measurements from a 38 mm × 42 mm area in the center of a CdTe layer grown on a 3 inch GaAs(211)B substrate.

5 mm × 10 mm area with 0.25 mm steps. In Figure 6.14, the measurement geometry is given. To evaluate the crystal quality from the PL measurements, the intensity ratio of E_g/E_Y was calculated at every measurement position. The resulting PL map is also shown in Figure 6.14. The center area has a larger E_g/E_Y ratio indicating a high crystal quality. On the other hand, the zones closer to the edges have a reduced E_g/E_Y ratio due to the high density of the dislocations. The results of the XRD, PL, and FTIR measurements suggest that the temperature was uniform during growth and annealing with the exception to the edges of the substrates.

The rotational symmetry of the substrate heater was removed to observe its effects on the crystal quality across the CdTe epilayers. A 3 inch GaAs(211)B was placed into the MBE GM CAR manipulator with a small angle of ~ 5° tilt. The manipulator has three legs with the tilt being directed into one of the legs position. The deoxidation, growth and the annealing was performed. The growth was carried out at 275 °C while the annealing was performed at 409 °C.

To study the uniformity of the crystal quality across the epilayers, series of XRD RC scans of CdTe(422) reflections were performed at the different positions of 3 inch CdTe layers. In Figure 6.15, XRD RC FWHM Map from a 52.5 mm × 52.5 mm area with 7 × 7 grid was shown. Distributions of RC FWHM across the wafer does not have a rotational symmetrical shape. The lowest FWHM value was observed where the distance between the heater and the sample was closest. The temperature of the center was 409 °C during the annealing process. The temperature of the right corner was 8-10 °C higher.

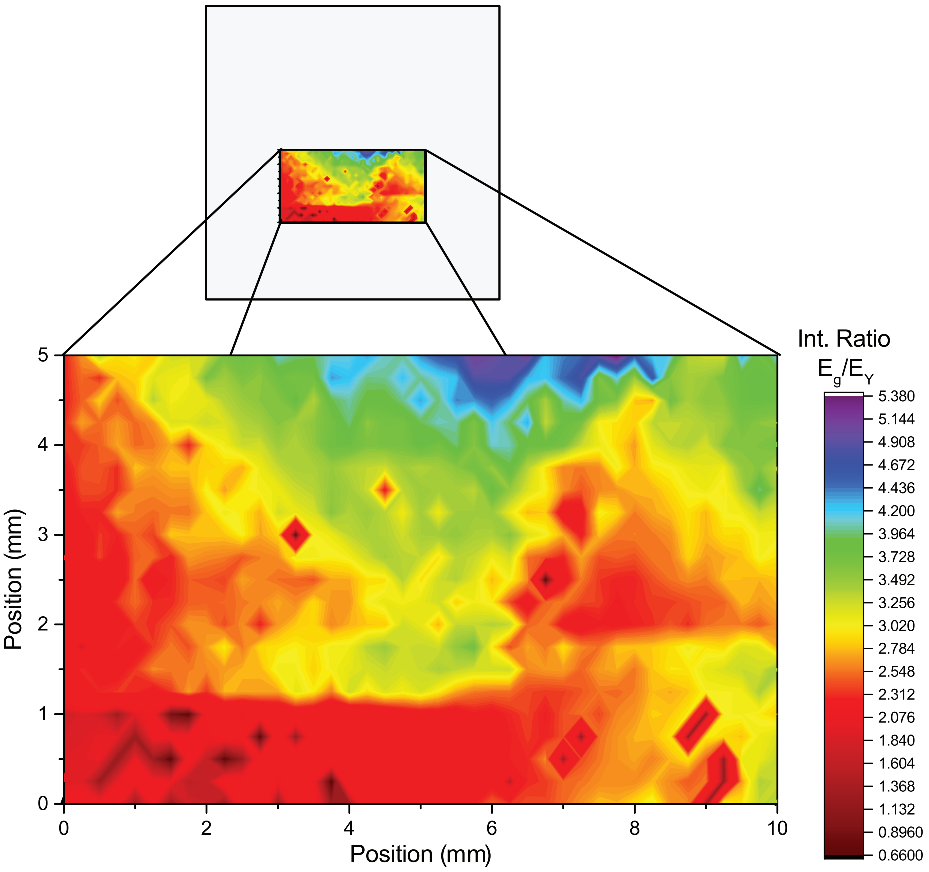

Figure 6.14.: Map of the Intensity ratio of E_g/E_Y emissions at a 5 mm × 10 mm area with 0.25 mm steps from a 20 mm × 20 mm CdTe layer.

The annealing at ~ 420 °C provided better crystal quality which is in good agreement with the results of the previous section. Removal of the rotational symmetry of heating resulted in a inhomogenous distribution of defects across the CdTe wafer.

To determine the change in the RC FWHM near the right corner of the 3 inch CdTe layer, FTIR transmission measurements were performed on a 37 mm × 47 mm area with a 10 × 10 grid (Figure 6.16). The change in the overall thickness of the CdTe layer was 6.3 %. The thickness distribution across the epilayer has a rotational symmetry but it was slightly translated to a position closer to the right corner of the wafer.

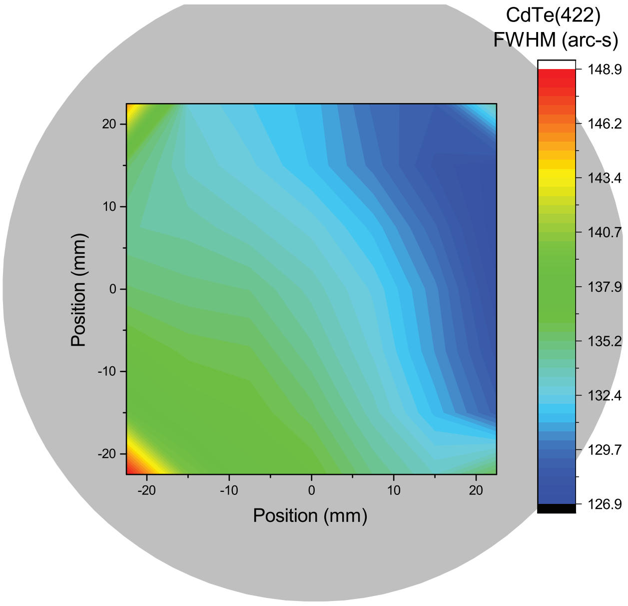

Figure 6.15.: XRD RC FWHM Map from a 52.5 mm × 52.5 mm area with 7 × 7 grid.

6.3. Conclusions

A systematic study of the annealing of the CdTe layers on the deoxidized of GaAs(211)B surfaces has been performed by investigating the effect of the annealing temperature on the surface and crystal quality of the CdTe epilayers. By using *in situ* RHEED, the surface reconstruction of the CdTe layer from Te-stabilized (211) to bare (211) surface was detected. The reconstruction of the surface was monitored at 355±2 °C. Additionally, a blue shift in E_1 and a red shift in E_1+Δ_1 CP energies were detected from *in situ* SE measurements during annealing. The shift of E_1 was related to the reduction in the biaxial stress while the shift in the E_1+Δ_1 was originated from a change in the electronic structure of the material. The crystal quality of the epilayers was further investigated with the ex situ defect decorative etching, XRD, and PL (80 K) measurements. The results of the RC and EPD were inconsistent. To analyze the inconsistency, azimuthal XRD RC measurements were performed. The broadening in the azimuthal XRD RC were fitted with a model containing contributions from two types of dislocations.

The density of dislocations of type A defects was reduced by increasing the annealing temperature which was in well agreement with the EPD results. On the other hand, density of the dislocations of type B defects was increased when the annealing

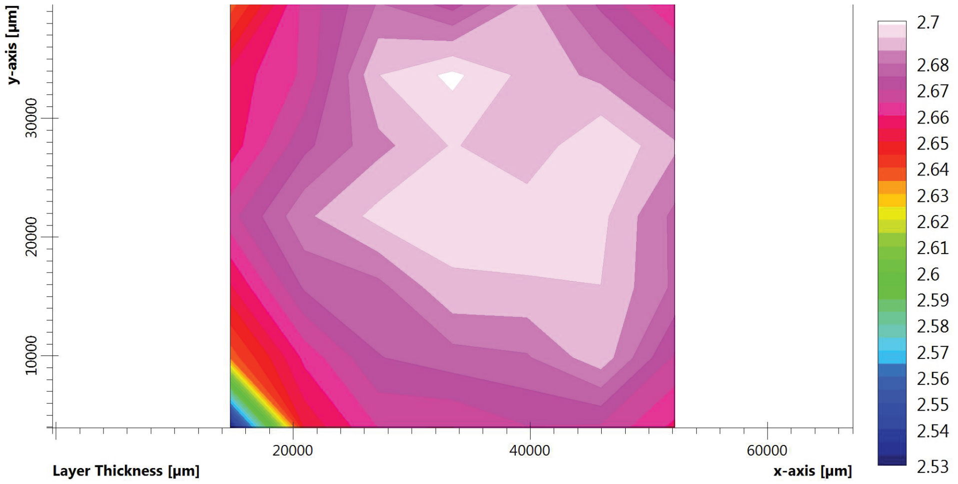

Figure 6.16.: Thickness map from the FTIR transmission measurements from a 37 mm × 37 mm area in the center of a CdTe layer grown on a 3 inch GaAs(211)B substrate.

temperature was increased. Defect decorative etching was found to be sensitive to type A defects. A correlation between the dislocation density of type B defects and intensity ratio of E_Y/E_g was detected which suggest that the 1.47 eV emission in the PL spectra of the CdTe epilayers was originated from the dislocations of type B defects. An increase in the dislocation density of the electronically active point defects was detected from the low temperature PL and 297 K SE measurements. CdTe layer with the highest crystal quality was obtained with the annealing at 419 °C. The effect of the annealing temperature on the surface morphology of the CdTe epilayers was investigated by Nomarski microscopy and AFM. The CdTe layers with smoothest surface and with a low surface roughness of 1.73 nm and a near zero SK value was obtained by annealing these layers at 411°C.

The effect of the temperature uniformity during growth and annealing was investigated by XRD RC, PL and FTIR transmission maps. A rotational symmetry in the crystal quality and the thickness of the CdTe layers was detected when the CdTe layers grown with a rotational symmetric substrate heater. Removal of the rotational symmetry of substrate heating also removed the rotational symmetry of crystal quality of the epilayer.

CHAPTER 7

CONCLUSIONS

There is a significant effort to improve the crystal quality of CdTe epilayers grown on various substrates. High quality CdTe layers are required for solar cells, x-ray detectors, electro-optical modulators, and especially for $Hg_{1-x}Cd_xTe$ infra-red detectors. The state-of-the-art $Hg_{1-x}Cd_xTe$ layers grown on Si and Ge alternative substrates by MBE has a threading dislocation density of ~ 10^7 cm^{-2} [128]. The lowest reported EPD value for the CdTe layers grown on the GaAs substrate is 4×10^6 cm^{-2} [27]. However, the reported EPD values were obtained from the CdTe layers with thickness over 10 μm. The EPD values needs to be reduced to the mid-10^5 cm^{-2} range for high-performance LWIR detectors and other devices.

In this study, a wide range of experimental techniques has been used to characterize GaAs substrates and epitaxial CdTe layers. The systematic study of the thermal deoxidation of GaAs(211)B surface under As_4 and In fluxes demonstrated that interface quality has a critical role to obtain high quality CdTe layers. Thermal deoxidation under In flux was applied to GaAs(211) surface prior to the growth of the CdTe layers. Optimized deoxidation parameters for In assisted oxide desorption were determined as In flux of ~ 1×10^{-8} Torr BEP, deoxidation duration of ~ 200 s at ~ 532 °C, In related material desorption duration of ~ 200 s at ~ 552 °C. Similarly, optimized deoxidation parameters for As_4 assisted deoxidation were found as deoxidation duration of 270 s at ~ 604 °C with a As_4 flux of 4.2×10^{-8} Torr BEP. HRXRD RC FWHM for CdTe layers grown on deoxidized GaAs(211)B under As_4 and In fluxes were as low as 138 arc-s (2.7 μm) and 118 arc-s (2.85 μm) arc-s, respectively. To compare the XRD RC FWHM of the CdTe layers with different thickness values, the FWHM values were normalized with the relation of FWHM*h, where h is the thickness of the CdTe layer. The FWHM*h values were calculated to be as 372 and 336 for the CdTe layers grown on the deoxidized GaAs(211)B substrates under As_4 and In fluxes, respectively. These result suggest that the CdTe layer grown on the deoxidized GaAs(211)B under In flux resulted in a layer with better crystal quality.

The conditions affecting the growth of CdTe layers were investigated. An analysis of XRD Gonio scans and RHEED patterns for CdTe layers have shown that to suppress twin formation in the CdTe layers, the growth has to be initiated at temperatures below

230 °C. It has been shown that the continuous growth of the CdTe layer following the nucleation with a slow temperature ramp of ~ 4 °C/min to 275°C resulted in a CdTe layer with a smooth surface and high crystal quality. The optimum Te/Cd flux ratio to obtain a CdTe layer simultaneously with a smooth surface and high crystal quality was determined to be as 3.45 from the results of the RHEED, HRXRD, PL, SE, defect decorative etching, and Nomarski microscopy. In addition, the inverse of the E_1 CP energy from the SE measurements has been found to be well correlated with the surface temperatures suggesting that it can be used for the temperature measurements during the growth of the CdTe layers.

The effect of the cyclic annealing with different temperature values was studied. A surface reconstruction from the bare (211) surface to Te-stabilized (211) surface was monitored at a surface temperature of 355±2 °C. An optimum annealing temperature to obtain a highly crystalline CdTe layer with good surface morphology was 411 °C. Increasing the annealing temperature above this value resulted in surface defects on the CdTe layer which was believed to be originating from the desorption of Cd and Te atoms from the surface.

A new approach to study the dislocations with different types of cores was applied to the zinc blende (211) crystal orientation [136]. Azimuthal XRD RC scans were performed to measure FWHM of RC from CdTe(422) reflections. A model based on dislocation induced broadening was used to fit XRD RC FWHM values. The model predicted two types of the dislocations which might be related to the dislocations with Te and Cd atoms in their cores. It has been shown that the growth and annealing conditions affect the density of the type A and type B dislocations in a different way. A correlation between the dislocation density of the type A and EPD values is established which might suggest that the Everson type etching reveals the dislocations with type A defects. Finally, it was determined that the experimental techniques probing the dislocation density in CdTe layers are not well correlated with each other due to the dual origin of the dislocations.

The compressive and biaxial stresses building in the CdTe layers due to growth and annealing conditions are resolved with the investigation of the optical properties of the CdTe layers.

REFERENCES

[1] D.A. Cusano. CdTe solar cells and photovoltaic heterojunctions in II-VI compounds. *Solid-State Electronics*, 6:217–218, 1963.

[2] Csaba Szeles. CdZnTe and CdTe materials for X-ray and gamma ray radiation detector applications. In *Physica Status Solidi (B) Basic Research*, volume 241, pages 783–790. WILEY-VCH Verlag, 2004.

[3] Y. Eisen and A. Shor. CdTe and CdZnTe materials for room-temperature X-ray and gamma ray detectors. *Journal of Crystal Growth*, 184-185:1302–1312, 1998.

[4] Kiefer J.E. and Yariv A. Electro-Optic Characteristics of CdTe at 3.39 and 10.6 um. *Applied Physics Letters*, 15(1):26–27, 1969.

[5] J. E. Kiefer, T. A. Nussmeier, and F. E. Goodwin. Intracavity CdTe Modulators for C02 lasers. *IEEE Journal of Quantum Electronics*, 8(2):173–179, 1972.

[6] M. G. Astles, H. Hill, G. Blackmore, S. Courtney, and N. Shaw. The sources and behaviour of impurities in LPE-grown (Cd,Hg)Te layers on CdTe(111) substrates. *Journal of Crystal Growth*, 91(1-2):1–10, 1988.

[7] J.E. Hails, G.J. Russell, A.W. Brinkman, and J. Woods. The effect of CdTe substrate orientation on the Movpe growth of CdxHg1-xTe. *Journal of Crystal Growth*, 79(1-3):940–945, 1986.

[8] J. M. Arias. Dislocation density reduction by thermal annealing of HgCdTe epilayers grown by molecular beam epitaxy on GaAs substrates. *Journal of Vacuum Science & Technology B: Microelectronics and Nanometer Structures*, 9(3):1646, 1991.

[9] W. E. Hoke, P. J. Lemonias, and R. Traczewski. Metalorganic vapor deposition of CdTe and HgCdTe epitaxial films on InSb and GaAs substrates. *Applied Physics Letters*, 44(11):1046–1048, 1984.

[10] R. Kay, R. Bean, K. Zanio, C. Ito, and D. McIntyre. HgCdTe photovoltaic detectors

on Si substrates. *Applied Physics Letters*, 51(26):2211–2212, 1987.

[11] R. Sporken, S. Sivananthan, K. K. Mahavadi, G. Monfroy, M. Boukerche, and J. P. Faurie. Molecular beam epitaxial growth of CdTe and HgCdTe on Si (100). *Applied Physics Letters*, 55(18):1879–1881, 1989.

[12] Antoni Rogalski. Infrared detectors: An overview. *Infrared Physics and Technology*, 43(3-5):187–210, 2002.

[13] P Norton. HgCdTe Infrared Detectors. *Opto-Electronics Review*, 10(3):159–174, 2002.

[14] Antoni Rogalski. HgCdTe infrared detector material: history, status and outlook. *Reports on Progress in Physics*, 68(10):2267–2336, 2005.

[15] P. Capper and J. W. Garland. *Mercury Cadmium Telluride*. John Wiley & Sons Ltd, Singapore, 2011.

[16] B F Jones. A reappraisal of the use of infrared thermal image analysis in medicine. *IEEE transactions on medical imaging*, 17(6):1019–1027, 1998.

[17] Ian Gatley, D L DePoy, and A M Fowler. Astronomical Imaging with Infrared Array Detectors. *Science*, 242(4883):pp. 1264–1270, 1988.

[18] Yusuf S. *HgCdTe Heterojunctions Grown by MBE for Infrared Detection Applications: An In Situ Doping Approach*. PhD thesis, University of Illinois at Chicago, 2004.

[19] W.D. Lawson, S. Nielsen, E.H. Putley, and A.S. Young. Preparation and properties of HgTe and mixed crystals of HgTe-CdTe. *Journal of Physics and Chemistry of Solids*, 9(3-4):325–329, 1959.

[20] Wen Lei, Jarek Antoszewski, and Lorenzo Faraone. Progress, challenges, and opportunities for HgCdTe infrared materials and detectors. *Applied Physics Reviews*, 2(4), 2015.

[21] J. P. Faurie and A. Million. Molecular beam epitaxy of II-VI compounds: CdHgTe.

Journal of Crystal Growth, 54(3):582–585, 1981.

[22] Michael A. Kinch. *State-of-the-art infrared detector technology*. SPIE Press, 2014.

[23] R.N. Jacobs, C. Nozaki, L.a. Almeida, M. Jaime-Vasquez, C. Lennon, J.K. Markunas, D. Benson, P. Smith, W.F. Zhao, D.J. Smith, C. Billman, J. Arias, and J. Pellegrino. Development of MBE II-VI Epilayers on GaAs(211)B. *Journal of Electronic Materials*, 41(10):2707–2713, 2012.

[24] J. D. Benson, L. O. Bubulac, P. J. Smith, R. N. Jacobs, J. K. Markunas, M. Jaime-Vasquez, L. a. Almeida, a. Stoltz, J. M. Arias, G. Brill, Y. Chen, P. S. Wijewarnasuriya, S. Farrell, and U. Lee. Growth and analysis of HgCdTe on alternate substrates. *Journal of Electronic Materials*, 41(10):2971–2974, 2012.

[25] S M Johnson, D R Rhiger, J P Rosbeck, J M Peterson, S M Taylor, and M E Boyd. Effect of dislocations on the electrical and optical properties of long-wavelength infrared HgCdTe photovoltaic detectors. *Journal of Vacuum Science & Technology B: Microelectronics and Nanometer Structures Processing, Measurement, and Phenomena*, 10(4):1499–1506, 1992.

[26] M. Carmody, A. Yulius, D. Edwall, D. Lee, E. Piquette, R. Jacobs, D. Benson, a. Stoltz, J. Markunas, a. Almeida, and J. Arias. Recent Progress in MBE Growth of CdTe and HgCdTe on (211)B GaAs Substrates. *Journal of Electronic Materials*, 41(10):2719–2724, 2012.

[27] J. D. Benson, L. O. Bubulac, C. M. Lennon, R. N. Jacobs, P. J. Smith, J. K. Markunas, M. Jaime-Vasquez, L. a. Almeida, a. Stoltz, J. a. Arias, G. Brill, Y. Chen, P. S. Wijewarnasuriya, M. F. Vilela, J. Peterson, S. M. Johnson, D. D. Lofgreen, D. Rhiger, E. a. Patten, and J. Bangs. Impurity gettering in (112)B HgCdTe/CdTe/alternate substrates. *Journal of Electronic Materials*, 42(11):3217–3223, 2013.

[28] L. He, L. Chen, Y. Wu, X.L. Fu, Y.Z. Wang, J. Wu, M.F. Yu, J.R. Yang, R.J. Ding, X.N. Hu, Y.J. Li, and Q.Y. Zhang. MBE HgCdTe on Si and GaAs substrates. *Journal of Crystal Growth*, 301-302:268–272, 2007.

[29] Y. Chen, S. Farrell, G. Brill, P. Wijewarnasuriya, and N. Dhar. Dislocation reduction in CdTe/Si by molecular beam epitaxy through in-situ annealing. *Journal of Crystal Growth*, 310(24):5303–5307, 2008.

[30] S. Farrell, G. Brill, Y. Chen, P. S. Wijewarnasuriya, Mulpuri V. Rao, N. Dhar, and K. Harris. Ex situ thermal cycle annealing of molecular beam epitaxy grown HgCdTe/Si layers. *Journal of Electronic Materials*, 39(1):43–48, 2010.

[31] A. J. Stoltz, J. D. Benson, M. Carmody, S Farrell, P. S. Wijewarnasuriya, G. Brill, R. Jacobs, and Y. Chen. Reduction of dislocation density in HgCdTe on Si by producing highly reticulated structures. *Journal of Electronic Materials*, 40(8):1785–1789, 2011.

[32] T. Seldrum, R. Bommena, L. Samain, J. Dumont, S. Sivananthan, and R. Sporken. Selective growth of CdTe on patterned CdTe/Si(211). *Journal of Vacuum Science & Technology B: Microelectronics and Nanometer Structures*, 26(3):1105, 2008.

[33] WA Harrison, EA Kraut, JR Waldrop, and RW Grant. Polar heterojunction interfaces. *Physical Review B*, 18(8):4402–4410, 1978.

[34] John Ayers. *Heteroepitaxy of Semiconductors*. CRC Press, New York, 2007.

[35] J H Bahng, M S Jang, M Lee, J C Choi, H L Park, K J Kim, and C Lee. Strain dependence and deformation potential of the E 1 and E 1 D 1 transitions of ZnTe grown on a GaAs (001) substrate. 120:343–346, 2001.

[36] M. S. Jang, S. H. Oh, K. H. Lee, J. H. Bahng, J. C. Choi, K. H. Jeong, H. L. Park, D. C. Choo, D. U. Lee, and T. W. Kim. The dependence of the strain effects on the ZnTe layer thicknesses in ZnTe/GaAs heterostructures. *Journal of Physics and Chemistry of Solids*, 64(2):357–360, 2003.

[37] Yong Chang, C. R. Becker, C. H. Grein, J. Zhao, C. Fulk, T. Casselman, R. Kiran, X. J. Wang, E. Robinson, S. Y. An, S. Mallick, S. Sivananthan, T. Aoki, C. Z. Wang, D. J. Smith, S. Velicu, J. Zhao, J. Crocco, Y. Chen, G. Brill, P. S. Wijewarnasuriya, N. Dhar, R. Sporken, and V. Nathan. Surface morphology and defect formation mechanisms for HgCdTe (211)B grown by molecular beam epitaxy.

Journal of Electronic Materials, 37(9):1171–1183, 2008.

[38] Derek Hull, J.D. Bacon, and Materials. *Introduction to Dislocations*, volume 1. Elsevier Ltd., 2011.

[39] Y. Chen. *Molecular beam epitaxy growth of high quality cadmium telluride on silicon*. Ph.d. thesis, University of Illinois at Chicago, 1995.

[40] E Peissker, P Haasen, and H Alexander. Anisotropic plastic deformation of indium antimonide. *Philos. Mag.*, 7(80):1279–1303, 1962.

[41] R. L. Bell and A. F. W. Willoughby. Etch-pit studies of dislocations in indium antimonide. *Journal of Materials Science*, 1(3):219–228, 1966.

[42] T. Ninomiya. Velocities and internal friction of dislocations in III-V compounds. *Le Journal de Physique Colloques*, 40(C6):C6–143–C6–145, 1979.

[43] J. Petruzzello and M. R. Leys. Effect of the sign of misfit strain on the dislocation structure at interfaces of heteroepitaxial GaAsP films. *Applied Physics Letters*, 53(24):2414–2416, 1988.

[44] H. Alexander. Models of dislocation structure. *Le Journal de Physique Colloques*, 40(C6):C6–1–C6–6, 1979.

[45] M. Peach and J. S. Koehler. The forces exerted on dislocations and the stress fields produced by them. *Physical Review*, 80(3):436–439, 1950.

[46] Peter. Capper. *Properties of narrow gap cadmium-based compounds*, volume 8. IEE, INSPEC, London, 1994.

[47] M. Berding. Native defects in CdTe. *Physical Review B*, 60(12):8943–8950, 1999.

[48] Xiaowang Zhou, Donald K Ward, Bryan M Wong, F Patrick Doty, and Jonathan A Zimmerman. Molecular dynamics studies of dislocations in CdTe crystals from a new bond order potential. *Journal of Physical Chemistry C*, 116(33):17563–17571, 2012.

[49] J. L. Reno, M. J. Carr, and P. L. Gourley. The growth of high quality CdTe on GaAs by molecular beam epitaxy. *Journal of Vacuum Science & Technology A: Vacuum, Surfaces, and Films*, 8(2):1006–1012, 1990.

[50] M. Jaime-Vasquez, M. Martinka, R. N. Jacobs, and M. Groenert. In-situ spectroscopic study of the As and Te on the Si (112) surface for high-quality epitaxial layers. *Journal of Electronic Materials*, 35(6):1455–1460, 2006.

[51] Y. Nakamura, N. Otsuka, M. D. Lange, R. Sporken, and J. P. Faurie. Origin of dual epitaxy in the growth of CdTe on (211) GaAs. *Applied Physics Letters*, 60(211):1372–1374, 1992.

[52] S M Johnson, J B James, W L Ahlgren, W J Hamilton, M Ray, and G S Tompa. Mater. Res. Soc. Symp. Proc. Mater. Res. Soc. Pittsburgh, PA, 1991.

[53] S Y Woo, G A Devenyi, and R N Kleiman. Tilted epitaxy on (211) -oriented substrates. *Applied Physics Letters*, 132103:1–5, 2013.

[54] P. B. Rago, F. C. Jain, and J. E. Ayers. Effect of epilayer tilt on dynamical x-ray diffraction from uniform heterostructures with asymmetric dislocation densities. *Journal of Electronic Materials*, 42(11):3066–3070, 2013.

[55] Dieter Bonnet and Peter Meyers. Cadmium-telluride:Material for thin film solar cells. *Journal of Materials Research*, 13(10):2740–2753, 1998.

[56] A Y Cho. Morphology of Epitaxial Growth of GaAs by a Molecular Beam Method: The Observation of Surface Structures. *Journal of Applied Physics*, 41:2780, 1970.

[57] N. K. Dhar, P. R. Boyd, M. Martinka, J. H. Dinan, L. a. Almeida, and N. Goldsman. CdZnTe heteroepitaxy on 3 inch (112) Si: Interface, surface, and layer characteristics. *Journal of Electronic Materials*, 29(6):748–753, 2000.

[58] K Seshan. *Handbook of Thin Film Deposition*. Materials Science and Process Technology. Elsevier Science, 2001.

[59] C. Lavoie. Diffuse optical reflectivity measurements on GaAs during molecular-beam

epitaxy processing. *Journal of Vacuum Science & Technology A: Vacuum, Surfaces, and Films*, 10(4):930, 1992.

[60] L. A. Kosyachenko, V. M. Sklyarchuk, O. V. Sklyarchuk, and O. L. Maslyanchuk. Band gap of CdTe and Cd0.9Zn0.1Te crystals. *Semiconductors*, 45(10):1273–1280, 2011.

[61] Bart V Van Zeghbroeck. *Principles of Semiconductor Devices and Heterojunctions*. Prentince Hall, 2009.

[62] John A. Venables. *Introduction to Surface and Thin Film Processes*. Cambridge University Press, Cambridge, 2000.

[63] Ernst Bauer. Phänomenologische Theorie der Kristallabscheidung an Oberflächen. *Zeitschrift für Kristallographie*, 110:395–431, 1958.

[64] Ayahiko Ichimiya and Philip I Cohen. *Reflection high-energy electron diffraction*. Cambridge University Press, 2004.

[65] J. J. Sakurai. *Modern Quantum Mechanics, Revised Edition*. Pearson Ltd, 1995.

[66] Michael P. Marder. *Condensed Matter Physics, Second Edition*. John Wiley & Sons Ltd, 2011.

[67] C. Celebi, O. Arı, and R. T. Senger. Cleavage induced rows of missing atoms on ZnTe (110) surface. *Physical Review B*, 87(8):85308, 2013.

[68] P F Fewster. *X-ray Scattering from Semiconductors*. Imperial College Press, 2000.

[69] E Chason, T Mayer, E. Chason Mayer, and T.M. Mayer. Thin Film and Surface Characterization by Specular X-Ray Reflectivity. *Critical Reviews in Solid State and Materials Sciences*, 22(1):1–67, 1997.

[70] J. Wolstenholme J. F. Watts. *An introduction of Surface Analysis and XPS*. John Wiley & Sons, Ltd, 2003.

[71] C. L. Hinkle, M. Milojevic, B. Brennan, a. M. Sonnet, F. S. Aguirre-Tostado, G. J.

Hughes, E. M. Vogel, and R. M. Wallace. Detection of Ga suboxides and their impact on III-V passivation and Fermi-level pinning. *Applied Physics Letters*, 94(16):162101, 2009.

[72] Mathias Schubert. *Infrared Ellipsometry on Semiconductor Layer Structures*. Springer, 2005.

[73] Hiroyuki Fujiwara. *Spectroscopic Ellipsometry - Principles and Applications*. John Wiley & Sons Ltd, West Sussex, 2007.

[74] Gerald D. Mahan. *Many-Particle Physics*. Springer US, Boston, MA, 1990.

[75] Jaesun Lee, N C Giles, West Virginia, and D Rajavel. Room-temperature band-edge photoluminescence from cadmium telluride. *Physical Review B*, 49(3), 1994.

[76] Robert Furstenberg and Jeffrey O. White. Photoluminescence study of the 1.3-1.55 eV defect band in CdTe. *Journal of Crystal Growth*, 305(1):228–236, 2007.

[77] Peter Jonathan Eaton and Paul West. *Atomic force microscopy*. Oxford University Press, 2010.

[78] D.A. Allwood, S. Cox, N.J. Mason, R. Palmer, R. Young, and P.J. Walker. Monitoring epiready semiconductor wafers. *Thin Solid Films*, 412(1-2):76–83, 2002.

[79] T. Van Buuren, M. K. Weilmeier, I. Athwal, K. M. Colbow, J. A. Mackenzie, P. C. Wong, and K. A. R. Mitchell. Oxide thickness effect and surface roughening of the oxide from GaAs. *Applied Physics Letters*, 59(4):464–466, 1991.

[80] A.J. Spring Thorpe and S.J. Ingrey. Measurement of GaAs surface oxide desorption temperatures. *Applied Physics Letters*, 50(2):77–79, 1987.

[81] J.J.D. Lee, K.W. West, K.W. Baldwin, and L.N. Pfeiffer. Smoothness and cleanliness of the GaAs (100) surface after thermal desorption of the native oxide for the synthesis of high mobility structures using molecular beam epitaxy. *Journal of Crystal Growth*, 356:46–52, 2012.

[82] Guillén-Cervantes, Z. Rivera-Alvarez, M. López-López, E. López-Luna, and

I Hernández-Calderón. GaAs surface oxide desorption by annealing in ultra high vacuum. *Thin Solid Films*, 373(1-2):159–163, 2000.

[83] N. Isomura, S. Tsukamoto, K. Iizuka, and Y. Arakawa. Investigation on GaAs(001) surface treated by As-free high temperature surface cleaning method. *Journal of Crystal Growth*, 301-302:26–29, 2007.

[84] S. C. Ghosh, M. C. Biesinger, R. R. LaPierre, and P. Kruse. The role of proximity caps during the annealing of UV ozone oxidized GaAs. *Journal of Applied Physics*, 101(11):114321, 2007.

[85] C.C Surdu-Bob, S.O Saied, and J.L Sullivan. An X-ray photoelectron spectroscopy study of the oxides of GaAs. *Applied Surface Science*, 183(1-2):126–136, 2001.

[86] Stefan Zollner. Model dielectric functions for native oxides on compound semiconductors. *Applied Physics Letters*, 63(18):2523–2524, 1993.

[87] David Fuster, Laia Ginés, Yolanda González, Jesús Herranz, and Luisa González. Low temperature oxide desorption in GaAs (111)A substrates. *Thin Solid Films*, 537:70–75, 2013.

[88] Liu Feng, Lian-dong Zhang, Hui Liu, Xiang Gao, Zhuang Miao, Hong-chang Cheng, Long Wang, and Sen Niu. Characterization study of native oxides on GaAs(100) surface by XPS. *Proceedings of SPIE*, 8912(100):89120N, 2013.

[89] L. H. Li, E. H. Linfield, R. Sharma, and a. G. Davies. In-assisted desorption of native GaAs surface oxides. *Applied Physics Letters*, 99(6):2–5, 2011.

[90] Yuichi Ide. Role of Ga2O in the removal of GaAs surface oxides induced by atomic hydrogen. *Journal of Vacuum Science & Technology A: Vacuum, Surfaces, and Films*, 12(4):1858, 1994.

[91] Z. R. Wasilewski, J.-M. Baribeau, M. Beaulieu, X. Wu, and G. I. Sproule. Studies of oxide desorption from GaAs substrates via Ga[sub 2]O[sub 3] to Ga[sub 2]O conversion by exposure to Ga flux. *Journal of Vacuum Science & Technology B: Microelectronics and Nanometer Structures*, 22(3):1534, 2004.

[92] Y. S. Ryu, T. W. Kang, and T. W. Kim. Structural properties and interfacial atomic arrangements in CdTe thin films grown on GaAs (211) B substrates. *Journal of Materials Science*, 40(17):4699–4702, 2005.

[93] F Bastiman, R Hogg, M Skolnick, a G Cullis, and M Hopkinson. Temperature dependence of Ga-assisted oxide desorption on GaAs(001). *Journal of Physics: Conference Series*, 209:012066, 2010.

[94] Jae Jin Kim, R. N. Jacobs, L. a. Almeida, M. Jaime-Vasquez, C. Nozaki, and David J. Smith. TEM Characterization of HgCdTe/CdTe Grown on GaAs(211)B Substrates. *Journal of Electronic Materials*, 42(11):3142–3147, 2013.

[95] J. Reece Roth. Plasma Etching. In *Industrial Plasma Engineering*, pages 540–613. Taylor & Francis, 2001.

[96] D. A. Allwood, R. T. Carline, N. J. Mason, C. Pickering, B. K. Tanner, and P. J. Walker. Characterization of oxide layers on GaAs substrates. *Thin Solid Films*, 364(1):33–39, 2000.

[97] Jan Paul Antoni der Wagt. *Reflection High Energy Electron Diffraction during Molecular Beam Epitaxy*. PhD thesis, Stanford University, 1994.

[98] G Hollinger, R Skheyta-Kabbani, and M Gendry. Oxides on GaAs and InAs surfaces: An x-ray-photoelectron-spectroscopy study of reference compounds and thin oxide layers. *Phys. Rev. B*, 49(16):11159–11167, 1994.

[99] W. Storm, D. Wolany, F. Schröder, G. Becker, B. Burkhardt, L. Wiedmann, and A. Benninghoven. Analysis of stoichiometry and oxide growth of HF treated GaAs (100) by x-ray photoelectron spectroscopy and time-of-flight secondary ion mass spectrometry. *Journal of Vacuum Science & Technology B*, 12(1):147–153, 1994.

[100] E. A. Albanesi, S. J. Sferco, I. Lefebvre, G. Allan, and G. Hollinger. Electronic structure of binary and ternary Ga or As oxides. *Physical Review B*, 46(20):13260–13267, 1992.

[101] John T. Wolan, Charles K. Mount, and Gar B. Hoflund. Room-temperature oxidation of a GaAs(001) surface induced by the interaction of hyperthermal atomic oxygen and studied by x-ray photoelectron spectroscopy and ion scattering spectroscopy. *Applied Physics Letters*, 72(12):1469–1471, 1998.

[102] J. E. Ayers. Measurement of threading dislocation densities in semiconductor crystals by X-ray diffraction. *Journal of Crystal Growth*, 135(1-2):71–77, 1994.

[103] J. H. Lee, Zh. M. Wang, and G. J. Salamo. Survival of atomic monolayer steps during oxide desorption on GaAs (100). *Journal of Applied Physics*, 100(11):114330, 2006.

[104] F. Bastiman, J.C. Lin, a.G. Cullis, R. Hogg, and M. Skolnick. Ga assisted oxide desorption on GaAs(001) studied by scanning tunnelling microscopy. *Journal of Crystal Growth*, 312(10):1687–1692, 2010.

[105] Y. Asaoka. Desorption process of GaAs surface native oxide controlled by direct Ga-beam irradiation. *Journal of Crystal Growth*, 251(1):40–45, 2003.

[106] D. M. Schaadt, D. Z. Hu, and K. H. Ploog. Stress evolution during ripening of self-assembled InAs/GaAs quantum dots. *Journal of Vacuum Science & Technology B: Microelectronics and Nanometer Structures*, 24(4):2069, 2006.

[107] Evan H C Parker. *The technology and physics of molecular beam epitaxy*. Plenum Press New York, 1985.

[108] C.M. M. Lennon, L.a. a. Almeida, R.N. N. Jacobs, J.K. K. Markunas, P.J. J. Smith, J. Arias, a.E. E. Brown, and J. Pellegrino. Real-Time In Situ Monitoring of GaAs (211) Oxide Desorption and CdTe Growth by Spectroscopic Ellipsometry. *Journal of Electronic Materials*, 41(10):2965–2970, 2012.

[109] A A Lyamkina, Y G Galitsyn, D V Dmitriev, S P Moshchenko, and A I Toropov. Two-stage nucleation of indium droplets on GaAs (001) substrate. In *2009 International Conference and Seminar on Micro/Nanotechnologies and Electron Devices*, pages 40–42, 2009.

[110] Li He, Xiangliang Fu, Qingzhu Wei, Weiqiang Wang, Lu Chen, Yan Wu, Xiaoning Hu, Jianrong Yang, Qinyao Zhang, Ruijun Ding, Xiaoshuang Chen, and Wei Lu. MBE HgCdTe on alternative substrates for FPA applications. *Journal of Electronic Materials*, 37(9):1189–1199, 2008.

[111] M. Jaime-Vasquez, R. N. Jacobs, C. Nozaki, J. D. Benson, L. a. Almeida, J. Arias, and J. Pellegrino. Understanding the evolution of CdTe buffer layer surfaces on ZnTe/Si(211) and GaAs(211)B during cyclic annealing. *Journal of Electronic Materials*, 41(10):2975–2980, 2012.

[112] W. J. Everson, C. K. Ard, J. L. Sepich, B. E. Dean, G. T. Neugebauer, and H. F. Schaake. Etch pit characterization of CdTe and CdZnTe substrates for use in mercury cadmium telluride epitaxy. *Journal of Electronic Materials*, 24(5):505–510, 1995.

[113] R. J. Koestner and H. F. Schaake. Kinetics of molecular-beam epitaxial HgCdTe growth. *Journal of Vacuum Science & Technology A: Vacuum, Surfaces, and Films*, 6(4):2834–2839, 1988.

[114] M. D. Lange, R. Sporken, K. K. Mahavadi, J. P. Faurie, Y. Nakamura, and N. Otsuka. Molecular beam epitaxy and characterization of CdTe(211) and CdTe(133) films on GaAs(211)B substrates. *Applied Physics Letters*, 58(18):1988–1990, 1991.

[115] Yuan-Zhang Wang, Lu Chen, Yan Wu, Jun Wu, Mei-Fang Yu, and Li He. Heteroepitaxy of CdTe on tilting Si(211) substrates by molecular beam epitaxy. *Journal of Crystal Growth*, 290(2):436–440, 2006.

[116] N. K. Dhar, M. Zandian, J. G. Pasko, J. M. Arias, and J. H. Dinan. Planar p-on-n HgCdTe heterostructure infrared photodiodes on Si substrates by molecular beam epitaxy. *Applied Physics Letters*, 70(13), 1997.

[117] W. F. Zhao, R. N. Jacobs, M. Jaime-Vasquez, L. O. Bubulac, and David J. Smith. Microstructural Characterization of CdTe(211)B/ZnTe/Si(211) Heterostructures Grown by Molecular Beam Epitaxy. *Journal of Electronic Materials*, 40(8):1733–1737, 2011.

[118] S.M. Johnson, J.B. James, W.L. Ahlgren, W.J. Hamilton, M. Ray, and G.S. TOMPA. Heteroepitaxial HgCdTe/CdZnTe/GaAs/Si Materials for Infrared Focal Plane Arrays. *MRS Proceedings*, 216:141, 1990.

[119] J.E. Ayers, S.K. Ghandhi, and L.J. Schowalter. Crystallographic tilting of heteroepitaxial layers. *Journal of Crystal Growth*, 113(3-4):430–440, 1991.

[120] Ferenc Riesz. Rotated tilting in lattice-mismatched heteroepitaxial systems. *Journal of Crystal Growth*, 140(1-2):213–218, 1994.

[121] G. H. Olsen and R. T. Smith. Misorientation and tetragonal distortion in heteroepitaxial vapor-Grown III-V structures. *Physica Status Solidi (a)*, 31(2):739–747, 1975.

[122] T. Sasaki. Study of CdTe epitaxial growth on (211)B GaAs by molecular-beam epitaxy. *Journal of Vacuum Science & Technology B: Microelectronics and Nanometer Structures*, 10(4):1399, 1992.

[123] S. Rujirawat, David J. Smith, J. P. Faurie, G. Neu, V. Nathan, and S. Sivananthan. Microstructural and optical characterization of CdTe(211)B/ZnTe/Si(211) grown by molecular beam epitaxy. *Journal of Electronic Materials*, 27(9):1047–1052, 1998.

[124] Wan Jian Yin, Ji Hui Yang, Katherine Zaunbrecher, Tim Gessert, Teresa Barnes, Yanfa Yan, and Su Huai Wei. Surface stability and the selection rules of substrate orientation for optimal growth of epitaxial II-VI semiconductors. *Applied Physics Letters*, 107(14), 2015.

[125] Giacomo Badano, Xavier Baudry, and Ivan C. Robin. In situ spectroscopic ellipsometry of rough surfaces: Application to CdTe(211)B/Ge(211) grown by molecular-beam epitaxy. *Journal of Electronic Materials*, 38(8):1652–1660, 2009.

[126] J. D. Benson, R. N. Jacobs, J. K. Markunas, M. Jaime-Vasquez, P. J. Smith, L. a. Almeida, M. Martinka, M. F. Vilela, and U. Lee. Structural analysis of CdTe hetero-epitaxy on (211) Si. *Journal of Electronic Materials*, 37(9):1231–1236, 2008.

[127] Ys Wu, Cr Becker, a Waag, Mm Kraus, Rn Bicknell-Tassius, and G Landwehr. Correlation of the Cd-to-Te ratio on CdTe surfaces with the surface structure. *Physical review. B, Condensed matter*, 44(16):8904–8911, 1991.

[128] Giacomo Badano, Patrice Gergaud, Ivan C. Robin, Xavier Baudry, Benoît Amstatt, and Fredérique Gemain. Lattice relaxation and dislocation reduction in MBE CdTe(211)B/Ge(211). *Journal of Electronic Materials*, 39(7):908–911, 2010.

[129] C. M. Lennon, L. a. Almeida, R. N. Jacobs, J. D. Benson, P. J. Smith, J. K. Markunas, J. Arias, and J. Pellegrino. The Surface Kinetics of MBE-Grown CdTe (211)B During In Situ Cyclic Annealing. *Journal of Electronic Materials*, 42(11):3344–3348, 2013.

[130] J. D. Benson, a. J. Stoltz, J. B. Varesi, L. a. Almeida, E. P. G. Smith, S. M. Johnson, M. Martinka, a. W. Kaleczyc, J. K. Markunas, P. R. Boyd, and J. H. Dinan. Surface structure of plasma-etched (211)B HgCdTe. *Journal of Electronic Materials*, 34(6):726–732, 2005.

[131] P J Dean, G M Williams, and G Blackmore. Novel type of optical transition observed in MBE grown CdTe. *Journal of Physics D: Applied Physics*, 17(11):2291–2300, 2000.

[132] Shujie Wu, Yonghai Chen, Jinling Yu, Hansong Gao, Chongyun Jiang, Jianliang Huang, Yanhua Zhang, Yang Wei, and Wenquan Ma. In-plane optical anisotropy of InAs/GaSb superlattices with alternate interfaces. *Nanoscale Research Letters*, 8(1):298, 2013.

[133] RuÌêdiger Lange, Kelly E. Junge, Stefan Zollner, S. S. Iyer, a. P. Powell, and K. Eberl. Dielectric response of strained and relaxed Si1-x-yGexCy alloys grown by molecular beam epitaxy on Si(001). *Journal of Applied Physics*, 80(8):4578, 1996.

[134] G. Brill, Y. Chen, N. K. Dhar, and R. Singh. Nucleation of ZnTe/CdTe epitaxy on high-miller-index Si surfaces. *Journal of Electronic Materials*, 32(7):717–722, 2003.

[135] Renjie Gu, Chuan Shen, Yuying Guo, Weiqiang Wang, Xiangliang Fu, and Lu Chen.

In situ thickness and temperature measurements of CdTe grown by molecular beam epitaxy on GaAs substrate. *Journal of Vacuum Science & Technology B: Microelectronics and Nanometer Structures*, 30(4):041203, 2012.

[136] B. Yarlagadda, A. Rodriguez, P. Li, R. Velampati, J. F. Ocampo, E. N. Suarez, P. B. Rago, D. Shah, J. E. Ayers, and F. C. Jain. X-ray characterization of dislocation density asymmetries in heteroepitaxial semiconductors. *Applied Physics Letters*, 92(20), 2008.

[137] A. F. Schwartzman and R. Sinclair. Metastable and Equilibrium Defect Structure of II-VI / GaAs Interfaces. 20(10), 1991.

VITA

Date and Place of Birth: 19.10.1981, Bandırma-TURKEY

EDUCATION

Doctor of Philosophy in Physics, 2017

Graduate School of Engineering and Sciences, İzmir Institute of Technology,
İzmir -Turkey
Thesis Title: **Molecular Beam Epitaxy Growth and Characterization of CdTe Heterostructures on GaAs- Effect of Interface, Growth, and Annealing Conditions to Crystal Quality**
Supervisor: Prof. Dr. Orhan Öztürk
Co-Supervisor: Prof. Dr. Sivalingam Sivananthan
Previous-Supervisor: Assist. Prof. Dr. Yusuf Selamet

Master of Science in Physics, 2011

Graduate School of Engineering and Sciences, İzmir Institute of Technology,
İzmir -Turkey
Thesis Title: **Electronic, Spintronic, and Transport Properties of Carbon Based Nanowires**
Supervisor: Prof. Dr. Ramazan Tuğrul Senger

Bachelor of Physics, 2009

Department of Physics, Faculty of Science, Ege University,
İzmir - Turkey

PUBLICATIONS

1. M. Polat, O. Arı, O. Ozturk, Y. Selamet, Mat. Res. Exp., 4, 3, 35904, 2017.
2. O. Arı, E. Bilgilisoy, E. Ozceri, Y. Selamet, JoEM, 45, 10, 4736, 2016.
3. M. Karakaya, E. Bilgilisoy, O. Arı Y. Selamet, AIP Adv., 6 ,7, 075111, 2016
4. O. Arı, M. Polat, M. Karakaya, Y. Selamet, Phys Status Solidi C, 12, 9-11, 1211 2015.

Other Publications

5. A. Yanilmaz, A. Tomak, B. Akbali, C. Bacaksiz, E. Ozceri, O. Arı, R.T. Senger, Y. Selamet, H.M. Zareie, RSC Advances, 7, 45, 28383, 2017
6. C. Celebi, O. Arı, R.T. Senger, PRB, 87, 8, 085308, 2013.